



**WECC**

---

**Modes of Inter-Area Power Oscillations in the  
Western Interconnection**

Western Interconnection Modes Review Group

2021

## Executive Summary

Power system electromechanical oscillatory behavior is an inherent characteristic of the synchronous machines that are interconnected through transmission systems. As the system stress increases during high power transfers or system component outages, these oscillations can become undamped, creating a reliability risk. Inter-area oscillation is a wide-area phenomenon that involves generators in distant regions and affects several transmission paths. For example, north-south inter-area oscillation in the Western Interconnection involves generators in Canada and the Pacific Northwest oscillating against generators in the Desert Southwest and Southern California and is manifested in power swings on the California–Oregon Intertie (Path 66), Northwest–British Columbia (Path 3), and Northern–Southern California (Path 26). System planners need to understand the modes of oscillation so they can properly model them in studies and develop operating procedures and mitigation measures.

This document provides an up-to-date quantitative and qualitative description of the major modes of inter-area oscillation in the Western Interconnection. It is an update of the 2014 WECC Modes Report. The analyses in this report are based on two WECC transient stability base cases and many system-wide phasor measurement units (PMU) datasets collected from 2016 through 2019. This report is the most comprehensive and up-to-date assessment of the Western Interconnection’s electromechanical modes. The table below summarizes the properties of the system-wide modes within the Western Interconnection. Our overall understanding of the North-South A (NSA), North-South B (NSB), East-West A (EWA), and Montana (MT) modes is now well established. This report has especially improved our understanding of the EWA and Montana modes. Better comprehension of the excitability of the EWA mode is still needed.

**Summary of mode properties.**

Mode	Freq. (Hz)	Shape	Interaction Path(s)	Controllability	Grade	Comments
NSA	0.20–0.30	Alberta vs. System	Alberta–BC (Path 1) Northwest–CA (Path 3)	Alberta	Well understood	Well understood from 2014 report. Analysis for 2021 report confirms 2014 conclusions. An Alberta disconnect causes this mode to disappear.
NSB	0.35–0.45	Alberta vs. (BC + N. U.S.) vs. S. U.S.	COI (Path 66)	Widespread, incl. PDCI	Well understood	The most widespread mode in the system. An Alberta disconnect causes mode frequency and damping to decrease.
EWA	0.35–0.45	(Colorado + E. Wyo.) vs. System	Wyoming–ID (Path 19) Colorado–UT (Path 30) Colorado–NM (Path 31)	Colorado area	Marginally understood	Close in frequency to the NSB mode. Extensive new knowledge in 2021 report.
BCA	0.50–0.72	BC vs. N. U.S. vs. S. U.S.	Unknown	Unknown	Not understood	Model studies hypothesize two BC modes. Need improved PMU coverage in western BC (e.g., Kemanan).
BCB	0.60–0.72	W. edge vs. System vs. E. edge	Unknown	Unknown	Not understood	(See above.)

## Modes of Inter-Area Power Oscillations in the Western Interconnection

---

MT	0.70–0.90	Montana vs. System	Montana–NW (Path 8)	Montana, incl. Colstrip	Well understood	Sometimes confused with one of the BC modes. Extensive new knowledge in 2021 report.
----	-----------	--------------------	---------------------	-------------------------	-----------------	--

---

To date, our understanding of the British Columbia (BC) modes is poor. Based on simulation studies, this report hypothesizes the existence of two BC modes. One PMU measurement dataset confirms the properties of one of these modes. Although this report includes model-based analysis of the controllability and interaction paths for these modes, these results should be regarded as preliminary until they can be confirmed using field measurements.

Future work recommendations include:

1. Continued monitoring of all the modes from PMU measurements and field tests. This includes major switching events, system faults, major generation losses (with and without faults), and probing tests conducted using the Pacific DC Intertie (PDCI) and the Chief Joseph braking resistor.
2. Collection of high-quality synchrophasor data at Kemano/Minette for field tests designed to better excite the BC modes. Compare those measurements with data recorded at Shrum, Revelstoke, Cranbrook, and the surrounding Pacific Northwest. Large ambient datasets and event datasets are both desired.
3. Development and analysis of several simulation datasets designed to excite and investigate the BC area modes.
4. Assessment of cases in which Alberta is weakly connected to the rest of the system. Development of simulation base cases that reflect the operating conditions of interest. Collection and analysis of actual system data in which those conditions were observed.
5. Development of transient simulation base cases with initial power flow conditions coincident with system conditions in PMU-based datasets.
6. Include EHV fault analysis conducted via simulation. Sensitivity analysis is needed for single-line-to-ground, line-to-line, and three-phase faults. Sensitivity is also desired for normal clearing times and backup clearing times. This is expected to become more important with higher penetrations of inverter-based resources.
7. Investigating the excitability, controllability, and interaction paths of the modes with more detail using simulation studies. Initial analysis is presented in this report, but more work is needed to better refine the conclusions.
8. Development and testing of production-grade mode meter settings for the EWA and MT modes.
9. Studying the effect of the potential retirement of Colstrip units on the characteristics of the MT mode.
10. Conducting a study to investigate the effect of future grid configurations and resource dispatch patterns on the system modes. This study should consider the addition of new inverter-based



## Modes of Inter-Area Power Oscillations in the Western Interconnection

resources (IBR) and the retirement of existing generation. As accepted standards for IBR modeling are established, this study should be initiated. An initial study conducted by the Pacific Northwest National Laboratory (PNNL) is summarized in Appendix C: The Impact of Future Grid Configurations.

11. Continue efforts to share real-time inter-area oscillation detection data amongst utilities and Reliability Coordinators to validate the analysis tools.
12. Collaborate on data integrity issues related to the transmission of timing signals from the Global Positioning System (GPS) to satellite-synchronized clocks used by PMUs. Clock errors, GPS spoofing, and military activities can affect timing and are a concern. Some utilities are considering transitioning to centralized clocks with propagating signals to mitigate these risks.



## Table of Contents

<b>Introduction</b> .....	<b>1</b>
Simulation Models .....	2
Simulated Points of Measurement.....	4
Inter-Area Modes of the Western Interconnection.....	6
<b>Theoretical Background and Analysis Methods</b> .....	<b>8</b>
Electromechanical Dynamics.....	8
Correlation Analysis.....	10
Mode Meter Analysis.....	11
Ringdown Analysis.....	12
Direct Eigenanalysis.....	13
<b>North-South A Mode</b> .....	<b>14</b>
Mode Description.....	14
Mode Properties Measured from Simulation Models.....	15
Mode Properties Measured from PMU Data .....	18
Future Work.....	24
<b>North-South B Mode</b> .....	<b>25</b>
Mode Description.....	25
Mode Properties Measured from Simulation Models.....	25
Mode Properties Measured from PMU Data .....	29
Future Work.....	38
<b>East-West A Mode</b> .....	<b>38</b>
Mode Description.....	38
Mode Properties Measured from Simulation Models.....	38
Mode Properties Measured from PMU Data .....	42
Future Work.....	53
<b>BC Mode(s)</b> .....	<b>54</b>
Mode Description.....	54
BC Mode A Description .....	54



# Modes of Inter-Area Power Oscillations in the Western Interconnection

BC Mode B Description .....	58
Mode Properties Measured from PMU Data .....	61
Future Work.....	62
<b>Montana Mode.....</b>	<b>62</b>
Mode Description.....	62
Mode Properties Measured from Simulation Models.....	63
Mode Properties Measured from PMU Data .....	66
Future Work.....	70
<b>Conclusions and Future Work .....</b>	<b>71</b>
<b>Participants .....</b>	<b>73</b>
<b>References .....</b>	<b>74</b>
<b>Appendix A: Electromechanical Dynamic Theory.....</b>	<b>77</b>
The Physics of Electromechanical Dynamics .....	77
Foundations of Systems Theory.....	80
Modal Decomposition .....	81
<b>Appendix B: Analysis Methods .....</b>	<b>85</b>
Correlation Analysis .....	85
Mode Meter Analysis.....	87
Ringdown Analysis.....	91
Direct Eigenanalysis.....	94
<b>Appendix C: The Impact of Future Grid Configurations .....</b>	<b>97</b>
Preface.....	97
Introduction .....	98
Simulation Scenario Design.....	98
Generic Model Used for Inverter-Based Resources.....	100
Results and Discussion.....	103
Future Work on Systems with High RES Penetrations.....	108
<b>Appendix D: NSA Mode Analyses .....</b>	<b>109</b>
Correlation Analysis from 2016 through 2019 PMU Data.....	109



## Modes of Inter-Area Power Oscillations in the Western Interconnection

Mode Meter Analysis Results.....	122
Ringdown Analysis Results.....	124
<b>Appendix E: NSB Mode Analyses.....</b>	<b>127</b>
Correlation Analysis from 2016 through 2019 PMU Data.....	127
Mode Meter Analysis Results.....	140
Ringdown Analysis Results.....	142
<b>Appendix F: EWA Mode Analyses.....</b>	<b>147</b>
Correlation Analysis from 2016 through 2019 PMU Data.....	147
Mode Meter Analysis Results.....	161
<b>Appendix G: MT Mode Analyses.....</b>	<b>164</b>
Correlation Analysis from 2016 through 2019 PMU Data.....	164
Mode Meter Analysis Results.....	178



Introduction

Power system electromechanical oscillatory behavior is an inherent characteristic of the synchronous machines that are interconnected by transmission systems. As the system stress increases during high power transfers or system component outages, these oscillations can become undamped, creating a risk of power system outages such as occurred on August 10, 1996 [1]; see Figure 1.

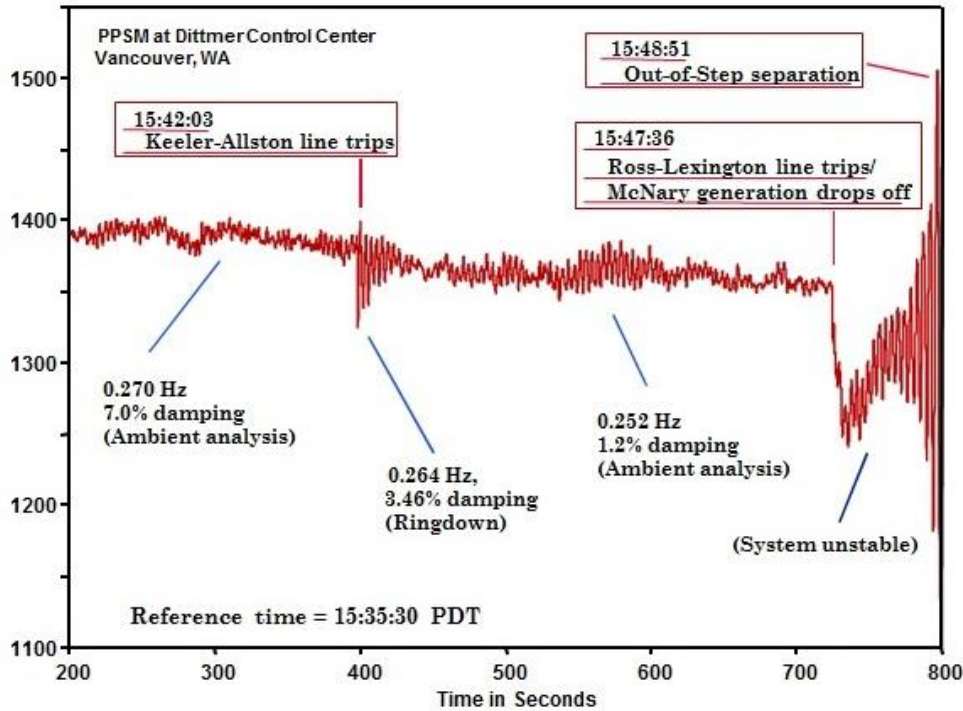


Figure 1: Malin-Round Mountain #1 MW flow during the Aug. 10, 1996, disturbance.

Inter-area oscillation is a wide-area phenomenon that involves generators in distant regions and affects several transmission paths. For example, north-south inter-area oscillation in the Western Interconnection involves generators in Canada and the Pacific Northwest oscillating against generators in the Desert Southwest and Southern California and manifested in power swings on the California–Oregon Intertie (Path 66), Northwest–British Columbia (Path 3), and Northern–Southern California (Path 26).

System planners must understand the modes of oscillation in an interconnection so that they can model them appropriately in power system studies and develop operating procedures and mitigation measures.

This document gives an up-to-date quantitative and qualitative description of the major inter-area modes of oscillation in the Western Interconnection and is an update of the 2014 WECC Modes Report [2]. This includes the addition of phasor measurement unit (PMU) data analyses from 2016 through 2019 as well as analyses of transient simulation models.



## Modes of Inter-Area Power Oscillations in the Western Interconnection

The 2014 report [2] was based primarily on analyses of actual-system PMU data from 2009 through 2013. It included analyses of periodic Pacific DC Intertie (PDCI) probing tests and Chief Joseph brake insertions conducted throughout the summer seasons of 2009, 2011, 2012, and 2013. The 2013 data was limited to one test case. The PMU measurement coverage of the 2012 tests was considerably wider than in the 2009 through 2011 tests. The measurement coverage in 2013 was even better, but only one 2013 dataset is included in [2]. Twenty-six tests were conducted in 2012. For the 2009 and 2011 tests, PMU coverage was limited to the Bonneville Power Administration (BPA) area, and a total of 30 tests were conducted.

Table 1 summarizes the PMU datasets available for the analysis presented in this report. All but one spans about 24 hours, giving the opportunity for diurnal analysis. All of them come from BPA/BPA-Partner data. In a few cases, the data appears to have been passed through a lossy compression algorithm. In these cases, the data is still useful with some repairs.

**Table 1: Available PMU datasets.**

Date(s)	Time Range (PDT)	Notes	PMU Coverage
2016/09/13	0800–1600	PDCI probing tests. Provides a 24-hour dataset. Alberta disconnected for some or all the dataset	BPA and BPA partner data. Partner data has good system-wide coverage. Some compression issues with SCE data.
2016/09/28 – 2016/09/29	0800 on 09/28 – 1659 on 09/29	PDCI probing tests and Chief Joseph brake pulses on both days. This is a 24+ hour dataset.	BPA and BPA partner data. Partner data has good system-wide coverage. Some compression issues with SCE data and one channel from SRP.
2017/05/16 – 2017/05/17	0800 on 05/16 – 0759 on 05/17	PDCI probing tests. Provides a 24-hour dataset.	BPA and BPA partner data. Partner data has good system-wide coverage. Some compression issues with channels from AESO and SRP.
2018/05/23 – 2018/05/24	0800 on 05/23 – 1659 on 05/24	PDCI probing tests on both days. Chief Joseph brake pulses on 05/23. Provides a 24+ hour dataset.	BPA and BPA partner data. Partner data has good system-wide coverage. Some compression issues with SCE data and one channel from SRP.
2019/05/07 – 2019/05/08	0800 on 05/07 – 0759 on 05/08	PDCI probing tests and Chief Joseph brake pulses. Provides a 24-hour dataset.	BPA and BPA partner data. Partner data has good system-wide coverage. APS and LADWP channels are effectively unusable. Potential compression issues with some BC Hydro data.
2019/08/21 – 2019/08/22	0800 on 08/21 – 0759 on 08/22	PDCI probing tests and Chief Joseph brake pulses. Provides a 24-hour dataset.	BPA and BPA partner data. A lot of partner data is 100% invalid: BC Hydro, IPCO, NWE, APS, PG&E, and SCE.

### Simulation Models

In addition to field measurements, this report presents electromechanical mode properties derived from analysis of simulation models. Because simulation provides an effectively noise-free environment, this approach can help provide insight into system behavior that may be difficult to observe in live measurements. Further, analyzing the interconnection-wide base cases serves as a type of model validation, ensuring that the mode properties of the simulation models match those observed in PMU



## Modes of Inter-Area Power Oscillations in the Western Interconnection

measurements. Table 2 summarizes two of the analyzed WECC base cases. These cases were selected because they were current and represented substantially different operating conditions.

**Table 2: Interconnection-wide base case generation statistics.**

Case	Description	Load	Synchr. Capacity	Renewable Gen.
20LSP1sa1	2020 Light Spring	93.6 GW	116.2 GW	8.9 GW (9.5%)
21HS3a1	2021 Heavy Summer	180.0 GW	185.1 GW	21.6 GW (12.0%)

The 2020 Light Spring case is representative of a lightly loaded operating condition occurring during the day. It features about 3 GW of utility-scale photovoltaic generation (by output), and another 5.9 GW of wind. In general, the frequency of the electromechanical modes is inversely proportional to the amount of inertia online in the system. So, in lightly loaded cases such as this one, the modes tend to appear at the top end of their nominal frequency ranges.

The 2021 Heavy Summer case is representative of a heavily loaded operating condition occurring before sunset. It features about 5.7 GW of utility-scale photovoltaic generation (by output), and another 15.9 GW of wind. The system load is roughly double that of the 2020 Light Spring case, and the online synchronous capacity is 59.3% higher.

Table 3 lists the net MW transfers on key transmission paths for each of these cases. The paths listed here were identified as top interaction paths for one or more of the inter-area modes through analysis of the simulation base cases. The “Mode” column lists the inter-area mode for which each path was identified as an interaction path. These interaction paths are preliminary, and it is possible that the transfers on paths not yet identified may also exhibit significant modal content. The “From Area” column indicates the reference direction for the MW transfers.

## Modes of Inter-Area Power Oscillations in the Western Interconnection

Table 3: MW transfers on key transmission paths.

No.	Mode	Path Name	From Area	Net Transfer (MW)	
				20LSP1sa1	21HS3a1
Path 1	NSA	Alberta–British Columbia	Alberta	400.6	-394.9
Path 3	NSA, BCA	Northwest–Canada	Canada	1400.6	-2305.8
Path 8	MT	Montana–Northwest	Northwest	1452.7	-5.1
Path 15	BCA	Midway–Los Banos (California)	N. California	306.6	-486.6
Path 16	NSB	Idaho–Sierra (Idaho–Nevada)	Nevada	160.5	176.5
Path 18	MT	Montana–Idaho	Idaho	158.6	296.6
Path 19	EWA	Bridger West (Wyoming–Idaho)	Wyoming	716.5	1954.7
Path 20	NSB	Path C (Idaho–Utah)	Utah	834.2	834.6
Path 24	BCB	PG&E–Sierra (California–Nevada)	Nevada	13.2	25.6
Path 30	EWA	TOT 1A (Colorado–Utah)	Colorado	427.8	192.9
Path 31	EWA	TOT 2A (Colorado–New Mexico)	New Mexico	-49.6	299.4
Path 46	BCA, BCB	West of Colorado River (WOR)	NV/AZ	1988.2	5870.3
Path 66	NSB, BCB	California–Oregon Intertie (COI)	Oregon	-268.3	3761.0
Path 76	BCB	Alturas Project (California–Nevada)	California	124.3	262.3
Path 78	BCA	TOT 2B1 (Utah South)	AZ/NM	91.2	-317.8
Path 80	MT	Montana Southeast	S.E. Montana	-96.7	-45.8
Path 83	NSA	Montana–Alberta Tie Line (MATL)	Alberta	-57.3	-61.3
Path 500	–	Total Southern California Imports	–	7343.4	13391.0

### Simulated Points of Measurement

There are over 500 PMUs installed in the Western Interconnection [3]. The findings in this report are based mostly on field data collected from a subset of these sensors. In the sections describing analysis of interconnection-wide base cases, simulated measurements were recorded at 40 buses and 40 nearby generators. This number made it possible to assemble an accurate picture of the electromechanical mode properties without resulting in highly correlated measurements. In most cases, the simulated sensor locations were selected to match those of actual PMU installations. To excite the modes of the system in simulation, a 1,200 MW dynamic braking resistor was inserted at one of 10 locations distributed throughout the system. Table 4 lists the simulated brake insertion locations. In the actual system, there is a dynamic brake installed near the Chief Joseph Dam; however, the remainder exist only in simulation. Figure 2 shows the buses monitored in simulation; the colored diamonds indicate braking resistor locations. Table 5 lists the names of the monitored buses and generators.



## Modes of Inter-Area Power Oscillations in the Western Interconnection

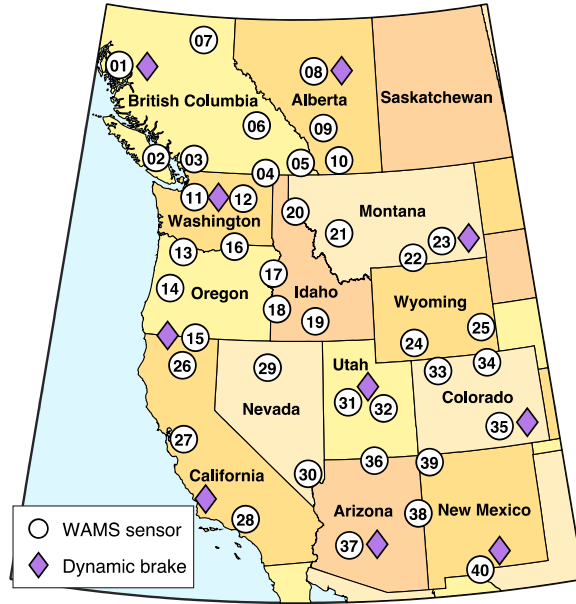


**Figure 2: Simulated points of measurement and perturbation.**

For the monitored buses, frequency measurements were recorded in the high-voltage network, e.g., on the high-voltage side of a station transformer. For the monitored generators, rotor speed measurements were recorded by directly capturing the simulated state trajectories. The monitored generators were selected to ensure that each unit was in service across both the analyzed base cases. So, for some cases, such as Valmy, the monitored generator is located at a different plant than implied by the name of the monitored bus. In these cases, the substitute generators were selected so they were as close to the monitored bus as possible given resource commitment and dispatch considerations.

**Table 4: Brake insertion locations.**

Closest Sensor	Nearby Bus/Generator	Closest Sensor	Nearby Bus/Generator
01	Kemano	28	Diablo Canyon
08	Genesee	31	Intermountain
11	Chief Joseph	35	Comanche
15	Malin	37	Palo Verde
23	Colstrip	40	Newman

## Modes of Inter-Area Power Oscillations in the Western Interconnection

Table 5: Buses and generators monitored in simulation.

No.	Monitored Bus	Monitored Generator	No.	Monitored Bus	Monitored Generator
01	Kemano	Kemano	21	Garrison	Dave Gates
02	Dunsmuir	Ladore	22	Yellowtail	Yellowtail
03	Ingledow	Ruskin	23	Colstrip	Colstrip
04	Selkirk	Waneta	24	Bridger	Jim Bridger
05	Cranbrook	Aberfeldie	25	Laramie	Laramie River
06	Revelstoke	Revelstoke	26	Round Mt.	James B. Black
07	Shrum	GM Shrum	27	Tesla	Walnut
08	Genesee	Genesee	28	Vincent	Haynes
09	Bennett	Shepard E.C.	29	Valmy	Newmont T.S. Power
10	Picture Butte	Oldman River	30	Harry Allen	Chuck Lenzie
11	Monroe	Jackson Powerhouse	31	Intermountain	Intermountain
12	Coulee	Grand Coulee	32	Emery	Huntington
13	Troutdale	Bonneville	33	Craig	Craig
14	Alvey	Carmen-Smith	34	Ault	Flatiron
15	Malin	Klamath Falls	35	Comanche	Comanche
16	McNary	McNary	36	Navajo	Glen Canyon
17	Brownlee	Brownlee	37	Palo Verde	Palo Verde
18	Hemingway	Swan Falls	38	Coronado	Coronado
19	Midpoint	Shoshone Falls	39	Four Corners	San Juan
20	Taft	Rathdrum Lancaster	40	Newman	Rio Grande

### Inter-Area Modes of the Western Interconnection

Theoretically, the Western Interconnection has thousands of modes, but only a handful show up as inter-area. The latest knowledge of the inter-area modes of the Western Interconnection is reflected below using historical information from the 2014 WECC Modes Report as a baseline [2]. The list below is comprehensive in that it includes all inter-area modes of oscillation that the Western Interconnection Modes Review Group (WIMRG) can observe in actual system measurements and analysis of simulation models. If any new inter-area modes appear in the future, either through changes in the system configuration or improvements in signal processing techniques, they will be added to this list in a subsequent revision.

- **North-South A (NSA) Mode**

- It is typically in the 0.20 Hz to 0.30 Hz range.
- The shape has Alberta oscillating against the rest of the system.
- For all datasets analyzed, the damping is very high (greater than 10%) when the 500 kV intertie between Alberta and BC is in service. Simulation models show the same.



## Modes of Inter-Area Power Oscillations in the Western Interconnection

- When Alberta disconnects from the rest of the system, which happens fairly often during summer line maintenance, the NSA mode disappears.
- There are two conditions in which Alberta will be weakly connected to the rest of the system: one in which the 500 kV line between Cranbrook and Bennett is out of service, leaving the 230/240 kV lines and 138 kV subtransmission intact; and the other in which only the 138 kV network remains. These conditions are not analyzed in detail here and will be the subject of future work.
- This report analyzes many PMU datasets for the NSA mode that were not available in 2014. These analyses affirm the conclusions from the 2014 WECC modes report [2].
- **North-South B (NSB) Mode**
  - It is typically in the 0.35 Hz to 0.45 Hz range.
  - It is the most geographically widespread mode in the Western Interconnection, and the observability is not dominant in any single location.
  - The mode shape has the Alberta area swinging against BC and the northern U.S., which in turn swings against the southern part of the U.S. The northern node or dividing line is typically south of Bennett on the Alberta–BC intertie. The other node is typically near northern California.
  - It is typically the lightest damped inter-area mode in the WECC. Typical damping is in the 5 to 10% range. The mode is accurately depicted in the simulation cases that were analyzed for this report.
  - The Alberta–BC intertie has a significant impact on the NSB mode. When Alberta disconnects from the rest of the system, mode frequency and damping decrease.
  - The prototype PDCI damping controller described in [4] offers significant controllability of the NSB mode. This controller is not currently used in operations (ca. 2021).
  - The 2014 modes report included many analyses of PMU datasets and strong conclusions for the NSB mode [2]. This report analyzes many additional datasets, and the conclusions support those presented in the 2014 report.
- **East-West A (EWA) Mode**
  - As with the NSB mode, it is typically in the 0.35 Hz to 0.45 Hz range.
  - The mode shape has the eastern part of the system centralized in Colorado oscillating against the rest of the system.
  - Available evidence suggests that the mode is typically well damped, but only a few PMU datasets discussed in this report were analyzed for damping.
  - The 2014 WECC report had only one dataset for this mode and only hypothesized its properties [2]. This report has many analyses of PMU datasets and stronger conclusions.
- **British Columbia (BC) Mode(s):**



## Modes of Inter-Area Power Oscillations in the Western Interconnection

- This report hypothesizes that there are two BC modes: “British Columbia A” and “British Columbia B.”
- Analysis of simulation models indicates the existence of at least two modes with high observability in British Columbia and similar frequencies, nominally in the range of 0.50 Hz to 0.72 Hz.
- The 2014 report has no analyses or conclusions for these modes [2]. This report posits the two-mode hypothesis with simulation results and analysis of one PMU dataset.
- More research is required to fully understand the BC mode(s). See “Conclusions and Future Work” for recommendations.
- **Montana (MT) Mode:**
  - It is typically in the 0.70 Hz to 0.90 Hz range.
  - The shape has eastern Montana generators swinging against the system (primarily the Pacific Northwest). Generators extending to eastern Washington tend to swing with the eastern Montana generators.
  - The damping for this mode was estimated to be near 10% in both simulation base cases analyzed, which represent substantially different operating conditions.
  - Limited mode meter analysis presented in this report shows that the actual-system modal damping to be in the 10-to-15% range.
  - The 2014 report has no analyses for the MT mode [2]. This report includes analysis of many PMU datasets and fairly strong conclusions. In some cases, it is difficult to discern between the MT mode and one or more of the BC modes.
  - Future work will examine the impact of Colstrip unit retirements on the characteristics of the MT mode.

## Theoretical Background and Analysis Methods

---

### Electromechanical Dynamics

Synchronous power systems are inherently multi-modal, under-damped systems due to the electromechanical physics. In theory, a system consisting of  $n$  interconnected synchronous machines will have  $n-1$  modes of oscillation. Most of these modes are localized to a small area and often involve only a few generators. But typically, a handful of the modes are widespread and involve several generators swinging (or moving) together against other groups of generators. Such modes are termed “inter-area” and are typically the most troublesome of the system. Inter-area modes usually have a frequency between 0.1 and 1 Hz. For details on the physics of electromechanical dynamics and the foundational mathematics used to describe them, the reader is referred to Appendix A:

Electromechanical Dynamic Theory. Critical descriptive terms include:

- **Mode frequency:** The frequency at which a given mode oscillates (typically in Hz).



## Modes of Inter-Area Power Oscillations in the Western Interconnection

- **Mode damping:** A measure of how long it takes for a given mode to dissipate in a transient. Typically measured in %D where  $\%D = 100 * (\text{damping ratio})$ . Note,  $1/(\text{damping ratio}) \cong$  the number of cycles of an oscillation before the oscillation completely dissipates. A damping ratio of 10% or more is considered high and safe. By contrast, a damping ratio below 5% is considered low, and below 3% very low.
- **Observability:** The content of a given mode in a given measured signal.
- **Mode Shape:** A measure of the observability of a given mode. Mode shape is a complex number and is associated with a given mode and system state (e.g., generator speed). The amplitude of the shape is a measure of the relative magnitude of the state variable in the modal oscillations. The angle of the shape is a measure of the relative phase of the state variable in the modal oscillations.
- **Node:** A dividing line for the mode shape. Generators on one side of the line tend to swing together against those on the other side of the line.
- **Controllability:** The extent to which a given mode can be damped from control of a given actuator at a given location in the grid.
- **Participation factor:** A measure of controllability of a given mode at a given location (typically a generator). The participation factor is a direct measure of how effectively a power system stabilizer (PSS) at a given generator can damp an oscillation associated with a particular mode.
- **Modal interaction:** Loosely defined as a measure of modal energy exchange between different areas of a system. For example, if two areas swing against each other at a given mode, modal energy is exchanged through one or more transmission lines. Interaction is a measure of modal energy being exchanged on a given line.
- **Modal excitability:** Loosely defined as a measure of how much a given contingency excites an oscillation containing a given mode.

Using Figure 3 as a reference, a power-system's dynamic response is classified into three types: ambient, transient, and a forced oscillation. During a complex disturbance, one or more of these response types may be occurring simultaneously.

- An *ambient response* is the response of the system to small, random changes within the system. These changes are typically small, random load changes. These small perturbations act as low-level excitation to the system's dynamics, so ambient responses contain information about the electromechanical modes. An ambient response is always present in measured signals and typically varies gradually throughout the day.
- A *transient response* is the response of the system immediately after a sudden disturbance such as a fault, line tripping, generator trip, or load tripping. Smaller-scale transient responses are typically characterized by a Natural Response. A Natural Response is an oscillation characterized by the oscillatory modes only. A transient response is typically much larger in amplitude than an ambient response.



- A *forced response* (or *forced oscillation*) is the response of the system associated with an external input or a malfunctioning apparatus. Examples include a malfunctioning steam valve cycling on and off, or an arc furnace inducing its dynamics into the grid. Forced oscillations may include harmonics resulting from the periodicity of the external inputs. Forced oscillations range in amplitude from very small to very large. If the frequency of the forced oscillation is near a frequency of an electromechanical mode where the system has high gain, the oscillation can be widely observed.

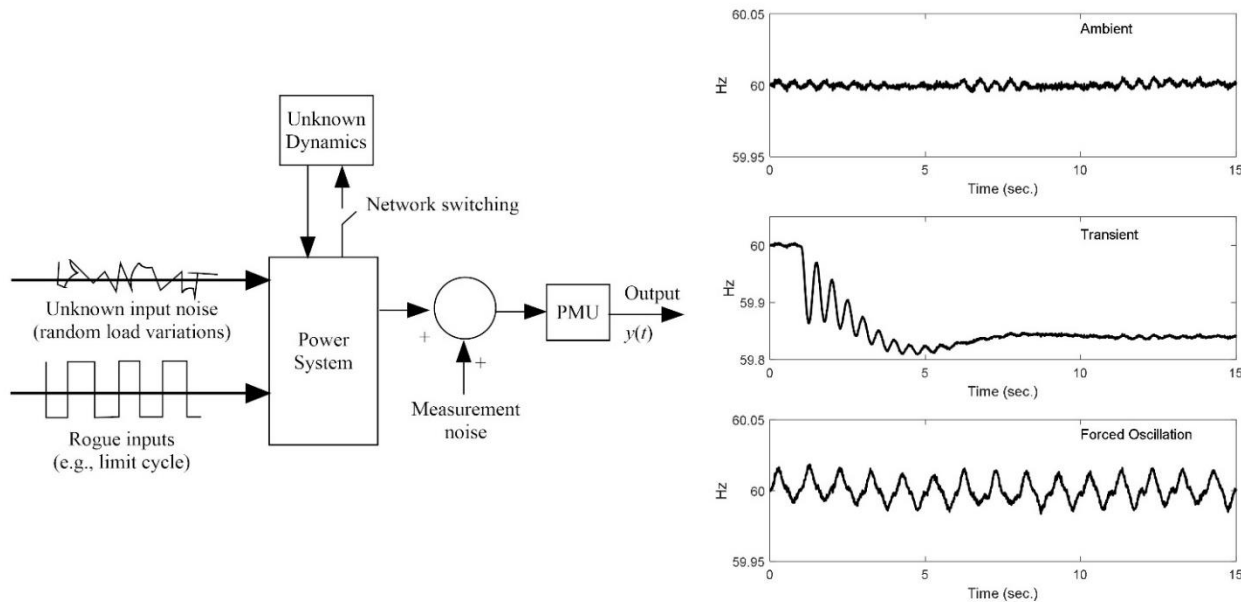


Figure 3: Power system dynamic response types.

### Correlation Analysis

Spectral correlation analysis is a powerful tool for accurately estimating the frequency and shape of a given mode. The theory of the approach is summarized in Appendix B: Analysis Methods and detailed examples are provided in “Estimating electromechanical mode shape from synchrophasor measurements” [5].

The assumption in using this approach to estimate the mode shape and frequency is that the system is primarily in an ambient condition or excited by a pseudorandom input. One such experiment that is often conducted in the Western Interconnection is to excite the system using the PDCI pole controls through a  $\pm 20$  MW pseudorandom signal. The pseudorandom signal is a multi-sinusoid signal designed to excite a particular frequency band [6] [7]. It is optimally designed to have maximum energy for a given peak-to-peak limit by adjusting the phase of each sinusoid. Figure 4 shows the PDCI probing signal that has been used for the past several years. As one can see, it has most of its content in the 0.1 Hz to 1 Hz range. For a typical test, this signal is applied to the PDCI for 10 to 20 minutes. It has proven to especially excite the NSB mode.

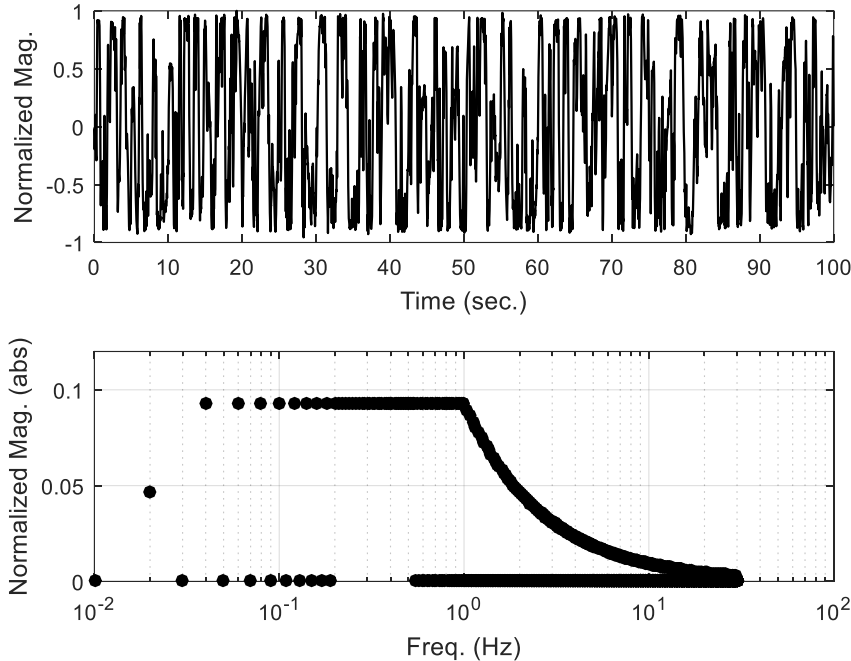


Figure 4: PDCI Multi-sine probing signal.

### Mode Meter Analysis

Random load changes and other small disturbances serve as a continuous excitation to a power system’s electromechanical dynamics—termed the ambient response. This excitation results in ambient noise that is apparent in PMU measurements, as displayed in Figure 5. This ambient noise is colored by the system’s dynamics, which means that consecutive measurements are correlated with each other. Because this correlation is introduced by the system’s dynamics, the ambient noise can be analyzed to extract frequency, damping ratio, and shape estimates of the system’s dominant inter-area electromechanical modes. The signal processing methods used to extract this information are called mode meters because they are typically used to provide continuous monitoring of a particular mode. Two mode meter algorithms were used for this report: least squares and Yule-Walker. Refer to Appendix B: Analysis Methods for descriptions of these algorithms. Many other mode meter algorithms have been developed. Further discussion of mode estimation algorithms from ambient data can be found in “Inter-area Oscillations in Power Systems: A Nonlinear and Nonstationary Perspective, Chapter 1” [8] and “IEEE Task Force Report—Identification of Electromechanical Modes in Power Systems” [9].

Performance of mode meters depend on several factors. In “On the Cramer-Rao bound of power system electromechanical mode meters,” Dosiek provides a more detailed discussion [10]. Mode meter algorithms rely on using several minutes of ambient data to provide the estimates of mode frequency, damping, and shape. This is due to the relatively small amplitude of ambient noise and its stochastic nature. This contrasts with ringdown analysis, which typically uses tens of seconds of data and has a

relatively large amplitude. The performance of mode meter algorithms also depends on the choice of signals analyzed. The mode of interest should have strong observability in the signals analyzed. It is common to use a linear combination of signals such that the combined signal is dominated by a particular mode of interest. Since the ambient data is stochastic in nature, there is always some variability in the mode estimates around the true value of the mode. The accuracy of the mode estimates can be further improved by using low level probing of the PDCI as described in “Overview of system identification for power systems from measured responses” [7] and “Inter-area Oscillations in Power Systems: A Nonlinear and Nonstationary Perspective, Chapter 1” [8].

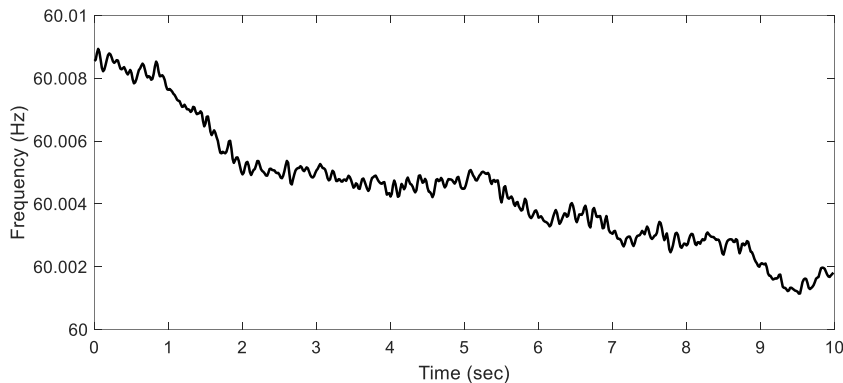


Figure 5: Frequency measurements from a PMU showing ambient noise.

### Ringdown Analysis

A *ringdown* is a signal or collection of signals that captures the system response to a disturbance. When studying the dynamics of structures, such as steel trusses, ringdowns are often initiated by striking the system with an impulse hammer. As the name implies, this tool is designed to facilitate estimation of the impulse response of the system. In power systems, the closest equivalent to the impulse hammer is a dynamic braking resistor, such as the 1,400 MW Chief Joseph Brake [11]. By pulsing the braking resistor, i.e., inserting and rapidly removing it, we can “ping” the system in a way that excites the electromechanical modes without changing the underlying operating point. Modal analysis can be conducted not only on ringdowns induced for testing, but also on those arising from unplanned disturbances.

Ringdown analysis involves using curve fitting techniques, e.g., regression, to identify a model that reproduces the observed system response as closely as possible under some mathematical criteria. Studying the dynamic properties of the model then provides insight about the modes of the system. The value of the conclusions drawn from this process hinges upon the accuracy of the model. No model provides a perfect facsimile of the power system; however, over time certain mathematical structures have been identified that provide useful modal information. Popular models employed in ringdown analysis include autoregressive (AR) models, autoregressive-moving-average (ARMA) models, and state-space models.

Broadly speaking, curve fitting techniques can be classified as either single-channel or multi-channel. As the name implies, single-channel methods determine the parameters of the model using a single signal. As a result, these methods return a different model, and so a different set of mode estimates, for each input signal. Care must be taken in evaluating the results of single-channel analysis because the system itself only has a single set of eigenvalues. Combining the mode estimates derived from each input signal, e.g., by averaging, often produces poor results. Consequently, mode estimates produced using single-channel methods are commonly based on analysis of particular signals, or linear combinations of signals, where the mode of interest is highly observable. In contrast, multi-channel methods identify a single model by processing a collection of signals simultaneously. As a result, they produce one comprehensive set of mode estimates for a given ringdown.

Figure 6 shows an example of a multi-channel curve fit arising from a simulated dynamic brake insertion. The dashed traces show the simulated system response recorded at two points of measurement and the colored traces the output of the mathematical model.

Two ringdown analysis algorithms were used for this report: Prony's method and a regularized form of dynamic mode decomposition (DMD). For more information about these algorithms, see Appendix B: Analysis Methods.

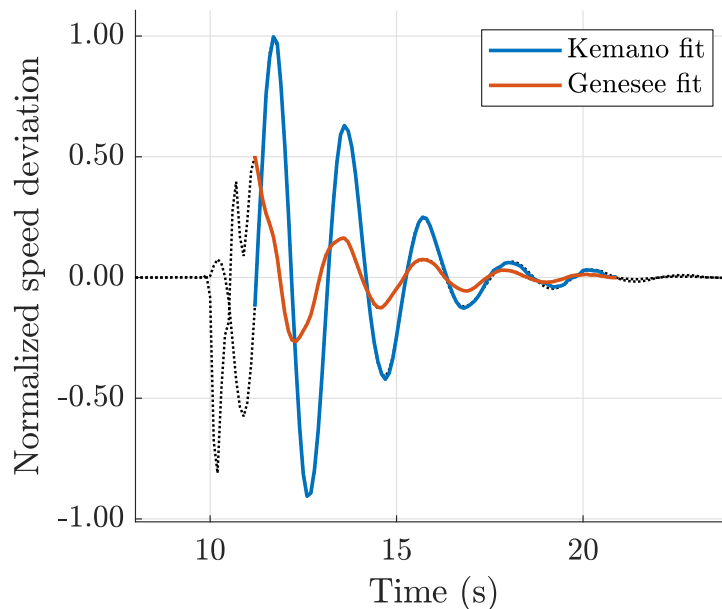


Figure 6: Multi-channel curve fit example arising from a simulated dynamic brake insertion.

### Direct Eigenanalysis

As with any large-scale power system, the dynamics of the Western Interconnection are inherently nonlinear; however, under small perturbations, changes in the system states may be well approximated by a linearized model. In contrast to the methods described above, direct eigenanalysis does not derive modal information from observed or simulated data. Rather, it is based on directly constructing a

linearized model of the system from a mathematical description of its dynamics. A key challenge in direct eigenanalysis is estimating the system matrix  $A$  corresponding to the linearized representation. As described in Appendix B: Analysis Methods, the system matrix is a Jacobian matrix of partial derivatives of the vector field with respect to the state variables. For the Western Interconnection, the system matrix is large because the number of states is on the order of 50,000. The number of partial derivatives that must be estimated to build the system matrix is equal to the number of states squared, or roughly 2.5 billion entries.

There are two common techniques used to estimate the entries of the system matrix: analytical differentiation and finite difference methods. In analytical differentiation, the partial derivatives of each of the differential equations making up the vector field are calculated using closed-form mathematical expressions. This approach is employed by the Small-Signal Stability Analysis Tool (SSAT), a commercial software package from PowerTech Labs. By contrast, finite difference methods aim to approximate the partial derivatives using discrete mathematics. This process, sometimes called numerical differentiation, involves iteratively perturbing each state variable in turn and evaluating the differential equations to determine the changes in the state derivatives. These changes are then used to approximate the entries of the system matrix. This approach is employed by the MATLAB-based Power System Toolbox (PST). In theory, it is possible for analytical differentiation to be slightly more accurate than finite difference methods; however, when implemented correctly, the differences are small. For large-scale power systems with many thousands of states, analytical differentiation may be more computationally efficient because it does not require iterative perturbation of each state.

After the system matrix has been constructed, its modal properties (e.g., eigenvalues and eigenvectors) may be studied using linear algebraic techniques. Since the system matrix may be large, it is often beneficial to employ advanced algorithms, such as Arnoldi iteration, to determine the eigenvalues and eigenvectors [12]. For additional information about the mathematical details of direct eigenanalysis, refer to Appendix B: Analysis Methods.

### North-South A Mode

---

#### Mode Description

The NSA mode is the lowest frequency inter-area mode within the Western Interconnection. It is typically in the 0.20 Hz to 0.30 Hz range and highly damped. The mode shape is characterized by Alberta area generators swinging against the rest of the system. Generators in BC and Washington state swing with the Alberta generators. The mode node tends to be near the California–Oregon border.

The mode showed up when Alberta first synchronized to the Western Interconnection in 1980 [13]. Its properties were well documented in the 2014 report primarily based on PMU data analysis [2]. This report is based on extensive PMU data analysis from 2016 through 2019 and simulation results. The conclusions derived from this analysis support those presented in the 2014 report.



### Mode Properties Measured from Simulation Models

This section discusses the properties of the NSA mode observed in simulation. Two simulation models were studied, the WECC 2020 Light Spring base case (20LSP1sa1) and the WECC 2021 Heavy Summer base case (21HS3a1). Basic facts about these cases, including system loading and approximate renewable penetration, are presented in the Simulation Models section of the Introduction. For each base case, 10 simulations were performed with each run corresponding to a 1,200 MW dynamic brake insertion (0.5 s duration) initiated at a different point in the system. Figure 2 shows the insertion locations used to perturb the system. Brake insertions at a subset of these locations excited the NSA mode. The mode properties were estimated by identifying a reduced-order state-space model from the free response portion of the ringdown. Details of the multi-channel curve fitting technique used to identify the system matrix are provided in the Regularized Dynamic Mode Decomposition section of Appendix B: Analysis Methods.

#### *Observability*

The shape of the NSA mode is characterized by generation units in Alberta oscillating against the rest of the system. Machines in British Columbia tend to oscillate in phase with those in Alberta. Figure 7 shows the shape of the NSA mode estimated from the 2020 Light Spring base case, and Figure 8 the shape from the 2021 Heavy Summer case. In simulation, the dividing node is observed to shift slightly based on the operating condition. In the 2020 Light Spring base case it is parallel to the Washington–Oregon border, and in the 2021 Heavy Summer case the California–Oregon border. This shift is a function of the dispatch pattern and the amount of power being transferred from the northern part of the system to the southern part. Table 6 presents a condensed list of locations at which the NSA mode is readily observable. This table is not exhaustive and includes only entries from the list of monitored buses and generators presented in Table 5. The entries listed in Group 1 are shown in red in Figure 7 and Figure 8, and those in Group 2 in Blue.

## Modes of Inter-Area Power Oscillations in the Western Interconnection

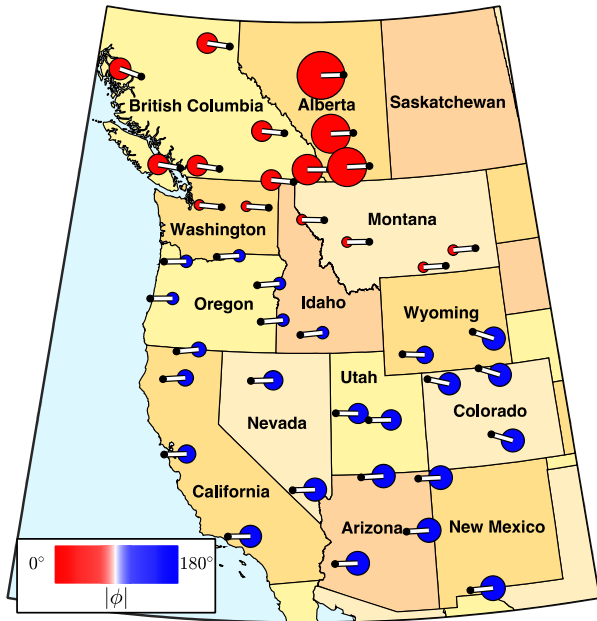


Figure 7: NSA mode shape, 0.28 Hz 17.5 %, 2020 Light Spring.

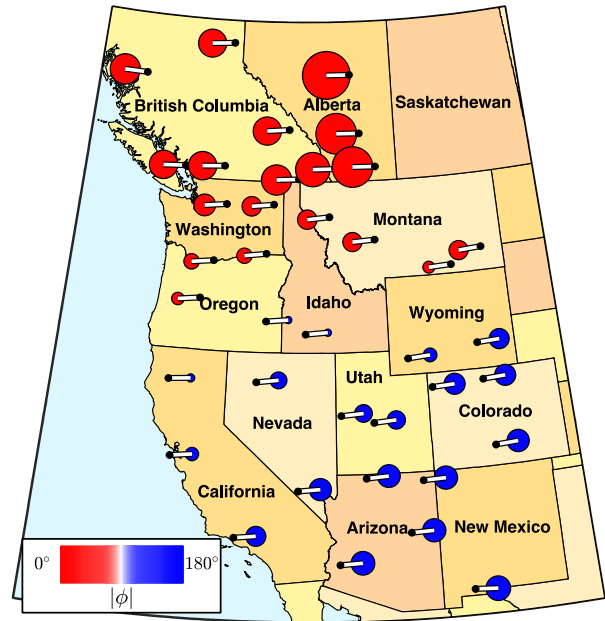


Figure 8: NSA mode shape, 0.24 Hz

Table 6: NSA mode observability short list.

	Bus frequency	Generator speed
Group 1 ●	Genesee, Bennett, Picture Butte	Genesee, Shepard E.C., Oldman River
Group 2 ●	Newman, Palo Verde, Coronado	Rio Grande, Palo Verde, Coronado

### Excitability

Mode excitability provides information about which disturbances excite a particular mode. This is a complex subject and characterizing it fully for the Western Interconnection will require significant future work. Two key aspects that affect excitability are the nature of the disturbance (e.g., type, magnitude, duration) and the location where it occurs. In the simulations performed here, the nature of the disturbance was intentionally kept consistent to gain insight into locational sensitivity. Table 7 provides a list of the brake insertion locations that made it possible to get a clear estimate of the NSA mode for both analyzed base cases. This suggests that a disturbance near one of these points that causes a mismatch in the generation-demand balance, such as a generator trip, would likely excite the NSA mode. Analysis of simulation indicates that the NSA mode is most excitable from Alberta or the southwestern U.S.

Table 7: NSA mode excitability short list.

Brake insertion location
Genesee, Diablo Canyon, Palo Verde, Newman

## Controllability

Here, controllability was assessed by estimating the participation factors associated with the NSA mode. For background about participation factors, see Appendix A: Electromechanical Dynamic Theory. Table 8 presents a condensed list of system states with consistently high participation factor magnitudes across both the 2020 Light Spring and 2021 Heavy Summer base cases. This analysis suggests that substation-based controls using bus frequency feedback located at Bennett, Picture Butte, and/or Cranbrook would be effective in damping the NSA mode. Likewise, PSSs at Shepard Energy Centre, Genesee, and Oldman River influence the damping of this mode. This table is not exhaustive and includes only entries from the list of monitored buses and generators presented in Table 5. For engineering purposes, the information listed in Table 8 should be regarded as a starting point for further time- and frequency-domain analysis to evaluate effective means of control.

**Table 8: NSA mode controllability short list.**

Bus frequency	Generator speed
Bennett, Picture Butte, Cranbrook	Shepard E.C., Genesee, Oldman River

## Interactions Paths

An interaction path is a transmission line or corridor over which significant energy corresponding to a particular oscillatory mode is exchanged. We can gain insight into the interaction paths by analyzing the modal content of the real power transferred from one point in the system to another (over ac lines). Here, the modal content was decomposed using Prony’s method. Figure 9 and Figure 10 show that for a brake insertion near Genesee, the modal content of the real power transfer on Path 3, Northwest–Canada, is dominated by the NSA mode. So, Path 3 is a key interaction path for the NSA mode.

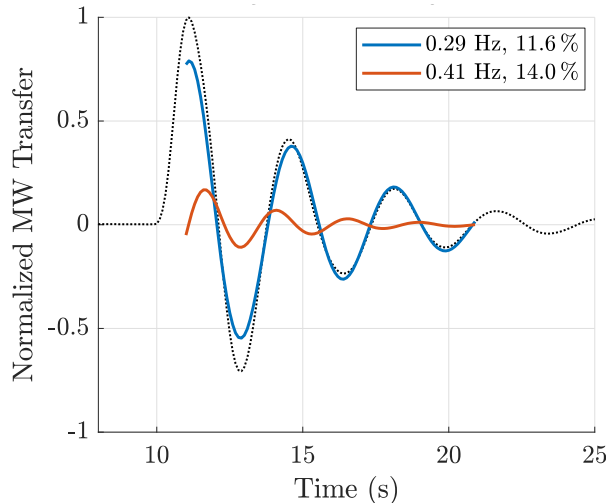


**Figure 9: Path 3, 2020 Light Spring**

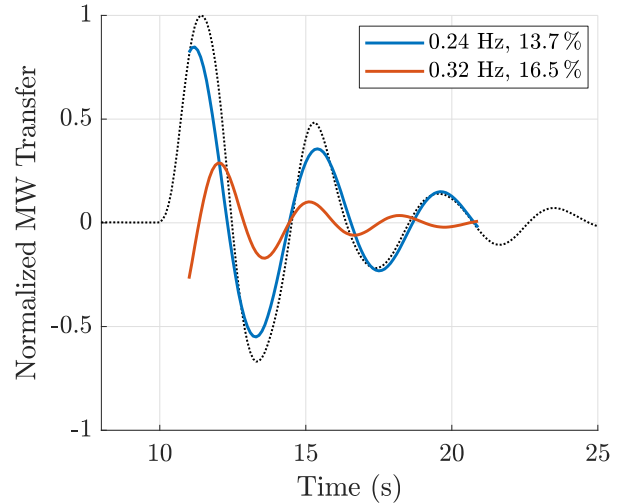


**Figure 10: Path 3, 2021 Heavy Summer.**

## Modes of Inter-Area Power Oscillations in the Western Interconnection

Table 9 provides a summary of the top interaction paths for the NSA mode identified using the interconnection-wide base cases. The transfers on other paths may also exhibit significant modal content at the NSA mode frequency.

**Table 9: Interaction path short list.**

No.	Path Name
Path 1	Alberta–British Columbia
Path 3	Northwest–Canada
Path 83	Montana–Alberta Tie Line (MATL)

### Mode Properties Measured from PMU Data

#### *Mode Shape Calculated via Correlation Analysis*

The NSA mode energy is dominant within the Alberta area of the Western Interconnection. As an example, Figure 11 shows the PSD of the frequency from five PMUs scattered across the system measured in 2018 during an ambient condition. The large peak near 0.24 Hz (circled) in the Sundance PMU is the NSA mode. The peak significantly decreases for other locations in the system. For every PMU data case studied, the mode shows up as a large peak in all measurements within the Alberta area of the Western Interconnection.

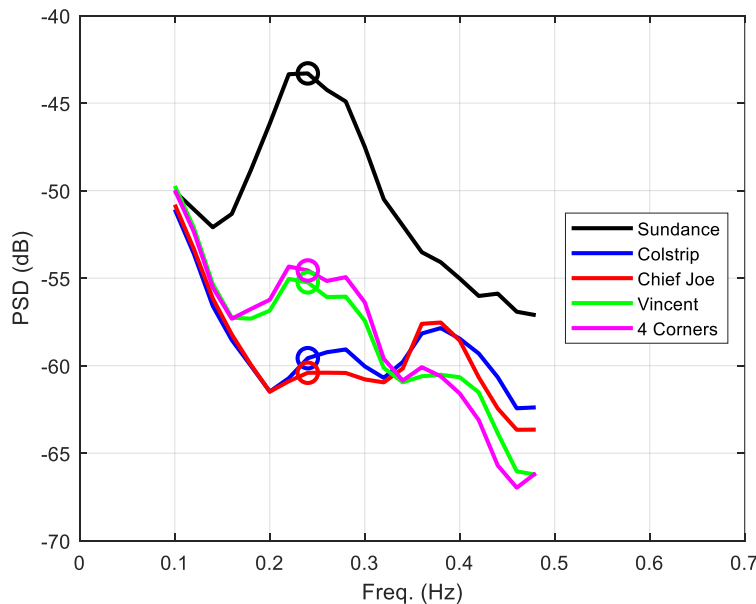


**Figure 11: PSD of five PMU-measured frequencies of ambient data on May 23, 2018, from**

Figure 12 shows the NSA mode shape and observability as measured from a 2018 PMU dataset—the same one used in Figure 11. The mode frequency during this time was measured as 0.24 Hz via the

## Modes of Inter-Area Power Oscillations in the Western Interconnection

peak in the mode reference signal in Figure 13. Sundance is used as the mode reference signal as it is well known to participate in the NSA mode.

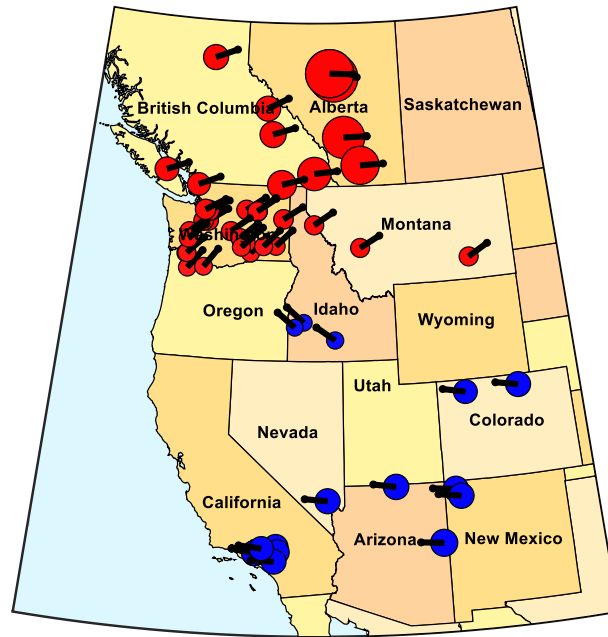
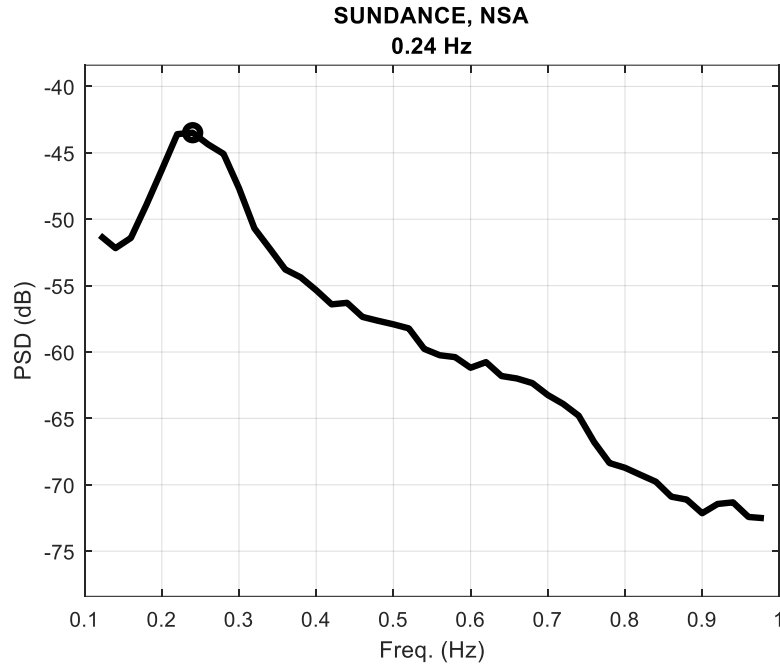


Figure 12: NSA-Mode shape and observability measured from PMU ambient

As Figure 13 shows, the Alberta area generators are swinging the most. Other generators in the upper north (e.g., BC area) are following the Alberta-area generators. Units in the far south are anti-phase to the Alberta-area generators but swing with a small amplitude. The dividing node is parallel to the California–Oregon border. The large circles in the Alberta area indicate these generators swing with a much larger amplitude, which is supported by the spectral energy shown in Figure 11. So, we conclude that this is primarily Alberta swinging against the rest of the system. Other units in the north move with Alberta.

## Modes of Inter-Area Power Oscillations in the Western Interconnection



**Figure 13: Mode reference signal for the mode shape estimated in Figure 12.**

Table 10 summarizes the estimated mode frequencies and shapes from several tests spanning 2016 through 2019. The PMU dataset from May 23, 2018, at 16:05 UTC is termed the “baseline” set. All other estimated mode shapes are qualitatively compared to this baseline and judged to match it as indicated in the fourth column of the table. The mode shape maps and spectrum of the reference signal for each of the rows of the table are contained in Appendix D: NSA Mode Analyses. In examining Table 10 and the many mode shape plots in the appendix, one sees that the NSA mode frequency and shape are highly consistent.

## Modes of Inter-Area Power Oscillations in the Western Interconnection

Table 10: Summary of NSA Mode frequency and shape, 2016 through 2019.

Date	Time (UTC)	Freq. (Hz)	Shape match baseline (Y = yes, P = Partial, N = no)	Notes
9/13/2016	17:10:02 to 17:30:00	NA	NA	Ambient condition. Alberta disconnected.
9/13/2016	18:30:01 to 18:50:01	NA	NA	PDCI Probing condition. Alberta disconnected.
9/13/2016	22:10:00 to 22:28:00	NA	NA	Ambient condition. Alberta disconnected.
9/13/2016	22:28:10 to 22:48:10	NA	NA	PDCI Probing condition. Alberta disconnected.
9/13/2016	23:10:00 to 23:30:00	NA	NA	Ambient condition. Alberta disconnected.
9/28/2016	15:10:00 to 15:30:00	0.24	Y	Ambient condition.
9/28/2016	16:30:12 to 16:40:12	0.24	Y	PDCI Probing condition.
9/28/2016	17:10:00 to 17:10:00	0.24	Y	Ambient condition.
9/28/2016	18:20:02 to 18:40:02	0.22	Y	PDCI Probing condition.
9/28/2016	18:46:00 to 18:59:00	0.24	Y	Ambient condition.
9/28/2016	20:30:09 to 20:40:09	0.24	Y	PDCI Probing condition.
9/28/2016	21:10:00 to 21:30:00	0.22	Y	Ambient condition.
9/29/2016	15:10:00 to 15:30:00	0.26	Y	Ambient condition.
9/29/2016	16:10:34 to 16:20:34	0.22	Y	PDCI Probing condition.
9/29/2016	17:10:01 to 17:20:01	0.24	Y	PDCI Probing condition.
9/29/2016	18:10:31 to 18:20:31	0.22	Y	PDCI Probing condition.
9/29/2016	19:10:00 to 19:30:00	0.24	Y	Ambient condition.
9/29/2016	20:10:31 to 20:20:31	0.24	Y	PDCI Probing condition.
9/29/2016	21:10:00 to 21:30:00	0.24	Y	Ambient condition.
5/16/2017	16:16:01 to 16:36:01	0.26	Y	PDCI Probing condition.
5/16/2017	16:36:05 to 16:50:00	0.24	Y	Ambient condition.
5/16/2017	20:15:01 to 20:35:01	0.24	Y	PDCI Probing condition.
5/16/2017	20:35:05 to 20:50:00	0.26	Y	Ambient condition.
5/23/2018	16:05:00 to 16:24:30	0.24	Baseline	Ambient condition. Baseline.
5/23/2018	16:28:00 to 16:48:00	0.26	Y	PDCI Probing condition.
5/23/2018	20:15:05 to 20:35:05	0.24	Y	PDCI Probing condition.
5/23/2018	20:36:00 to 20:55:00	0.22	Y	Ambient condition.
5/24/2018	00:10:00 to 00:30:00	0.24	Y	Ambient condition.
5/24/2018	17:14:05 to 17:34:05	0.22	Y	PDCI Probing condition.
5/24/2018	17:36:00 to 17:50:00	0.22	Y	Ambient condition.
5/7/2019	14:10:00 to 14:30:00	0.24	Y	Ambient condition.
5/7/2019	17:10:00 to 17:30:00	0.24	Y	Ambient condition.
5/7/2019	17:30:03 to 17:50:03	0.24	Y	PDCI Probing condition.
5/7/2019	21:20:03 to 21:40:03	0.24	Y	PDCI Probing condition.
5/7/2019	22:10:00 to 22:30:00	0.26	Y	Ambient condition.
5/8/2019	02:10:00 to 02:30:00	0.24	Y	Ambient condition.
5/8/2019	06:10:00 to 06:30:00	0.24	Y	Ambient condition.

### Mode Frequency and Damping

The NSA mode was included in a study of mode meter estimates spanning 2017–2018. Histograms of the mode’s frequency and damping estimates, which were updated every 15 minutes, are presented in Figure 14. The mode’s frequency tends to remain between 0.22 Hz and 0.25 Hz. The mode’s damping is quite good, normally remaining above 15% and almost always beyond 10%.



## Modes of Inter-Area Power Oscillations in the Western Interconnection

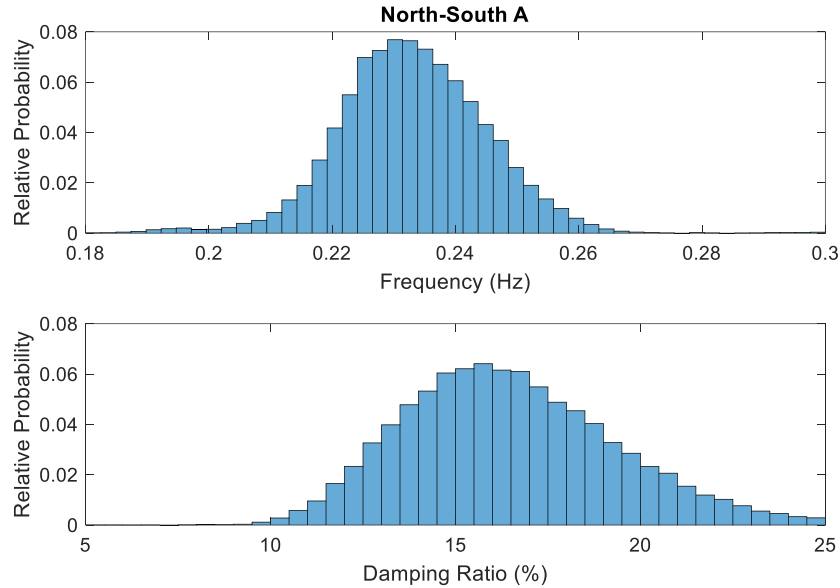


**Figure 14: Histograms of NSA frequency and damping ratio estimates collected from a mode meter every 15 minutes from 2017–2018.**

Mode meter and ringdown analysis results from several system tests are provided in Appendix D: NSA Mode Analyses. A typical set of results from the September 29, 2016, tests are presented in Figures 15 and 16. The mode meter results vary during the study period due to estimation errors and changes in the mode driven by changing operating conditions. The ringdown analysis results in Figure 15 are from the first and fourth Chief Joseph brake insertions. The brake does not excite the NSA mode as well as the NSB mode. As a result, reasonable results could not be obtained for the second and third insertions. The available ringdown analysis results show good agreement with the mode meter estimates. In Figure 16 the mode shape estimate from the first brake insertion shows the typical pattern for the NSA mode, with generators in Alberta swinging against the rest of the system.

## Modes of Inter-Area Power Oscillations in the Western Interconnection

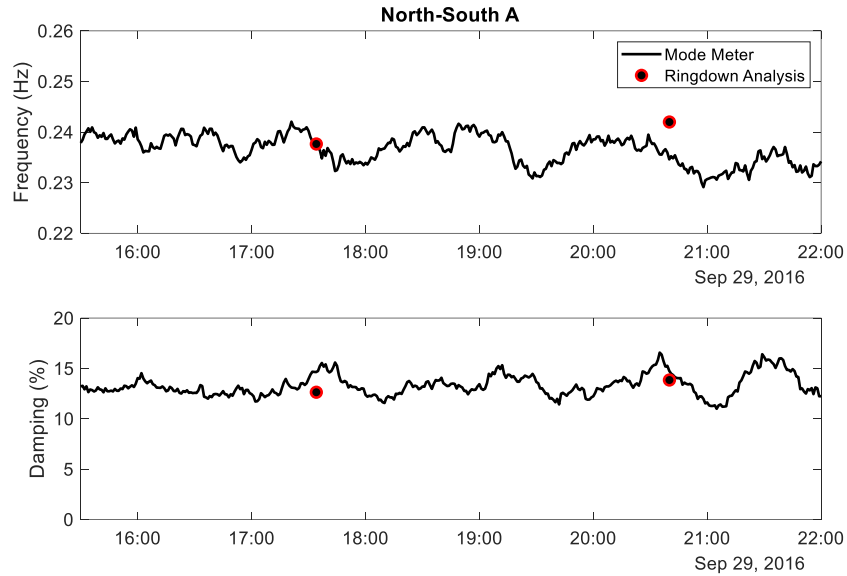


Figure 15: Estimates of the North-South A mode from mode meter and ringdown analyses for the 2016/09/29 system tests. (20160929\_Ring1\_NSA\_GENESSEE-CORONADO\_Prony).

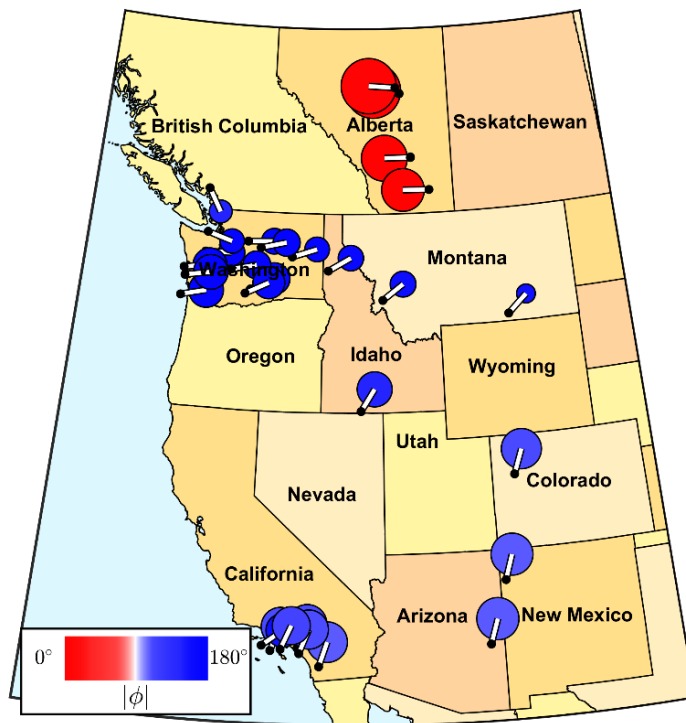


Figure 16: Mode shape estimate corresponding to the first ringdown results in Figure 15.

The mode meter and ringdown analysis results in this report were based on input signals designed to emphasize the mode of interest. The signals used in this design were first preprocessed by applying a first-order derivative filter to voltage angle measurements to obtain measures of the frequency

## Modes of Inter-Area Power Oscillations in the Western Interconnection

deviation from the nominal 60 Hz. The signals were then downsampled to more narrowly cover the frequency range associated with inter-area electromechanical modes. Final signals were created by selecting a preprocessed signal with a large mode shape magnitude and subtracting a signal with an opposing mode shape angle. The spectral coherence between the preprocessed signals was evaluated to ensure that they were participating in the same mode.

Figure 17 shows the locations of the PMUs used in signal designs for NSA. The colors on the map indicate the signals that were subtracted (blue) from reference signals (red). Multiple signals were designed to accommodate varying availability between datasets. The spectra for the four signals used to generate the mode estimates included in this report are also displayed in Figure 17. Note that the NSA mode is dominant in all spectra. The NSA mode is less dominant in the CUSTER-MALIN signal, but the required PMUs have good data availability and are significantly closer together.

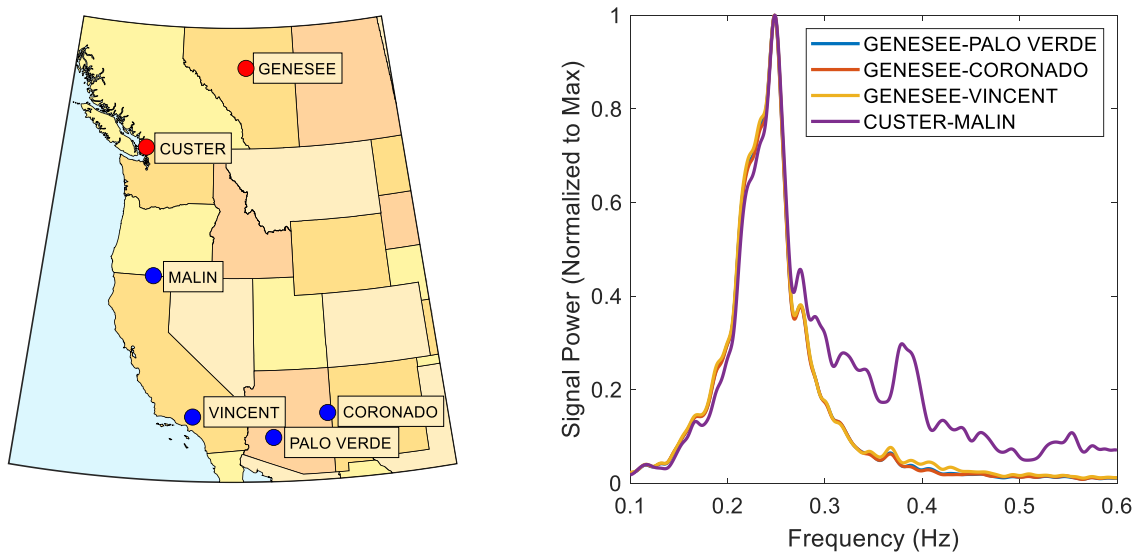


Figure 17: Locations of PMUs used in signal designs (left) and spectra of resulting signals (right).

### Future Work

The NSA mode is relatively well understood. Future recommendations include:

- Continued monitoring of the NSA mode from PMU measurements and field tests.
- Investigating the excitability, controllability, and interaction paths of the NSA mode with more detail using simulation studies. Initial work has been presented in this report.

### North-South B Mode

---

#### Mode Description

The North-South B (NSB) mode is the most widespread inter-area mode in the Western Interconnection. Under normal operating conditions, the mode frequency varies from 0.35 Hz to 0.45 Hz. For the past several years during heavy loading, the damping is typically between 5% and 10%. It primarily has the northern half of the system (excluding Alberta) swinging against the southern half of the system. The Alberta area swings against the northern half of the system (in phase with the south). The northern node or dividing line is typically just south of Bennett on the BC/Alberta intertie. The other node is typically near mid California. The observability is much more widespread than any other mode within the system. This report is based on extensive PMU data analysis from 2016 through 2019 and simulation results. The conclusions derived from this analysis support those presented in the 2014 report [2].

The strength of the interconnection between Alberta and the rest of the system has direct impacts on the NSA and NSB modes. There are two conditions where Alberta will be weakly connected to the rest of the system: one where the 500 kV line between Cranbrook and Bennett is out of service, leaving the 230/240 kV lines and 138 kV subtransmission intact; and the other where the only connection between Alberta and the rest of the system is through the 138 kV network. The 2014 report analyzed only the former case where both the 230/240 kV and 138 kV paths were in service. While the other weakly connected path (through 138 kV lines) might exhibit similar modal characteristics, that condition has not been assessed yet. This will be the subject of future work.

With Alberta weakly connected through the 230/240 kV lines, both North-South modes drop in frequency. In one such case analyzed in the 2014 report, the modes drop to 0.18 Hz for the NSA mode and 0.32 Hz for the NSB mode [2]. If Alberta completely disconnects from the Western Interconnection, the NSA mode disappears and the NSB remains at a lower frequency (e.g., 0.32 Hz) with reduced damping.

#### Mode Properties Measured from Simulation Models

This section discusses the properties of the NSB mode observed in simulation. Two simulation models were studied, the WECC 2020 Light Spring base case (20LSP1sa1) and the WECC 2021 Heavy Summer base case (21HS3a1). Basic facts about these cases, including system loading and approximate renewable penetration, are presented in the Simulation Models section of the Introduction. For each base case, 10 simulations were performed with each run corresponding to a 1,200 MW dynamic brake insertion (0.5 s duration) initiated at a different point in the system. Figure 2 shows the insertion locations used to perturb the system. Brake insertions at a subset of these locations excited the NSB mode. The mode properties were estimated by identifying a reduced-order state-space model from the free response portion of the ringdown. Details of the multi-channel curve fitting technique used to



## Modes of Inter-Area Power Oscillations in the Western Interconnection

identify the system matrix are provided in the Regularized Dynamic Mode Decomposition section of Appendix B: Analysis Methods.

### Observability

The shape of the NSB mode is characterized by generation units in British Columbia and the northwestern U.S. oscillating against the rest of the system. Machines in Alberta tend to oscillate out of phase with those in British Columbia. Figure 18 shows the shape of the NSB mode estimated from the 2020 Light Spring base case, and Figure 19 the shape from the 2021 Heavy Summer case. In simulation, the mode shape remains fairly consistent across different operating points. Depending on the location from which this mode is excited, units in Wyoming and Colorado are sometimes observed to oscillate in phase with British Columbia and sometimes out of phase. This mode is close in frequency to the EWA mode, so care must be taken to differentiate between the two. Table 11 presents a condensed list of locations at which the NSB mode is readily observable. This table is not exhaustive and includes only entries from the list of monitored buses and generators presented in Table 5. The entries listed in Group 1 are shown in red in Figure 18 and Figure 19, and those in Group 2 in Blue.

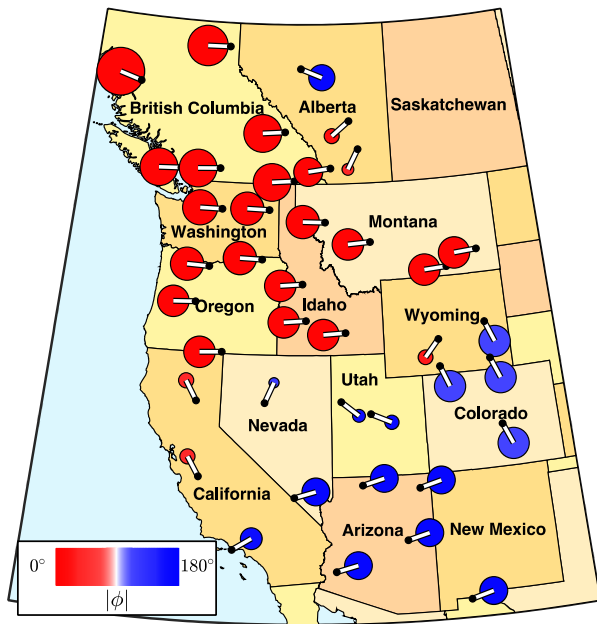


Figure 18: NSB mode shape, 0.45 Hz  
12.0%, 2020 Light Spring

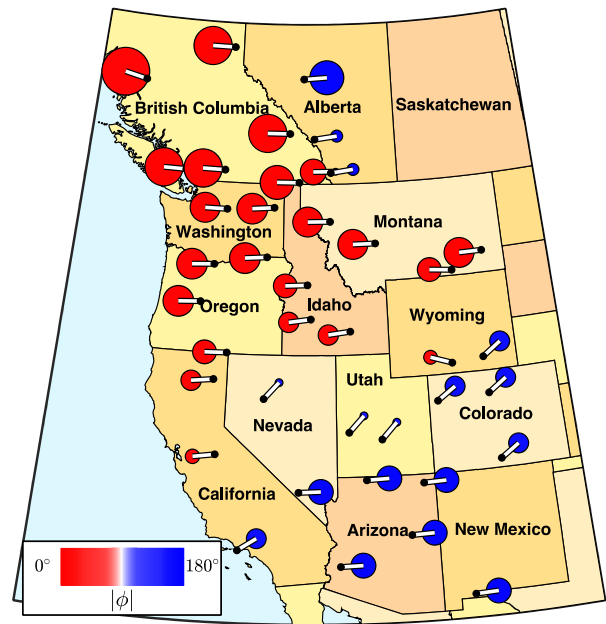


Figure 19: NSB mode shape, 0.36 Hz  
10.5%, 2021 Heavy Summer.

Table 11: NSB mode observability short list.

	Bus frequency	Generator speed
Group 1 ●	Kemano, Shrum, Revelstoke	Kemano, GM Shrum, Revelstoke
Group 2 ●	Genesee, Newman, Palo Verde	Genesee, Rio Grande, Palo Verde

### **Excitability**

Mode excitability provides information about which disturbances excite a particular mode. This is a complex subject and characterizing it fully for the Western Interconnection will require significant future work. Two key aspects that affect excitability are the nature of the disturbance (e.g., type, magnitude, duration) and the location where it occurs. In the simulations performed here, the nature of the disturbance was intentionally kept consistent to gain insight into locational sensitivity. Table 12 provides a list of the brake insertion locations that made it possible to get a clear estimate of the NSB mode for both analyzed base cases. This suggests that a disturbance near one of these points that causes a mismatch in the generation-demand balance, such as a generator trip, would likely excite the NSB mode. Analysis of simulation indicates that the NSB mode is highly excitable from British Columbia, the Pacific Northwest, and the southwestern U.S. Because the NSB mode is the dominant (i.e., most prevalent) oscillatory mode in the Western Interconnection, many different disturbances and points of origin excite it.

**Table 12: NSB mode excitability short list.**

Brake insertion location
Chief Joseph, Kemano, Palo Verde

### **Controllability**

Here, controllability was assessed by estimating the participation factors associated with the NSB mode. For background about participation factors, see Appendix A: Electromechanical Dynamic Theory. Table 13 presents a condensed list of system states with consistently high participation factor magnitudes across both the 2020 Light Spring and 2021 Heavy Summer base cases. This analysis suggests that substation-based controls using bus frequency feedback located at Selkirk, Cranbrook, and/or Round Mt. would be effective in damping the NSB mode. Likewise, PSSs at Revelstoke, GM Shrum, and Grand Coulee influence the damping of this mode. This table is not exhaustive and includes only entries from the list of monitored buses and generators presented in Figure 15. For engineering purposes, the information listed in Table 13 should be regarded as a starting point for further time- and frequency-domain analysis to evaluate effective means of control.

**Table 13: NSB mode controllability short list.**

Bus frequency	Generator speed
Selkirk, Cranbrook, Round Mt.	Revelstoke, GM Shrum, Grand Coulee

Considerable research using both simulation and field tests was conducted on the NSB mode controllability and excitability properties under the development of the prototype PDCI damping controller during the past several years [4]. The mode is highly excitable from many contingencies across the Western Interconnection. Large load and/or generator trips on the north and south ends of

the system especially excite the mode. Also, line trippings on major north-south transmission lines excite the mode. Examples include COI trips and Alberta-to-BC connections.

The NSB mode is highly controllable from the PDCI. In fact, the primary goal of the PDCI damping controller pilot project was to address this mode [4]. Both simulation and field tests demonstrate that the PDCI damping controller considerably improves the NSB mode damping (on the order of 4%).

### Interaction Paths

An interaction path is a transmission line or corridor over which significant energy corresponding to a particular oscillatory mode is exchanged. We can gain insight into the interaction paths by analyzing the modal content of the real power transferred from one point in the system to another (over ac lines). Here, the modal content was decomposed using Prony’s method. Figures 20 and 21 show that for a brake insertion near Palo Verde, the modal content of the real power transfer on Path 66, the California–Oregon Intertie (COI), is dominated by the NSB mode. So, Path 66 is a key interaction path for the NSB mode. Figure 14 provides a summary of the top interaction paths for the NSB mode identified using the interconnection-wide base cases. In addition to the COI, key interaction paths include Path 16 and Path 20. The transfers on other paths may also exhibit significant modal content at the NSB mode frequency.

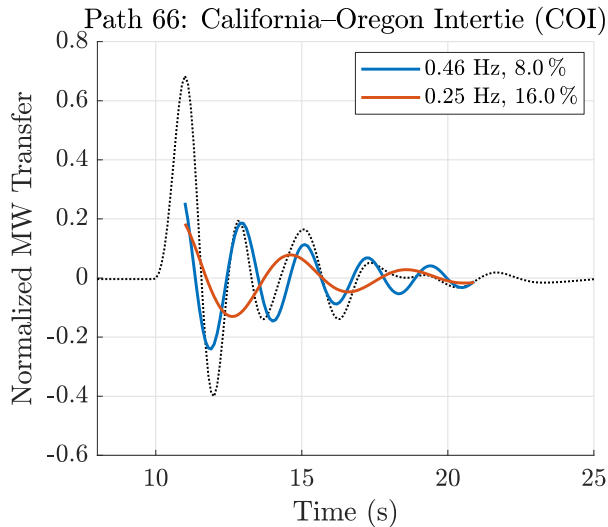


Figure 20: Path 66, 2020 Light Spring.

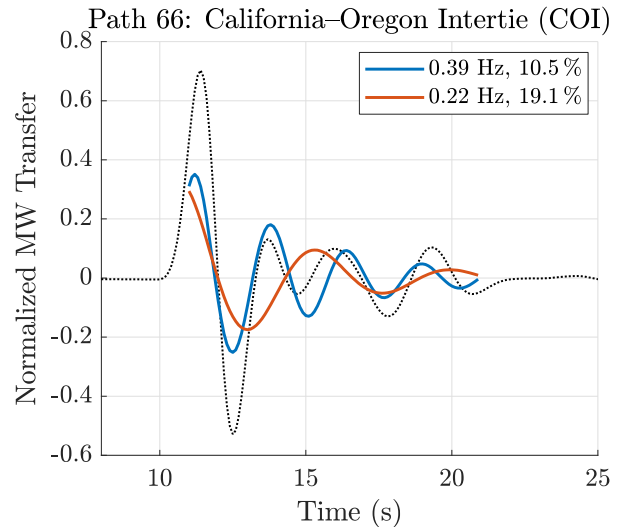


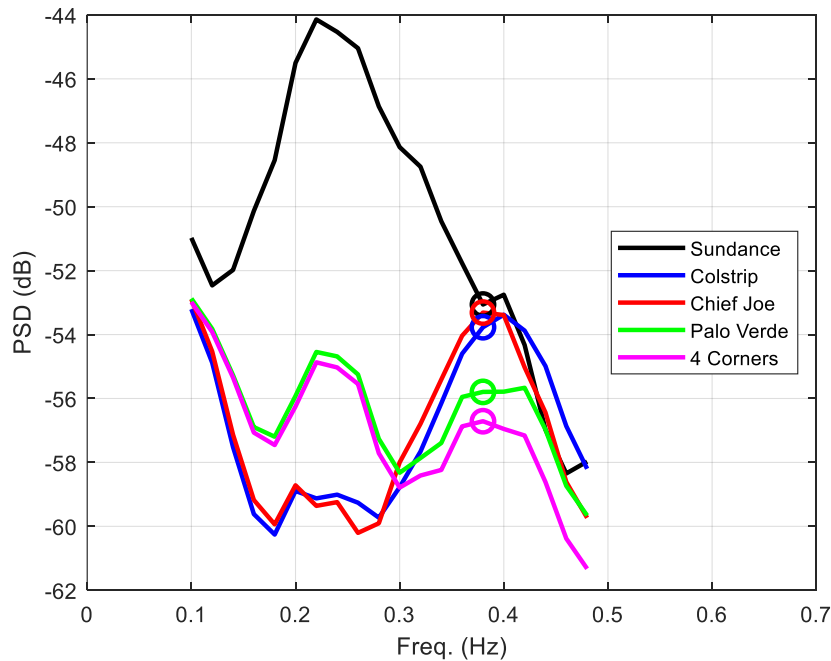
Figure 21: Path 66, 2021 Heavy Summer.

Table 14: NSB mode interaction path short list.

No.	Path Name
Path 16	Idaho–Sierra (Idaho–Nevada)
Path 20	Path C, Pre-Gateway (Idaho–Utah)
Path 66	California–Oregon Intertie (COI)

### Mode Properties Measured from PMU Data

The NSB mode is the most geographically widespread mode in the Western Interconnection. This is demonstrated by examining the spectral energy across the system. As an example, Figure 22 shows the PSD of the frequency from five PMUs scattered across the system measured in 2018 during a PDCI probing tests. The mode is excited by the PDCI probing, which helps accentuate the modal energy. The peak near 0.38 Hz (circled) is the NSB mode. The peak is obvious across the entire system except at Sundance where the spectral energy is dominated by the NSA mode, but the NSB mode is still observable.



**Figure 22: PSD of five PMU-measured frequencies of PDCI probing data on 2018/05/24 from 17:14:05 to 17:34:05 UTC. The NSB mode is at 0.38 Hz (indicated with circles).**

### Mode Shape Calculated via Correlation Analysis

Figure 23 shows the NSB mode shape and observability as measured from a May 24, 2018, dataset during a PDCI probing test—the same one used in Figure 22. The mode frequency during this time was measured as 0.38 Hz via the peak in the mode reference signal in Figure 24. John Day is used as the mode reference signal as it is well known to participate in the NSB mode. As shown in Figure 23, the NSB mode is widespread, with no single area dominating the amplitude. It has the northern part of the system (excluding Alberta) swinging against the southern half. Alberta swings against the remaining northern locations and is in phase with the southern part of the system. This pattern is nearly identical to those presented in the 2014 report [2].

## Modes of Inter-Area Power Oscillations in the Western Interconnection

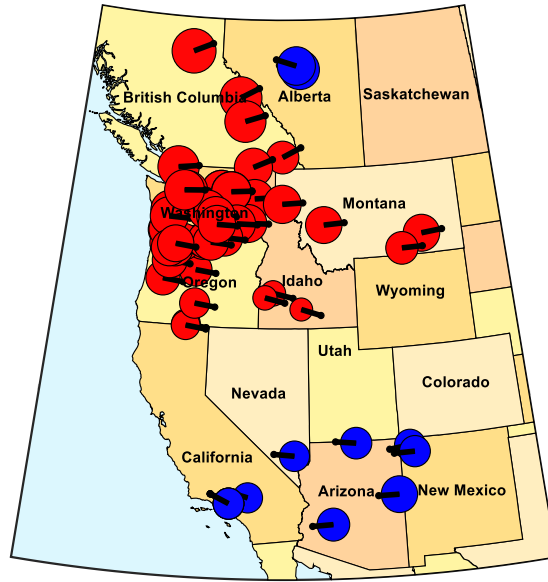


Figure 23: NSB mode shape and observability measured from PMU ambient data on 2018/05/24 from 17:14:05 to 17:14:30 UTC via correlation analysis.

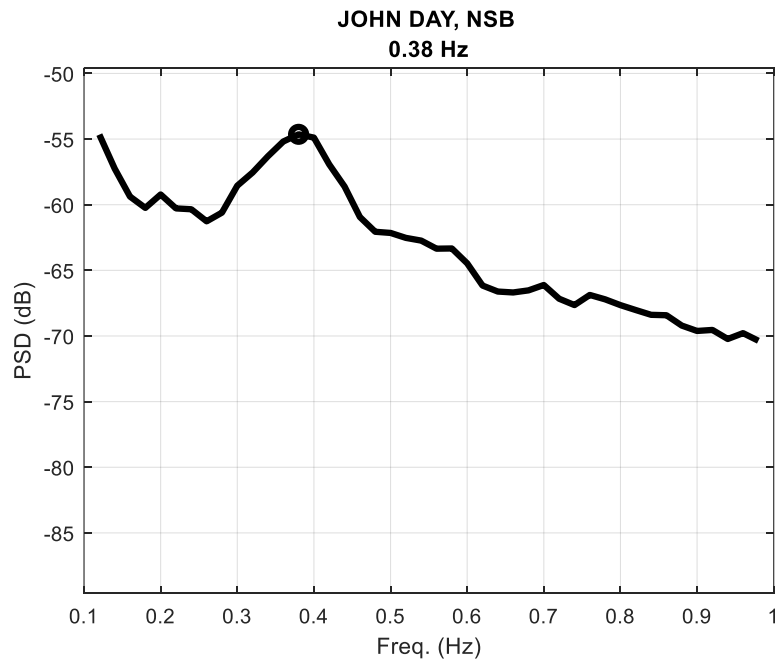


Figure 24: PSD of mode reference signal for the mode shape estimated in Figure 23.

Table 15 summarizes the estimated mode frequencies and shapes from several tests spanning from 2016 through 2019. The dataset from May 24, 2018, at 17:14 UTC is termed the “baseline” set. All other estimated mode shapes are qualitatively compared to this baseline and judged to match it, as indicated in the fourth column of the table. The mode shape map corresponding to each row is contained in subsection “Correlation Analysis from 2016 through 2019 PMU Data” of Appendix E: NSB Mode

## Modes of Inter-Area Power Oscillations in the Western Interconnection

Analyses. Table 15 and the mode shape plots show that the NSB mode frequency and shape are fairly consistent. In some cases, the correlation to the Alberta area is not large enough to merit inclusion in the shape. This indicates that, while the Alberta area swings at this mode, it is not dominant in this area.

**Table 15: Summary of NSB mode frequency and shape, 2016 through 2019.**

Date	Time (UTC)	Freq. (Hz)	Shape match baseline (Y = yes, P = Partial, N = no)	Notes
9/13/2016	17:10:02 to 17:30:00	0.34	Y	Ambient condition. Alberta disconnected.
9/13/2016	18:30:01 to 18:50:01	0.34	Y	PDCI Probing condition. Alberta disconnected.
9/13/2016	22:10:00 to 22:28:00	0.34	Y	Ambient condition. Alberta disconnected.
9/13/2016	22:28:10 to 22:48:10	0.34	Y	PDCI Probing condition. Alberta disconnected.
9/13/2016	23:10:00 to 23:30:00	0.34	Y	Ambient condition. Alberta disconnected.
9/28/2016	15:10:00 to 15:30:00	0.38	Y	Ambient condition.
9/28/2016	16:30:12 to 16:40:12	0.34	Y	PDCI Probing condition.
9/28/2016	17:10:00 to 17:10:00	0.36	P	Ambient condition. Alberta area coherency too low to estimate shape in this area.
9/28/2016	18:20:02 to 18:40:02	0.36	Y	PDCI Probing condition.
9/28/2016	18:46:00 to 18:59:00	NA	NA	Ambient condition. Mode not estimated due to low energy.
9/28/2016	20:30:09 to 20:40:09	0.36	Y	PDCI Probing condition.
9/28/2016	21:10:00 to 21:30:00	0.34	Y	Ambient condition.
9/29/2016	15:10:00 to 15:30:00	0.38	P	Ambient condition. Alberta area coherency too low to estimate shape in this area.
9/29/2016	16:10:34 to 16:20:34	0.38	P	PDCI Probing condition. Some error in mode shape estimate likely due to NSB freq being close to EWA freq. - Colorado area shape amplitude larger than expected.
9/29/2016	17:10:01 to 17:20:01	0.38	P	PDCI Probing condition. Alberta area coherency too low to estimate shape in this area.
9/29/2016	18:10:31 to 18:20:31	0.34	P	PDCI Probing condition. Southern area coherencies too low to estimate shape. Likely due to not enough data in analysis.
9/29/2016	19:10:00 to 19:30:00	0.38	P	Ambient condition. Some error in mode shape estimate likely due to NSB freq being close to EWA freq. - Colorado area shape amplitude larger than expected.
9/29/2016	20:10:31 to 20:20:31	0.38	Y	PDCI Probing condition.
9/29/2016	21:10:00 to 21:30:00	0.38	Y	Ambient condition.
5/16/2017	16:16:01 to 16:36:01	0.38	Y	PDCI Probing condition.
5/16/2017	16:36:05 to 16:50:00	NA	NA	Ambient condition. Mode not estimated due to low energy.
5/16/2017	20:15:01 to 20:35:01	0.38	Y	PDCI Probing condition.
5/16/2017	20:35:05 to 20:50:00	NA	NA	Ambient condition. Mode not estimated due to low energy.
5/23/2018	16:05:00 to 16:24:30	0.36	P	Ambient condition. Southern area coherencies too low to estimate shape in this area.
5/23/2018	16:28:00 to 16:48:00	0.36	Y	PDCI Probing condition.
5/23/2018	20:15:05 to 20:35:05	0.38	Y	PDCI Probing condition.
5/23/2018	20:36:00 to 20:55:00	0.38	Y	Ambient condition.
5/24/2018	00:10:00 to 00:30:00	0.36	Y	Ambient condition.
5/24/2018	17:14:05 to 17:34:05	0.38	Baseline	PDCI Probing condition. Very clear NSB modal peak. EWA mode not at the same freq.
5/24/2018	17:36:00 to 17:50:00	0.36	P	Ambient condition. Colorado area shape amplitude larger than expected and southern PMU coherencies too low to estimate. Error likely due to NSB freq being close to EWA freq. or too little of data for the estimation algorithm?
5/7/2019	14:10:00 to 14:30:00	0.38	P	Ambient condition. Alberta area coherency too low to estimate shape in this area.
5/7/2019	17:10:00 to 17:30:00	0.38	Y	Ambient condition.
5/7/2019	17:30:03 to 17:50:03	0.38	Y	PDCI Probing condition.
5/7/2019	21:20:03 to 21:40:03	0.38	Y	PDCI Probing condition.
5/7/2019	22:10:00 to 22:30:00	NA	NA	Ambient condition. Not enough energy to estimate mode accurately.
5/8/2019	02:10:00 to 02:30:00	0.38	P	Ambient condition. Alberta area coherency too low to estimate shape in this area.
5/8/2019	06:10:00 to 06:30:00	0.38	P	Ambient condition. Alberta area coherency too low to estimate shape in this area.



## Alberta Disconnect

When Alberta disconnects from the Western Interconnection, the NSA mode disappears and the NSB mode drops in frequency. The datasets from September 13, 2016, in Table 15 were collected while Alberta was disconnected. Figure 25 shows the reference signal spectrum and mode shape for one of these cases (taken from the appendix). The NSB mode frequency dropped to 0.34 Hz.

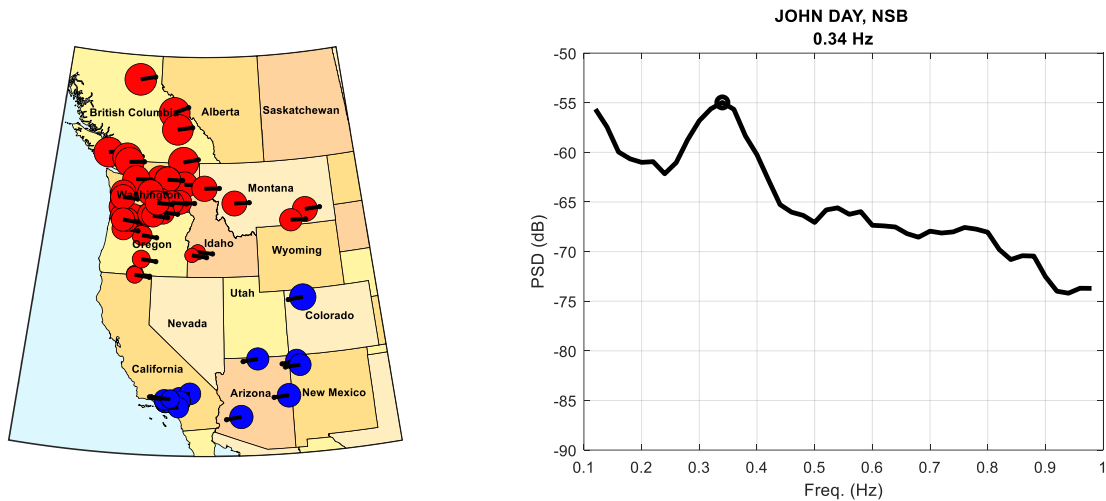


Figure 25: 2016/09/13 from 18:30:01 to 18:50:01 UTC. Alberta disconnected, ambient condition.

The NSA and NSB mode frequencies and damping for a typical Alberta disconnect are shown in Figures 26 and 27 for a dataset from 2012 (these are taken from the 2014 report [2]). The modes are estimated with an automated mode meter. The Alberta disconnect occurs just before the 1100-minute point. After the disconnect, the NSA mode disappears and the frequency and damping of the NSB mode suddenly decrease. This response is typical of an Alberta disconnect and continues to be seen today.

## Modes of Inter-Area Power Oscillations in the Western Interconnection

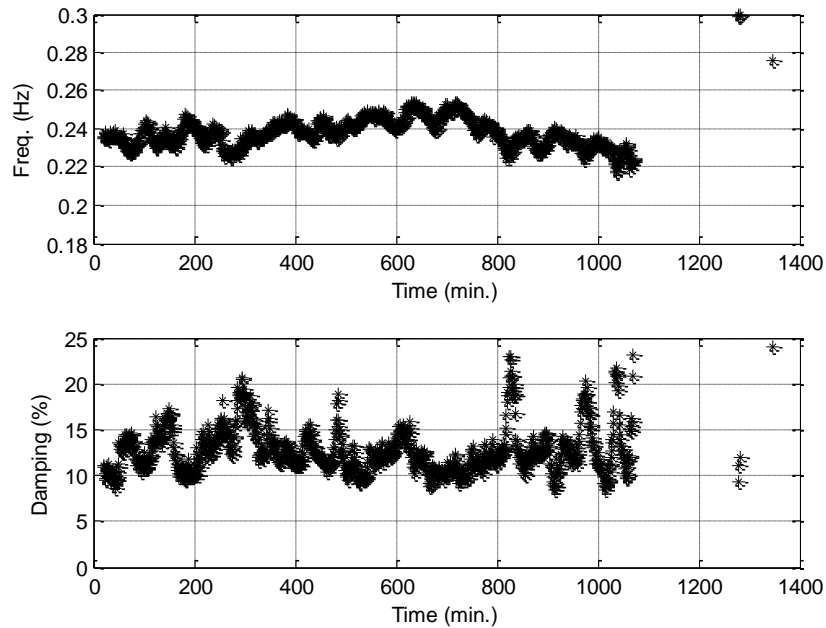


Figure 26: NSA mode meter estimates for 2012/06/18. Plot starts at midnight GMT (5:00 pm PDT).

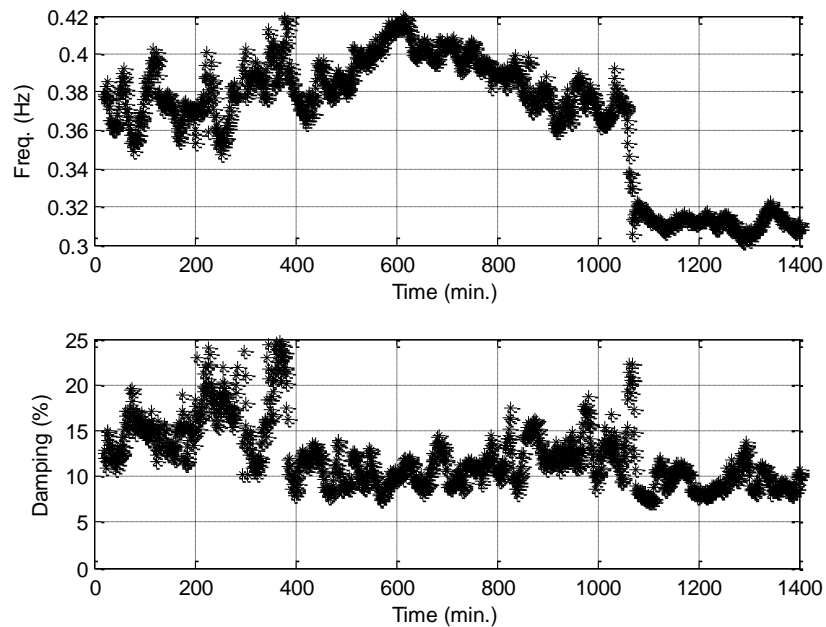


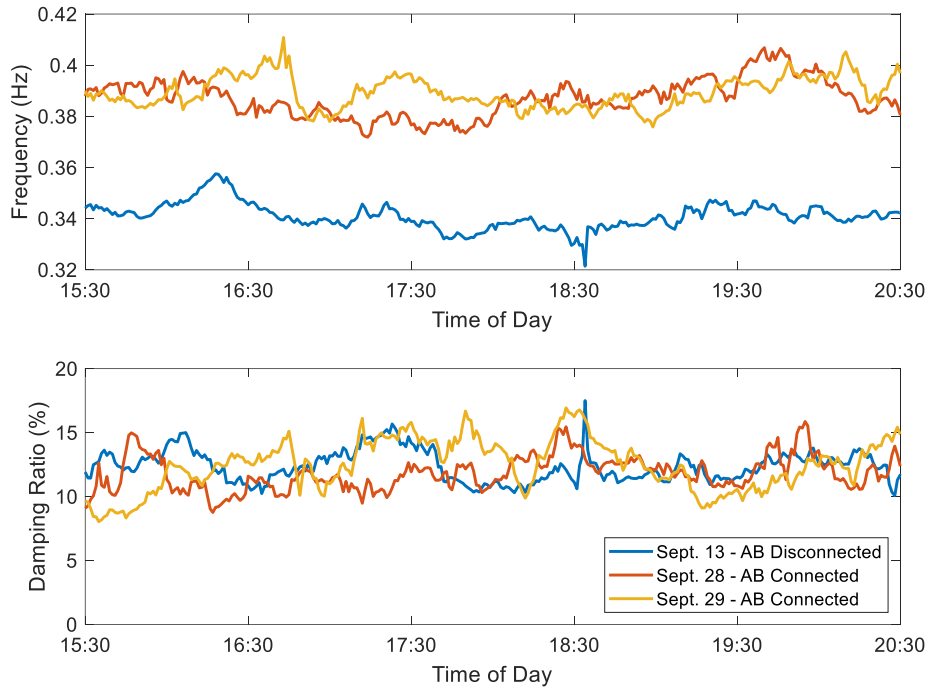
Figure 27: NSB mode meter estimates for 2012/06/18. Plot starts at midnight GMT (5:00 pm PDT).

Figure 28 compares NSB mode meter estimates for several hours from three days in 2016. On one of the days (Sep. 13), Alberta is disconnected. The NSB mode frequency is lower for the day when Alberta is disconnected. The damping for all three days is basically the same.



## Modes of Inter-Area Power Oscillations in the Western Interconnection

Future editions of this report will aim to provide updated analysis of Alberta disconnections and cases in which Alberta is weakly connected to the rest of the system.



**Figure 28: Mode meter results for 3 days in 2016. Alberta is disconnected for the September 13 data and connected for the September 28 and 29 data.**

### ***Mode Frequency and Damping***

The NSB mode was included in a study of mode meter estimates spanning 2017–2018. Histograms of the mode’s frequency and damping estimates, which were updated every 15 minutes, are presented in Figure 29. The mode’s frequency is centered just below 0.4 Hz and tends to remain between 0.35 Hz and 0.45 Hz. The NSB mode’s damping is lower than the NSA mode (see Figure 14 for comparison with Figure 29). Damping ratios between 5% and 10% are common but are most often between 10% and 15%.

## Modes of Inter-Area Power Oscillations in the Western Interconnection

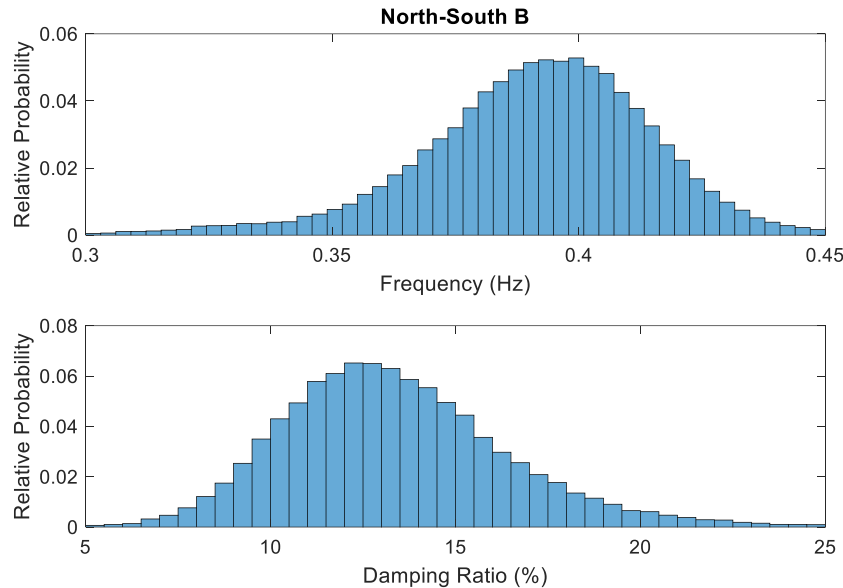


**Figure 29: Histograms of NSB frequency and damping ratio estimates collected from a mode meter every 15 minutes from 2017–2018.**

NSB mode meter and ringdown analysis results have been conducted for many events over the years. A good sample is contained in Appendix E: NSB Mode Analyses. A typical set of results from the September 29, 2016, tests are presented in Figures 30 and 31. The mode meter results vary during the study period due to estimation errors and changes in the mode driven by changing operating conditions. The ringdown analysis results in Figure 30 are from four Chief Joseph brake insertions and show good agreement with the mode meter estimates. In Figure 31, the mode shape estimate from the second brake insertion shows the typical pattern for the NSB mode, with generators in the Pacific Northwest swinging against those in Alberta and the Southwest. The report, “Design of the Pacific DC Intertie wide area damping controller,” [4] also contains many ringdown analysis cases for the NSB mode.

## Modes of Inter-Area Power Oscillations in the Western Interconnection

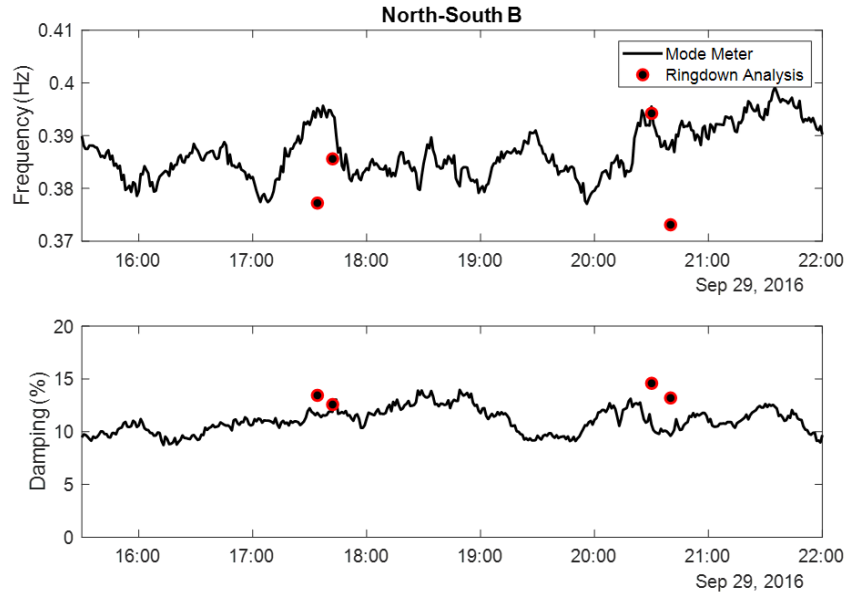


Figure 30: Estimates of the North-South B mode from mode meter and ringdown analyses for the 2016/09/29 system tests.

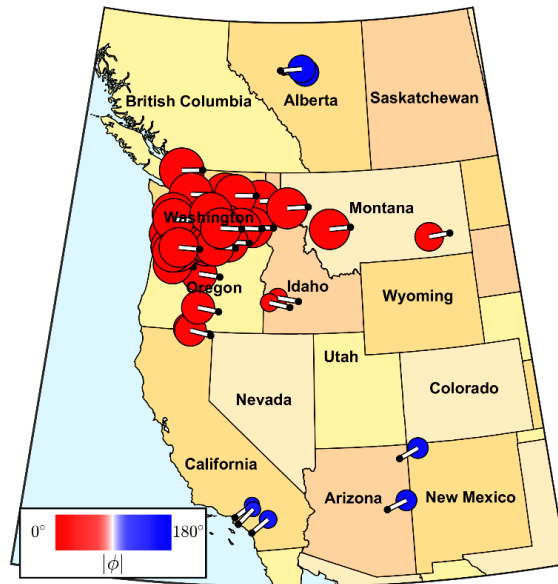


Figure 31: Mode shape estimates corresponding to the second ringdown results in Appendix E: NSB Mode Analyses. (20160929\_Ring2\_NSB\_CUST-GENESEE\_Prony).

The signals used to estimate the NSB mode were designed with the principles outlined in the NSA section. Figures 32 and 33 show the locations of the PMUs used in signal designs for NSB. Two figures are included because not all signals were available in any one dataset. The colors on the map indicate the signals that were subtracted (blue) from reference signals (red). Multiple signals were designed to

## Modes of Inter-Area Power Oscillations in the Western Interconnection

accommodate varying availability between datasets. The spectra for the five signals used to generate the mode estimates included in this report are also displayed in the figures. Though the NSA mode remains dominant, the NSB mode is also prominent near 0.4 Hz. As demonstrated by the SNOHOMISH-GENESEEE-CORONADO signal, subtracting two signals, one from Alberta and one from the southwest, can diminish the NSA peak, further highlighting the NSB mode.

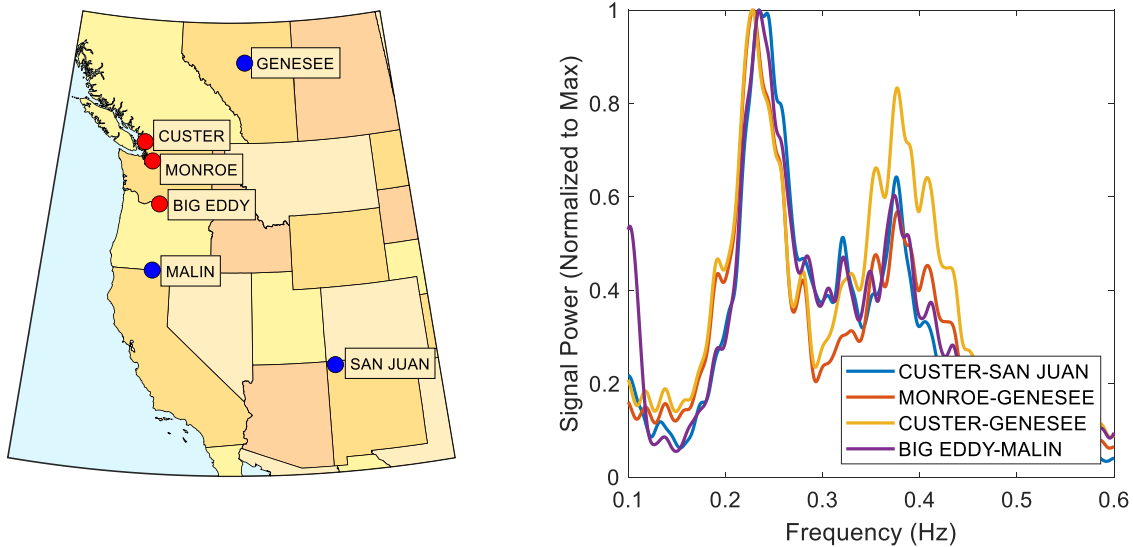


Figure 32: Locations of PMUs used in signal designs (left) and spectra of resulting signals (right). (Dataset 1)

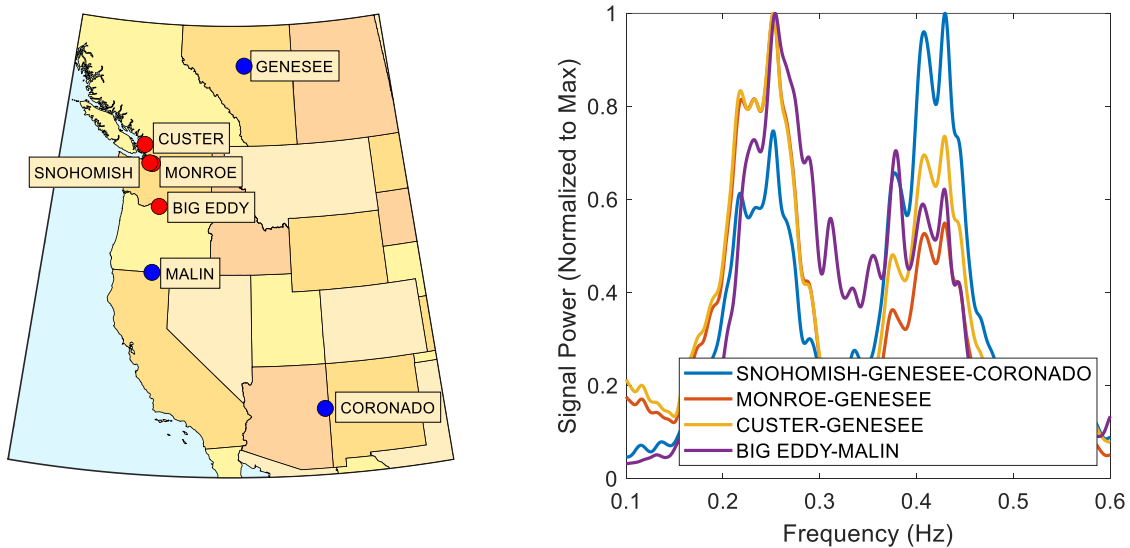


Figure 33: Locations of PMUs used in signal designs (left) and spectra of resulting signals (right). (Dataset 2)

### Future Work

The NSB mode is relatively well understood. Future recommendations include:

- Continued monitoring of the NSB mode from PMU measurements and field tests.
- Investigating the excitability and interaction paths of the NSB mode with more detail using simulation studies. Initial work has been presented in this report. The controllability of the mode is well understood based primarily on experimental results from the PDCI damping controller development [4]. (This controller is not currently used in operations, ca. 2021.)
- Analyze several fault types (SLG, LL, 3-phase, etc.) at several locations and voltage levels to expand our knowledge of the risks to the NSB mode being excited by more common occurrences, and to potentially observe the influence of increasing levels of IBR penetration on the modes.
- Analyze more recent Alberta area weak interconnection and islanding cases. Several recent cases were identified from 2017 through 2020; but the analysis team lacked time to include results in this report.

### East-West A Mode

---

#### Mode Description

The EWA mode was first presented as an inter-area mode in the 2014 WECC modes report based on a few PMU datasets from 2013 [2]. It also exists in a simplified-system eigenanalysis. A recommendation from the 2014 report included building a much better understanding of the EWA mode. This report includes extensive PMU-based measurement of this mode using data from 2016 through 2019. The mode is consistently in the 0.35 Hz to 0.45 Hz range. Its shape is consistent, with the eastern portion of the system, centralized in Colorado, oscillating against the rest of the system. In many of the measurements, parts of the Wyoming–Montana border (e.g., Yellowtail Dam) and PMUs in Idaho (e.g., Midpoint) swing in phase with Colorado PMUs. In some cases, the mode can also be observed with a smaller amplitude in southern California and/or the lower Columbia on the Washington–Oregon border.

The EWA mode is near in frequency to the better-known NSB mode. In some cases, the two modes are exactly at the same frequency. Therefore, discerning between these two modes is often difficult.

Correlation analysis is used in this report to separate the modes to accurately estimate their respective shapes.

#### Mode Properties Measured from Simulation Models

This section discusses the properties of the EWA mode observed in simulation. Two simulation models were studied, the WECC 2020 Light Spring base case (20LSP1sa1) and the WECC 2021 Heavy Summer



base case (21HS3a1). Basic facts about these cases, including system loading and approximate renewable penetration, are presented in the “Simulation Models” section of the Introduction. For each base case, ten simulations were performed with each run corresponding to a 1,200 MW dynamic brake insertion (0.5 s duration) initiated at a different point in the system. Figure 2 shows the insertion locations used to perturb the system. Brake insertions at a subset of these locations excited the EWA mode. The mode properties were estimated by identifying a reduced-order state-space model from the free response portion of the ringdown. Details of the multi-channel curve fitting technique used to identify the system matrix are provided in the “Regularized Dynamic Mode Decomposition” section of Appendix B: Analysis Methods.

### ***Observability***

The shape of the EWA mode is characterized by generation units in Colorado and eastern Wyoming oscillating against the rest of the system. Machines in Utah and eastern Montana tend to oscillate in phase with those in Colorado. Figure 34 shows the shape of the EWA mode estimated from the 2020 Light Spring base case. Figure 35 shows the shape from the 2021 Heavy Summer case. In the simulation models, the dividing node is located near the Nevada-Utah border. Table 16 presents a condensed list of locations at which the EWA mode is readily observable. This table is not exhaustive and includes only entries from the list of monitored buses and generators presented in Table 5. In Figure 34 and Figure 35, the entries listed in Group 1 are shown in red, and those in Group 2 are blue. In some cases, the generation units in Colorado may oscillate more against BC and the Pacific Northwest, and in other cases against units in California and the southwestern U.S. So, the observability at the points listed in Group 2 may vary.

## Modes of Inter-Area Power Oscillations in the Western Interconnection

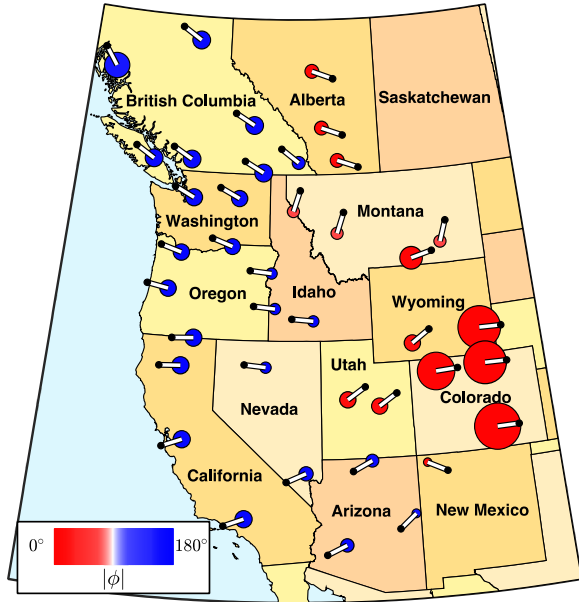


Figure 34: EWA mode shape, 0.44 Hz 11.5%, 2020 Light Spring.

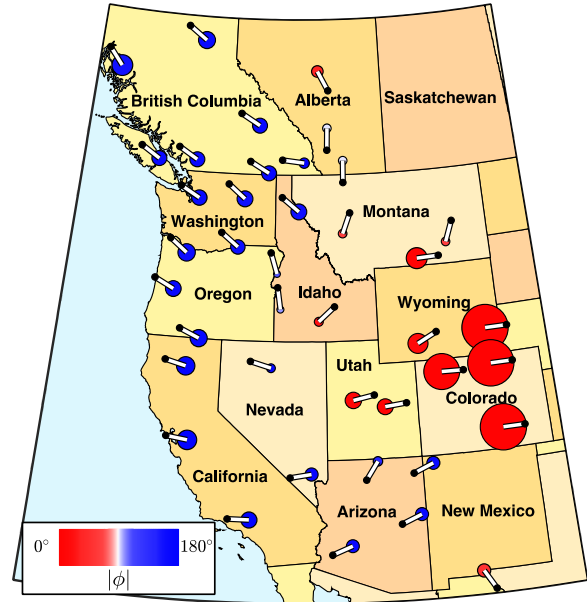


Figure 35: EWA mode shape, 0.36 Hz 14.5%, 2021 Heavy Summer.

Table 16: EWA mode observability short list.

	Bus frequency	Generator speed
Group 1 ●	Comanche, Laramie, Ault	Comanche, Laramie River, Craig
Group 2 ●	Kemano, Shrum, Tesla, Vincent	Kemano, GM Shrum, Walnut, Haynes

### Excitability

Mode excitability provides information about which disturbances excite a particular mode. This is a complex subject and characterizing it fully for the Western Interconnection will require significant future work. Two key aspects that affect excitability are the nature of the disturbance (e.g., type, magnitude, duration) and the location where it occurs. In the simulations performed here, the nature of the disturbance was intentionally kept consistent to gain insight into locational sensitivity. Table 17 provides a list of the brake insertion locations that made it possible to get a clear estimate of the EWA mode for both analyzed base cases. This suggests that a disturbance near one of these points that causes a mismatch in the generation-demand balance, such as a generator trip, would likely excite the EWA mode. Analysis of simulation indicates that the EWA mode is highly excitable from Colorado or eastern Wyoming, and moderately excitable from California and Utah.

Table 17: EWA excitability short list.

Brake insertion location
Comanche, Diablo Canyon, Intermountain

### **Controllability**

Here, controllability was assessed by estimating the participation factors associated with the EWA mode. For background about participation factors, see Appendix A: Electromechanical Dynamic Theory. Table 18 presents a condensed list of system states with consistently high participation factor magnitudes across both the 2020 Light Spring and 2021 Heavy Summer base cases. This analysis suggests that substation-based controls using bus frequency feedback located at Laramie and Ault would be effective in damping the EWA mode. Moreover, it indicates that similar controls located at Selkirk or near the Navajo site (now retired) would also be beneficial. Likewise, PSSs at Laramie River, Comanche, and Craig influence the damping of this mode. This table is not exhaustive and includes only entries from the list of monitored buses and generators presented in Table 5. For engineering purposes, the information listed in Table 18 should be regarded as a starting point for further time- and frequency-domain analysis to evaluate effective means of control.

**Table 18: EWA mode controllability short list.**

Bus frequency	Generator speed
Laramie, Ault, Selkirk, Navajo	Laramie River, Comanche, Craig

### **Interaction Paths**

An interaction path is a transmission line or corridor over which significant energy corresponding to a particular oscillatory mode is exchanged. We can gain insight into the interaction paths by analyzing the modal content of the real power transferred from one point in the system to another (over ac lines). Here, the modal content was decomposed using Prony’s method. Figure 36 and Figure 37 show that for a brake insertion near Comanche, the modal content of the real power transfer on Path 19, Bridger West (Wyoming–Idaho), is dominated by the EWA mode. So, Path 19 is a key interaction path for the EWA mode. Table 19 provides a summary of the top interaction paths for the EWA mode identified using the interconnection-wide base cases. In addition to Bridger West, key interaction paths include Path 30 and Path 31. The transfers on other paths may also exhibit significant modal content at the EWA mode frequency.

## Modes of Inter-Area Power Oscillations in the Western Interconnection

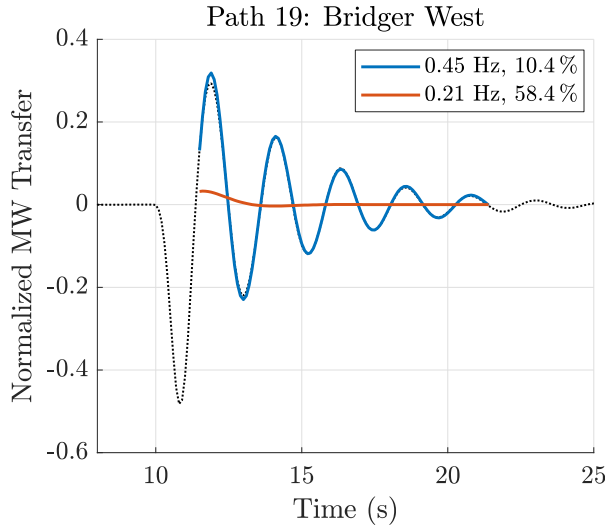


Figure 36: Path 19, 2020 Light Spring.

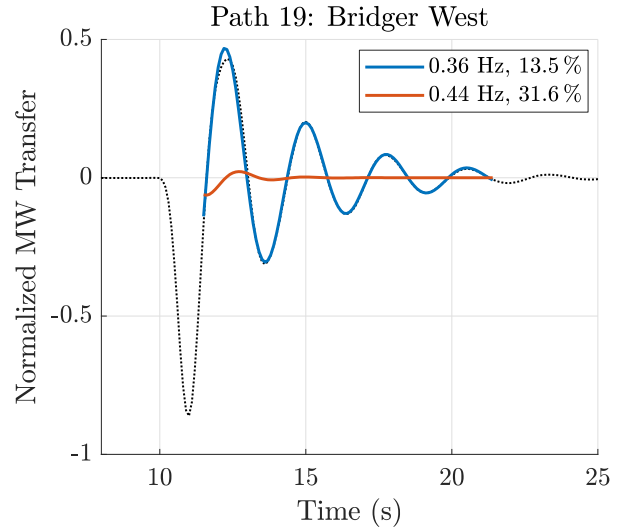


Figure 37: Path 19, 2021 Heavy Summer.

Table 19: EWA mode interaction path short list.

No.	Path Name
Path 19	Bridger West (Wyoming–Idaho)
Path 30	TOT 1A (Colorado–Utah)
Path 31	TOT 2A (Colorado–New Mexico)

### Mode Properties Measured from PMU Data

#### *Distinguishing Between the EWA and NSB Modes*

The NSB and EWA modes are close in frequency. In some cases, the two modes are at nearly the exact same frequency making it often difficult to discern between the two. As an example, consider the PSD plot in Figure 38. It shows the PSD for the EWA mode reference signal and the NSB mode reference signal. The peaks in the PSD for each reference signal is used to identify the associated mode (0.38 Hz for the NSB mode, and 0.4 Hz for the EWA mode). While the modes are close in frequency, there are two distinct modal peaks. The black trace is from Ault, which is the reference signal for the EWA mode; the red trace is from John Day, which is the reference signal for the NSB mode. The black circle is at the EWA mode frequency (0.42 Hz), and the red circle is at the NSB frequency (0.38 Hz).

## Modes of Inter-Area Power Oscillations in the Western Interconnection

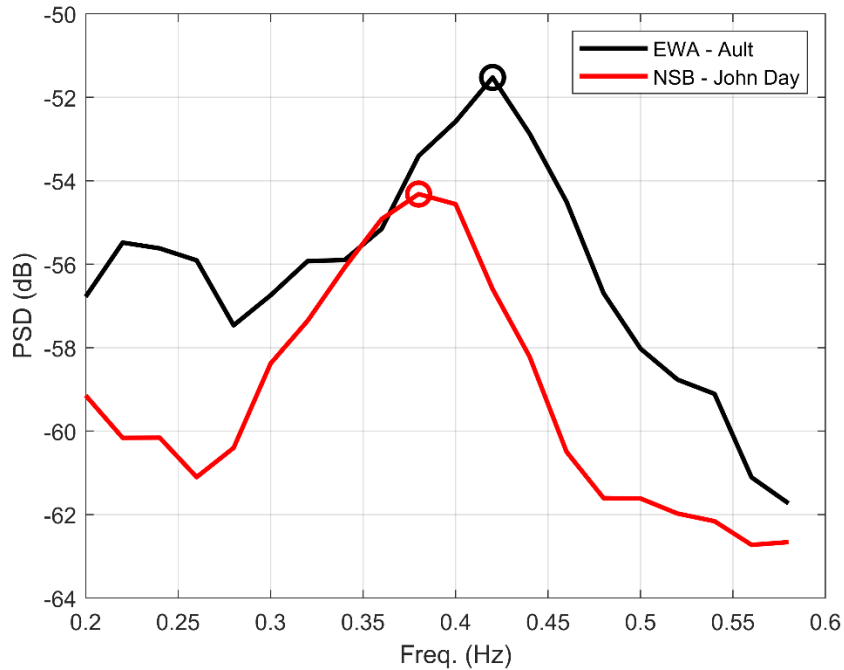


**Figure 38: PSD of PMU-measured frequencies during a PDCI probing test on 2018/05/24 from 17:14:05 to 17:34:05 UTC.**

Correlation via spectral coherency analysis is useful in distinguishing between these two closely spaced modes. Figure 39 and Figure 40 demonstrate this for the data case in Figure 38 at some select locations across this system. Figure 39 shows the analyses for the EWA mode where the reference signal is Ault, and the mode frequency is 0.42 Hz. If a particular location's coherency at 0.42 Hz is below 0.5, this location is judged to not participate in the EWA mode. Yellowtail is the only location that participates, and that participation is not significant (barely above a coherency of 0.5). This indicates the EWA mode is primarily Ault moving against the system.

Similarly, Figure 40 shows the coherency analysis for the NSB mode with John Day as the reference signal and the mode measured at 0.38 Hz. All locations except Ault have a significant correlation to John Day (well above 0.5) indicating that these locations participate in the NSB mode. The Ault location with a Coherency well below 0.5 does not participate in the NSB mode.

## Modes of Inter-Area Power Oscillations in the Western Interconnection

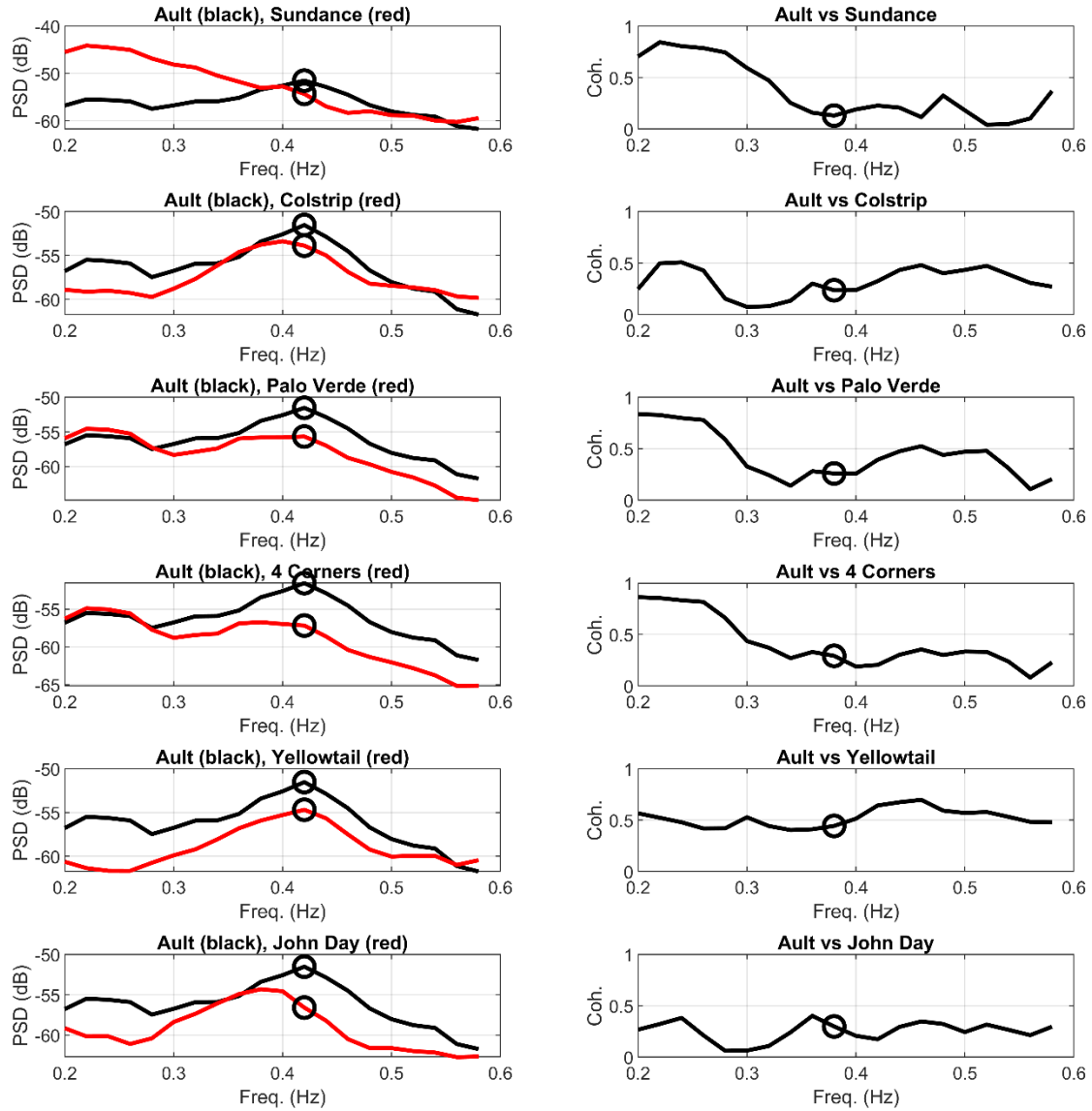


Figure 39: PSD and coherency plots for the EWA mode for the dataset from Figure 38. Plots on the left are the PSD, plots on the right are the corresponding coherency using Ault as the reference signal.

## Modes of Inter-Area Power Oscillations in the Western Interconnection

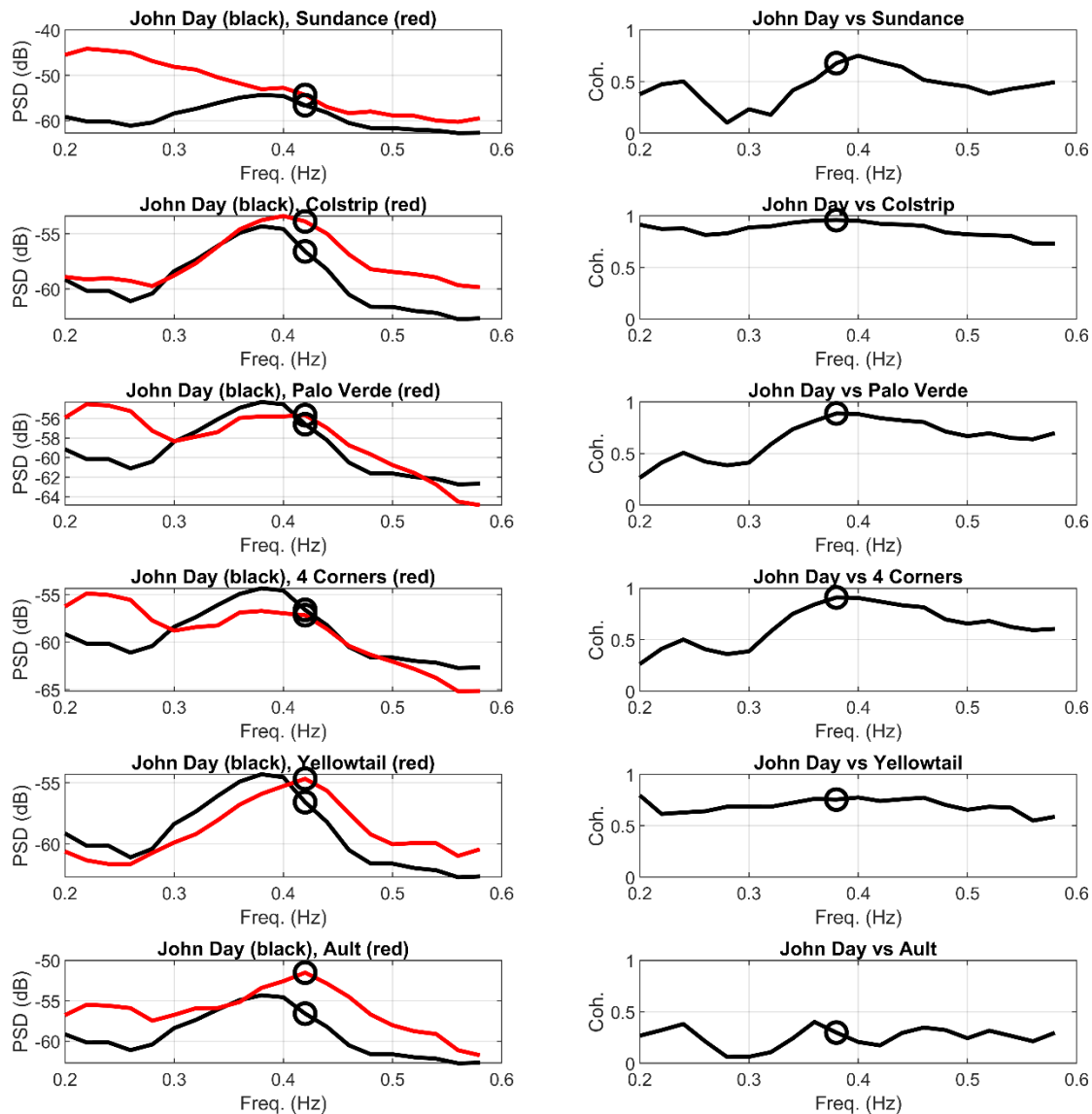


Figure 40: PSD and Coherency plots for the NSB mode for the dataset from Figure 38. Plots on the left are the PSD, plots on the right are the corresponding Coherency using John Day as the reference signal.

### Mode Shape Calculated via Correlation Analysis of PMU Data

Figure 41 shows the EWA mode shape and observability as measured from a May 24, 2018, dataset during an ambient condition. The mode frequency during this time was measured as 0.4 Hz via the peak in the mode reference signal in Figure 42. Ault is used as the mode reference signal as it is well known to participate in the EWA. The mode shape shows that the mode had the Colorado area swinging against the system. This mode shape is amazingly consistent for nearly every measurement set as summarized in Table 20. The dataset from May 24, 2018, at 17:36 UTC is termed the “baseline” set. All other estimated mode shapes are qualitatively compared to this baseline and judged to match it



## Modes of Inter-Area Power Oscillations in the Western Interconnection

as indicated in the fourth column of the table. The mode shape maps for each of the rows of the table is contained in subsection “Correlation Analysis from 2016 through 2019 PMU Data” of Appendix F: EWA Mode Analyses.

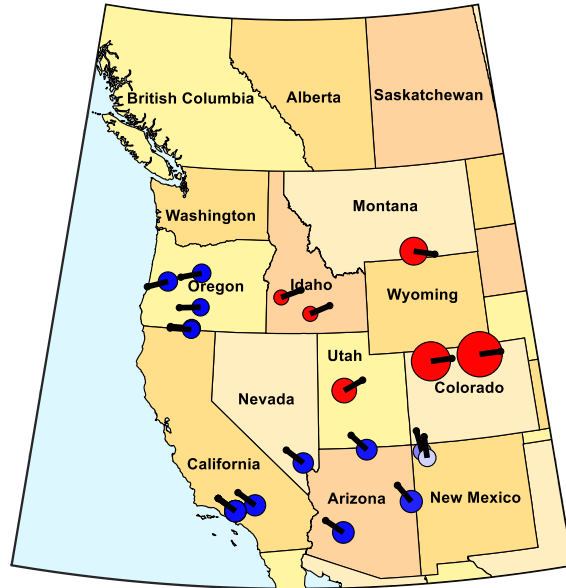


Figure 41: EWA mode shape and observability measured from PMU ambient data on 2018/05/24 from 17:36:00 to 17:20:00 UTC via correlation analysis.

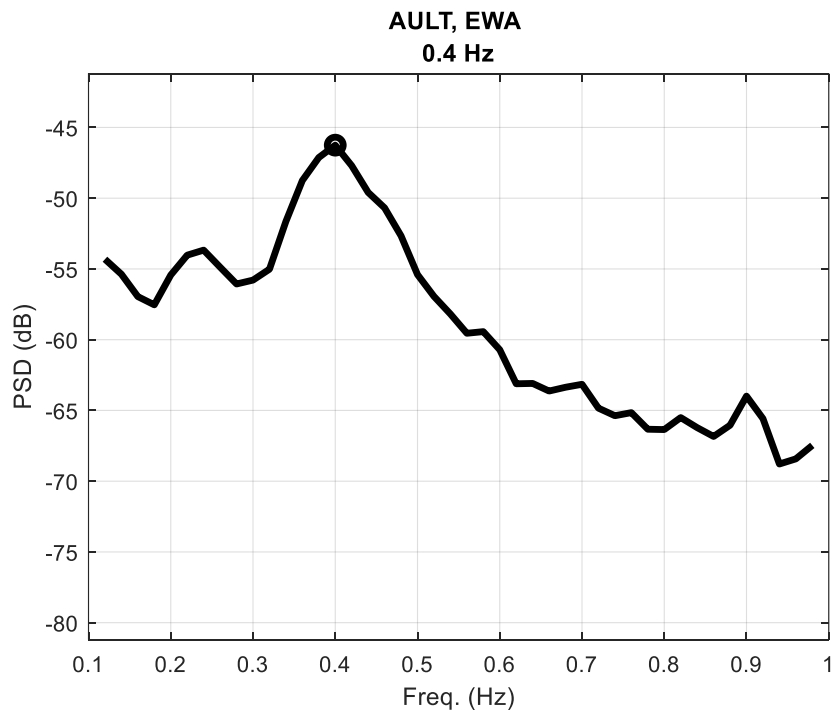


Figure 42: Mode reference signal for the mode shape estimated in Figure 41.

## Modes of Inter-Area Power Oscillations in the Western Interconnection

Table 20: Summary of EWA mode frequency and shape, 2016 through 2019.

Date	Time (UTC)	Freq. (Hz)	Shape match baseline (Y = yes, P = Partial, N = no)	Notes
9/13/2016	17:10:02 to 17:30:00	0.40	Y	Ambient condition. Alberta disconnected.
9/13/2016	18:30:01 to 18:50:01	0.40	Y	PDCI Probing condition. Alberta disconnected.
9/13/2016	22:10:00 to 22:28:00	0.40	Y	Ambient condition. Alberta disconnected.
9/13/2016	22:28:10 to 22:48:10	0.40	Y	PDCI Probing condition. Alberta disconnected.
9/13/2016	23:10:00 to 23:30:00	0.40	Y	Ambient condition. Alberta disconnected.
9/28/2016	15:10:00 to 15:30:00	0.42	Y	Ambient condition.
9/28/2016	16:30:12 to 16:40:12	0.40	Y	PDCI Probing condition.
9/28/2016	17:10:00 to 17:10:00	0.38	Y	Ambient condition.
9/28/2016	18:20:02 to 18:40:02	0.38	Y	PDCI Probing condition.
9/28/2016	18:46:00 to 18:59:00	0.38	Y	Ambient condition.
9/28/2016	20:30:09 to 20:40:09	0.38	Y	PDCI Probing condition.
9/28/2016	21:10:00 to 21:30:00	0.38	Y	Ambient condition.
9/29/2016	15:10:00 to 15:30:00	0.42	Y	Ambient condition.
9/29/2016	16:10:34 to 16:20:34	0.42	Y	PDCI Probing condition.
9/29/2016	17:10:01 to 17:20:01	0.40	Y	PDCI Probing condition.
9/29/2016	18:10:31 to 18:20:31	0.42	P	PDCI Probing condition. Generators in MT and ID participating more strongly.
9/29/2016	19:10:00 to 19:30:00	0.42	Y	Ambient condition.
9/29/2016	20:10:31 to 20:20:31	0.40	Y	PDCI Probing condition.
9/29/2016	21:10:00 to 21:30:00	0.40	Y	Ambient condition.
5/16/2017	16:16:01 to 16:36:01	0.42	P	PDCI Probing condition. So Cal shape is larger than usual.
5/16/2017	16:36:05 to 16:50:00	0.42	Y	Ambient condition.
5/16/2017	20:15:01 to 20:35:01	0.42	P	PDCI Probing condition. So Cal shape is larger than usual.
5/16/2017	20:35:05 to 20:50:00	0.42	Y	Ambient condition.
5/23/2018	16:05:00 to 16:24:30	0.40	Y	Ambient condition.
5/23/2018	16:28:00 to 16:48:00	0.40	Y	PDCI Probing condition.
5/23/2018	20:15:05 to 20:35:05	0.36	P	PDCI Probing condition. The shape matches the baseline, but, the freq peak is likely due to the NSB mode. Difficult to distinguish between the two since they are so close in freq.
5/23/2018	20:36:00 to 20:55:00	0.38	Y	Ambient condition.
5/24/2018	00:10:00 to 00:30:00	0.40	Y	Ambient condition.
5/24/2018	17:14:05 to 17:34:05	0.42	Y	PDCI Probing condition.
5/24/2018	17:36:00 to 17:50:00	0.40	Baseline	Ambient condition.
5/7/2019	14:10:00 to 14:30:00	0.42	Y	Ambient condition.
5/7/2019	17:10:00 to 17:30:00	0.42	Y	Ambient condition.
5/7/2019	17:30:03 to 17:50:03	0.42	Y	PDCI Probing condition.
5/7/2019	21:20:03 to 21:40:03	0.42	Y	PDCI Probing condition.
5/7/2019	22:10:00 to 22:30:00	0.42	Y	Ambient condition.
5/8/2019	02:10:00 to 02:30:00	0.42	Y	Ambient condition.
5/8/2019	06:10:00 to 06:30:00	0.44	Y	Ambient condition.

### Mode Frequency and Damping

Research level mode meter tests have recently been conducted for the EWA mode with some results presented in Appendix F: EWA Mode Analyses. In these test cases, the mode's frequency tends to vary from 0.37 Hz to 0.45 Hz, though in one case the frequency dropped below 0.33 Hz. The damping ratio was most often in the range of 10 to 15%, with deviations from this range tending high. A typical set of mode meter results for the EWA mode are presented in Figure 43. The estimates span nearly 24 hours



## Modes of Inter-Area Power Oscillations in the Western Interconnection

over May 7 and 8, 2019. The mode meter results vary during the study period due to estimation errors and changes in the mode driven by changing operating conditions.

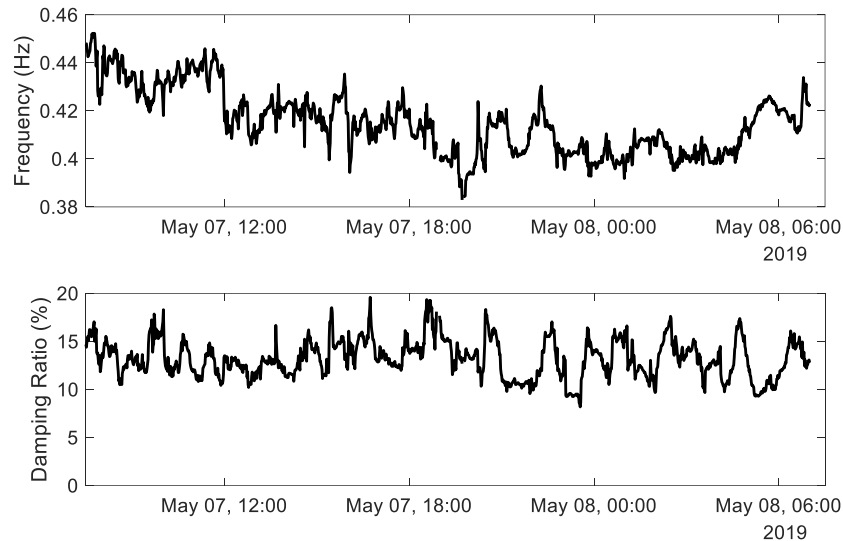


**Figure 43: Estimates of the EWA mode from a mode meter analysis for the 2019/05/07 system tests.**

The signals used to estimate the EWA mode were designed with the principles outlined in the NSA section. Figure 44 shows the locations of the PMUs used in signal designs for EWA. The colors on the map indicate the signals that were subtracted (blue) from reference signals (red). Multiple signals were designed to accommodate varying availability between datasets. The spectra for the four signals used to generate the mode estimates included in this report are also displayed in Figure 44. Note that the EWA mode is dominant in all spectra.

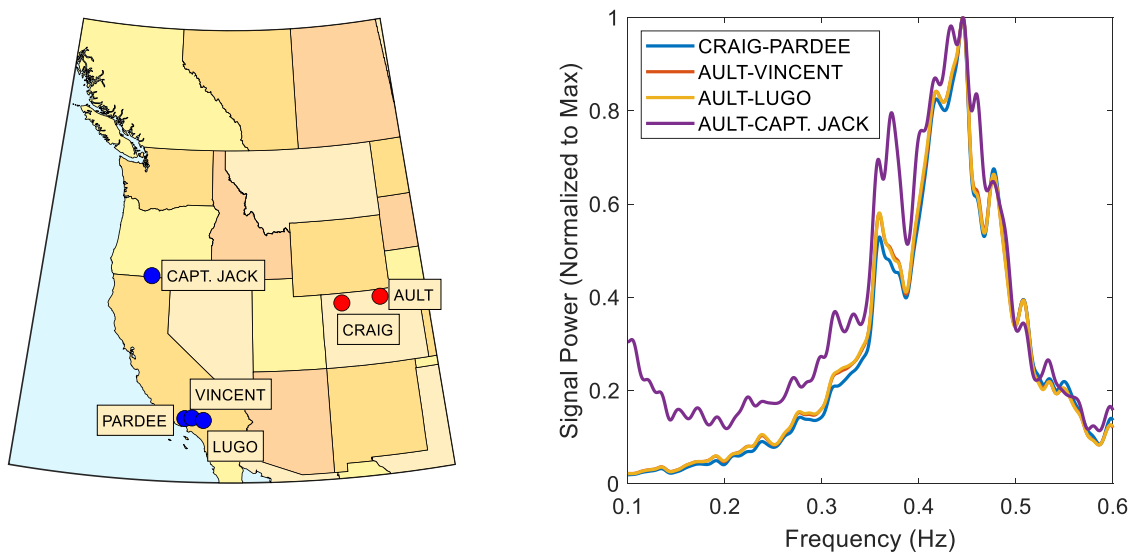


**Figure 44: Signal selection for EWA mode meter.**

## Modes of Inter-Area Power Oscillations in the Western Interconnection

### January 29, 2021, Event

On January 29, 2021, a forced stimulus originating from the Colorado region resonated the EWA mode two times with short burst durations. The first instance occurred from 10:13:00 PM CST to 10:13:45 PM CST, and the second instance occurred from 10:33:38 PM CST to 10:34:32 PM CST. In Figure 45, PMU frequency data from Southwest Power Pool's monitoring displays show the substations of Mead (in purple) and Ault (in blue) oscillating against each other.

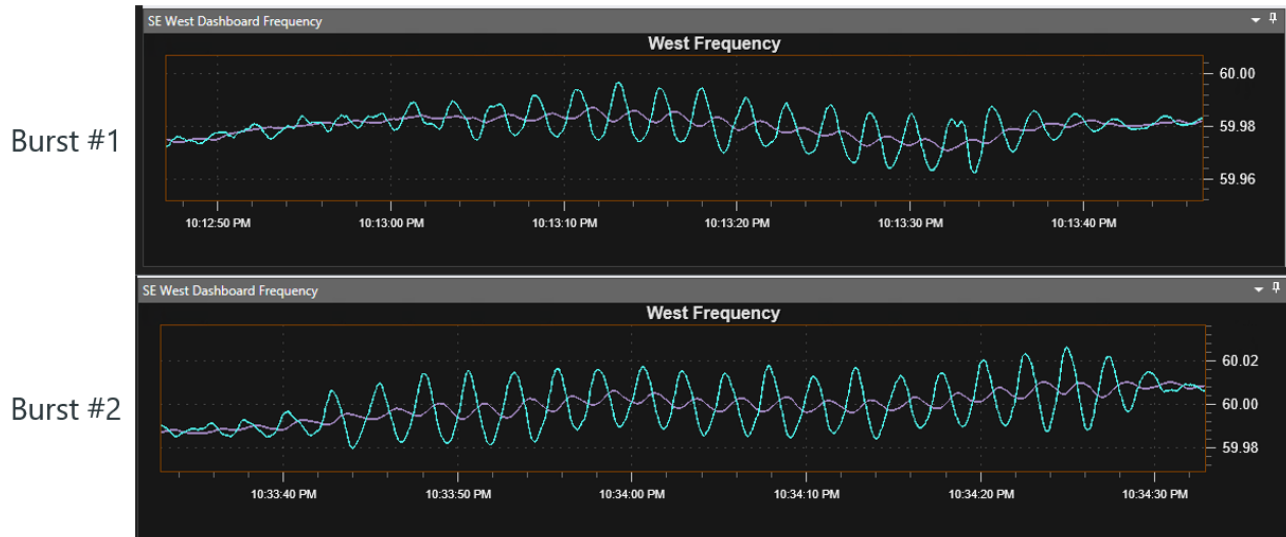
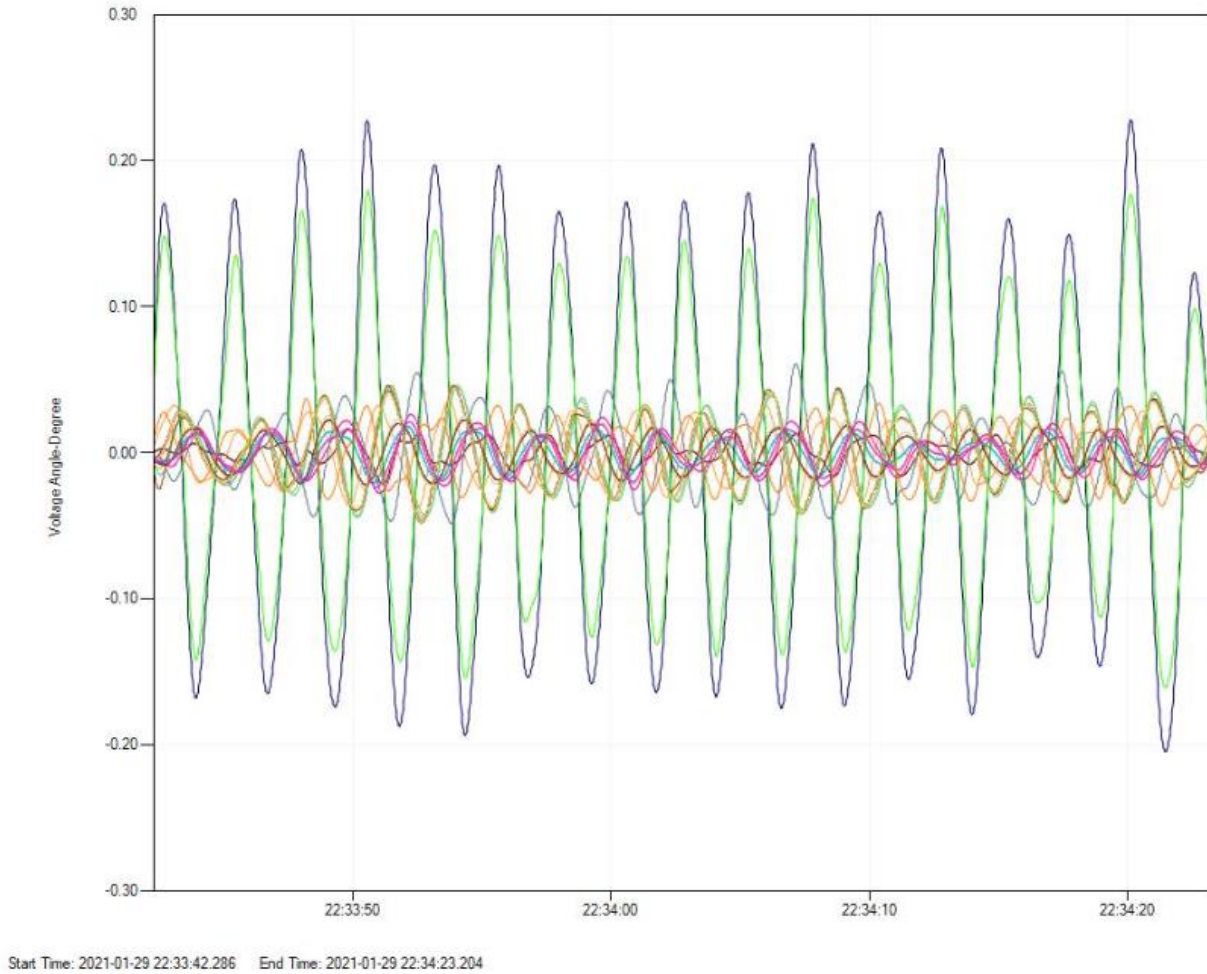


Figure 45: Frequency PMU data of the two individual bursts at Mead (purple) and Ault (blue).

In Figure 46, voltage angle derivative signals during the second burst from PMUs across the Western Interconnection with a 0.15 Hz to 1.5 Hz bandpass filter show that the oscillation was felt across the interconnection at varying degrees, indicating the resonance condition.

## Modes of Inter-Area Power Oscillations in the Western Interconnection



**Figure 46: Voltage Angle Derivative PMU data across the Western Interconnection during the second burst event—CST time.**

The estimated frequency of the resonance was 0.404 Hz and the oscillation shape of the second burst using Ault as the shape reference, shown in Figure 47 matches well with other estimations of the EWA mode presented in this document.

## Modes of Inter-Area Power Oscillations in the Western Interconnection

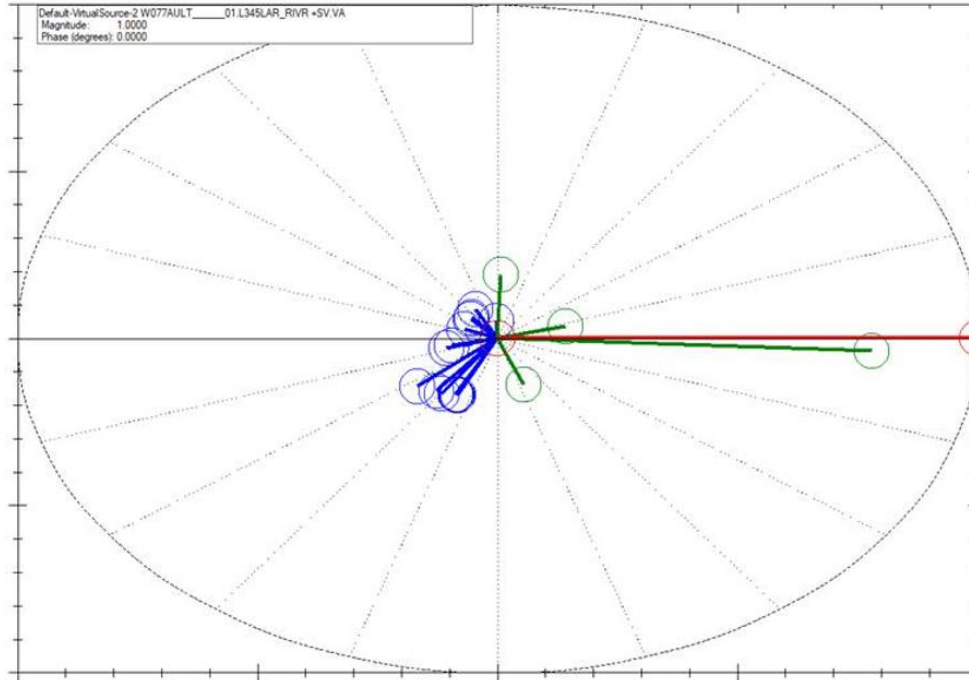


Figure 47: Oscillation Shape of Voltage Angle Derivative PMU data during the second burst event.

During this event, the mode meter configured for the EWA mode at Southwest Power Pool (SPP) reported unusually low damping, as depicted in Figure 48. A follow-up investigation revealed that the onset of the two periods of low damping estimates coincided with the oscillations depicted in Figure 49, which show the inputs to the mode meter. Note that Figure 45 and Figure 49 show the same events; one uses Central Standard Time (CST), the other uses Coordinated Universal Time (UTC). Though both oscillations lasted for less than one minute, they continued to cause low damping estimates while in the mode meter's 10-minute analysis window. This is why each period of low damping estimates lasts for about 10 minutes.

It is unclear at this time what led to the oscillations, but initial results indicate that they were not due to poor damping of the EWA mode. Further investigation is necessary to determine whether the oscillations were caused by a malfunctioning piece of equipment, a local mode of oscillation, or something else. Initial results also suggest that the oscillations may be prominent examples of a regularly occurring behavior. The mode meter's input signal was derived from the voltage angle difference between the Ault substation in northeastern Colorado and the Mead substation in southern Nevada. The oscillations were much larger in the Ault signal. As depicted in Figure 50, which is based on data collected on a different day, the Ault signal regularly exhibits intermittent increases in signal energy. A similarly preprocessed voltage angle signal from the Custer substation in Washington is included in the figure for comparison. It is unknown whether the oscillations in Figure 49 are dramatic examples of these intermittent increases in energy or the result of a different process.

## Modes of Inter-Area Power Oscillations in the Western Interconnection

Recently, modifications were developed for mode estimation algorithms to prevent sudden shifts in their damping ratio estimates following transients. Figure 51 shows that the modified Yule-Walker algorithm can provide more consistent mode estimates by ignoring the oscillations in Figure 49. The modified algorithm is currently in the research stage. Used alongside tools to detect the sudden onset of oscillations like those in Figure 49, these modified algorithms could provide system operators with more reliable estimates of the system's small-signal stability margin.

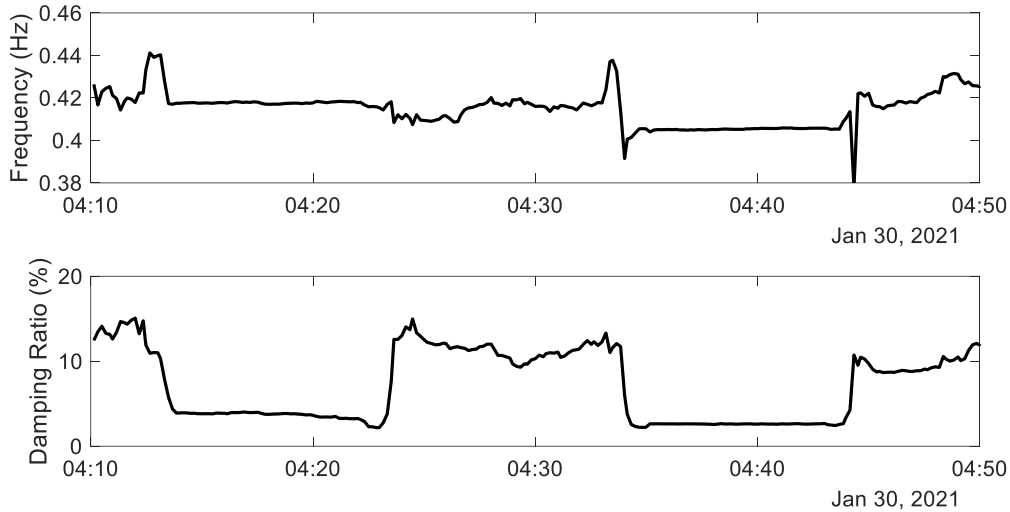


**Figure 48: Estimates of the EWA mode showing two periods of low damping later found to be erroneous (UTC time).**

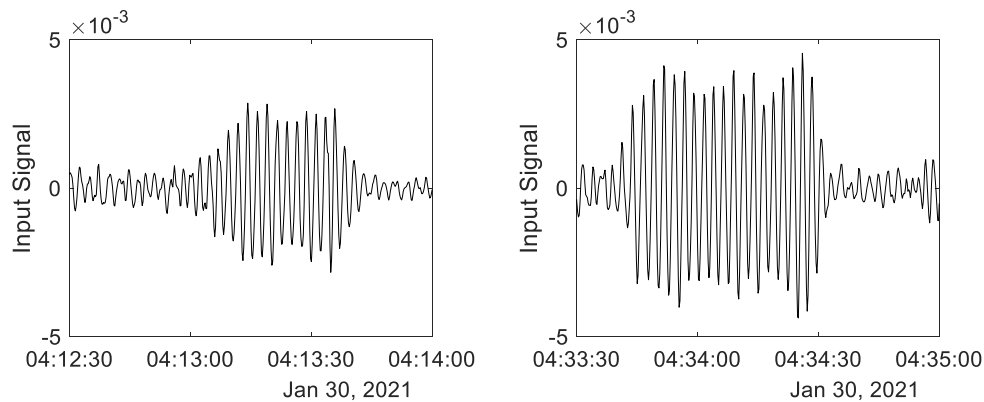


**Figure 49: Oscillations in the input signal to the EWA mode meter that resulted in two periods of low damping estimates (UTC time).**

## Modes of Inter-Area Power Oscillations in the Western Interconnection

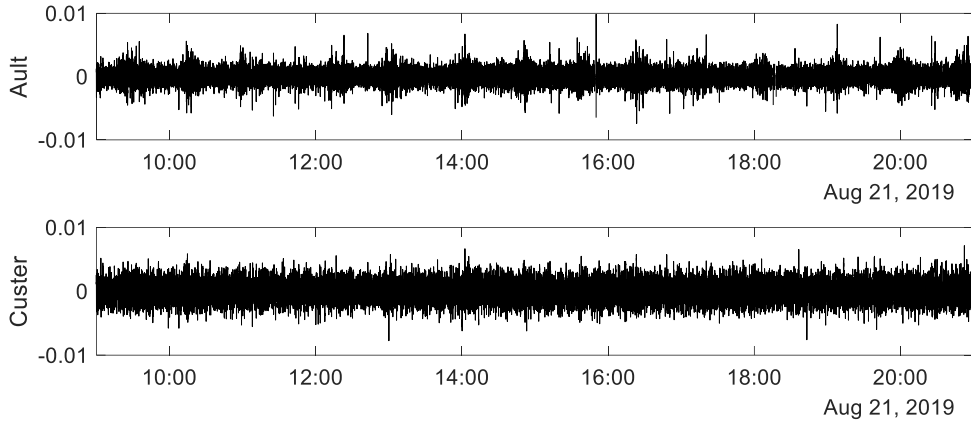


**Figure 50: Preprocessed voltage angle signals. The Ault signal (top) can be used to estimate the EWA mode and exhibits intermittent increases in signal energy. The Custer signal (bottom), which can be used to estimate the North-South B mode, does not exhibit this characteristic (UTC time).**

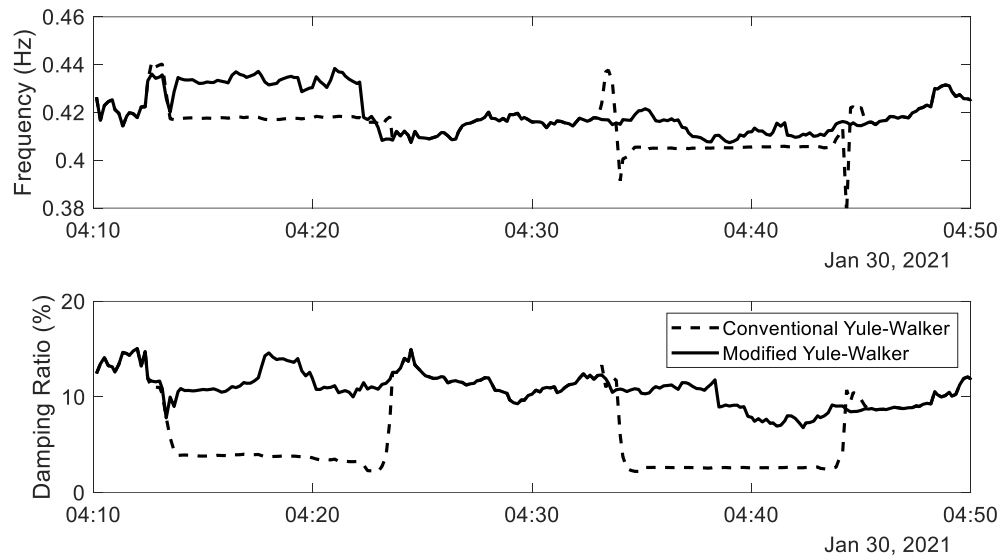


**Figure 51: Estimates of the EWA mode the from conventional and modified versions of the Yule-Walker algorithm (UTC time).**

## Future Work

The results in this report are the first detailed investigation of the EWA mode. Future recommendations include:

- Continued monitoring of the EWA mode from PMU measurements and field tests.
- Investigating the excitability, controllability, and interaction paths of the EWA mode with more detail using simulation studies. Initial work has been presented in this report.
- Development and testing of production-grade mode meter settings for the EWA mode.

### BC Mode(s)

---

#### Mode Description

The analysis performed during the preparation of this report revealed that the British Columbia (BC) mode may be less well understood than previously thought. Analysis of simulation models revealed the existence of at least two modes with high observability in BC and similar frequencies, nominally in the range of 0.50 Hz to 0.72 Hz. Here, we posit the existence of two distinct mode shapes, the British Columbia A (BCA) mode and the British Columbia B (BCB) mode. This creates a situation like the one that exists with the NSB and EWA modes where multiple oscillatory modes exist at almost the same frequency but with distinct shapes. In cases like these, care must be taken to differentiate between the modes because the appropriate mitigation and control strategies may be different.

It should be noted that at present, the existence of multiple BC modes is a hypothesis supported primarily by analysis of simulation models. Important research questions remain, such as how best to excite the BC modes for estimation both in simulation and field tests. Also, extensions of existing signal processing approaches may be required to fully characterize these modes. As acknowledged in the 2014 WECC modes report [2], PMU data from the Kemano/Minette area is crucial to characterizing oscillatory behavior in BC. For example, one of the key differentiating factors between the posited BCA and BCB mode shapes is the phase of Kemano relative to generation units in the rest of British Columbia. Unfortunately, datasets containing measurements from Kemano/Minette have been limited, placing a constraint on the certainty of the conclusions presented here. In future work, acquiring datasets with high quality PMU measurements recorded in this area will be a top priority.

#### BC Mode A Description

This section discusses the properties of the BCA mode observed in simulation. Two simulation models were studied, the WECC 2020 Light Spring base case (20LSP1sa1) and the WECC 2021 Heavy Summer base case (21HS3a1). Basic facts about these cases, including system loading and approximate renewable penetration, are presented in the “Simulation Models” section of the Introduction. For each base case, ten simulations were performed with each run corresponding to a 1,200 MW dynamic brake insertion (0.5 s duration) initiated at a different point in the system. Figure 2 shows the insertion locations used to perturb the system. Brake insertions at a subset of these locations excited the BCA mode. The mode properties were estimated by identifying a reduced-order state-space model from the free response portion of the ringdown. Details of the multi-channel curve fitting technique used to identify the system matrix are provided in the “Regularized Dynamic Mode Decomposition” section of Appendix B: Analysis Methods.

### Observability

The shape of the BCA mode is characterized by generation units in BC oscillating against the northwestern U.S., with the dividing node near the Washington–BC border. This mode appears to be only moderately observable in Alberta, and generation units located there may oscillate either in or out of phase with BC depending on the operating condition. Generation units in the southwestern U.S. also oscillate in phase with British Columbia, with the southern dividing node near the Utah–Arizona border. It is hypothesized that this is the shape historically associated with the BC mode of oscillation. For example, in the 2014 report, the shape of this mode was summarized as, “the BC area swinging against the Pacific NW U.S. [2]. It also ripples into the south with a lower magnitude.” This is precisely what we observe in Figure 52 and Figure 53, which show the mode shapes estimated from the 2020 Light Spring and 2021 Heavy Summer base cases, respectively.

In simulation, the mode shape remains fairly constant across different operating points; however, the mode frequency changes by about 0.2 Hz between the heavy and light loading conditions. As described above, analysis of the simulations indicates that this mode is close in frequency to the BCB mode, so care must be taken to differentiate between the two. Table 21 presents a condensed list of locations at which the BCA mode is readily observable. This table is not exhaustive and includes only entries from the list of monitored buses and generators presented in Table 5. The entries listed in Group 1 are shown in red in Figure 52 and Figure 53, and those in Group 2 in Blue.

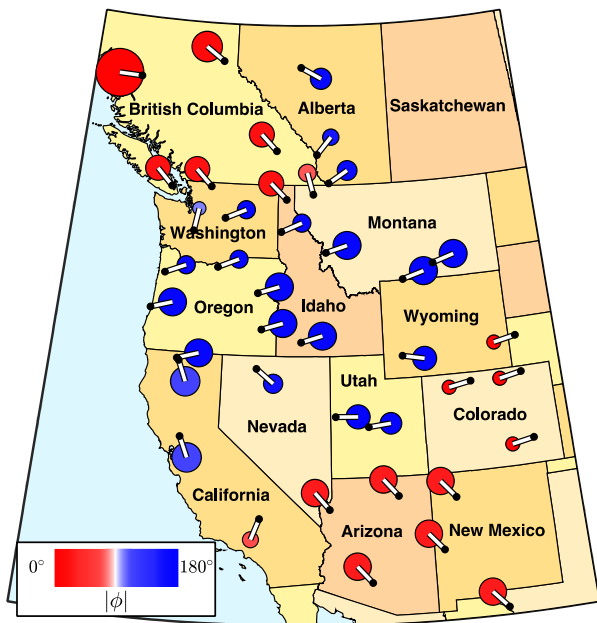


Figure 52: BCA mode shape, 0.71 Hz, 10.0%, 2020 Light Spring.

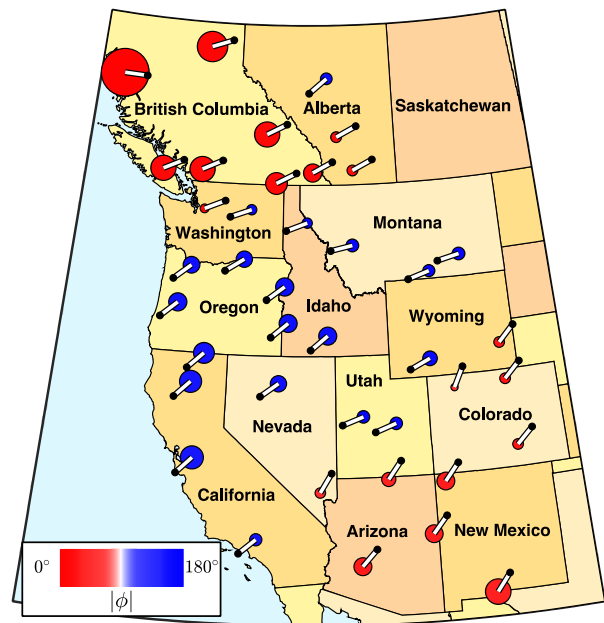


Figure 53: BCA mode shape, 0.53 Hz, 11.5%, 2021 Heavy Summer.

## Modes of Inter-Area Power Oscillations in the Western Interconnection

**Table 21: BCA mode observability short list.**

	Bus frequency	Generator speed
Group 1 ●	Kemano, Shrum, Revelstoke, Newman	Kemano, GM Shrum, Revelstoke
Group 2 ●	Tesla, Round Mt., Malin, Alvey	Walnut, Klamath Falls, James B. Black

### **Excitability**

Mode excitability provides information about which disturbances excite a particular mode. This is a complex subject and characterizing it fully for the Western Interconnection will require significant future work. Two key aspects that affect excitability are the nature of the disturbance (e.g., type, magnitude, duration) and the location where it occurs. In the simulations performed here, the nature of the disturbance was intentionally kept consistent to gain insight into locational sensitivity. Table 22 provides a list of the brake insertion locations that made it possible to get a clear estimate of the BCA mode for both analyzed base cases. This suggests that a disturbance near one of these points that causes a mismatch in the generation-demand balance, such as a generator trip, would likely excite the BCA mode. Analysis of simulation indicates that the BCA mode is most excitable from BC, and moderately excitable from the southwestern U.S. Further analysis of simulation and field test data is required to build confidence in conclusions surrounding the excitability of this mode.

**Table 22: BCA mode excitability short list.**

Brake insertion location
Kemano, Diablo, Palo Verde

### **Controllability**

Here, controllability was assessed by estimating the participation factors associated with the BCA mode. For background about participation factors, see Appendix A: Electromechanical Dynamic Theory. Table 23 presents a condensed list of system states with consistently high participation factor magnitudes across both the 2020 Light Spring and 2021 Heavy Summer base cases. This analysis suggests that substation-based controls using bus frequency feedback located at Selkirk or Cranbrook would be effective in damping the BCA mode. Moreover, it indicates that similar controls located at Round Mt. or Malin would also be beneficial. Likewise, PSSs at Walnut, Klamath Falls, and Revelstoke influence the damping of this mode. This table is not exhaustive and includes only entries from the list of monitored buses and generators presented in Table 5. For engineering purposes, the information listed in Table 23 should be regarded as a starting point for further time- and frequency-domain analysis to evaluate effective means of control.

## Modes of Inter-Area Power Oscillations in the Western Interconnection

Table 23: BCA mode controllability short list.

Bus frequency	Generator speed
Selkirk, Cranbrook, Round Mt., Malin	Walnut, Klamath Falls, Revelstoke

### Interaction Paths

An interaction path is a transmission line or corridor over which significant energy corresponding to a particular oscillatory mode is exchanged. We can gain insight into the interaction paths by analyzing the modal content of the real power transferred from one point in the system to another (over ac lines). Here, the modal content was decomposed using Prony’s method. Figure 54 and Figure 55 show that, for a brake insertion near Malin, the modal content of the real power transfer on Path 15, Midway–Los Banos, is dominated by the BCA and EWA modes. So, Path 15 appears to be a key interaction path for the BCA mode. Table 24 provides a summary of the top interaction paths for the BCA mode identified using the interconnection-wide base cases. In addition to Midway–Los Banos, key interaction paths include Path 3, Path 46, and Path 78. The transfers on other paths may also exhibit significant modal content at the BCA mode frequency.

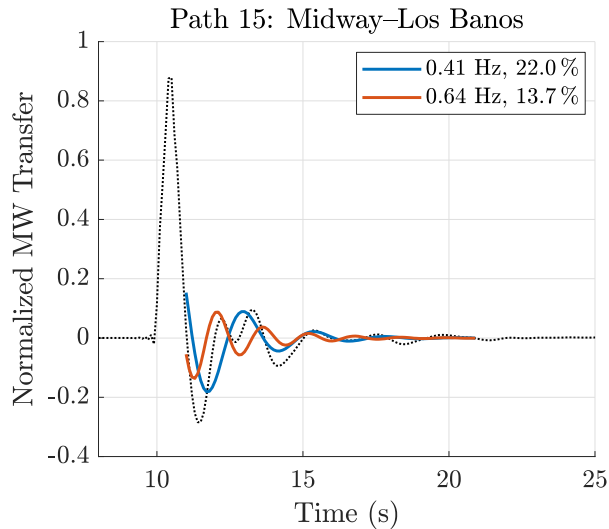


Figure 54: Path 15, 2020 Light Spring.

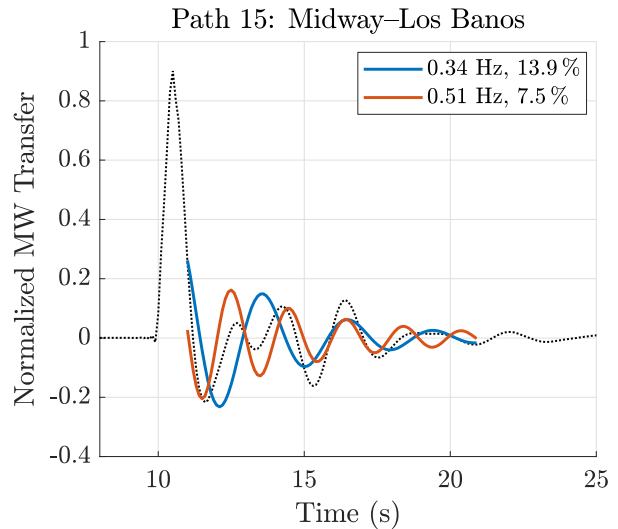


Figure 55: Path 15, 2021 Heavy Summer.

Table 24: BCA mode interaction path short list.

No.	Path Name
Path 3	Northwest–Canada
Path 15	Midway–Los Banos (California)
Path 46	West of Colorado River (WOR)
Path 78	TOT 2B1 (Utah South)



### BC Mode B Description

This section discusses the properties of the BCB mode observed in simulation. The findings presented here were determined using the same method described above for the BCA mode. This analysis should be considered provisional until it can be further supported by field measurements.

#### Observability

The shape of the BCB mode is complex, with Kemano oscillating out of phase with the other generators in British Columbia. Throughout the rest of the system, a central corridor spanning from the Pacific Northwest into New Mexico (through Utah) oscillates against units along the eastern and western boundaries of the interconnection. In the 2020 Light Spring case, this mode was observed at 0.72 Hz, almost the same frequency as the BCA mode (0.71 Hz). This close relationship in frequency means that signal processing techniques that do not account for the existence of both modes may mistake one for the other. In practice, this could result in unforeseen discrete changes in online estimates of mode frequency and damping generated for monitoring purposes. Figure 56 shows the shape of the BCB mode estimated from the 2020 Light Spring base case. Figure 57 shows the shape from the 2021 Heavy Summer case. Table 25 presents a condensed list of locations at which the BCB mode is readily observable. This table is not exhaustive and includes only entries from the list of monitored buses and generators presented in Table 5. The entries listed in Group 1 are shown in red in Figure 56 and Figure 57, and those in Group 2 in Blue.

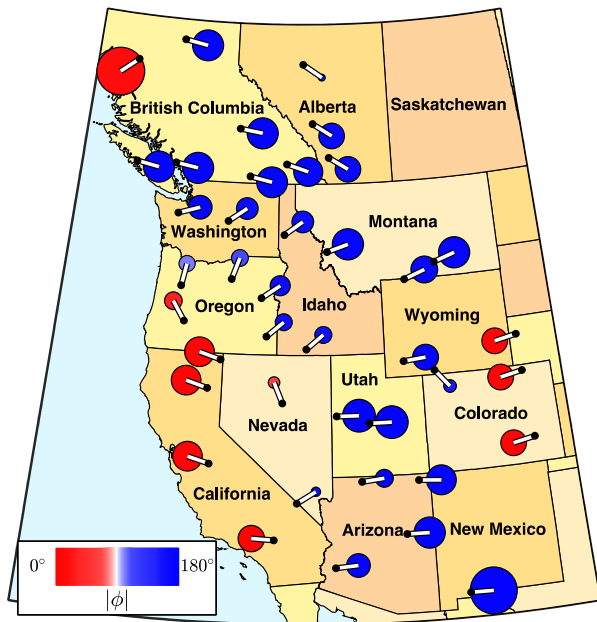


Figure 56: BCB mode shape, 0.72 Hz 12.5%, 2020 Light Spring.

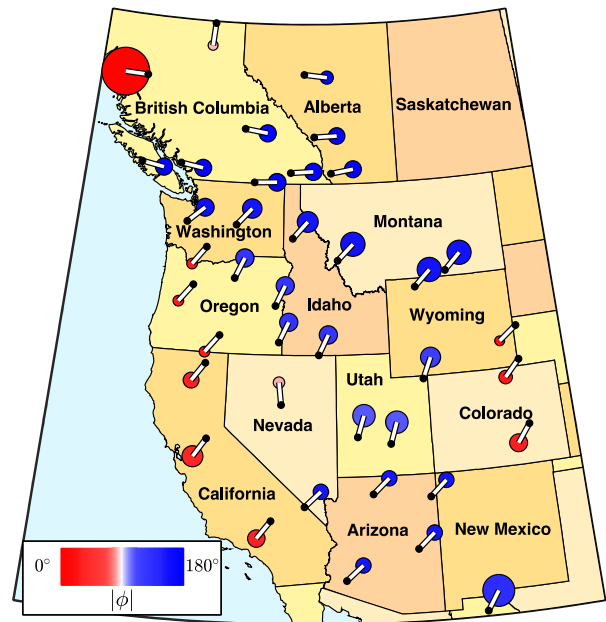


Figure 57: BCB mode shape, 0.62 Hz 12.5%, 2021 Heavy Summer.

## Modes of Inter-Area Power Oscillations in the Western Interconnection

**Table 25: BCB mode observability short list.**

	Bus frequency	Generator speed
Group 1 ●	Kemano, Tesla, Comanche	Kemano, Walnut, Comanche
Group 2 ●	Newman, Intermountain, Colstrip	Rio Grande, Intermountain, Colstrip

### **Excitability**

Table 26 provides a list of the brake insertion locations that made it possible to get a clear estimate of the BCB mode for both analyzed base cases. This suggests that a disturbance near one of these points that causes a mismatch in the generation-demand balance, such as a generator trip, would likely excite the BCB mode. Analysis of simulation indicates that the BCB mode is most excitable from California or Colorado, and moderately excitable from Utah. The points of excitability highlighted in Table 26 are the same as those listed for the EWA mode. This highlights the fact that in addition to observability in BC, this mode also has an East–West component to its shape in the southern portion of the interconnection. Further analysis of simulation and field test data is required to build confidence in conclusions surrounding the excitability of this mode.

**Table 26: BCB mode excitability short list.**

Brake insertion location
Comanche, Diablo, Intermountain

### **Controllability**

As described above, controllability was assessed by estimating the participation factors associated with the BCB mode. Table 27 presents a condensed list of system states with consistently high participation factor magnitudes across both the 2020 Light Spring and 2021 Heavy Summer base cases. This analysis suggests that substation-based controls using bus frequency feedback located at Selkirk or Cranbrook would be effective in damping the BCB mode. Moreover, it indicates that similar controls located at Round Mt. or Malin would also be beneficial. The identified locations at which substation-based controls using bus frequency feedback would be effective in damping the BCB mode is the same as for the BCA mode. Participation factor analysis indicated that PSSs at Colstrip, Grand Coulee, Intermountain, and Walnut influence the damping of this mode. This table is not exhaustive and includes only entries from the list of monitored buses and generators presented in Table 5. These are preliminary findings, and further analysis is required to confirm the efficacy of controls placed at these locations.

**Table 27: BCB mode controllability short list.**

Bus frequency	Generator speed
Selkirk, Cranbrook, Round Mt., Malin	Colstrip, Grand Coulee, Intermountain, Walnut



**Interaction Paths**

Figure 58 and Figure 59 show that for a brake insertion near Diablo Canyon, the modal content of the real power transfer on Path 46, West of the Colorado River (WOR), is strongly influenced by the BCB mode. So, Path 46 appears to be a key interaction path for the BCB mode. Table 28 provides a summary of the top interaction paths for the BCB mode identified using the interconnection-wide base cases. In addition to WOR, key interaction paths include Path 24, Path 66, and Path 76. The transfers on other paths may also exhibit significant modal content at the BCB mode frequency.

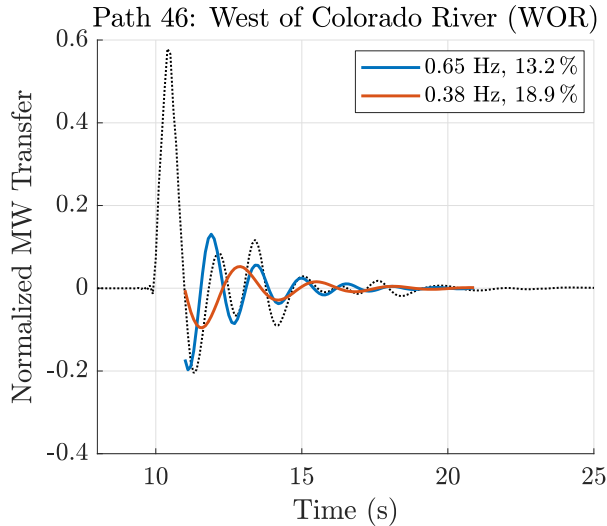


Figure 58: Path 46, 2020 Light Spring.

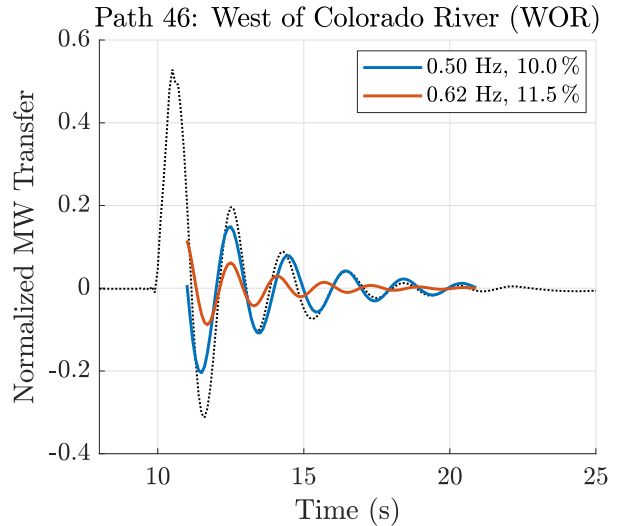


Figure 59: Path 46, 2021 Heavy Summer.

Table 28: BCB mode interaction path short list.

No.	Path Name
Path 24	PG&E–Sierra (California–Nevada)
Path 46	West of Colorado River (WOR)
Path 66	California–Oregon Intertie (COI)
Path 76	Alturas Project (California–Nevada)

## Mode Properties Measured from PMU Data

As reflected above, the simulation results indicate two BC modes. For both modes, the Kemano power plant in BC Canada is the largest participant. To date, no Kemano PMU measurements are available. But, the May 7, 2019, dataset (per Table 1) does contain valid PMU measurements from the Minette bus, which is electrically close to Kemano.

Figure 60 shows the PSD of ambient data collected at Minette on May 7, 2019. There is a clear modal peak at 0.6 Hz; but no second peak is detected. Using Minette as the reference signal, the mode shape in Figure 60 results via correlation analysis. The pattern matches the BCA mode shape hypothesis from the simulation results in the prior section.

Certainly, more datasets are needed to fully comprehend the BC modes.

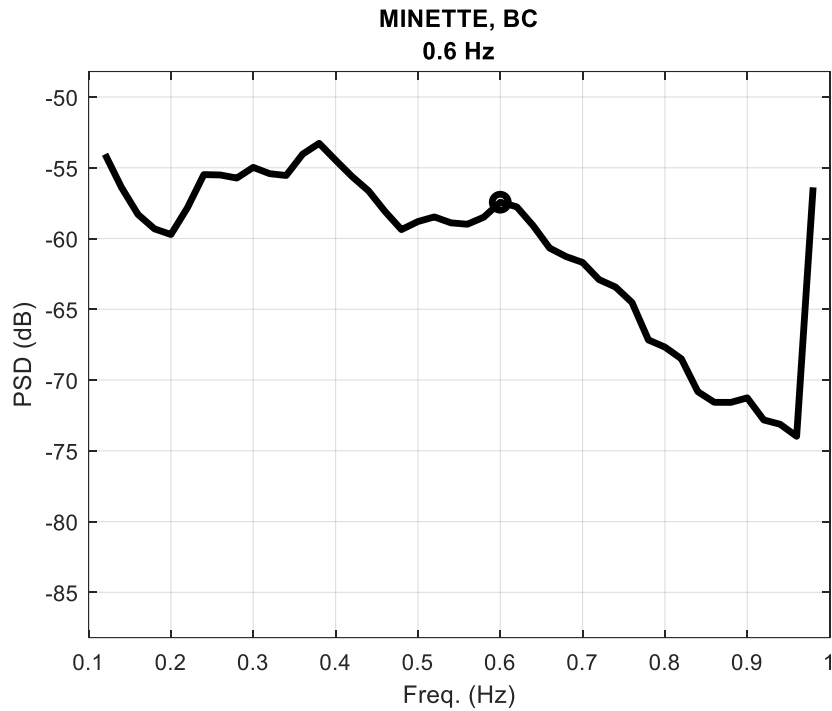


**Figure 60: PSD of Minette frequency measured from the ambient data on 2019/05/07 from 14:10:00 to 14:30:00 UTC.**

## Modes of Inter-Area Power Oscillations in the Western Interconnection



Figure 61: BCA mode shape and observability measured from PMU ambient data corresponding to Figure 60.

### Future Work

While we have hypothesized the existence of two BC modes, considerably more work is required to fully comprehend the properties of these modes. This includes:

- Collection of high-quality data at Kemano/Minette for field tests designed to better excite the BC modes. Compare with data recorded at Shrum, Revelstoke, Cranbrook, and the surrounding Pacific Northwest. Both large ambient datasets and event datasets are desired.
- Development and analysis of several simulation datasets designed to excite and investigate the BC area modes.
- Research and development on signal processing techniques for differentiating between modes with similar frequencies but distinct shapes (such as the BCA and BCB modes) in ambient data, e.g., using multi-channel processing.
- Identifying reference signals for BC mode meter(s). Development and testing of appropriate accompanying settings.

### Montana Mode

---

#### Mode Description

The MT mode has Montana oscillating against the Pacific Northwest. It is dominated by the Colstrip and Yellowtail power plants in southeast Montana. It is basically a localized mode for eastern Montana

with most of the other generators in the state swinging in phase with Colstrip and Yellowtail. Because Colstrip is a large radial plant, the mode is low in frequency (relative to other local modes) and ripples throughout the system. The MT mode is normally well-damped; however, outages of 500 kV lines, which often require bypass of series capacitors to mitigate subsynchronous resonance, can result in a weak condition when the mode can become marginally damped.

While the 2014 WECC modes report contains no analysis of the MT mode, this report presents many PMU and simulation cases [2]. For all the cases presented, the MT mode is in the 0.70 Hz to 0.90 Hz range. Its shape is consistently the eastern Montana generators, led by Colstrip, swinging against the rest of the system.

### Mode Properties Measured from Simulation Models

This section discusses the properties of the MT mode observed in simulation. Two simulation models were studied, the WECC 2020 Light Spring base case (20LSP1sa1) and the WECC 2021 Heavy Summer base case (21HS3a1). Basic facts about these cases, including system loading and approximate renewable penetration, are presented in the “Simulation Models” section of the Introduction. For each base case, ten simulations were performed with each run corresponding to a 1,200 MW dynamic brake insertion (0.5 s duration) initiated at a different point in the system. Figure 2 shows the insertion locations used to perturb the system. Brake insertions at a subset of these locations excited the MT mode. The mode properties were estimated by identifying a reduced-order state-space model from the free response portion of the ringdown. Details of the multi-channel curve fitting technique used to identify the system matrix are provided in the “Regularized Dynamic Mode Decomposition” section of Appendix B: Analysis Methods.

### *Observability*

The shape of the MT mode is characterized by generation units in Montana oscillating against the rest of the system. It tends to be most observable near Colstrip and Yellowtail. Machines in Washington and Oregon may oscillate either in or out of phase with Montana depending on the operating condition. Figure 62 shows the shape of the MT mode estimated from the 2020 Light Spring base case, and Figure 63 shows the shape from the 2021 Heavy Summer case. Table 29 presents a condensed list of locations at which the MT mode is readily observable. This table is not exhaustive and includes only entries from the list of monitored buses and generators presented in Table 5. The entries listed in Group 1 are shown in red in Figure 62 and Figure 63, and those in Group 2 in blue. In some cases, the generation units in Montana may oscillate more against BC, and in others against units in Colorado and eastern Wyoming. So, the observability at the points listed in Group 2 may vary.

## Modes of Inter-Area Power Oscillations in the Western Interconnection

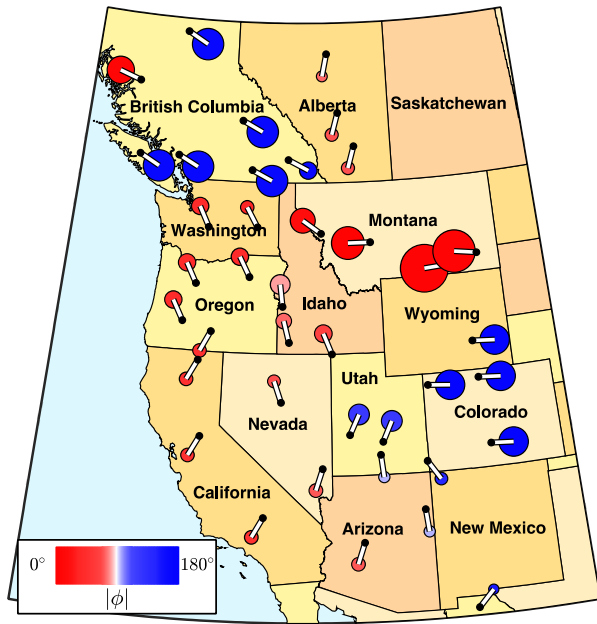


Figure 62: MT mode shape, 0.83 Hz, 10.5%, 2020 Light Spring.

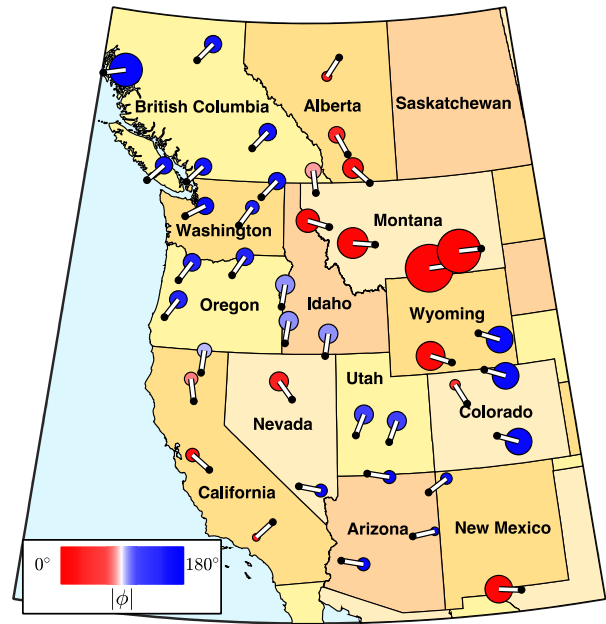


Figure 63: MT mode shape, 0.89 Hz, 11.5%, 2021 Heavy Summer.

Table 29: MT mode observability short list.

	Bus frequency	Generator speed
Group 1 ●	Colstrip, Yellowtail, Garrison	Colstrip, Yellowtail, Dave Gates
Group 2 ●	Kemano, Shrum, Comanche, Ault	Kemano, GM Shrum, Comanche

### Excitability

Mode excitability provides information about which disturbances excite a particular mode. This is a complex subject and characterizing it fully for the Western Interconnection will require significant future work. Two key aspects that affect excitability are the nature of the disturbance (e.g., type, magnitude, duration) and the location where it occurs. In the simulations performed here, the nature of the disturbance was intentionally kept consistent to gain insight into locational sensitivity. Table 30 provides a list of the brake insertion locations that made it possible to get a clear estimate of the MT mode for both analyzed base cases. This suggests that a disturbance near one of these points that causes a mismatch in the generation-demand balance, such as a generator trip, would likely excite the MT mode. Analysis of simulation indicates that the MT mode is highly excitable from Montana, and moderately excitable from Colorado. In some operating conditions, this mode may also be excited by disturbances originating in the Pacific Northwest or BC.

**Table 30: MT mode excitability short list.**

Brake insertion location
Colstrip, Comanche

### ***Controllability***

Here, controllability was assessed by estimating the participation factors associated with the MT mode. For background about participation factors, see Appendix A: Electromechanical Dynamic Theory. Table 31 presents a condensed list of system states with consistently high participation factor magnitudes across both the 2020 Light Spring and 2021 Heavy Summer base cases. This analysis suggests that substation-based controls using bus frequency feedback located at Garrison or Taft would be effective in damping the MT mode. Moreover, it indicates that similar controls located at Cranbrook or Selkirk would also be beneficial. Likewise, PSSs at Colstrip, Yellowtail, Brownlee, and Revelstoke influence the damping of this mode. This table is not exhaustive and includes only entries from the list of monitored buses and generators presented in Table 5. For engineering purposes, the information listed in Table 31 should be regarded as a starting point for further time- and frequency-domain analysis to evaluate effective means of control.

**Table 31: MT mode controllability short list.**

Bus frequency	Generator speed
Garrison, Taft, Cranbrook, Selkirk	Colstrip, Yellowtail, Brownlee, Revelstoke

### ***Interaction Paths***

An interaction path is a transmission line or corridor over which significant energy corresponding to a particular oscillatory mode is exchanged. We can gain insight into the interaction paths by analyzing the modal content of the real power transferred from one point in the system to another (over ac lines). Here, the modal content was decomposed using Prony’s method. Figure 64 and Figure 65 show that for a brake insertion near Colstrip, the modal content of the real power transfer on Path 8, Montana–Northwest, is dominated by the MT mode. So, Path 8 is a key interaction path for the MT mode. Table 32 provides a summary of the top interaction paths for the MT mode identified using the interconnection-wide base cases. In addition to Montana–Northwest, key interaction paths include Path 18 and Path 80. The transfers on other paths may also exhibit significant modal content at the MT mode frequency.

## Modes of Inter-Area Power Oscillations in the Western Interconnection

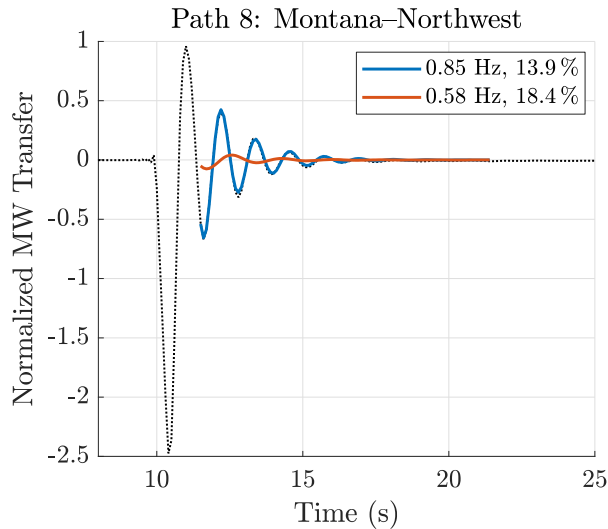


Figure 64: Path 8, 2020 Light Spring.

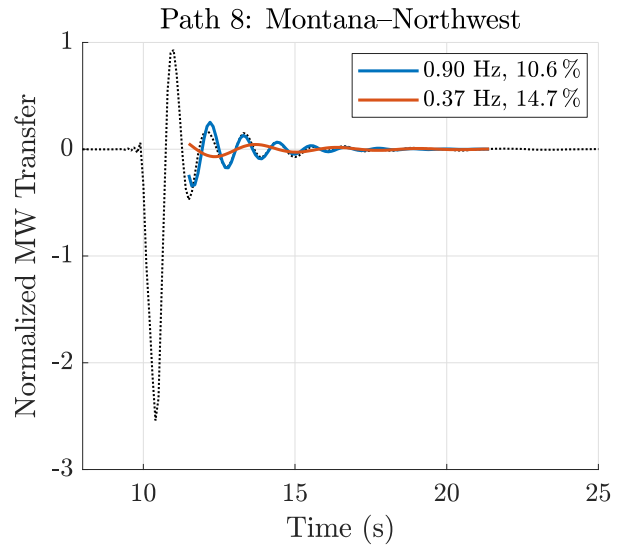


Figure 65: Path 8, 2021 Heavy Summer.

Table 32: MT mode interaction path short list.

No.	Path Name
Path 8	Montana-Northwest
Path 18	Montana-Idaho
Path 80	Montana Southeast

### Mode Properties Measured from PMU Data

Figure 66 shows the PSD of the frequency from five PMUs scattered across areas connected to the Montana region of the WI. The peak near 0.8 Hz (circled) is the MT mode. Note the large peak at Colstrip and Yellowtail indicating high modal participation. As one moves away from Montana, the spectral peak (and modal observability) falls off considerably. This indicates that the mode is localized primarily in Montana.

## Modes of Inter-Area Power Oscillations in the Western Interconnection

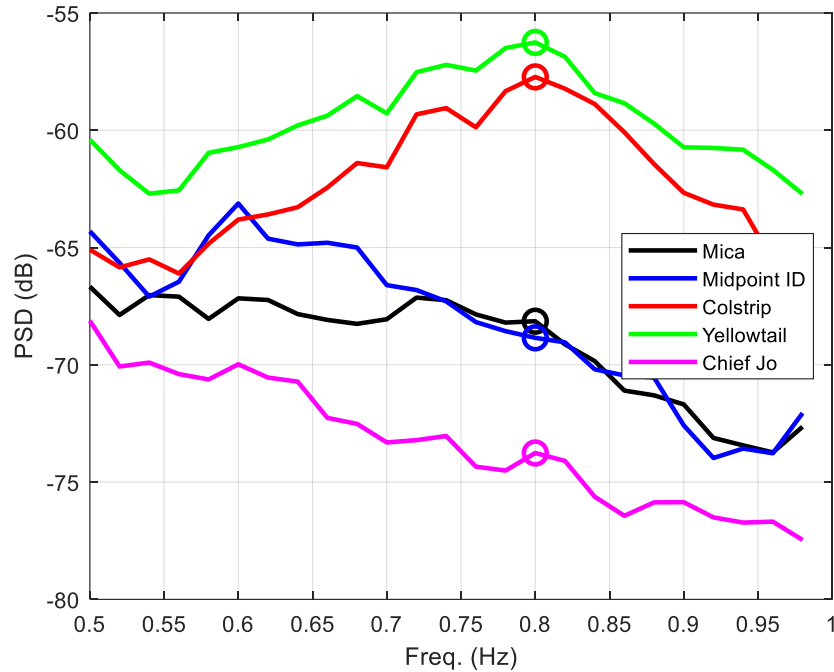


**Figure 66:** PSD of five PMU-measured frequencies of ambient data on 2016/09/28 from 15:10:00 to 15:30:00 UTC. The MT mode is at 0.8 Hz (indicated with circles).

### ***Mode Shape Calculated via Correlation Analysis***

Figure 67 shows the MT mode shape and observability as measured from a September 28, 2016, dataset during an ambient condition—the same one used in Figure 66. The mode frequency during this time was measured as 0.8 Hz via the peak in the mode reference signal in (Colstrip). Figure 67 shows that the MT mode is basically Montana swinging against the rest of the system. The coherency is large enough in surrounding areas to indicate modal observability in neighboring areas (e.g., the Pacific Northwest), but the amplitude of the mode shapes indicate that the participation is relatively small. The dividing node is typically near Grand Coulee in eastern Washington as indicated in Figure 67. In other cases, the participation outside of Montana is so small that the coherency indicates no participation. The mode basically behaves as a Montana area local mode against the system.

## Modes of Inter-Area Power Oscillations in the Western Interconnection

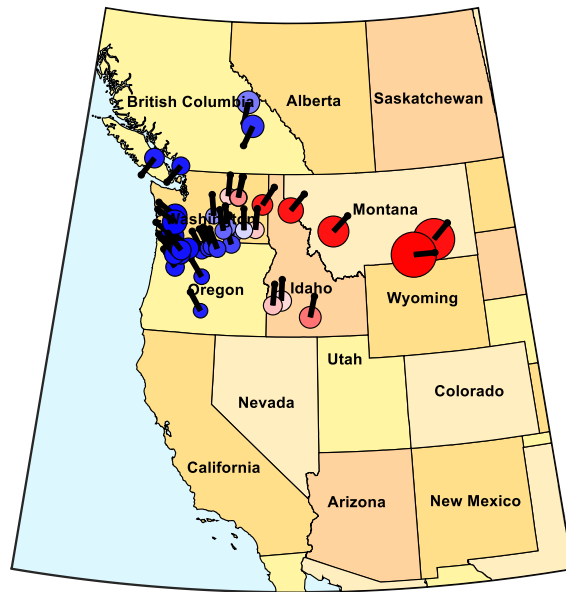


**Figure 67: MT mode shape and observability measured from PMU ambient data on 2016/09/28 from 15:10:00 to 15:30:00 UTC via correlation analysis.**

Table 33 summarizes the estimated MT mode frequencies and shapes from several tests spanning 2016 through 2019. The dataset from September 28, 2016, discussed above is termed the “baseline” set. All other estimated mode shapes are qualitatively compared to this baseline and judged to match it as indicated in the fourth column of the table. The mode shape maps for each of the rows of the table is contained in subsection “Correlation Analysis from 2016 through 2019 PMU Data” of Appendix G: MT Mode Analyses. In examining Table 33 and the many mode shape plots in the appendix, one sees that the MT mode frequency and shape are consistent. In some cases, the coherency outside of Montana is too small to merit inclusion in the shape. Also, in some cases, the mode frequency is as low as 0.72 Hz. In these cases, the identified mode may be the hypothesized BCB mode described in the previous section.

## Modes of Inter-Area Power Oscillations in the Western Interconnection

**Table 33: Summary of MT mode frequency and shape, 2016 through 2019.**

Date	Time (UTC)	Freq. (Hz)	Shape match baseline (Y = yes, P = Partial, N = no)	Notes
9/13/2016	17:10:02 to 17:30:00	0.70	Y	Ambient condition. Alberta disconnected.
9/13/2016	18:30:01 to 18:50:01	0.72	Y	PDCI Probing condition. Alberta disconnected.
9/13/2016	22:10:00 to 22:28:00	0.74	Y	Ambient condition. Alberta disconnected.
9/13/2016	22:28:10 to 22:48:10	0.74	P	PDCI Probing condition. Alberta disconnected. Mode shape amplitudes in WA relatively larger than baseline.
9/13/2016	23:10:00 to 23:30:00	0.78	Y	Ambient condition. Alberta disconnected.
9/28/2016	15:10:00 to 15:30:00	0.80	Baseline	Ambient condition.
9/28/2016	16:30:12 to 16:40:12	0.74	P	PDCI Probing condition. Some locations in south have coherency large enough to show up, but shape magnitudes are very small.
9/28/2016	17:10:00 to 17:10:00	0.78	Y	Ambient condition.
9/28/2016	18:20:02 to 18:40:02	0.76	Y	PDCI Probing condition.
9/28/2016	18:46:00 to 18:59:00	0.82	Y	Ambient condition.
9/28/2016	20:30:09 to 20:40:09	0.78	Y	PDCI Probing condition.
9/28/2016	21:10:00 to 21:30:00	0.74	Y	Ambient condition.
9/29/2016	15:10:00 to 15:30:00	0.74	Y	Ambient condition.
9/29/2016	16:10:34 to 16:20:34	NA	NA	PDCI Probing condition. Modal peak not distinguished enough.
9/29/2016	17:10:01 to 17:20:01	0.72	Y	PDCI Probing condition.
9/29/2016	18:10:31 to 18:20:31	0.72	Y	PDCI Probing condition.
9/29/2016	19:10:00 to 19:30:00	0.72	Y	Ambient condition.
9/29/2016	20:10:31 to 20:20:31	0.74	Y	PDCI Probing condition.
9/29/2016	21:10:00 to 21:30:00	0.76	Y	Ambient condition. Very strong modal peak.
5/16/2017	16:16:01 to 16:36:01	0.74	P	PDCI Probing condition. Northern BC strongly participating (Shrum?)
5/16/2017	16:36:05 to 16:50:00	0.78	Y	Ambient condition.
5/16/2017	20:15:01 to 20:35:01	0.82	Y	PDCI Probing condition. So Cal shape is larger than usual.
5/16/2017	20:35:05 to 20:50:00	0.78	Y	Ambient condition.
5/23/2018	16:05:00 to 16:24:30	0.80	P	Ambient condition. Part of BC participating.
5/23/2018	16:28:00 to 16:48:00	0.80	P	PDCI Probing condition. Some locations in south CA have coherency large enough to show up, but shape magnitudes are small.
5/23/2018	20:15:05 to 20:35:05	0.78	P	PDCI Probing condition. Some locations in south have coherency large enough to show up, but shape magnitudes are very small.
5/23/2018	20:36:00 to 20:55:00	0.80	Y	Ambient condition.
5/24/2018	00:10:00 to 00:30:00	0.82	Y	Ambient condition.
5/24/2018	17:14:05 to 17:34:05	0.80	P	PDCI Probing condition. Parts of BC participating.
5/24/2018	17:36:00 to 17:50:00	0.82	Y	Ambient condition.
5/7/2019	14:10:00 to 14:30:00	0.76	Y	Ambient condition.
5/7/2019	17:10:00 to 17:30:00	0.72	Y	Ambient condition.
5/7/2019	17:30:03 to 17:50:03	0.78	Y	PDCI Probing condition.
5/7/2019	21:20:03 to 21:40:03	0.72	Y	PDCI Probing condition.
5/7/2019	22:10:00 to 22:30:00	0.74	Y	Ambient condition.
5/8/2019	02:10:00 to 02:30:00	0.80	Y	Ambient condition.
5/8/2019	06:10:00 to 06:30:00	0.76	Y	Ambient condition.

### Mode Frequency and Damping

Research level mode meter tests have been conducted for the MT mode with some results presented in Appendix G: MT Mode Analyses. In these test cases, the mode's frequency tends to vary from 0.75 Hz to 0.85 Hz, and the damping ratio was most often in the range of 10 to 15%. A typical set of mode meter results for the Montana mode are presented in Figure 68. The estimates span 6.5 hours on September 29



## Modes of Inter-Area Power Oscillations in the Western Interconnection

during system tests. The mode meter results vary during the study period due to estimation errors and changes in the mode driven by changing operating conditions.

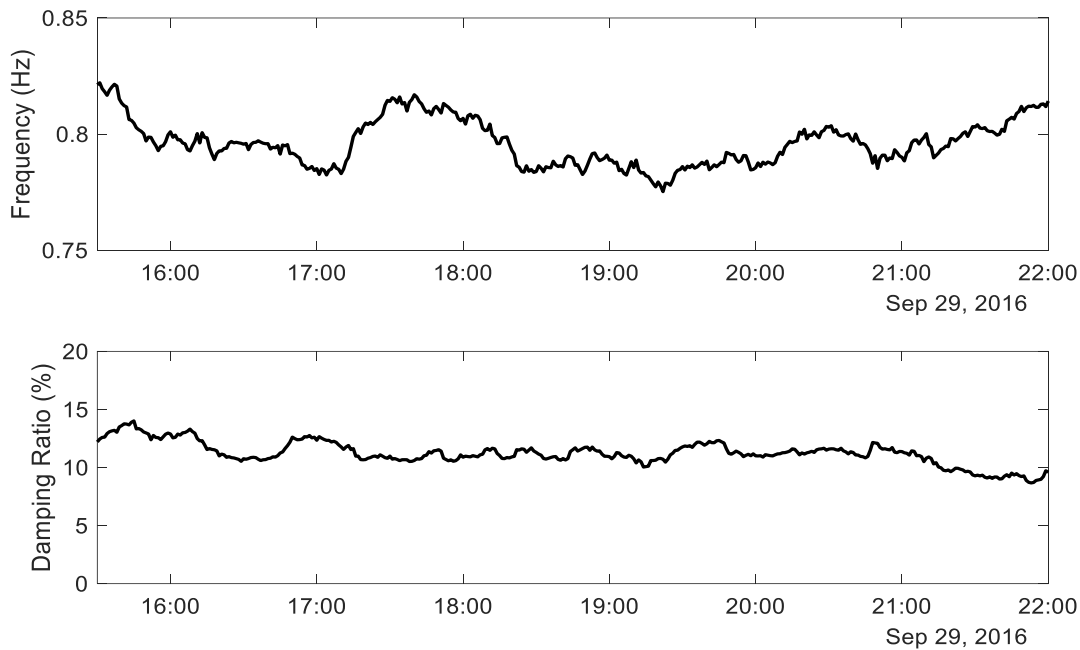


Figure 68: Estimates of the Montana mode from a mode meter analysis of the 2016/09/29 system tests.

### Future Work

The results in this report are the first detailed investigation of the MT mode. Future recommendations include:

- Continued monitoring of the MT mode from PMU measurements and field tests. Focus should be especially on the impact of pending changes at Colstrip power plant and the integration of more wind energy sources.
- Differentiating the MT mode from the BC mode(s). In some cases, it is difficult to distinguish between these.
- Investigating the excitability, controllability, and interaction paths of the mode with more detail using simulation studies. Initial work has been presented in this report.
- Development and testing of production-grade mode meter settings for the MT mode.
- Studying the impact of the potential retirement of Colstrip units on the characteristics of the MT mode.

## Conclusions and Future Work

The purpose of this document is to provide an up-to-date quantitative and qualitative description of the major modes of inter-area oscillation in the Western Interconnection and represents an update of the 2014 WECC modes report [2]. The analyses are based on two WECC transient stability base cases and many system-wide PMU datasets collected from 2016 through 2019. The results in this report are the most comprehensive and up-to-date assessment of the Western Interconnection’s electromechanical modes.

Table 34 summarizes the properties of the system-wide modes within the Western Interconnection. This report has especially added new understanding of the EWA and MT modes. The overall understanding of the NSA, NSB, EWA, and MT modes is now well established. Better comprehension of the excitability of the EWA mode is still needed.

To date, the understanding of the BC modes is relatively poor. Based on simulation studies, this report hypothesizes the existence of two BC modes. One PMU measurement dataset confirms the properties of one of these modes.

**Table 34: Summary of mode properties.**

Mode	Freq. (Hz)	Shape	Interaction Path(s)	Controllability	Grade	Comments
NSA	0.20–0.30	Alberta vs. System	Alberta–BC (Path 1) Northwest–CA (Path 3)	Alberta	Well understood	Well understood from 2014 report. Analysis for 2021 report confirms 2014 conclusions. An Alberta disconnect causes this mode to disappear.
NSB	0.35–0.45	Alberta vs. (BC + N. U.S.) vs. S. U.S.	COI (Path 66)	Widespread, incl. PDCI	Well understood	The most widespread mode in the system. An Alberta disconnect causes mode frequency and damping to decrease.
EWA	0.35–0.45	(Colorado + E. Wyo.) vs. System	Wyoming–ID (Path 19) Colorado–UT (Path 30) Colorado–NM (Path 31)	Colorado area	Marginally understood	Close in frequency to the NSB mode. Extensive new knowledge in 2021 report.
BCA	0.50–0.72	BC vs. N. U.S. vs. S. U.S.	Unknown	Unknown	Not understood	Model studies hypothesize two BC modes. Need improved PMU coverage in western BC (e.g., Kemano).
BCB	0.60–0.72	W. edge vs. System vs. E. edge	Unknown	Unknown	Not understood	(See above.)
MT	0.70–0.90	Montana vs. System	Montana–NW (Path 8)	Montana, incl. Colstrip	Well understood	Sometimes confused with one of the BC modes. Extensive new knowledge in 2021 report.

Future work recommendations include:

1. Continued monitoring of the all the modes from PMU measurements and field tests. This includes major switching events, system faults, major generation losses (with and without faults), and probing tests conducted using the PDCI and the Chief Joseph braking resistor.



## Modes of Inter-Area Power Oscillations in the Western Interconnection

2. Collection of high-quality synchrophasor data at Kemano/Minette for field tests designed to better excite the BC modes. Compare those measurements with data recorded at Shrum, Revelstoke, Cranbrook, and the surrounding Pacific Northwest. Both large ambient datasets and event datasets are desired.
3. Development and analysis of several simulation datasets designed to excite and investigate the BC area modes.
4. Assessment of cases in which Alberta is weakly connected to the rest of the system. Development of simulation base cases that reflect the operating conditions of interest. Collection and analysis of actual system data in which those conditions were observed.
5. Development of transient simulation base cases with initial power flow conditions coincident with system conditions in PMU-based datasets.
6. Include EHV fault analysis conducted via simulation. Sensitivity analysis is needed for single-line-to-ground, line-to-line, and 3 phase faults. Sensitivity is also desired for normal clearing times and backup clearing times. This is expected to become more important with higher penetrations of inverter-based resources.
7. Investigating the excitability, controllability, and interaction paths of the modes with more detail using simulation studies. Initial analysis has been presented in this report, but more work is needed to better refine the conclusions.
8. Development and testing of production-grade mode meter settings for the EWA and MT modes.
9. Studying the impact of the potential retirement of Colstrip units on the characteristics of the MT mode.
10. Conducting a study to investigate the impact of future grid configurations and resource dispatch patterns on the system modes. This study should consider the addition of new inverter-based resources (IBRs) and the retirement of existing generation. As accepted standards for IBR modeling are established, this study should be initiated. An initial study conducted by PNNL is summarized in Appendix C: The Impact of Future Grid Configurations.
11. Continue efforts to share real-time inter-area oscillation detection data amongst utilities and Reliability Coordinators to validate the analysis tools.
12. Collaborate on data integrity issues related to the transmission of timing signals from the Global Positioning System (GPS) to satellite-synchronized clocks used by PMUs. Clock errors, GPS spoofing, and military activities can affect timing and are a concern. Some utilities are considering transitioning to centralized clocks with propagating signals to mitigate these risks.

### Participants

---

This document was produced by the Western Interconnection Modes Review Group (WIMRG), an advisory group within WECC. When the WIMRG was formed, it attracted members from related WECC groups, including the Joint Synchronized Information Subcommittee (JSIS) and the Oscillation Analysis Working Group (OAWG). The members of the WIMRG include subject matter experts from industry, academia, and research laboratories. We thank those who contributed to this report, in particular Dr. Trudnowski who helped guide this project from its inception. Contributing authors include:

**Daniel Trudnowski**, *Chair*  
**Evan Paull**, *WECC Staff Liaison*

Urmila Agrawal	Ryan Lott
Ryan Elliott	John Pierre
Jim Follum	

In addition to the contributing authors, we would like to thank everyone who attended WIMRG meetings, asked questions during presentations, and provided feedback on drafts of this report. These members include:

Aftab Alam	Arif Khan
Robert Cummings	Cody Parker
Hassan Ghoudjehbklou	David Schoenwald
Daniel Goodrich	Michael Yao
Mahdi Hajian	Jimmy Zhang

### References

---

- [1] D. N. Kosterev, C. W. Taylor and W. A. Mittelstadt, "Model validation for the August 10, 1996 WSCC system outage," *IEEE Transactions on Power Systems*, vol. 14, no. 3, p. 967–976, 1999.
- [2] WECC/JSIS, "Modes of Inter-Area Power Oscillations in Western Interconnection," 2014.
- [3] Peak Reliability, *Western Interconnection Synchrophasor Program*, 2014.
- [4] B. Pierre, F. Wilches-Bernal, D. Schoenwald, R. Elliott, D. Trudnowski, R. Byrne and J. Neely, "Design of the Pacific DC Intertie wide area damping controller," *IEEE Transactions on Power Systems*, vol. 23, no. 5, 2019.
- [5] D. Trudnowski, "Estimating electromechanical mode shape from synchrophasor measurements," *IEEE Transactions on Power Systems*, vol. 23, no. 3, p. 1188–1195, August 2008.
- [6] J. W. Pierre, N. Zhou, F. K. Tuffner, J. F. Hauer, D. Trudnowski and W. A. Mittelstadt, "Probing signal design for power system identification," *IEEE Transactions on Power Systems*, vol. 25, no. 2, p. 835–843, May 2010.
- [7] J. W. Pierre, D. Trudnowski, M. Donnelly, N. Zhou, F. K. Tuffner and L. Dosiek, "Overview of system identification for power systems from measured responses," *International Federation of Automatic Controls (IFAC) Proceedings Volumes*, vol. 45, no. 16, p. 989–1000, July 2012.
- [8] D. Trudnowski and J. W. Pierre, *Inter-area Oscillations in Power Systems: A Nonlinear and Nonstationary Perspective*, 2009 ed., A. R. Messina, Ed., New York: Springer, 2009, p. 1–36.
- [9] C. Canizares, L. Dosiek, H. Ghasemi, M. Gibbard, E. Johansson, G. Lewich, R. Martin, E. Martinez, L. Vanfretti, D. Vowles, R. Wies and N. Zhou, "Mode-Meter Analysis Methods," in *Identification of Electromechanical Modes in Power Systems, IEEE Task Force Report*, vol. Special Publication TP462, J. Pierre and D. Trudnowski, Eds., IEEE Power and Energy Society, 2012, p. 2:1–2:62.
- [10] L. Dosiek, "On the Cramer-Rao bound of power system electromechanical mode meters," *IEEE Transactions on Power Systems*, vol. 34, no. 6, p. 4674–4683, November 2019.
- [11] M. L. Shelton, P. F. Winkelman, W. A. Mittelstadt and W. J. Bellerby, "Bonneville Power Administration 1400-MW braking resistor," *IEEE Transactions on Power Apparatus and Systems*, vol. 94, no. 2, p. 602–611, March 1975.

- [12] L. Wang and A. Semlyen, "Application of sparse eigenvalue techniques to the small signal stability analysis of large power systems," *IEEE Transactions on Power Systems*, vol. 5, no. 2, p. 635–642, May 1990.
- [13] J. F. Hauer, "Emergence of a new swing mode in the western power system," *IEEE Transactions on Power Apparatus and Systems*, Vols. PAS-100, no. 4, p. 2037–2045, April 1981.
- [14] G. Rogers, *Power System Oscillations*, Boston: Kluwer Academic Publishers, 2000.
- [15] P. Kundur, N. Balu and M. Lauby, *Power System Stability and Control (Series EPRI Power Systems Engineering)*, New York, NY: McGraw-Hill, 1994.
- [16] F. K. Tuffner, L. W. Dosiak, J. W. Pierre and D. Trudnowski, "Weighted update method for spectral mode shape estimation from PMU measurements," *Proceedings from IEEE Power & Energy Society General Meeting*, July 2010.
- [17] N. Zhou, Z. Huang, L. Dosiak, D. Trudnowski and J. Pierre, "Electromechanical mode shape estimation based on transfer function identification using PMU measurements," *2009 IEEE Power & Energy Society General Meeting*, p. 1–7, July 2009.
- [18] L. Dosiak, D. J. Trudnowski and J. W. Pierre, "New algorithms for mode shape estimation using measured data," *2008 IEEE Power and Energy Society General Meeting - Conversion and Delivery of Electrical Energy in the 21st Century*, p. 1–8, July 2008.
- [19] L. Dosiak, J. W. Pierre, D. J. Trudnowski and N. Zhou, *2009 IEEE Power & Energy Society General Meeting*, p. 1–8, July 2009.
- [20] L. Dosiak and J. W. Pierre, "Estimating electromechanical modes and mode shapes using the multichannel ARMAX model," *IEEE Transactions on Power Systems*, vol. 28, no. 2, p. 1950–1959, May 2013.
- [21] L. Dosiak, N. Zhou, J. W. Pierre, Z. Huang and D. J. Trudnowski, "Mode shape estimation algorithms under ambient conditions: A comparative review," *IEEE Transactions on Power Systems*, vol. 28, no. 2, p. 779–787, May 2013.
- [22] J. S. Bendat and A. G. Piersol, *Engineering Applications of Correlation and Spectral Analysis*, 2nd ed., New York: John Wiley & Sons, 1993.
- [23] P. Stoica and R. Moses, *Spectral Analysis of Signals*, Upper Saddle River, New Jersey: Pearson Prentiss Hall, 2005.
- [24] D. J. Trudnowski, J. M. Johnson and J. F. Hauer, "Making Prony analysis more accurate using multiple signals," *IEEE Transactions on Power Systems*, vol. 14, no. 1, p. 226–231, February 1999.

- [25] J. F. Hauer, C. J. Demeure and L. L. Scharf, "Initial results in Prony analysis of power system response signals," *IEEE Transactions on Power Systems*, vol. 5, no. 1, p. 80–89, February 1990.
- [26] M. Grant and S. Boyd, "CVX: Matlab software for disciplined convex programming," January 2020. [Online]. Available: <http://cvxr.com/cvx/>. [Accessed May 2021].
- [27] R. Elliott, R. Byrne, A. Ellis and L. Grant, "Impact of increased photovoltaic generation on inter-area oscillations in the Western North American power system," *2014 IEEE PES General Meeting | Conference & Exposition*, p. 1–5, 2014.
- [28] R. H. Byrne, R. J. Conception, J. Neely, F. Wilches-Bernal, R. T. Elliott, O. Lavrova and J. E. Quiroz, "Small signal stability of the western North American power grid with high penetrations of renewable generation," *2016 IEEE 43rd Photovoltaic Specialists Conference (PVSC)*, p. 1784–1789, 2016.
- [29] J. Quintero, V. Vittal, G. T. Heydt and H. Zhang, "The impact of increased penetration of converter control-based generators on power system modes of oscillation," *IEEE Transactions on Power Systems*, vol. 29, no. 5, p. 2248–2256, September 2014.
- [30] L. Wu, S. You, X. Zhang, Y. Cui and Y. Liu, "Statistical analysis of the FNET/grideye-detected inter-area oscillations in Eastern Interconnection (EI)," *2017 IEEE Power & Energy Society General Meeting*, p. 1–5, 2017.
- [31] S. You, G. Kou, Y. Liu, X. Zhang, Y. Cui, M. J. Till and W. Yao, "Impact of High PV Penetration on the Inter-Area Oscillations in the U.S. Eastern Interconnection," *IEEE Access*, vol. 5, pp. 4361–4369, 2017.

## Appendix A: Electromechanical Dynamic Theory

The following is an overview of the theory of electromechanical dynamics. Many textbooks have been written on the topic, such as *Power System Oscillations* [14] and *Power System Stability and Control* [15].

### The Physics of Electromechanical Dynamics

To understand the beginnings of electromechanical modes, consider the single-machine infinite-bus (SMIB) system in Figure A-1, which uses the notation in Table A-1.

Table A-1: Mathematical notation.

Symbol	Meaning	Units
$\tau_m$	mechanical torque input into the generator	(pu)
$P_e$	electrical power out of the generator (pu)	(pu)
$\tau_e$	electrical torque on the shaft (pu)	(pu)
$\omega$	speed of the generator (pu)	(pu)
$\delta$	generator angle w.r.t. synchronism	(rad)
$\omega_b$	electrical speed base	(rad/s)
$H$	generator inertia constant	(s)
$D$	generator damping constant	(pu)

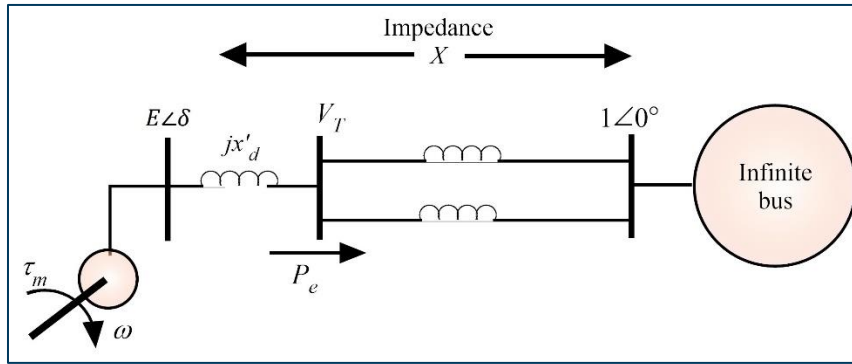


Figure A-1: Simple one-machine infinite-bus example system.

Using a simple classical generator model, the system equations are

$$\dot{\delta} = \omega_b(\omega - 1) \quad (\text{A.1})$$

$$2H\dot{\omega} = \tau_m - \tau_e - D(\omega - 1) \quad (\text{A.2})$$

$$\tau_e = P_e/\omega \quad (\text{A.3})$$

$$P_e = \frac{E}{X} \sin(\delta), \quad (\text{A.4})$$

## Modes of Inter-Area Power Oscillations in the Western Interconnection

where  $E$  is the internal stator voltage magnitude and  $X$  the sum of the synchronous reactance and the line reactance between the terminals of the machine and the infinite bus.

To study the modal properties of the system, we linearize (A.1)–(A.4) about a power-flow steady-state operating point defined by constants  $E_0$ ,  $\tau_{m0}$ ,  $\delta_0$  and  $\omega_0 = 1$ . This results in a second-order linear differential equation:

$$\begin{bmatrix} \Delta \dot{\delta} \\ \Delta \dot{\omega} \end{bmatrix} = \begin{bmatrix} 0 & \omega_b \\ -\frac{E_0 \cos(\delta_0)}{2HX} & \frac{E_0 \sin(\delta_0)}{2HX} - \frac{D}{2H} \end{bmatrix} \begin{bmatrix} \Delta \delta \\ \Delta \omega \end{bmatrix} + \begin{bmatrix} 0 & 0 \\ \frac{1}{2H} & -\frac{\sin(\delta_0)}{2HX} \end{bmatrix} \begin{bmatrix} \Delta \tau_m \\ \Delta E \end{bmatrix}. \quad (\text{A.5})$$

The characteristic equation for this system is

$$s^2 + \left( \frac{D}{2H} - \frac{E_0 \sin(\delta_0)}{2HX} \right) s + \left( \frac{E_0 \omega_b \cos(\delta_0)}{2HX} \right) = s^2 + 2\zeta \omega_n s + \omega_n^2, \quad (\text{A.6})$$

where the roots of the characteristic equation are the system eigenvalues (or modes) and are defined by

$$s = -\zeta \omega_n \pm j2\pi f_d \quad (\text{A.7})$$

$$f_d = \frac{\omega_n \sqrt{1 - \zeta^2}}{2\pi} \quad (\text{A.8})$$

The electromechanical modal frequency is described by  $f_d$  in Hz. The percent damping is described by  $100\zeta$ , where  $\zeta$  is the damping ratio.

An interesting perspective is to examine the modal frequency and damping as a function of system loading. Figure A-2 shows the variation of the frequency and damping as a function of  $\delta_0$ . From (A.4), we see that the larger  $\delta_0$  becomes, the higher the system loading. Notice as the system loading increases, the modal frequency and damping decrease.



## Modes of Inter-Area Power Oscillations in the Western Interconnection

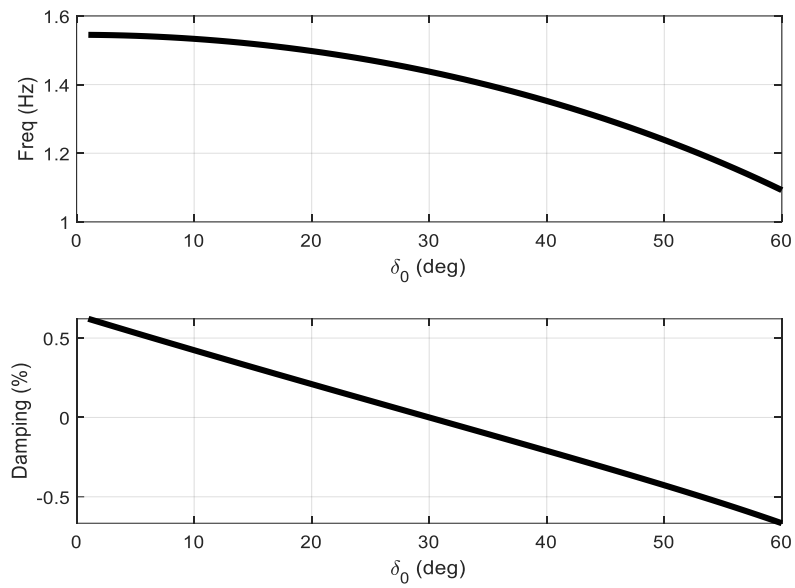


**Figure A-2: Modal frequency ( $f_d$ ) and damping ( $100\zeta$ ) versus system loading ( $\delta_0$ ) for a system with  $H = 2$ ,  $D = 0.5$ , and  $E_0 = 1$ .**

## Foundations of Systems Theory

The nonlinear dynamics governing the behavior of a large-scale power system may be expressed as

$$\dot{x}(t) = f(x(t), u(t)), \quad (\text{A.9})$$

where  $u(t) \in \mathbb{R}^m$  is the *input vector* and  $x(t) \in \mathbb{R}^n$  the *state vector* at time  $t$ . The input vector includes quantities that introduce an external force on the system, such as the mechanical power supplied by the prime mover of a synchronous generator. The state vector includes quantities that evolve over time in a way that depends on their present values and the value of the input vector, such as the rotor speed of a synchronous machine. In (A.9),  $f: \mathbb{R}^n \times \mathbb{R}^m \rightarrow \mathbb{R}^n$  is a function called the *vector field* that returns the time rate of change of the states based on the values of the state and input vectors. Together, (A.1) and (A.2) define  $f$  for the single-machine infinite-bus (SMIB) system discussed in the previous section.

For analysis and control design, engineers often linearize (A.9) around a static operating point  $\{x_0, u_0\}$ . This leads to a *small-signal* approximation of the original system. The state and input vectors can be expressed in relation to the operating point of interest as

$$x(t) = x_0 + \Delta x(t) \quad (\text{A.10})$$

$$u(t) = u_0 + \Delta u(t), \quad (\text{A.11})$$

where  $\Delta u(t)$  is the *input deviation* and  $\Delta x(t)$  the *state deviation* at time  $t$ . Substituting (A.10) and (A.11) back into (A.9) gives

$$\dot{x}(t) = f(x_0 + \Delta x(t), u_0 + \Delta u(t)), \quad (\text{A.12})$$

which is equivalent to the original nonlinear system. A first-order, i.e., linear, approximation of (A.12) is given by

$$\dot{x}(t) \approx f(x_0, u_0) + D_x f(x_0, u_0) \Delta x(t) + D_u f(x_0, u_0) \Delta u(t), \quad (\text{A.13})$$

where the operator  $D_x$  returns the Jacobian matrix of partial derivatives of  $f$  with respect to the state variables, and  $D_u$  the matrix of partial derivatives with respect to the input variables. Now, let

$$A = D_x f(x_0, u_0) \text{ and } B = D_u f(x_0, u_0), \quad (\text{A.14})$$

where the *system matrix*  $A \in \mathbb{R}^{n \times n}$  describes the sensitivity of the state derivatives to deviations in the state variables, and the *input matrix*  $B \in \mathbb{R}^{n \times m}$  the sensitivity to deviations in the input variables. The partial derivatives in (A.14) are evaluated at  $\{x_0, u_0\}$ , i.e., the operating point around which the system is linearized. So, the matrices  $A$  and  $B$  possess the following structure

$$A = \begin{bmatrix} \frac{\partial f_1}{\partial x_1} & \frac{\partial f_1}{\partial x_2} & \dots & \frac{\partial f_1}{\partial x_n} \\ \frac{\partial f_2}{\partial x_1} & \frac{\partial f_2}{\partial x_2} & \dots & \frac{\partial f_2}{\partial x_n} \\ \vdots & \vdots & \ddots & \vdots \\ \frac{\partial f_n}{\partial x_1} & \frac{\partial f_n}{\partial x_2} & \dots & \frac{\partial f_n}{\partial x_n} \end{bmatrix}_{x_0, u_0} \quad \text{and } B = \begin{bmatrix} \frac{\partial f_1}{\partial u_1} & \frac{\partial f_1}{\partial u_2} & \dots & \frac{\partial f_1}{\partial u_m} \\ \frac{\partial f_2}{\partial u_1} & \frac{\partial f_2}{\partial u_2} & \dots & \frac{\partial f_2}{\partial u_m} \\ \vdots & \vdots & \ddots & \vdots \\ \frac{\partial f_n}{\partial u_1} & \frac{\partial f_n}{\partial u_2} & \dots & \frac{\partial f_n}{\partial u_m} \end{bmatrix}_{x_0, u_0}. \quad (\text{A.15})$$



Using this notation, the linear approximation in (A.13) may be restated as

$$\dot{x}(t) \approx f(x_0, u_0) + A\Delta x(t) + B\Delta u(t). \quad (\text{A.16})$$

Most commonly, the operating point  $\{x_0, u_0\}$  reflects a condition where the system resides at a static equilibrium, that is  $f(x_0, u_0) = 0$ . When this condition is satisfied, the system is said to be in *steady state*, or *at rest*. For example,  $\{x_0, u_0\}$  may correspond to the values of the state and input vectors at a particular operating condition of interest, such as the hour at which the system experiences peak demand. For the SMIB example discussed above,  $x_0 = [\delta_0, \omega_0]^T$  and  $u_0 = [\tau_{m0}, E_0]^T$ . When  $\{x_0, u_0\}$  corresponds to a static equilibrium, (A.13) may be simplified to produce a *state-space* representation of the system:

$$\dot{x}(t) \approx A\Delta x(t) + B\Delta u(t), \quad (\text{A.17})$$

where  $\dot{x}(t) = \Delta\dot{x}(t)$  because  $x_0$  is held fixed. For the SMIB system, (A.5) is the linearized representation of the system dynamics, which is a specific example of the form in (A.17). Equation (A.17) approximates the true nonlinear system that is only valid in the neighborhood of the operating point of interest, i.e., under small perturbations. The state and input perturbations are said to be “small” when higher-order terms are not needed to accurately reproduce the dynamics of the original system.

### Modal Decomposition

As described above, we assume that the dynamics of a large-scale power system may be linearized about an operating point. The underlying assumption is that small motions of the power system may be well approximated by a linear system of the form

$$\begin{aligned} \Delta\dot{x}(t) &= A\Delta x(t) + B\Delta u(t) \\ \Delta y(t) &= C\Delta x(t) + D\Delta u(t), \end{aligned} \quad (\text{A.18})$$

where the vector  $\Delta x$  represents deviations in the system states, including rotor angles and speeds. Similarly,  $\Delta u$  represents deviations in the exogenous inputs, and  $\Delta y$  deviations in the measurable outputs. The eigenvalues and eigenvectors of the system in (A.18) are related by

$$Av_i = \lambda_i v_i \quad (\text{A.19})$$

$$w_i^T A_i = \lambda_i w_i^T \quad (\text{A.20})$$

$$w_i^T v_j = \begin{cases} 1, & i = j \\ 0, & i \neq j \end{cases} \quad (\text{A.21})$$

where  $\lambda_i \in \mathbb{C}$  is the  $i$ th eigenvalue,  $v_i \in \mathbb{C}^n$  the  $i$ th right eigenvector, and  $w_i \in \mathbb{C}^n$  the  $i$ th left eigenvector. So, given matrices

$$V = [v_1 \quad \cdots \quad v_n], \text{ and } W = [w_1 \quad \cdots \quad w_n], \quad (\text{A.22})$$

it holds that

$$W^T V = V^T W = I, \quad (\text{A.23})$$

where  $I$  is the  $n \times n$  identity matrix.



The eigenvalues and eigenvectors convey information about the modal properties of the system. Let  $\lambda_i = \sigma_i + j\omega_i$  be the  $i$ th eigenvalue. The frequency of the mode associated with  $\lambda_i$  is given by  $\omega_i$  in (rad/s), and the damping is determined by the *damping ratio*  $\zeta_i$

$$\zeta_i = \frac{-\sigma_i}{\sqrt{\sigma_i^2 + \omega_i^2}} = -\cos(\tan^{-1}(\omega_i/\sigma_i)), \quad (\text{A.24})$$

which is commonly expressed as a percentage, i.e.,  $100\zeta_i$ . If the eigenvalue  $\lambda_i$  is in the left half of the complex plane, i.e., it has a negative real part, then the mode is said to have *positive* damping and vice versa.

As shown in *Power System Oscillations* [14], under small perturbations, the state deviations may be expressed as

$$\Delta x(t) = \sum_{i=1}^n z_i(t)v_i, \quad (\text{A.25})$$

where

$$z_i(t) = w_i^T \Delta x(t), \quad (\text{A.26})$$

$$\dot{z}_i(t) = \lambda_i z_i(t) + w_i^T B \Delta u(t), \quad (\text{A.27})$$

for  $i \in \{1, \dots, n\}$ . The solution of (A.27) gives  $z_i(t)$ , which is the response of the  $i$ th mode to the input  $\Delta u(t)$ . So, (A.25) provides information about how the modes are combined to create the system states.

Let  $v_{i,k}$  be the  $k$ th element of the  $i$ th right eigenvector. Examination of (A.25) reveals that  $v_{i,k}$  provides critical information about the  $i$ th mode in the  $k$ th state. The magnitude  $|v_{i,k}|$  indicates the amplitude of the modal response  $z_i$  in state  $\Delta x_k$ . It is a direct measure of the *observability* of the  $i$ th mode in the  $k$ th state. The angle  $\angle v_{i,k}$  provides the information about the phasing of  $z_i$  in state  $\Delta x_k$ . By comparing the angle  $\angle v_{i,k}$  for a common dynamic state, such as generator speed, one can determine the relative phasing of the oscillations for the  $i$ th mode. Since it describes both oscillation amplitude and phase,  $v_i$  is referred to as the “mode shape” vector for the  $i$ th mode. Knowledge of  $v_i$  provides all information necessary to determine the relative amplitude and phase of oscillations in the dynamic system states for the  $i$ th mode. For the results presented in this document, all mode shapes for a common state are normalized such that the maximum value of  $|v_{i,k}|$  is equal to one for each mode.

Although the right eigenvector provides critical information about mode observability, it does not provide information about the *controllability* of the mode. Controllability is best described by the *participation factors*. Let  $p_{i,k}$  be the participation factor for the  $i$ th mode and  $k$ th state;  $p_{i,k}$  describes the sensitivity of the eigenvalue  $\lambda_i$  to the  $k$ th state. When studying electromechanical modes of oscillation, it is common to select a generator’s speed state. Mathematically, the participation factor  $p_{i,k}$  is defined in relation to the left and right eigenvectors as

$$p_{i,k} \triangleq w_{i,k} v_{i,k}. \quad (\text{A.28})$$



## Modes of Inter-Area Power Oscillations in the Western Interconnection

The participation factor can be interpreted using the feedback system depicted in Figure A-3. As Rogers shows [14], the sensitivity of the  $i$ th eigenvalue to the feedback gain is then

$$\frac{\partial \lambda_i}{\partial K} = p_{i,k}. \quad (\text{A.29})$$

Equation (A.29) is the foundation for determining which generators with PSS units will damp a given mode the most. For example, assume the state  $x_k$  is the speed of a generator. **The equation shows that the vector of departure in the root locus is equal to the participation factor when controlling the speed state of a generator through the torque on the shaft.** In this sense, it is a direct measure of the controllability for the generator associated with state  $k$  on mode  $i$ . The magnitude  $|p_{i,k}|$  is the rate at which the locus leaves the open-loop pole, and the angle  $\angle p_{i,k}$  is the angle of departure. The participation factor is a measure of how well control on a given generator can damp a particular mode.

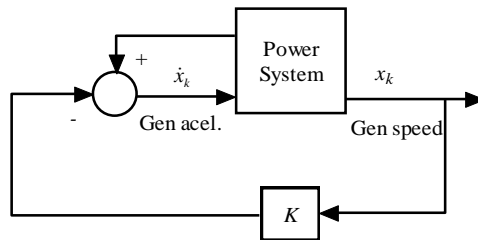


Figure A-3: Feedback system perspective of participation factors.

### A Simple Example

Electromechanical modes are typically classified as *local* or *inter-area*. Local modes have a single generator or power plant oscillating against the system. By contrast, inter-area modes are characterized by groups of generators located in different parts of the system oscillating against one another.

As a simple example, consider the four-machine system below. The system has three electro-mechanical modes described in Table A-2. Mode 2 is a local mode that has generators 1 and 2 swinging against each other. Similarly, Mode 3 is a local mode that has generators 3 and 4 swinging against each other.

Mode 1 is an inter-area mode. The mode shape is shown in Table A-3. The table shows that for Mode 1, Generators 1 and 2 swing together against Generators 3 and 4. Also, for a given disturbance, Generators 1 and 2 will have about half the amplitude of swing at the 0.51 Hz mode.

This is demonstrated with the simple transient simulation shown in Figure A-5. The system's response is a superposition of the three modes in Table A-2. Careful examination of Figure A-5 shows that at the lowest modal frequency of 0.51 Hz, generators 1 and 2 move in-phase while generators 3 and 4 swing together 180 degrees out of phase from generators 1 and 2. This was predicted by the mode shape shown in Table A-3. Also note in Figure A-5 that generators 1 and 2 have roughly half the amplitude of movement at the 0.51 Hz mode compared to generators 3 and 4.

## Modes of Inter-Area Power Oscillations in the Western Interconnection

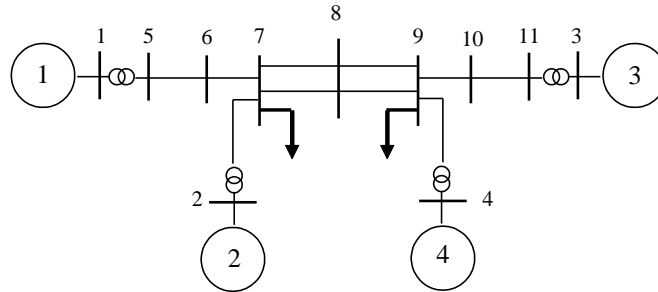


Figure A-4: Simple 4-machine example system.

Table A-2: 4-machine modes.

Mode	Freq., $\omega_i/2\pi$	Damp., $100\zeta_i$
1	0.51 Hz	7.8%
2	1.19 Hz	3.4%
3	1.22 Hz	3.3%

Table A-3: 0.51 Hz mode shape.

Gen	Angle, $\angle v_i^k$	Mag., $ v_i^k $
3	$-180^\circ$	1.00
4	$-180^\circ$	0.84
1	$0^\circ$	0.42
2	$0^\circ$	0.31

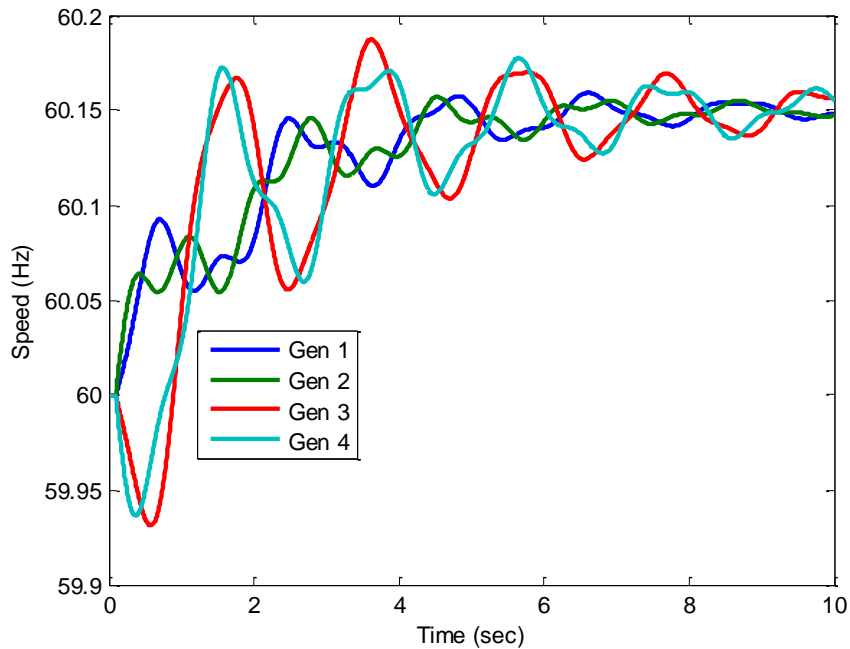


Figure A-5: Transient simulation for the 4-machine system.

## Appendix B: Analysis Methods

---

The following three sections provide an overview on estimating electromechanical modal properties (frequency, damping, and shape) primarily from signal processing techniques. Four primary sections are provided: Correlation Analysis, Mode Meter Analysis, Ringdown Analysis, and Direct Eigenanalysis.

### Correlation Analysis

Like the modal damping and frequency information, near-real-time operational knowledge of a power system's mode shape properties may provide critical information for control decisions. For example, modal shape may someday be used to optimally determine generator and/or load tripping schemes to improve the damping of a dangerously low-damped mode. The optimization involves minimizing load shedding and maximizing improved damping. This section describes how mode shape can be estimated from time-synchronized measurements.

As discussed in Appendix A: Electromechanical Dynamic Theory, mode shape is defined to be components of the right eigenvector of a linearized system model. The first published result for estimating mode shape from time-synchronized ambient measurements is contained in "Estimating electromechanical mode shape from synchrophasor measurements" [5]. Since then, several improvements have been published, including those found in "Weighted update method for spectral mode shape estimation from PMU measurements," [16] "Electromechanical mode shape estimation based on transfer function identification using PMU measurements," [17] "New algorithms for mode shape estimation using measured data," [18] "A channel matching approach for estimating electromechanical mode shape and coherence," [19] "Estimating electromechanical modes and mode shapes using the multichannel ARMAX model," [20] and "Mode shape estimation algorithms under ambient conditions: A comparative review," [21].

The question here is: how can mode shape, i.e., the properties of the right eigenvectors of the system, be estimated from direct power system measurements without the dependence on the linear differential model in (A.18)? The following describes an approach using spectral and correlation analysis.

#### *Estimating Mode Shape from Spectral Analysis*

The first published approach for estimating the mode shape from synchronized measurements is found in Trudnowski's "Estimating electromechanical mode shape from synchrophasor measurements" [5]. The following is a summary. Begin by defining two spectral functions.

$$S_{k,l}(\omega) = \lim_{T \rightarrow \infty} \frac{1}{T} E\{Y_k^*(\omega)Y_l(\omega)\} \quad (\text{B.1})$$

$$S_{k,k}(\omega) = \lim_{T \rightarrow \infty} \frac{1}{T} E\{Y_k^*(\omega)Y_k(\omega)\}, \quad (\text{B.2})$$

where  $S_{k,l}(\omega)$  is the cross-spectral density (CSD) function between general signals  $y_k(t)$  and  $y_l(t)$ ,  $S_{k,k}(\omega)$  is the power-spectral density (PSD) of signal  $y_k(t)$ ,  $Y_k(\omega)$  is the discrete Fourier transform of signal  $y_k(t)$  at frequency  $\omega$ ,  $Y_k^*(\omega)$  is the complex conjugate of  $Y_k(\omega)$ , and  $E\{\cdot\}$  is the expectation operator. These definitions are found in many signal processing textbooks, such as *Engineering Applications of Correlation and Spectral Analysis* [22].

Now assume that  $\lambda_i$  is a lightly damped mode with

$$\lambda_i = \alpha_i + j\omega_i \quad (\text{B.3})$$

where  $\alpha_i \ll \omega_i$ . As shown by Trudnowski [5], the following relationships result:

$$\angle S_{k,l}(\omega_i) \cong \angle v_{i,l} - \angle v_{i,k} \quad (\text{B.4})$$

$$S_{k,k}(\omega_i) \cong |v_{i,k}|^2 K_{\text{noise}}, \quad (\text{B.5})$$

where  $v_{i,l}$  and  $v_{i,k}$  are the  $l$ th and  $k$ th components of the right eigenvector  $v_i$ , and  $K_{\text{noise}}$  is an unknown constant.

Equations (B.4) and (B.5) are used to estimate the mode shape. Assume for the moment that all generator speed signals are time-synchronized sampled. Also assume that the frequency of the oscillation mode  $\omega_i$  is known. The PSD is calculated for each generator speed signal. From (B.5), the PSD of each signal is scaled by  $|v_{i,k}|^2$ ; therefore, the PSD is a direct measure of the observability of the mode at that generator.

The phasing of the mode among the generators is directly estimated from the angle of the CSD by (B.4). A reference generator with high mode observability is chosen as the reference generator  $k$ . The angle of the CSD is calculated for all other generators at mode frequency  $\omega_i$ . From (B.4), the angle of the CSD for generator  $l$  represents the phasing of the oscillation.

The squared-coherency function is defined as

$$\gamma_{k,l}^2(\omega) = \frac{|S_{k,l}(\omega)|^2}{S_{k,k}(\omega)S_{l,l}(\omega)}. \quad (\text{B.6})$$

It represents a measure of the correlation between two signals as a function of frequency [5]. As the two signals become uncorrelated, the coherency converges to zero. Similarly, as the signals become totally correlated, the coherency converges to unity. It is a measure of percent correlation.

The coherency function can be used to determine whether a mode of oscillation is due to one mode or multiple modes at the same frequency. For example, given two signals  $y_1(t)$  and  $y_2(t)$ , if both  $S_{1,1}(\omega)$  and  $S_{2,2}(\omega)$  have peaks at frequency  $\omega_i$ , this indicates that the system contains one or more modes at this frequency. If  $\gamma_{1,2}^2(\omega_i)$  is near unity, then the same mode is contained in both  $y_1$  and  $y_2$ . Conversely, if  $\gamma_{1,2}^2(\omega_i)$  is near zero, then the system contains at least two different modes at frequency  $\omega_i$ .

The true PSD and CSD are unknown. Therefore, they are estimated from synchrophasor measurements using standard signal process methods. For the results in this report, they were estimated using the Welch periodogram method [23]. To arrive at satisfactory estimates, several minutes of synchrophasor measurements are required.

In “Weighted update method for spectral mode shape estimation from PMU measurements,” [16] a method of using efficient weighted updates was applied to this mode shape estimation method to provide recursive estimates of mode shape and coherence in an online environment. It was able to successfully track mode shape and coherence through system changes in near real time. Many other methods have been developed for mode shape estimation from synchrophasor data.

### Mode Meter Analysis

The mode meter algorithms used in this study operate by estimating the parameters of an Autoregressive Moving Average (ARMA) model. In this model, PMU data is expressed as the constant coefficient difference equation

$$y(k) = - \sum_{i=1}^{n_a} a_i y(k-i) + \sum_{i=1}^{n_b} b_i e(k-i) + e(k), \quad (\text{B.7})$$

where  $k$  is the sample index corresponding to time  $t = kT$  with sampling interval  $T$  and  $e(k)$  models aggregated random system perturbations. The model is parametrized by the AR coefficients  $a_i$  and the MA coefficients  $b_i$ . The transfer function of the ARMA model is obtained by applying the  $z$ -transform to (B.7) and rearranging as

$$\frac{Y(z)}{E(z)} = \frac{z^{n_a} (1 + \sum_{i=1}^{n_b} b_i z^{-i})}{z^{n_a} + a_1 z^{n_a-1} + \dots + a_{n_a-1} z + a_{n_a}}. \quad (\text{B.8})$$

The poles of this transfer function are the complex valued  $z_i$  for which the denominator equals zero:

$$z_i^{n_a} + a_1 z_i^{n_a-1} + \dots + a_{n_a-1} z_i + a_{n_a} = 0. \quad (\text{B.9})$$

As the system's poles, the values of the  $z_i$  determine the system's stability. A subset of these poles corresponds to the system's dominant inter-area electromechanical modes. The discrete-time  $z_i$  are related to their continuous-time counterparts through the expression

$$\frac{1}{T} \ln(z_i) = \lambda_i = \sigma_i + j\omega_i. \quad (\text{B.10})$$

The frequency and damping of the mode follow as

$$f_i = \frac{\omega_i}{2\pi} \quad (\text{B.11})$$

$$\zeta_i = - \frac{\sigma_i}{|\lambda_i|} \times 100\%. \quad (\text{B.12})$$

## Modes of Inter-Area Power Oscillations in the Western Interconnection

The mode meter algorithms used in this study operate by estimating the coefficients in (B.7), finding the roots of the denominator polynomial in (B.8), and converting to continuous-time poles via (B.10). The frequency and damping ratio of electromechanical modes can then be obtained using (B.11) and (B.12). In the following sections, the two methods that were used in this study to estimate the AR coefficients in (B.7) are described.



**Least Squares**

In this study, the least squares method was applied to a rolling 30-minute window of data. Let  $k = 1, 2, \dots, K$  denote the samples of this window. Equation (B.7) can be written in matrix notation for  $k = n_a + 1, n_a + 2, \dots, K$  as

$$\underline{y} = [Y \mid E]\underline{\theta} + \underline{e}, \tag{B.13}$$

where

$$\underline{y} = [y(n_a + 1) \quad y(n_a + 2) \quad \dots \quad y(K)]^T \tag{B.14}$$

$$Y = \begin{bmatrix} y(n_a) & y(n_a - 1) & \dots & y(1) \\ y(n_a + 1) & y(n_a) & \dots & y(2) \\ \vdots & \vdots & \dots & \vdots \\ y(K - 1) & y(K - 2) & \dots & y(K - n_a) \end{bmatrix} \tag{B.15}$$

$$E = \begin{bmatrix} e(n_b) & e(n_b - 1) & \dots & e(1) \\ e(n_b + 1) & e(n_b) & \dots & e(2) \\ \vdots & \vdots & \dots & \vdots \\ e(K - 1) & e(K - 2) & \dots & e(K - n_b) \end{bmatrix} \tag{B.16}$$

$$\underline{\theta} = [a_1 \quad \dots \quad a_{n_a} \quad b_1 \quad \dots \quad b_{n_b}]^T \tag{B.17}$$

$$\underline{e} = [e(n_a + 1) \quad e(n_a + 2) \quad \dots \quad e(K)]^T. \tag{B.18}$$

The vector  $\underline{y}$  and matrix  $Y$  are made up of measured PMU data. The process noise in  $\underline{e}$  and  $E$  must be estimated. This is done by first estimating the parameters of a high-order AR model, a step that is not described in detail here. See the two-stage least squares algorithm description in “Spectral Analysis of Signals” [23] for details. The least squares estimate of the parameter vector is given by

$$\hat{\underline{\theta}} = [Y \mid E]^\dagger \underline{y}, \tag{B.19}$$

where  $\dagger$  indicates the pseudoinverse. This solution minimizes the sum of squared differences between  $\bar{y}$  and

$$\hat{\underline{y}} = [Y \mid E]^\dagger \hat{\underline{\theta}}. \tag{B.20}$$

With the parameter estimates in  $\hat{\underline{\theta}}$ , estimation of the electromechanical modes proceeds by finding the roots of the denominator polynomial in (B.8).

### **Yule-Walker**

The Yule-Walker algorithm was also applied to a rolling 30-minute window of data. The method is also based on the ARMA model, but it focuses on the relationship between current and past values of  $y(k)$  through the autocovariance sequence:

$$r(g) = E\{y(k)y(k-g)\} \quad (\text{B.21})$$

where  $E\{\cdot\}$  denotes the expectation operator. Applying this definition to the expression for  $y(k)$  in (B.7) leads to the property

$$r(g) = -\sum_{i=1}^{n_a} a_i r(g-i), \text{ for } g > n_b. \quad (\text{B.22})$$

Writing this expression out for  $g = n_b + 1, n_b + 2, \dots, n_b + L$  leads to the matrix equation

$$\begin{bmatrix} r(n_b + 1) \\ r(n_b + 2) \\ \vdots \\ r(n_b + L) \end{bmatrix} = - \begin{bmatrix} r(n_b) & r(n_b - 1) & \cdots & r(n_b - n_a + 1) \\ r(n_b + 1) & r(n_b) & \cdots & r(n_b - n_a + 2) \\ \vdots & \vdots & \ddots & \vdots \\ r(n_b + L - 1) & r(n_b + L - 2) & \cdots & r(n_b - n_a + L) \end{bmatrix} \begin{bmatrix} a_1 \\ a_2 \\ \vdots \\ a_{n_a} \end{bmatrix}. \quad (\text{B.23})$$

Next, the autocovariance sequence values in this expression are replaced with estimates given by

$$\hat{r}(g) = \begin{cases} \frac{1}{K} \sum_{k=g+1}^K y(k)y(k-g) & 0 \leq g \leq (K-1) \\ \hat{r}(-g) & -(K-1) \leq g \leq 0 \end{cases}. \quad (\text{B.24})$$

Writing the result in matrix notation,

$$\underline{\hat{r}} = -\hat{R}\underline{a}. \quad (\text{B.25})$$

The least squares solution for this equation leads to the parameter estimates:

$$\underline{\hat{a}} = -\hat{R}^\dagger \underline{\hat{r}}. \quad (\text{B.26})$$

These parameter estimates can then be used to estimate the electromechanical modes, as described previously.

## Ringdown Analysis

Ringdown analysis involves using curve fitting techniques, e.g., regression, to identify a model that reproduces the observed system response as closely as possible under some mathematical criteria. Studying the dynamic properties of the model then provides insight about the modes of the system. Here we discuss the two methods used to perform ringdown analysis for this report: Prony's method and a regularized form of Dynamic Mode Decomposition (DMD). There are many other ringdown analysis methods.

### Prony's Method

Prony's method is based on fitting a linear prediction model to the free-response portion of a ringdown. The underlying assumption is that the trajectory of the modeled state follows an autoregressive (AR) process. Although it is possible to extend Prony's method to incorporate multiple input signals, in its standard form it is a single-channel method [24]. Let the observed continuous input signal  $x(t)$  be modeled by a sum of damped sinusoids such that  $\hat{x}(t) \approx x(t)$

$$\begin{aligned}\hat{x}(t) &= \sum_{i \in J} A_i e^{\sigma_i t} \cos(\omega_i t + \phi_i) \\ &= \sum_{i \in J} \frac{1}{2} A_i e^{j\phi_i} e^{(\sigma_i + j\omega_i)t} + \frac{1}{2} A_i e^{-j\phi_i} e^{(\sigma_i - j\omega_i)t},\end{aligned}\tag{B.27}$$

where  $J$  is the set of oscillatory modes, and  $\sigma_i \pm j\omega_i$  is the complex eigenvalue pair associated with the  $i$ th mode. Here,  $A_i$  is the amplitude and  $\phi_i$  the phase of mode  $i$  observed in the input signal  $x(t)$ . Prony's method uses the input signal  $x(t)$  to produce an approximate solution for these unknown variables. In the study of electromechanical modes,  $x(t)$  often corresponds to a dynamic state associated with a synchronous machine, such as rotor speed. If recorded rotor speeds are not available, measurements of bus frequency may be used as a proxy because they contain similar information about the dynamic response of the system.

If  $\hat{x}(t)$  is sampled at a constant rate  $F_s = 1/T$ , then (B.27) may be rewritten as

$$\begin{aligned}\hat{x}(kT) &= \sum_{i \in J} \frac{1}{2} A_i e^{j\phi_i} e^{(\sigma_i + j\omega_i)kT} + \frac{1}{2} A_i e^{-j\phi_i} e^{(\sigma_i - j\omega_i)kT} \\ &= \sum_{l \in \mathcal{L}} B_l e^{\lambda_l kT},\end{aligned}\tag{B.28}$$

where  $k$  is the sample index, and  $\mathcal{L}$  the set of eigenvalues. Suppose (B.28) can be well approximated by a linear prediction model of the form

$$\hat{x}(kT) = a_1 \hat{x}[(k-1)T] + \dots + a_r \hat{x}[(k-r)T]\tag{B.29}$$

where  $r$  is the number of previous samples used to make the prediction. The characteristic equation of (B.29) is then



$$d(z) = 1 - (a_1 z^{-1} + \dots + a_r z^{-r}), \quad (\text{B.30})$$

where  $z$  is the discrete-time delay operator from the Z-transform.

Given the framework delineated above, Prony's method can be described as a three-step process:

- 1.) Solve for the parameters  $\{a_1, \dots, a_r\}$  of the linear prediction model. To do this, substitute  $\hat{x} = x$  in (B.29) and build an overdetermined system of equations where the curve fitting window captures the ringdown. Identify the least-squares solution to the resulting system of equations.
- 2.) Solve for the roots of the characteristic polynomial (B.30), i.e., identify the values of  $z$  for which  $d(z) = 0$ . These roots correspond to the discrete-time poles (eigenvalues), which can then be translated into continuous time. This step produces estimates of the frequency and damping of the modes.
- 3.) Solve for the output residues  $B_l$  in (B.28) given the eigenvalues calculated in Step 2. As in Step 1, this is achieved by determining the least-squares solution to an overdetermined system of equations. This step can be used to produce estimates of mode shape.

For details about how to execute the steps listed above, see Hauer, Demeure, & Scharf, "Initial results in Prony analysis of power system response signals" [25]. There are many variations of Prony's method, e.g., [24].

### ***Regularized Dynamic Mode Decomposition***

Dynamic Mode Decomposition (DMD) is a multi-channel modal analysis technique. It is based on fitting a discrete-time state-space model to the free response portion of the ringdown

$$x_{k+1} = \hat{A}x_k, \quad (\text{B.31})$$

where  $\hat{A} \in \mathbb{R}^{n \times n}$  is the discrete-time system matrix, and  $x_k \in \mathbb{R}^n$  the state vector at time index  $k$ . Recall that during the free response period the input, i.e., forcing function, goes to zero so that  $u_k = 0$ . Let the data matrices  $X$  and  $Z$  be organized such that

$$\begin{aligned} X &= [x_k \quad \dots \quad x_{k+p-1}] \\ Z &= [x_{k+1} \quad \dots \quad x_{k+p}], \end{aligned} \quad (\text{B.32})$$

where  $p$  is the number of samples contained within the curve fitting window. Here  $X$  represents the collection of observed or simulated signals recorded during the free response portion of the ringdown. Similarly,  $Z$  is a time-advanced version of the data matrix that allows us to rewrite (B.31) in matrix form

$$Z = \hat{A}X. \quad (\text{B.33})$$

In DMD, the system matrix  $\hat{A}$  is estimated by calculating the minimum-norm solution of (B.33). When  $X$  is invertible, (B.33) has the exact solution  $\hat{A} = ZX^{-1}$ . When the number of states is less than the number

of samples in the curve fitting window, i.e.,  $n < p$ , (B.33) is overdetermined and does not have an exact solution. So, we may approach it as an optimization problem

$$\underset{\hat{A} \in \mathbb{R}^{n \times n}}{\text{minimize}} \frac{1}{2} \|Z - \hat{A}X\|_F^2, \quad (\text{B.34})$$

where  $\|\cdot\|_F$  represents the *Frobenius norm*. This objective function corresponds to the minimization of squared error, as in least-squares regression. When the rows of the data matrix  $X$  are linearly independent, (B.34) has the closed form solution

$$\hat{A}_* = ZX^T(XX^T)^{-1}. \quad (\text{B.35})$$

After the optimal discrete-time system matrix  $\hat{A}_*$  has been identified, we may retrieve the continuous-time system matrix by

$$A_* = \log(\hat{A}_*)/T, \quad (\text{B.36})$$

where  $T$  is the sampling period of the input data, and  $\log(\cdot)$  denotes the matrix logarithm.

For the base case analysis presented in this report, we employed a regularized form of DMD that introduces an additional term to the objective function in (B.34)

$$\underset{\hat{A} \in \mathbb{R}^{n \times n}}{\text{minimize}} \frac{1}{2} \|Z - \hat{A}X\|_F^2 + \mu \|\hat{A}\|_*. \quad (\text{B.37})$$

The regularization term is based on the so-called *nuclear norm*  $\|\cdot\|_*$ , which returns the sum of the singular values of  $\hat{A}$ . For matrices in which all the singular values are less than or equal to one, the nuclear norm is the convex relaxation of the rank function. So, adjusting the value of  $\mu$  provides control over the model order, i.e., the number of oscillatory modes it contains. The basic idea of this regularization approach is to provide a mechanism to balance time- and frequency-domain (i.e., spectral) considerations. The problem (B.37) can be solved using convex optimization techniques or off-the-shelf software packages such as CVX [26].

## Direct Eigenanalysis

The first step in direct eigenanalysis is to estimate the entries of the linearized system matrix using a mathematical model of the power system. As described in Appendix A: Electromechanical Dynamic Theory, the nonlinear dynamics of the power system may be expressed as

$$\dot{x}(t) = f(x(t), u(t)), \quad (\text{B.38})$$

where  $u(t) \in \mathbb{R}^m$  is the input vector and  $x(t) \in \mathbb{R}^n$  the state vector at time  $t$ . Under small perturbations, the motion of the system about a fixed operating point  $\{x_0, u_0\}$  may be approximated as

$$\Delta\dot{x}(t) \approx A\Delta x(t) + B\Delta u(t), \quad (\text{B.39})$$

where  $\Delta x(t) = x(t) - x_0$  and  $\Delta u(t) = u(t) - u_0$ . The matrix  $A$  is called the *system matrix* (or *state matrix*), and  $B$  the *input matrix*. Stemming from the definition of the multivariate Taylor series, we have

$$A = \left[ \begin{array}{ccc} \frac{\partial f_1}{\partial x_1} & \cdots & \frac{\partial f_1}{\partial x_n} \\ \vdots & \ddots & \vdots \\ \frac{\partial f_n}{\partial x_1} & \cdots & \frac{\partial f_n}{\partial x_n} \end{array} \right]_{x_0, u_0}, \quad (\text{B.40})$$

where each entry is the partial derivative of a differential equation with respect to a state variable. There are two main techniques for estimating the entries of the matrix in (B.40): analytical differentiation and finite difference methods. These methods are summarized below.

After the system matrix has been constructed, its modal properties (e.g., eigenvalues and eigenvectors) may be studied using linear algebraic techniques. Since the system matrix may be large, it is often beneficial to employ advanced algorithms, such as Arnoldi iteration, to determine the eigenvalues and eigenvectors [12].

### Analytical Differentiation

In analytical differentiation, the entries of (B.40) are calculated using closed-form mathematical expressions. As a simple example, consider the swing equation for the SMIB system discussed in Appendix A: Electromechanical Dynamic Theory, restated here as

$$\dot{\omega}(t) = -\frac{D}{2H} [\omega(t) - 1] + \frac{1}{2H} \left[ \tau_m(t) - \frac{P_e(t)}{\omega(t)} \right]. \quad (\text{B.41})$$

For the system as a whole, (B.41) represents one element of the vector field  $f$ , which we label as  $f_2$ . Similarly, suppose we arrange the state vector such that the rotor speed  $\omega$  is the second element, meaning it acquires the label  $x_2$ . Per convention, we linearize the system around a steady-state operating point, where the machine is rotating at its synchronous speed. The entry in the second row, second column of the system matrix in (B.40) would then be the partial derivative of (B.41) with respect to the rotor speed  $\omega$ . Carrying out this analysis, we have



$$\left. \frac{\partial \dot{\omega}}{\partial \omega} \right|_{x_0, u_0} = \frac{P_e^0}{2H} - \frac{D}{2H} = \frac{E_0 \sin \delta_0}{2HX} - \frac{D}{2H}, \quad (\text{B.42})$$

where  $E_0$  is the initial internal stator voltage magnitude, and  $\delta_0$  the initial power angle. Checking this result against (A.5) from Appendix A: Electromechanical Dynamic Theory, we see that (B.42) matches the entry in the second row, second column of the system matrix. This example shows the general outline of the analytical differentiation process, in which the partial derivatives in (B.40) are calculated mathematically one-by-one. For dynamic states that interact through the network, the calculations are more intricate, but the main idea is the same [14].

### Finite Difference Methods

Rather than calculating the entries of (B.40) using closed-form mathematical expressions, we can instead approximate them using discrete mathematics. This process is known as *numerical differentiation*. The derivative of a generic function  $f: \mathbb{R} \rightarrow \mathbb{R}$  is defined as

$$\left. \frac{df}{dx} \right|_{x_0} = \lim_{\Delta x \rightarrow 0} \frac{f(x_0 + \Delta x) - f(x_0)}{\Delta x}. \quad (\text{B.43})$$

The underlying principle of finite difference methods is that the exact definition in (B.43) can be well approximated by simple expressions. For example, we see that when  $\Delta x$  is small

$$\left. \frac{df}{dx} \right|_{x_0} \approx \frac{f(x_0 + \Delta x) - f(x_0)}{\Delta x}, \quad (\text{B.44})$$

which is the simplest approximation of (B.43). Notice that (B.43) requires us to analyze the value of the right-hand side as the perturbation  $\Delta x$  becomes infinitesimally small. In contrast, (B.44) is an approximation that performs well when  $\Delta x$  is small but finite. So, the term  $f(x_0 + \Delta x) - f(x_0)$  is referred to as a *finite difference*. The specific approximation (B.44) is called the *forward difference* method. Another common approximation of (B.43) is the so-called *central difference* method

$$\left. \frac{df}{dx} \right|_{x_0} \approx \frac{f(x_0 + \Delta x) - f(x_0 - \Delta x)}{2\Delta x}, \quad (\text{B.45})$$

which is slightly more accurate than (B.44) and only modestly more computationally expensive.

Consider the SMIB example discussed in the section on analytical differentiation. Suppose we wanted to approximate the partial derivative in (B.42) using the forward difference method (B.44) rather than calculus. Evaluating the terms in the numerator of (B.44), we have

$$f(x_0 + \Delta x) = -\frac{D}{2H}[\omega_0 + \Delta\omega - 1] + \frac{1}{2H} \left[ \tau_m^0 - \frac{P_e^0}{\omega_0 + \Delta\omega} \right] \quad (\text{B.46})$$

$$f(x_0) = -\frac{D}{2H}[\omega_0 - 1] + \frac{1}{2H} \left[ \tau_m^0 - \frac{P_e^0}{\omega_0} \right], \quad (\text{B.47})$$



where the initial speed  $\omega_0$  is equal to the synchronous speed of the machine, e.g., 1 pu. Calculating the forward difference yields

$$\begin{aligned} f(x_0 + \Delta x) - f(x_0) &= -\frac{D\Delta\omega}{2H} - \frac{1}{2H} \left[ \frac{P_e^0}{\omega_0 + \Delta\omega} - \frac{P_e^0}{\omega_0} \right] \\ &= \frac{P_e^0}{2H} \left( \frac{\Delta\omega}{1 + \Delta\omega} \right) - \frac{D\Delta\omega}{2H}. \end{aligned} \quad (\text{B.48})$$

To determine the numerical derivative, we divide by the state perturbation  $\Delta\omega$

$$\frac{f(x_0 + \Delta x) - f(x_0)}{\Delta x} = \frac{P_e^0}{2H} \left( \frac{1}{1 + \Delta\omega} \right) - \frac{D}{2H}. \quad (\text{B.49})$$

Comparing with the exact expression (B.42), we see that

$$\left. \frac{\partial \dot{\omega}}{\partial \omega} \right|_{x_0, u_0} = \frac{P_e^0}{2H} - \frac{D}{2H} \approx \frac{P_e^0}{2H} \left( \frac{1}{1 + \Delta\omega} \right) - \frac{D}{2H}. \quad (\text{B.50})$$

For this example, the forward difference (B.44) provides a close approximation of (B.43) provided that the state perturbation  $\Delta\omega$  is small. A common range for the state perturbation in finite difference analysis is  $10^{-3}$  to  $10^{-5}$ . For the case where  $D = 0$  and  $\Delta\omega = 10^{-4}$ , the forward difference method matches the analytical expression (B.42) to within 0.01%.

This example illustrates the accuracy of finite difference methods in a setting that is familiar to power system engineers. In practice, the finite difference calculations (B.46)–(B.49) are not carried out analytically (i.e., by hand). Rather, we simply perturb the state and evaluate the individual differential equations that make up the vector field (i.e.,  $f_1$ ,  $f_2$  and so on). In power system simulation software, these differential equations are specified as functions because they are required to determine the state derivatives. During a simulation, these state derivatives serve as inputs to the numerical integration scheme that approximates the state trajectories. By using numerical differentiation to build the system matrix, we can reuse functions that already exist in the program without having to manually calculate any partial derivatives of the vector field. This tends to make finite difference methods easier to implement and maintain in software than analytical differentiation techniques.

### Appendix C: The Impact of Future Grid Configurations

---

#### Preface

This report is meant to be a reference for practicing engineers that summarizes the current understanding of the modal properties of the system as it exists today (ca. 2021). Nevertheless, the generation mix in the Western Interconnection is undergoing rapid transformation with conventional thermal generation, particularly coal-fired units, being displaced by inverter-based renewable resources. It will be of vital importance to monitor how the properties of the inter-area modes change as the use of renewable generation increases. In this section, we describe the results of a model-based study performed by PNNL that explores this relationship. For more studies with a similar focus, see [27], [28], [29], [30], and [31].

There is a large degree of uncertainty that is inherent in many factors that may influence the system modes as the generation mix changes. These factors include, but are not limited to:

- The pace of generator retirements, and which units are decommissioned;
- The utility-scale generation mix, particularly the renewable penetration level;
- Changes in the system loading and load dynamics; and,
- The amount of inverter-based generation installed in distribution systems, and how it is geographically distributed throughout the interconnection.

Unlike synchronous machines, the dynamics of inverter-based resources are determined almost solely by the control strategies and protection logic programmed in their software. As the penetration of renewable generation increases, the standards outlining the permitted capabilities and interconnection requirements for inverter-based resources may change. Due to these complexities, the results of model-based studies are sensitive to the specific dynamic models and control settings used to represent the inverter-based resources. At present there are no WECC-approved generic dynamic models available to represent grid-forming inverters that operate by specifying a commanded voltage phasor at their terminals. Further complicating this picture is the potential for control-driven forced oscillations emanating from inverter-based resources, and how those oscillations may interact with the inter-area modes. Depending on the frequency of a control-driven oscillation, it may not even be possible to study these interactions in tools like PSLF, PSS/E, or PowerWorld.

Despite these limitations, there is still value in investigating the impact of an increasing penetration of renewable generation on the modal properties of the system. For instance, there is less uncertainty in near-term scenarios in which the renewable penetration increases modestly from the levels seen today. And evaluating long-range cases can still be instructive, provided that the assumptions used to construct those cases are well founded and well understood by the reader. The confidence with which conclusions can be stated will improve as the future grid comes into focus.



### Introduction

Several states throughout the U.S. have established renewable portfolio standards (RPS) to promote clean and sustainable energy sources. Achieving these mandates will require replacing traditional synchronous generation with inverter-based renewable energy sources (IBRES). This shift in the generation mix will have a significant impact on system behavior including natural oscillations. Oscillations are inherent in power systems because of their electro-mechanical nature. These oscillations can either involve generators within the same area oscillating against each other (arising from local modes) or generators in different areas oscillating against each other (arising from inter-area modes). The system oscillatory behavior is largely determined by system dynamics and topology. The displacement of synchronous machines by inverter-based generation sources will result in changes to the system topology and other grid properties, such as system inertia, which are usually associated with the synchronous machines. These changes in system dynamics will further result in changes to the system oscillatory behavior. It is essential that these changes in the oscillatory behavior be fully understood so that timely measures can be adopted to maintain reliable system operation.

This section provides an overview of the model-based oscillation study done by PNNL to understand the impact of changes in the generation mix on system oscillatory behavior. In this study, the change in the generation mix represents a future scenario in which many of the existing synchronous generators will be replaced by fully converter-based RES generation sources. Several scenarios were considered, including area-specific and system-wide increases in the RES penetration.

### Simulation Scenario Design

The model-based, wide-area oscillation assessment was carried out using 2018 heavy summer (HS) operating WECC model as the base case to identify trends associated with increased RES penetration on system modes for different scenarios. The 2018 HS case has a RES penetration level of ~8.5% with a total system inertia of 919 GW-s and total system load of 173 GW. The area-wise generation mix and inertia for the base case is provided in Figure C-1. Two simulation scenarios were analyzed to investigate the impact of increased IBRES penetration level on system modes. In each scenario, a group of generators in several areas was selected and replaced by fully converter-based generation sources representing inverter-based solar and wind generation sources. The details of the model used to represent IBRESs is discussed in the next section.

## Modes of Inter-Area Power Oscillations in the Western Interconnection

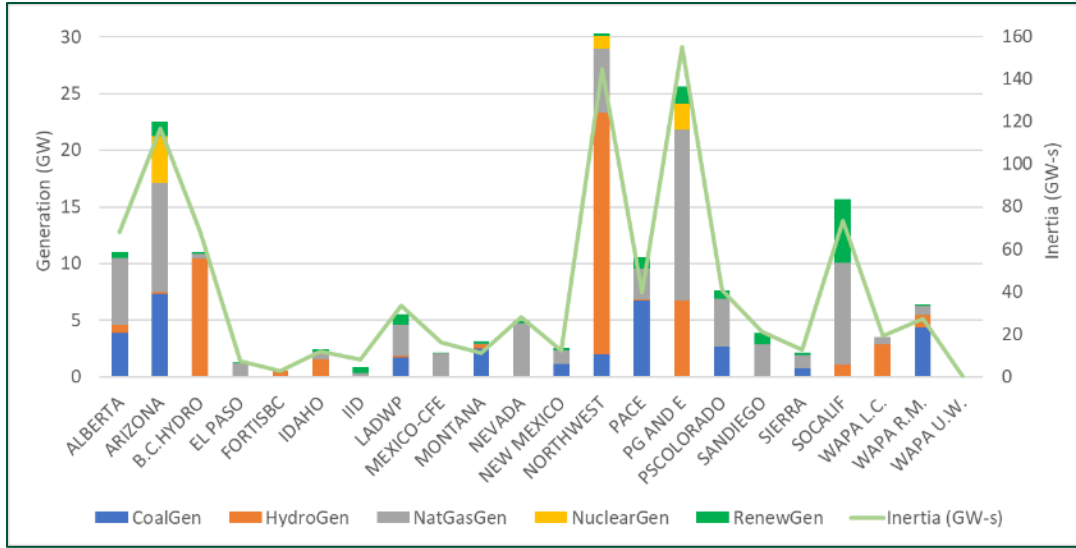


Figure C-1: Area-wise generation mix and inertia for 2018 HS operating case.

### Scenario 1: System-Wide Increase in RES Penetration

In Scenario 1 (S1), synchronous generators were replaced by IBRES simultaneously in all areas of the WECC system by a certain percentage based on the generation in each area. Here, coal-based generation was replaced first, followed by natural gas, nuclear, and others. Generation based on clean sources of energy such as hydro and geothermal were not replaced. Figure C-1 provides information on area-wise and system-wide RES penetration levels for different cases and Figure C-3 provides the corresponding inertia. In Figure C-2 and from here onward, unless otherwise specified, case 0 refers to the 2018 HS operating base case having a system-wide RES penetration level of ~8.5%. As a major proportion of generation in the Northwest and B.C. comes from hydro sources, RES penetration level in these areas could be increased up to 30% and 8% only. A total of 12 use-cases were created by increasing the system-wide renewable penetration level by close to 5% in consecutive use-cases such that the total system-wide RES penetration level was 70% in case 12. Power flow, system load, and generation dispatch remained the same for all cases. All other scenarios described in this section are derived from this scenario.

### Scenario 2: Reversing the Order in Which the Group of Generators Were Replaced

Scenario 2 (S2) is a modified version of S1. In this scenario, the order in which the group of generators was replaced to obtain an additional 12 cases in S1 was reversed. This means the generators replaced in case 1 in S1 were replaced in case 12 in S2. Generators replaced in case 2 in S1 were replaced in case 11 in S2, and so on. This scenario examined whether the trends observed in the system modes were a function of increased renewable penetration level or were determined by the group of generators replaced.

## Modes of Inter-Area Power Oscillations in the Western Interconnection

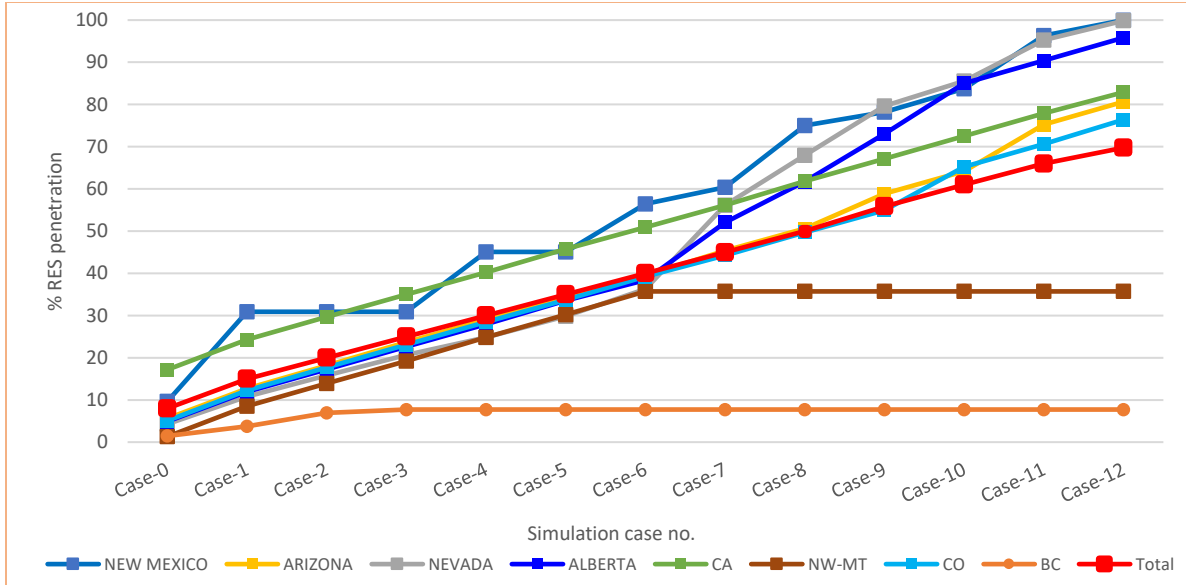


Figure C-2: Percent RES penetration in several areas and total system for different cases in S1.

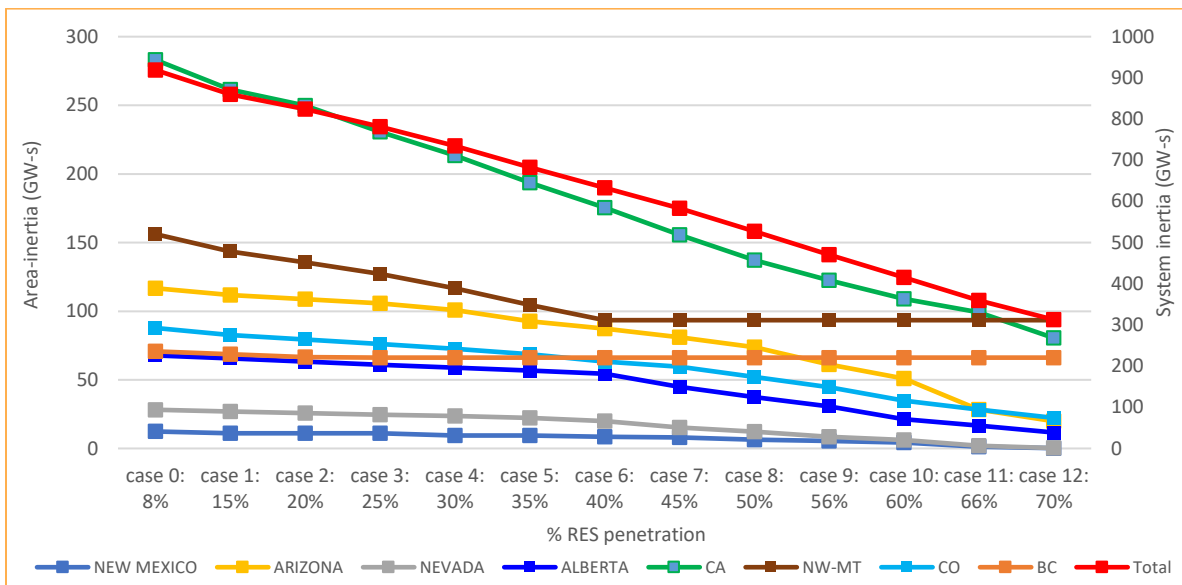


Figure C-3: Area-wise and total system inertia as a function of percent RES penetration for different cases in S1.

### Generic Model Used for Inverter-Based Resources<sup>1</sup>

In the study described in this appendix, the synchronous machines were replaced by generic models available for IBRES. For this, WECC-approved first generation type-4 WT4 models were used. This WT4 modeling package, which is based on GE's wind turbine model, consists of three models:

<sup>1</sup> [https://www.esig.energy/wiki-main-page/wt4-generic-wind-model/#Turbine\\_Model\\_.28wt4t.29](https://www.esig.energy/wiki-main-page/wt4-generic-wind-model/#Turbine_Model_.28wt4t.29)



generator/converter (WT4G), converter control (WT4E), and wind turbine (WT4T). The parameters for these models were obtained from the dynamic models available in the 2018 HS WECC operating case. A description on these models is provided next.

### WT4G - Generator/Converter Model for Type 4 First-Generation Generic Wind Model

The WT4G model, shown in Figure C-4, is an equivalent of the generator and the field converter providing the interface between the WTG and the network. This model receives the filtered active and reactive power commands,  $I_{PCMD}$  and  $E_{QCMD}$  respectively, from the electrical control module WT4E. The WT4G model then calculates the current injection to the grid based on these input values of  $I_{PCMD}$  and  $I_{QCMD}$ . Both active and the reactive components of the injected current are processed under the high and low voltage conditions using a special logic embedded in the high-voltage reactive current management and low voltage active current management block modules as shown in Figure C-4. The high-voltage reactive current management block module is designed for limiting the reactive current injected into the grid such that the machine terminal voltage  $V_T$  is within the nominal voltage limit  $V_{lim}$  if the converter is within current limits. The low voltage active current management block module is designed to limit the active current injection into the grid under low voltage conditions. The active power current decreases as a function of the voltage limit in a linear fashion as shown in Figure C-4. This linear function starts at  $Lvpnt1$  p.u. voltage and declines to zero at  $Lvpnt0$  p.u. voltage.

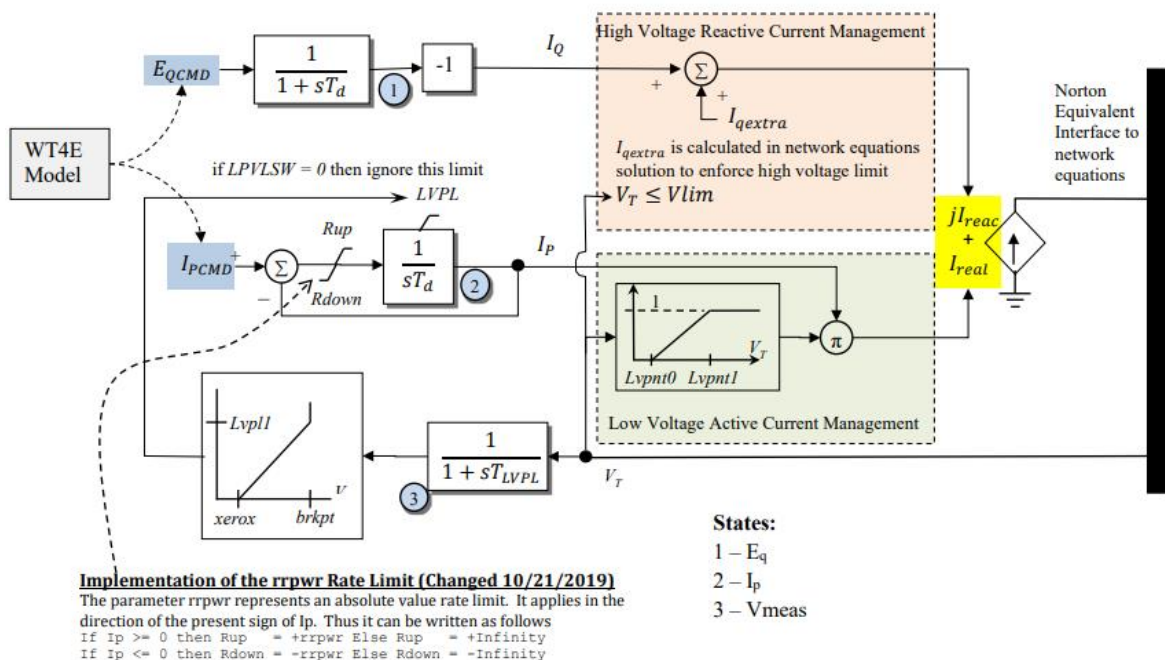


Figure C-4: Block diagram of generator/converter model (WT4G)<sup>2</sup>.

<sup>2</sup> [https://www.powerworld.com/WebHelp/Content/TransientModels\\_HTML/Machine%20Model%20WT4G.htm](https://www.powerworld.com/WebHelp/Content/TransientModels_HTML/Machine%20Model%20WT4G.htm)

**WT4E—Electrical Control Model for the Type 4 First-Generation Generic Wind Model**

The WT4E model, shown in Figure C-5, is an equivalent of the controller for the power converter.

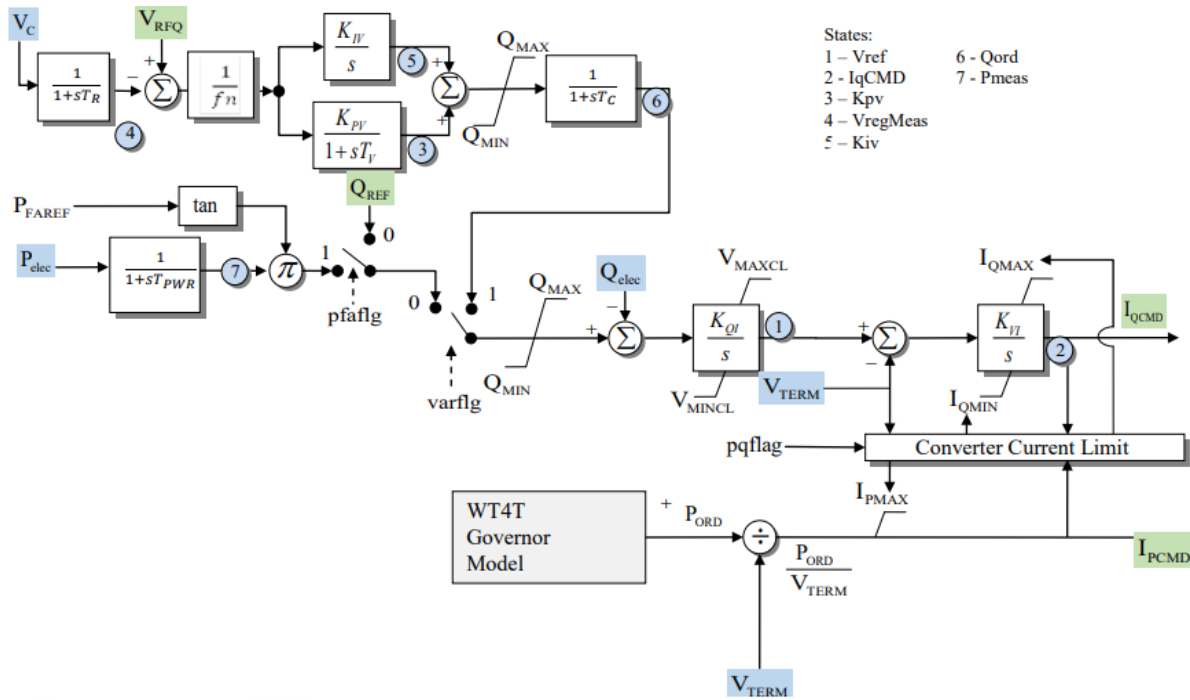


Figure C-5: Block diagram of electrical control model (WT4E)<sup>3</sup>.

**WT4T—Turbine Model for the Type 4 First-Generation Generic Wind Model**

The WT4T model, shown in Figure C-6 is an equivalent of the simplified wind turbine model. Note that for type-4 wind plants, this model just behaves as a standard PI controller for the Pref signal.

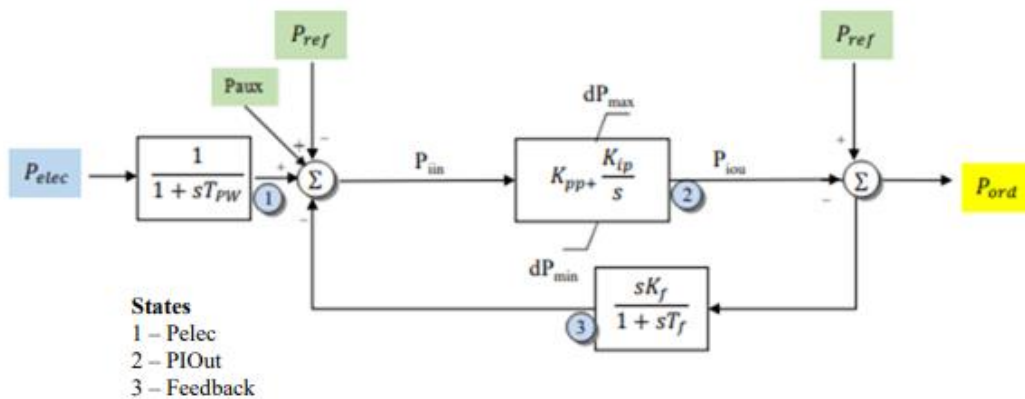


Figure C-6: Block diagram of the simplified governor model (WT4T)<sup>4</sup>.

<sup>3</sup> [https://www.powerworld.com/WebHelp/Content/TransientModels\\_HTML/Exciter%20WT4E.htm](https://www.powerworld.com/WebHelp/Content/TransientModels_HTML/Exciter%20WT4E.htm)

<sup>4</sup> [https://www.powerworld.com/WebHelp/Content/TransientModels\\_HTML/Governor%20WT4T.htm](https://www.powerworld.com/WebHelp/Content/TransientModels_HTML/Governor%20WT4T.htm)



### Results and Discussion

For the two scenarios described in the previous subsection, modal analysis was performed to identify the trends observed in the North-South A (NSA) and North-South B (NSB) system modes for different renewable penetration levels. The modal analysis was performed using both simulated data-based Prony method and model-based eigenvalue analysis.

#### *Modal Analysis Using Prony’s Method*

PowerWorld simulator was used to generate simulated data consisting of ringdown oscillations resulting from Chief Joseph brake insertion event. Frequency measurements calculated from rotor-angle measurements of generators from all areas were used for estimating system modes using the multi-channel formulation of Prony’s method [24]. The estimated modes were then validated by comparing the preprocessed signal with the signal reconstructed using mode estimates as described in “Initial results in Prony analysis of power system response signals” [25]. Figure C-7 through Figure C-10 summarize the results obtained for the two scenarios, S1 and S2, for analyzing the impact of increased renewable penetration level on the frequency and damping ratio of the NSA and NSB modes.

#### *Impact on the Frequency of the NSA and NSB Modes*

As seen in Figure C-7 and Figure C-8, the frequency of the NSA and NSB modes increased for the two scenarios with increase in renewable penetration level and subsequent reduced system inertia. Also, the trends observed in the frequency of the two modes with respect to the increased renewable penetration level were affected by reversing the order of the group of generators that were replaced. Further study done by PNNL showed that the increase in the frequency of system modes is not directly proportional to the decrease in the system inertia.

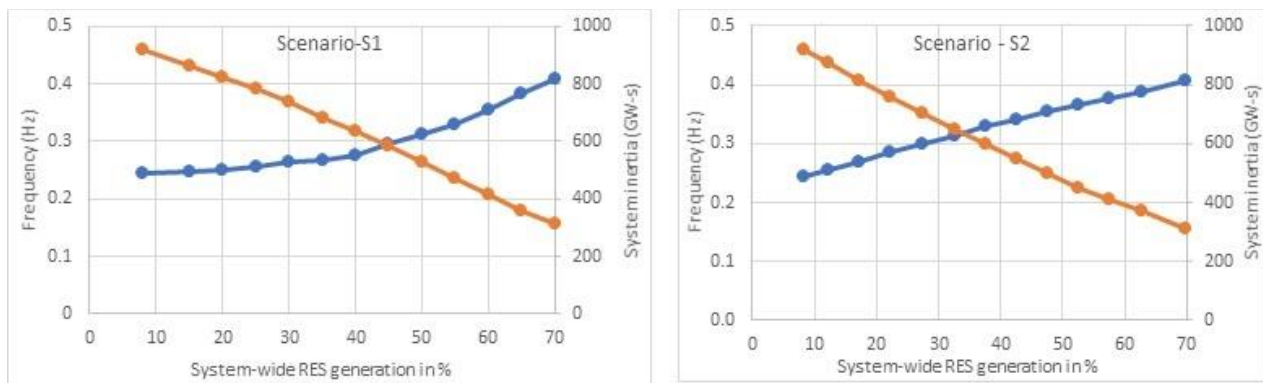


Figure C-7: Assessment of the impact of increased renewable penetration on the frequency of the NSA mode for S1 (left) and S2 (right).

## Modes of Inter-Area Power Oscillations in the Western Interconnection

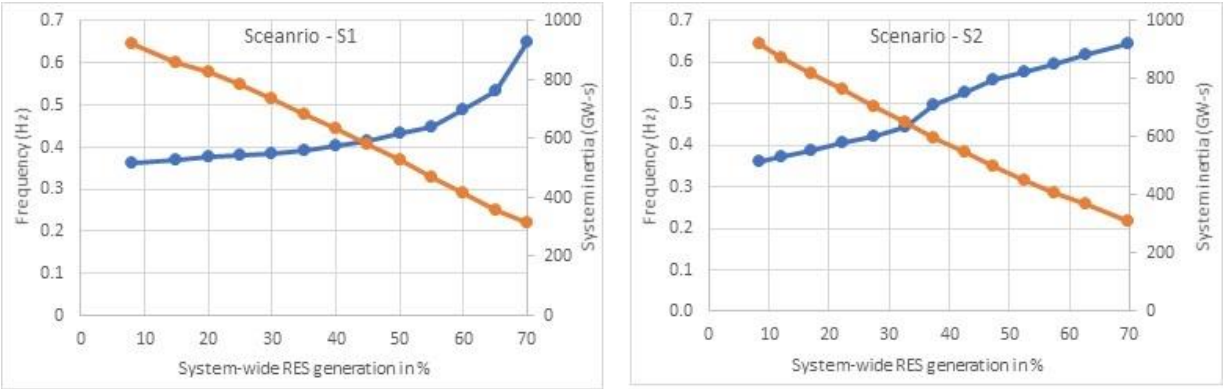


Figure C-8: Assessment of the impact of increased renewable penetration on the frequency of the NSB mode for S1 (left) and S2 (right).

### Impact on the Damping Ratio of NSA and NSB Modes

Figure C-9 shows the impact of increased renewable penetration on the damping ratio of NSA for scenarios S1 and S2. In S1, the damping ratio of NSA initially increased slightly and, after the system-wide renewable penetration further increased beyond 40%, damping ratio declined sharply. From this result, one could erroneously conclude that an increase in the penetration level beyond a certain value inevitably results in a significant decrease in the damping ratio of system modes. Therefore, analysis was carried out with S2 in which the order of generators replaced in S1 was reversed. Comparing results for S1 and S2 shows that the trends observed in the damping ratio of the NSA mode reversed when the order of generators replaced was reversed. This is strong evidence that the change in the damping ratio is not a function of increased renewable penetration level or reduced system inertia but is determined by the generators that are replaced and how remaining synchronous generators interact among each other. As seen in Figure C-10, the damping ratio of NSB was not as affected by the increased renewable penetration level as NSA in the two scenarios. Except for some cases in S2, the damping ratio of NSB in all other cases and scenarios were comparable to that in the base case.

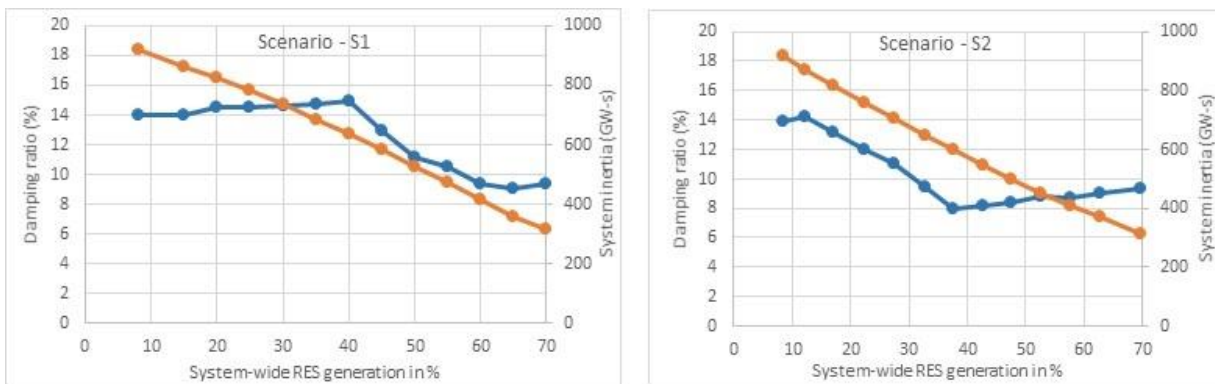
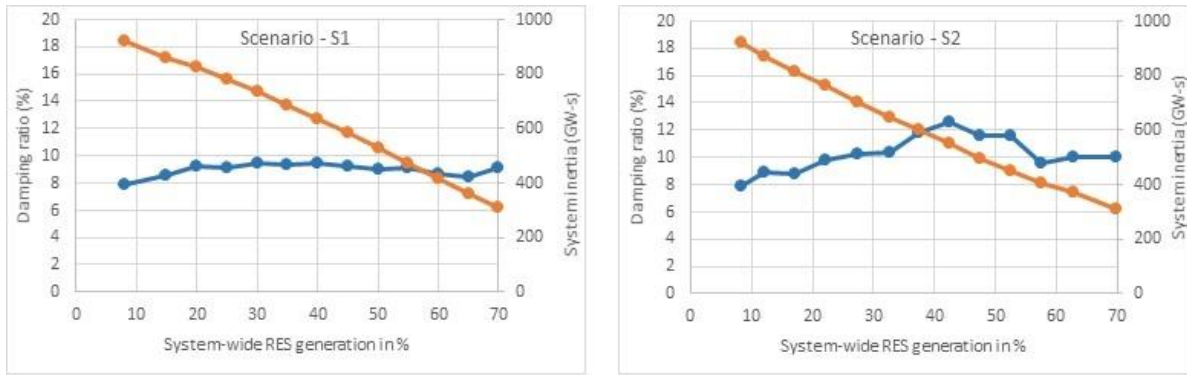


Figure C-9: Assessment of the impact of increased renewable penetration on the damping ratio of NSA for S1 (left) and S2 (right).

## Modes of Inter-Area Power Oscillations in the Western Interconnection



**Figure C-10: Assessment of the impact of increased renewable penetration on the damping ratio of NSB for S1 (left) and S2 (right).**

From this set of results for the NSA and NSB modes, it can be concluded that the change in the frequency and damping ratio of modes cannot be directly related to the change in the system inertia or increased renewable penetration level. Other factors also need to be considered, such as participation factor of generators that are replaced, topology of the online synchronous generators, etc. PNNL also performed a detailed eigenvalue analysis to have a better understanding of the trends observed in the NSA and NSB modes with increased renewable penetration level as discussed next.

### ***Eigenvalue Analysis Using SSAT***

SSAT developed by PowerTech Labs was used to perform eigenvalue analysis to study the variations in the participation factor of the synchronous generators for both NSA and NSB modes as the renewable penetration level increased in the system. Here, in this report, an example of the analysis is shown for NSA mode for S1.

Figure C-11 shows the variations observed in the participation factor of generators in several areas with increased renewable penetration. In this figure, the participation factor of only those generators is included that had a value of at least 0.05 in the base case. Also, in this figure, the missing part of the line represents generators that were replaced in the earlier cases. By analyzing participation factor of generators for all cases in Figure C-11, it was found that the trends observed in NSA for S1 could be explained with respect to the participation factor of generators. As shown in Figure C-12, the participation factor of generators for cases 0–6 did not change much, even when the system-wide renewable penetration level increased to 40% in case 6. The same trend was also observed in the damping ratio of NSA, which did not change much for these cases. From case 6 onward, the participation factor of generators changed significantly as shown in Figure C-13, which is exactly what was observed in the damping ratio.

The participation factor of the remaining synchronous generators in Alberta increased up to case 9, after which it started decreasing. In case 12, the remaining synchronous generators in Alberta had low participation factor. The participation factor of generators in B.C. Hydro area increased up to case 10



## Modes of Inter-Area Power Oscillations in the Western Interconnection

and then it started decreasing. The renewable penetration level in this area could only be increased up to 8%, so generators were only replaced in Cases 1 and 2. The participation factor of generators increased in all other areas, including California, Arizona, and others with the increased renewable penetration level, with Palo Verde units in Arizona becoming those with the highest participation factor from Case 10 onward. The participation factor of generators in Montana and the Northwest had a low participation factor for all generators in all cases, as shown in Figure C-14. The participation factor of some Grand Coulee units increased slightly up to Case 10, then decreased, while the Boundary Gate unit increased for all cases.

From this study performed by PNNL, it was concluded that the trends seen in the damping ratio and frequency of modes cannot be directly related to the renewable penetration level or system inertia. These trends are determined by which generators are replaced and how remaining synchronous generators interact with each other with respect to their mode shape and participation factor. As the penetration level of IBRES generation increases, the controllability of the generators for a mode can change and, depending on the contribution of the generators having high controllability to the damping of that mode, the damping ratio could be affected. Therefore, it will be important to perform eigenvalue analysis of the system as it evolves to identify generators having high controllability for each mode and tune the PSS of those generators to improve the damping of the corresponding mode.

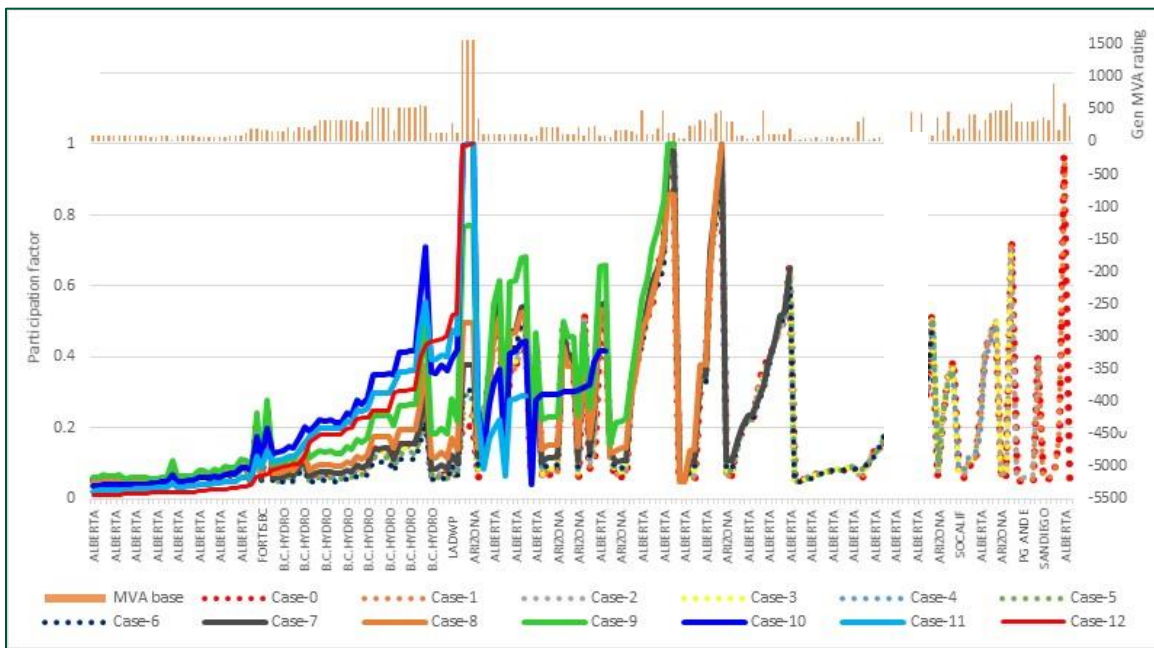


Figure C-11: Participation factor of generators for all cases of S1 for NSA.

## Modes of Inter-Area Power Oscillations in the Western Interconnection

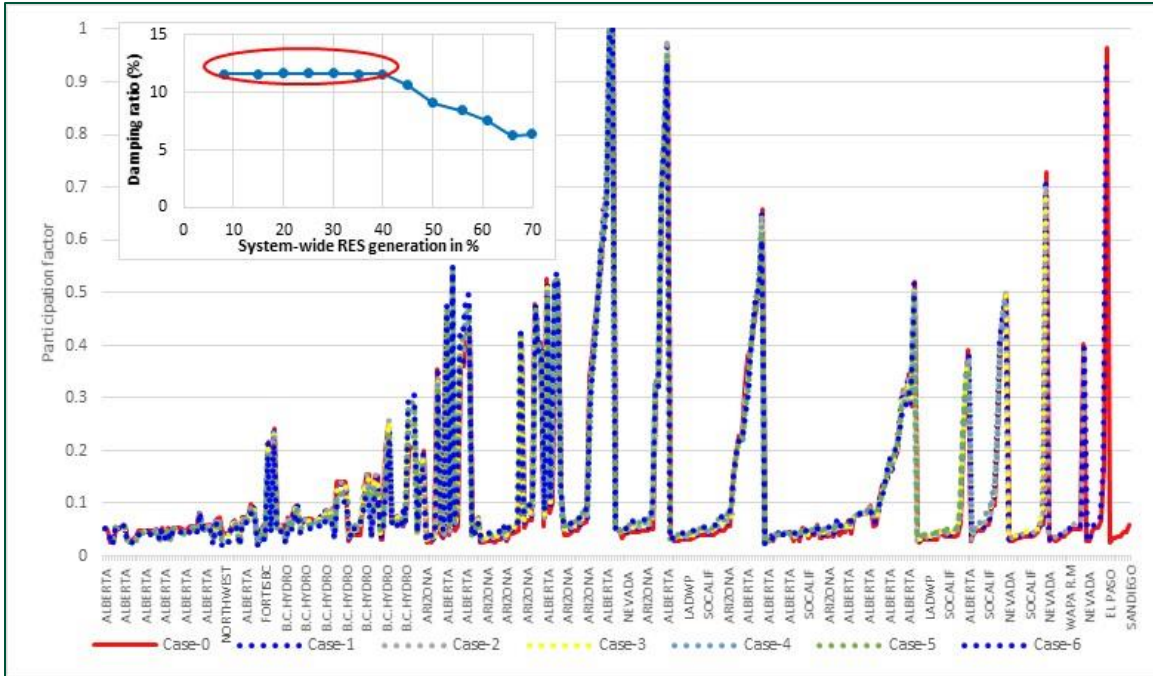


Figure C-12: Participation factor of generators for cases 0-6 of S1 for NSA.

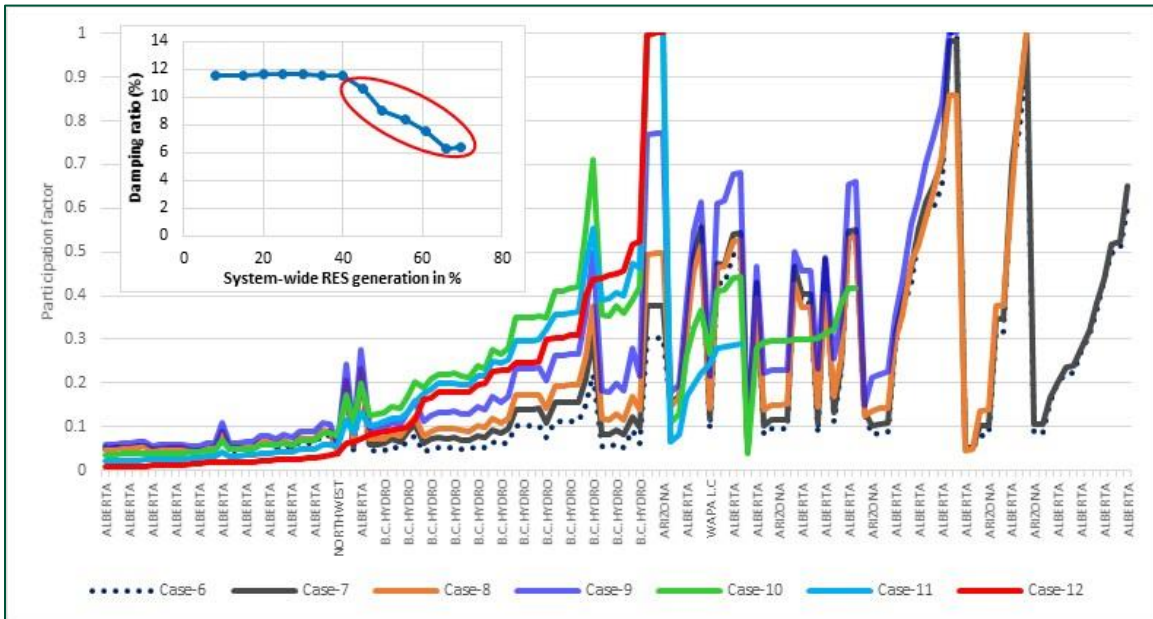


Figure C-13: Participation factor of generators for cases 6-12 of S1 for NSA.

## Modes of Inter-Area Power Oscillations in the Western Interconnection

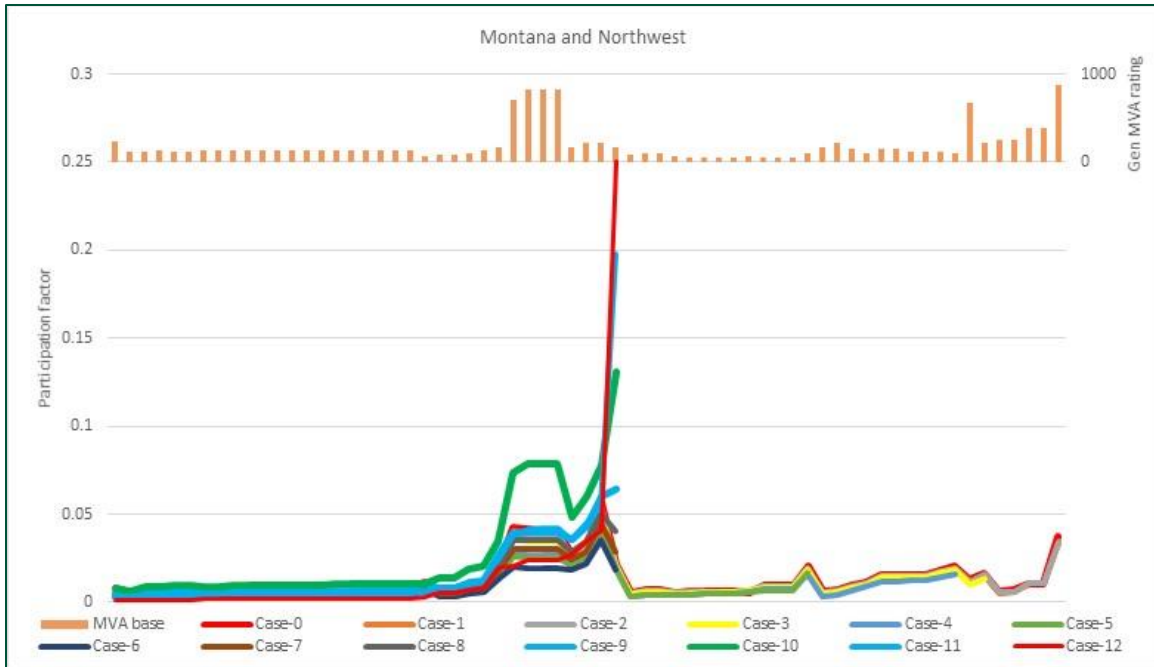


Figure C-14: Participation factor of generators in Montana and the Northwest in S1 for NSA.

### Future Work on Systems with High-RES Penetrations

Work done so far studied the impact of increased inverter-based renewable penetration level on existing modes only. This work was done by replacing synchronous generation machines with grid-following type of inverter-based machines. Future work will focus on performing analysis by using a proportion of grid-forming and grid-following inverters and study the impact on new modes, which could be electromechanical and control modes, if any. We will also be analyzing the impact of stochastic nature of renewable generation on dynamic interactions among several electromechanical and or control equipment and resulting impact on modes. This will be done by using production cost model to generate hourly use-cases for several days based on the generator retirement plan by WECC.

## Appendix D: NSA Mode Analyses

### Correlation Analysis from 2016 through 2019 PMU Data

The following are the mode shape estimates for all the conditions in Table 10 from the section titled, "North-South A Mode." The mode shape is shown on the left and the mode reference signal PSD is shown on the right.

#### 2016 Data

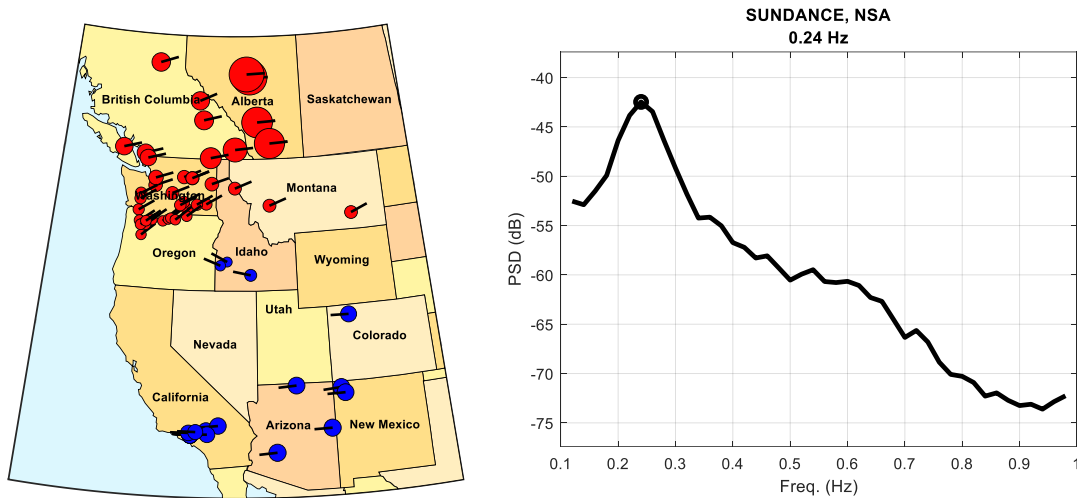


Figure D-1: 2016/09/28 from 15:10:00 to 15:30:00 UTC. Ambient condition.

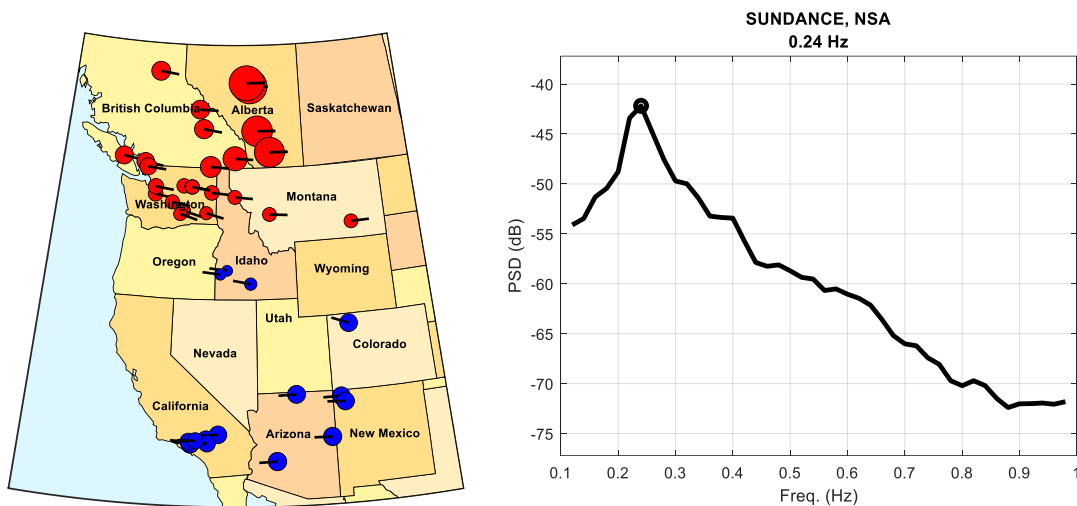


Figure D-2: 2016/09/28 from 16:30:12 to 16:40:12 UTC. PDCI probing condition.

## Modes of Inter-Area Power Oscillations in the Western Interconnection

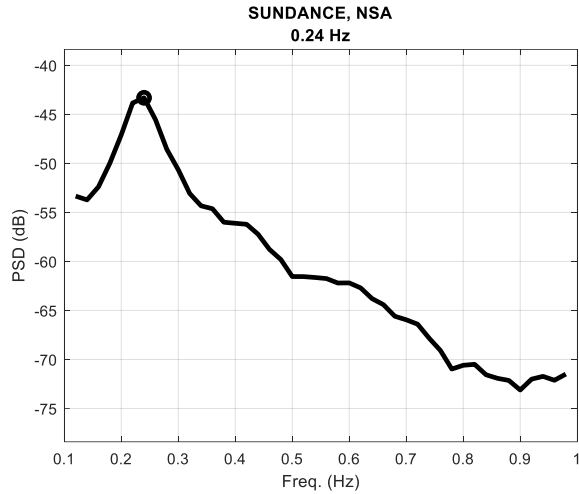
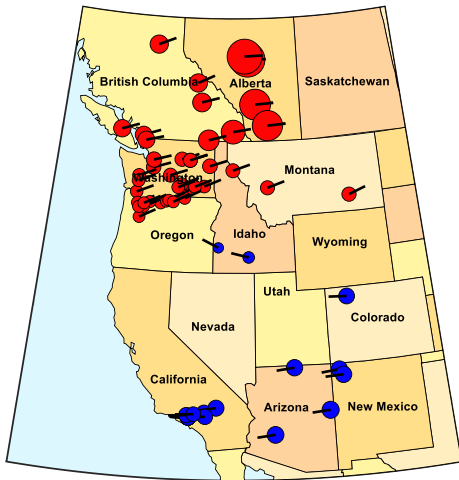


Figure D-3: 2016/09/28 from 17:10:00 to 17:30:00 UTC. Ambient condition.

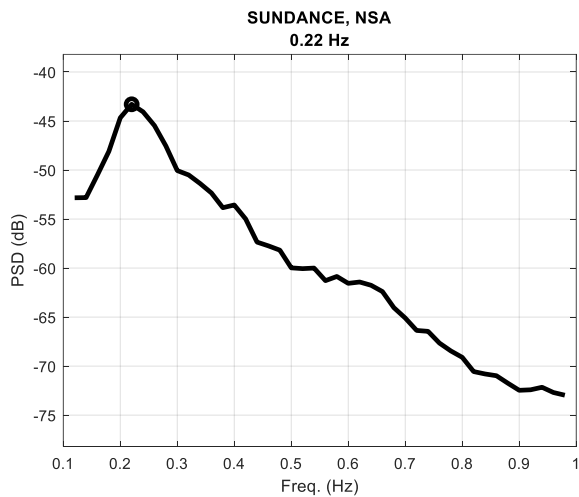
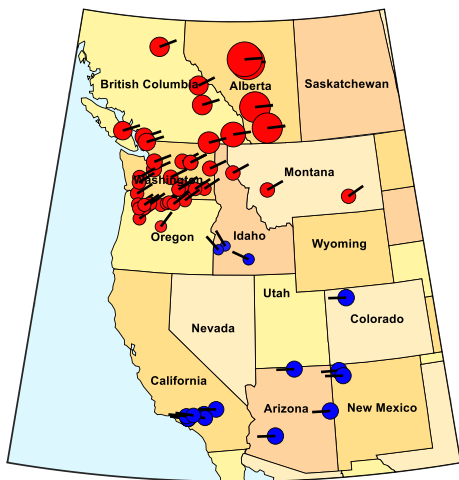


Figure D-4: 2016/09/28 from 18:20:02 to 18:40:02 UTC. PDCI probing condition.

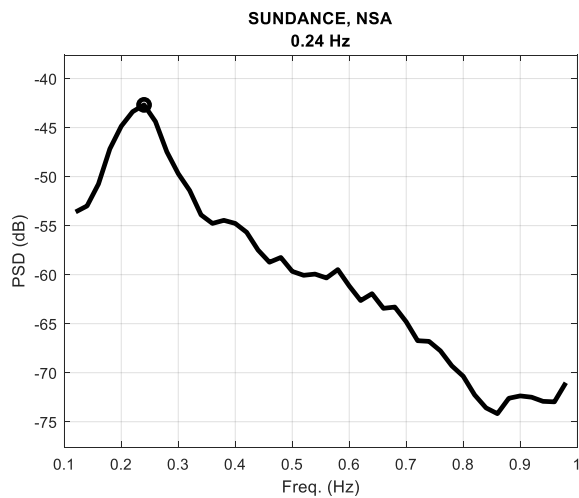
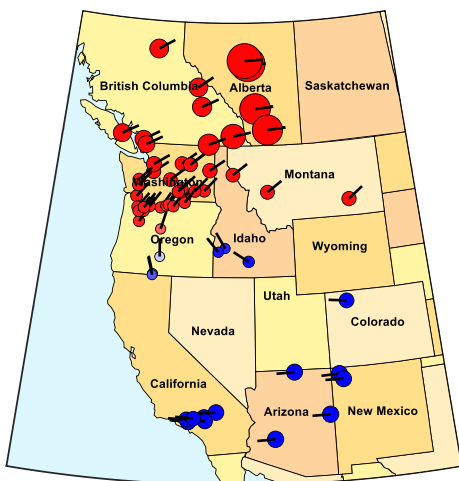


Figure D-5: 2016/09/28 from 18:46:00 to 18:59:00 UTC. Ambient condition.

# Modes of Inter-Area Power Oscillations in the Western Interconnection

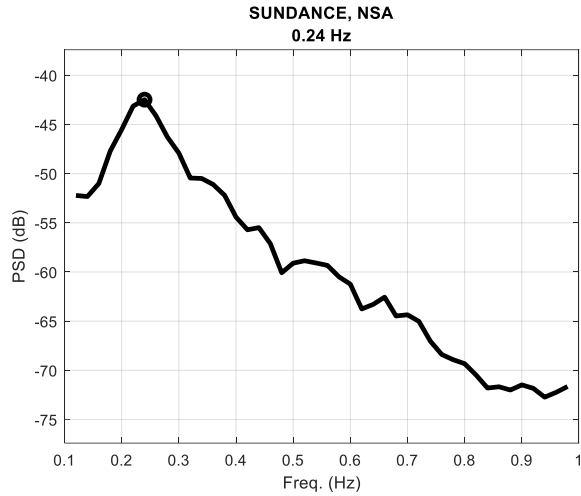
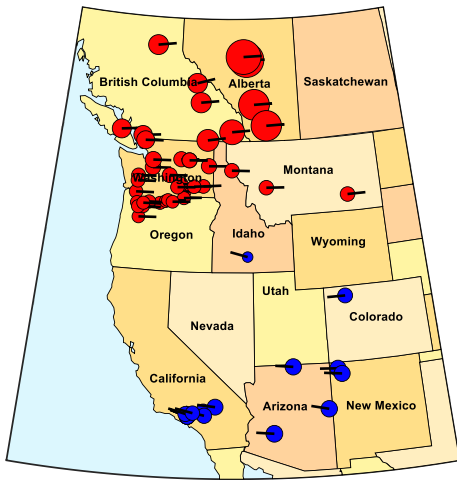


Figure D-6: 2016/09/28 from 20:30:09 to 20:40:09 UTC. PDCI probing condition.

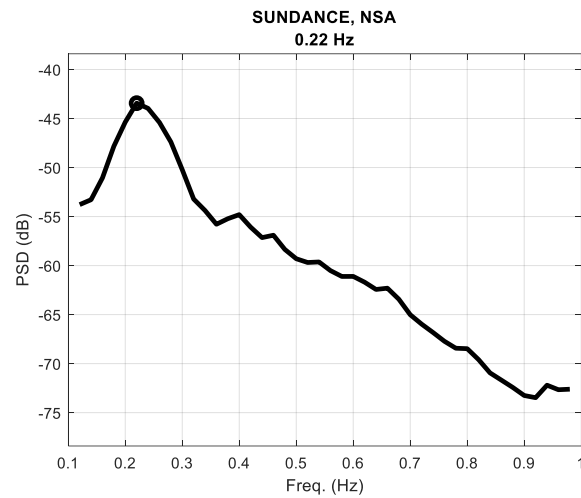
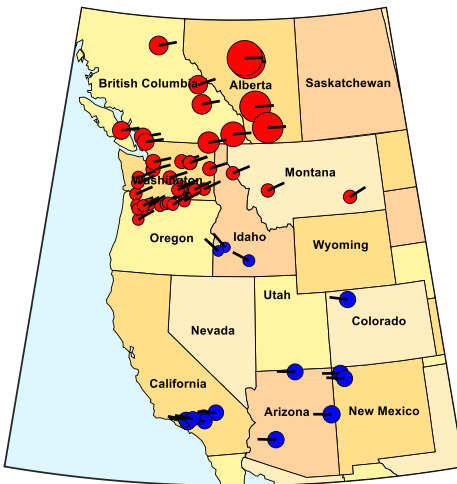


Figure D-7: 2016/09/28 from 21:10:00 to 21:30:00 UTC. Ambient condition.

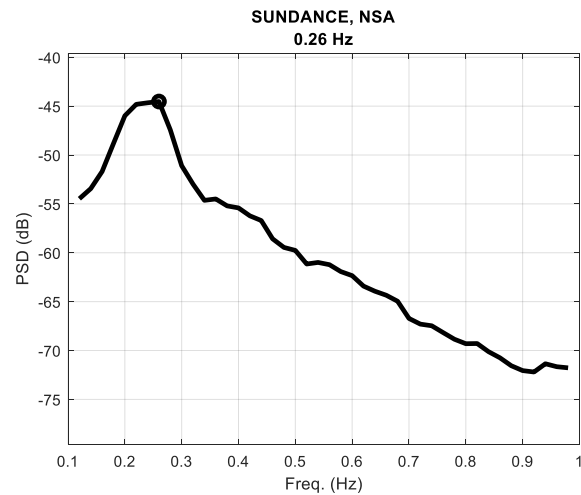
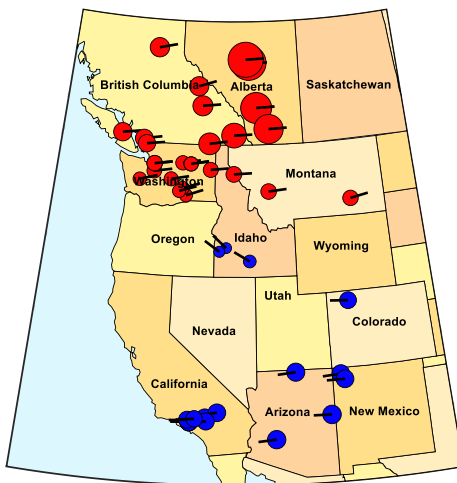


Figure D-8: 2016/09/29 from 15:10:30 to 15:30:00 UTC. Ambient condition.

# Modes of Inter-Area Power Oscillations in the Western Interconnection

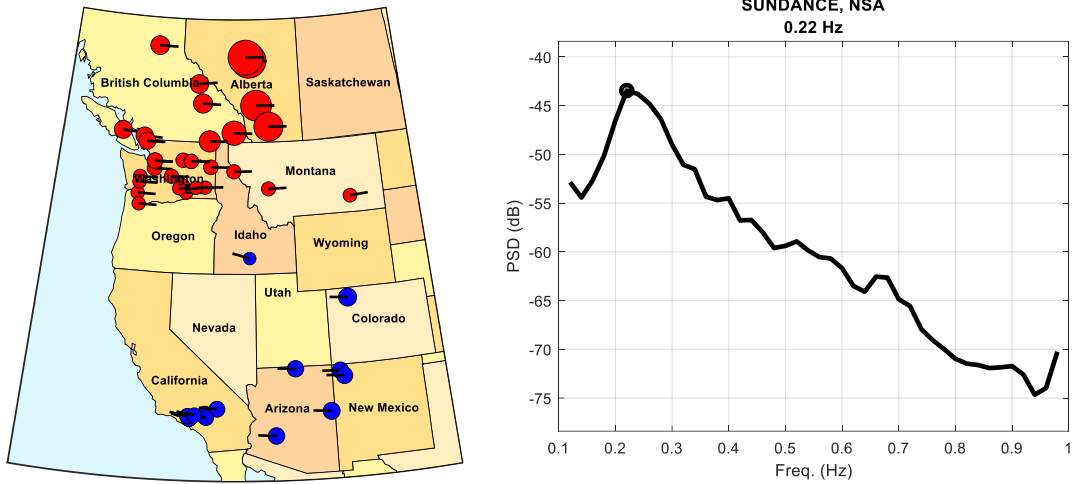


Figure D-9: 2016/09/29 from 16:10:34 to 16:20:34 UTC. PDCI probing condition.

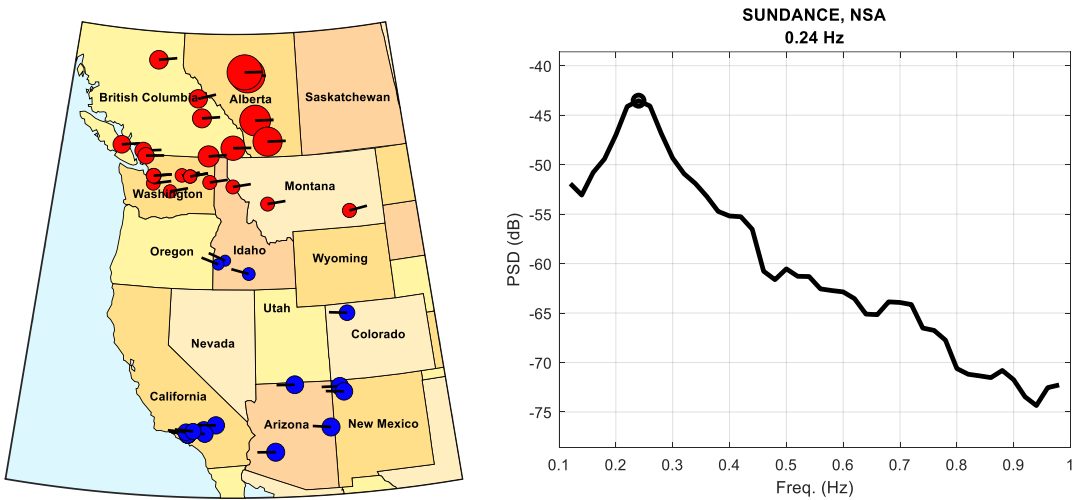


Figure D-10: 2016/09/29 from 17:10:01 to 17:20:01 UTC. PDCI probing condition.

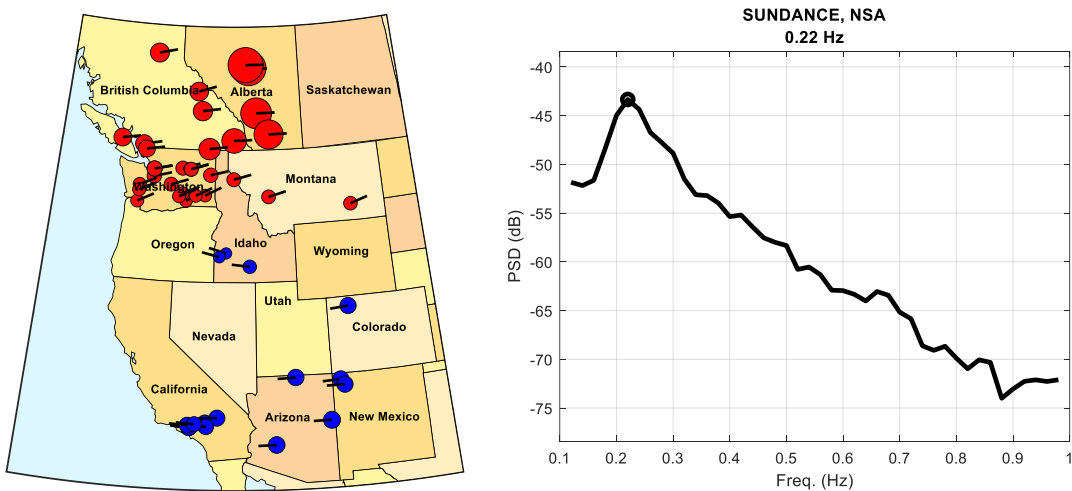


Figure D-11: 2016/09/29 from 18:10:31 to 18:20:31 UTC. PDCI probing condition.

# Modes of Inter-Area Power Oscillations in the Western Interconnection

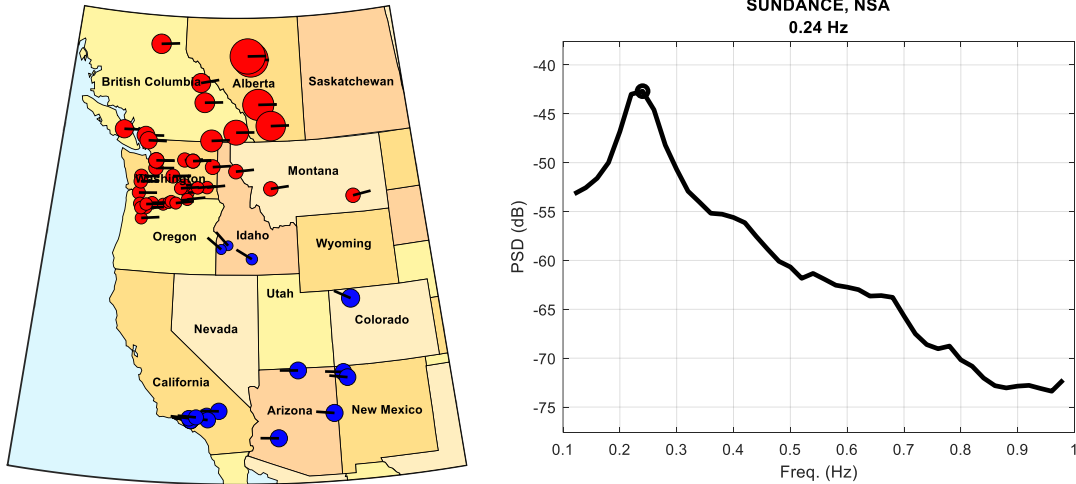


Figure D-12: 2016/09/29 from 19:10:00 to 19:30:00 UTC. Ambient condition.

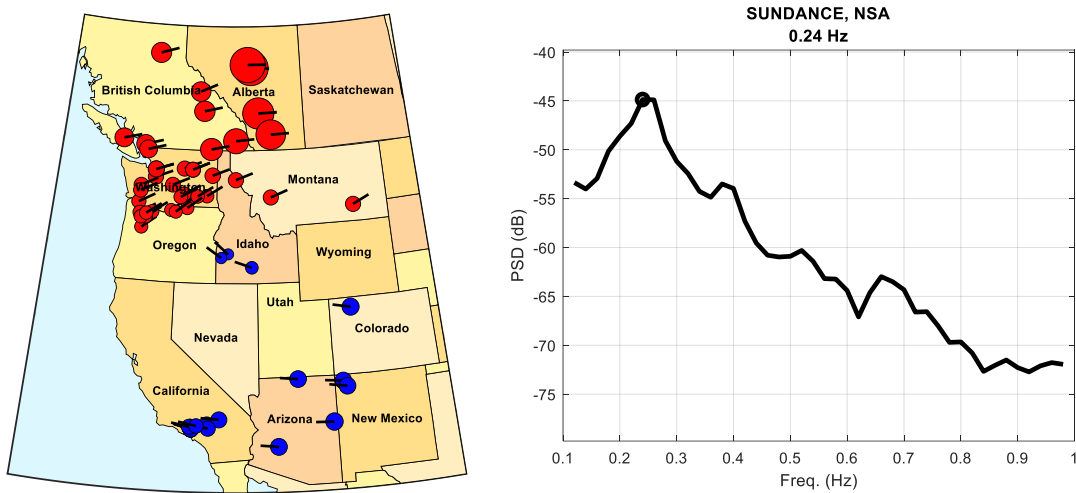


Figure D-13: 2016/09/29 from 20:10:31 to 20:20:31 UTC. PDCI probing condition.

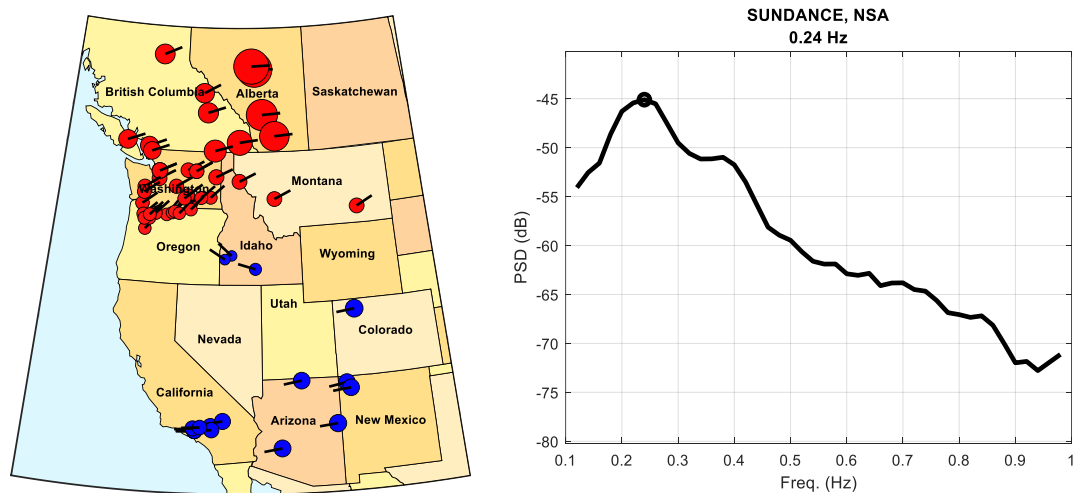


Figure D-14: 2016/09/29 from 21:10:00 to 21:30:00 UTC. Ambient condition.



# Modes of Inter-Area Power Oscillations in the Western Interconnection

2017 Data

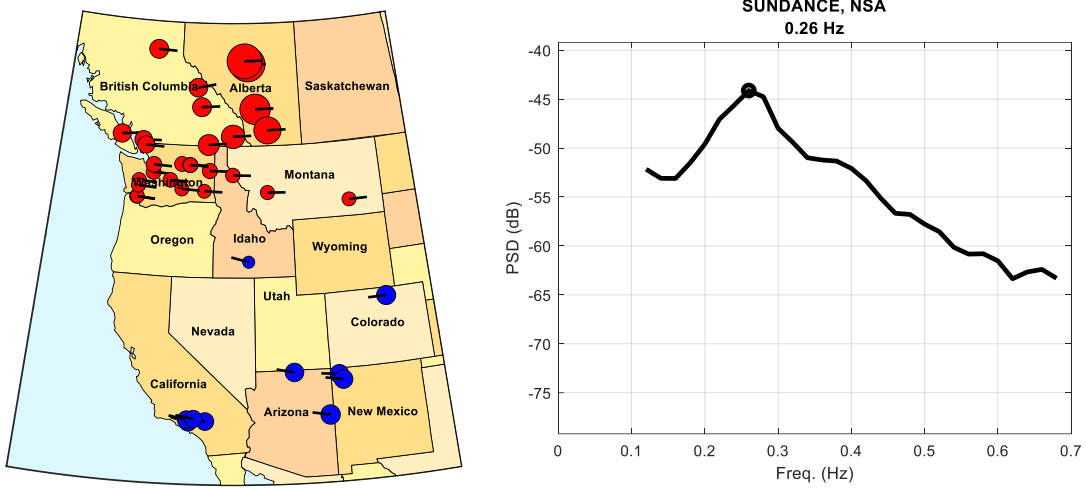


Figure D-15: 2017/05/16 from 16:16:01 to 16:36:01 UTC. PDCI probing condition.

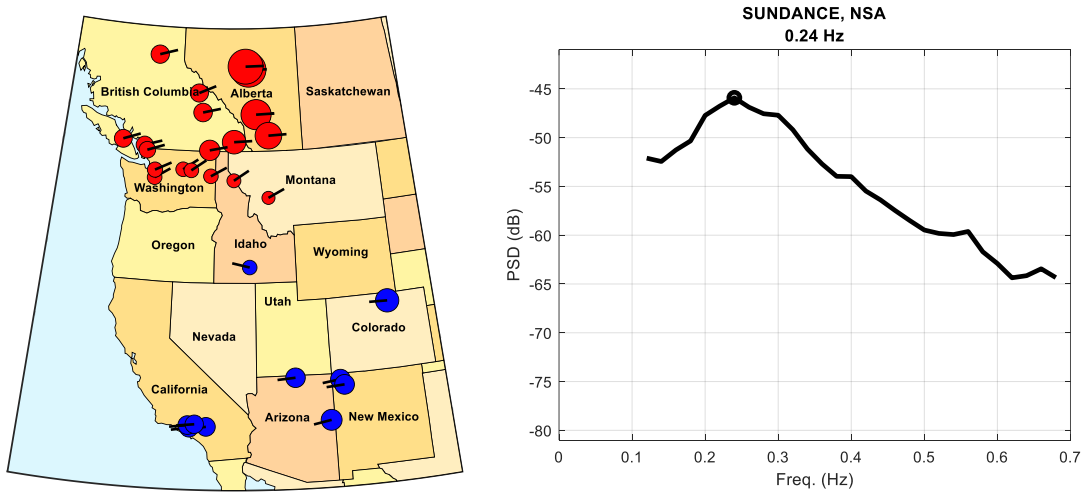


Figure D-16: 2017/05/16 from 16:36:05 to 16:50:00 UTC. Ambient condition.

# Modes of Inter-Area Power Oscillations in the Western Interconnection

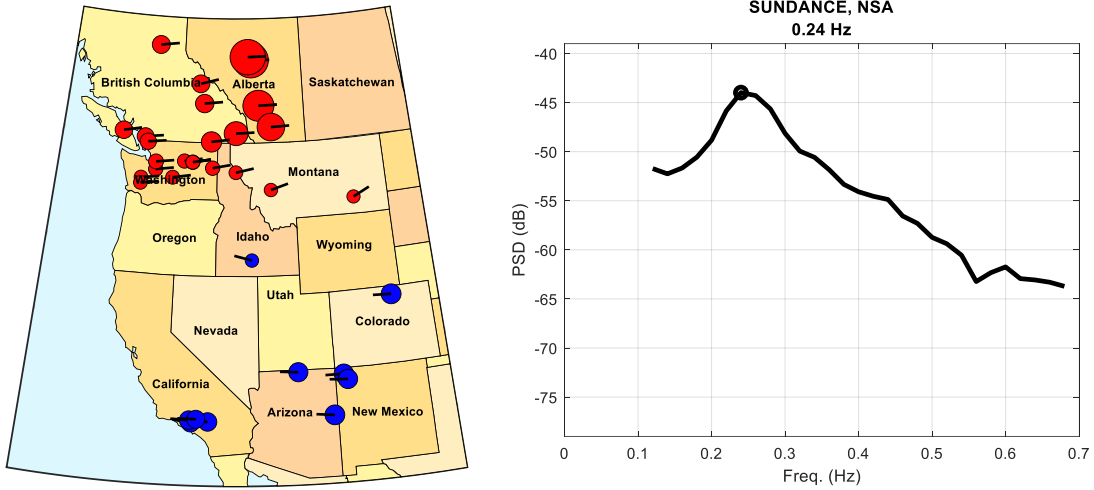


Figure D-17: 2017/05/16 from 20:15:01 to 20:35:01 UTC. PDCI probing condition.

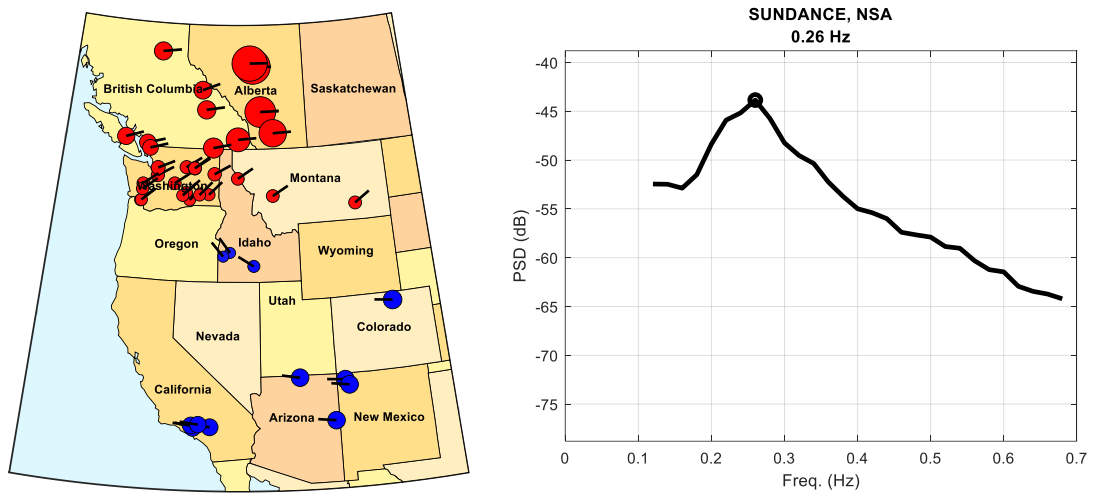


Figure D-18: 2017/05/16 from 20:35:05 to 20:50:00 UTC. Ambient condition.

# Modes of Inter-Area Power Oscillations in the Western Interconnection

2018 Data

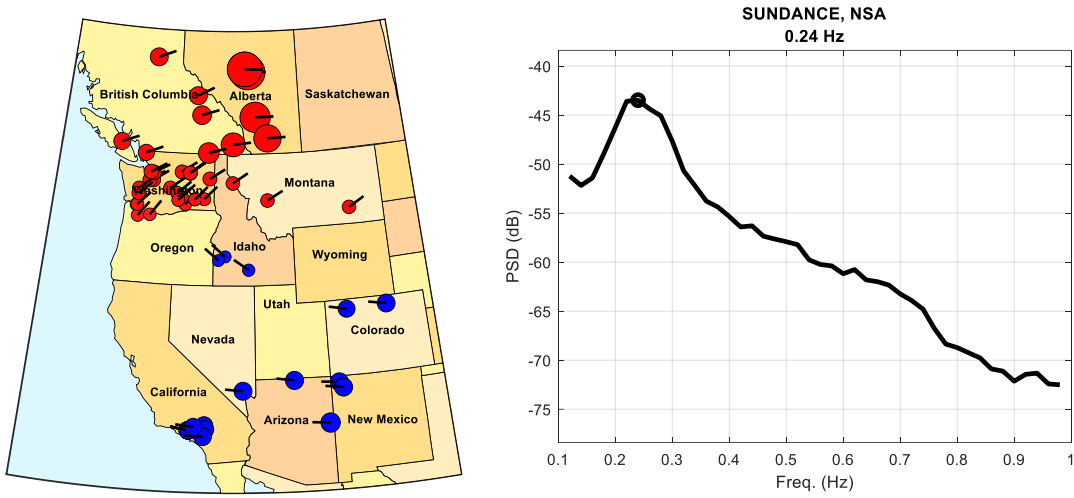


Figure D-19: 2018/05/23 from 16:05:00 to 16:24:30 UTC. Ambient condition.

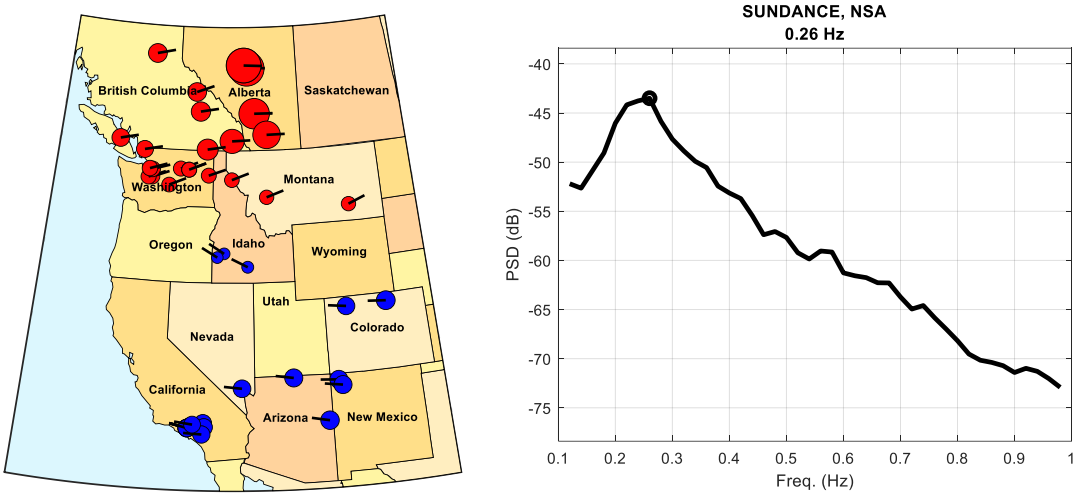


Figure D-20: 2018/05/23 from 16:28:00 to 16:48:00 UTC. PDCI probing condition.

## Modes of Inter-Area Power Oscillations in the Western Interconnection

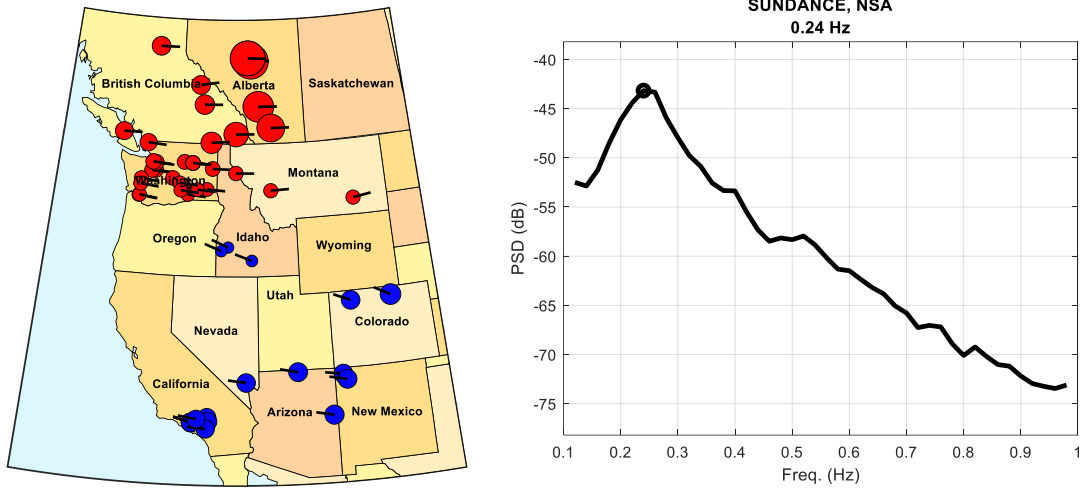


Figure D-21: 2018/05/23 from 20:15:00 to 20:35:00 UTC. PDCI probing condition.

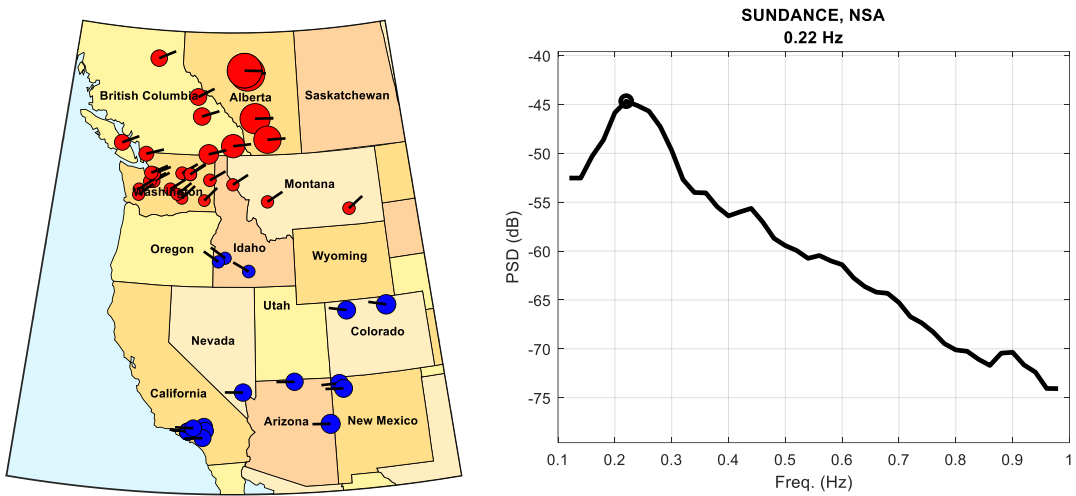


Figure D-22: 2018/05/23 from 20:36:00 to 20:55:00 UTC. Ambient condition.

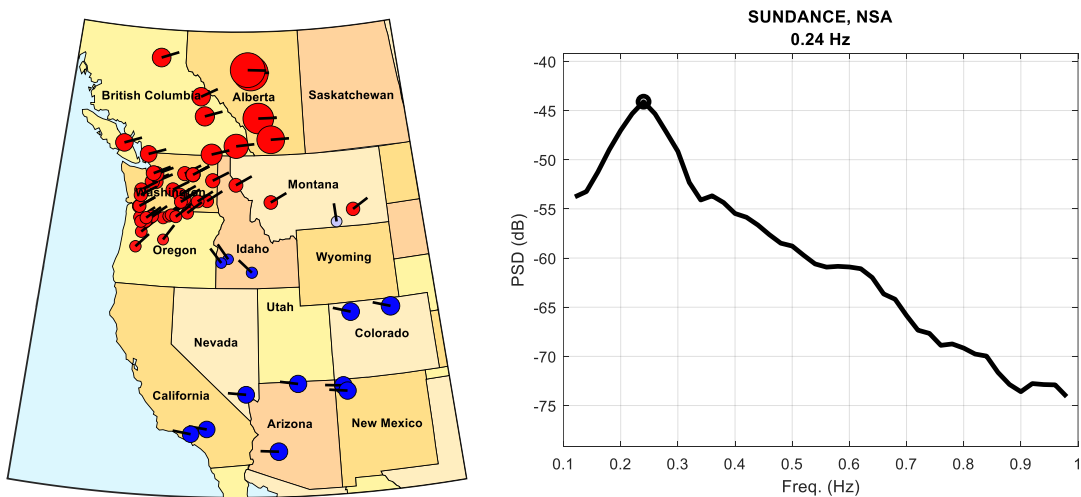


Figure D-23: 2018/05/24 from 00:10:00 to 00:30:00 UTC. Ambient condition.

# Modes of Inter-Area Power Oscillations in the Western Interconnection

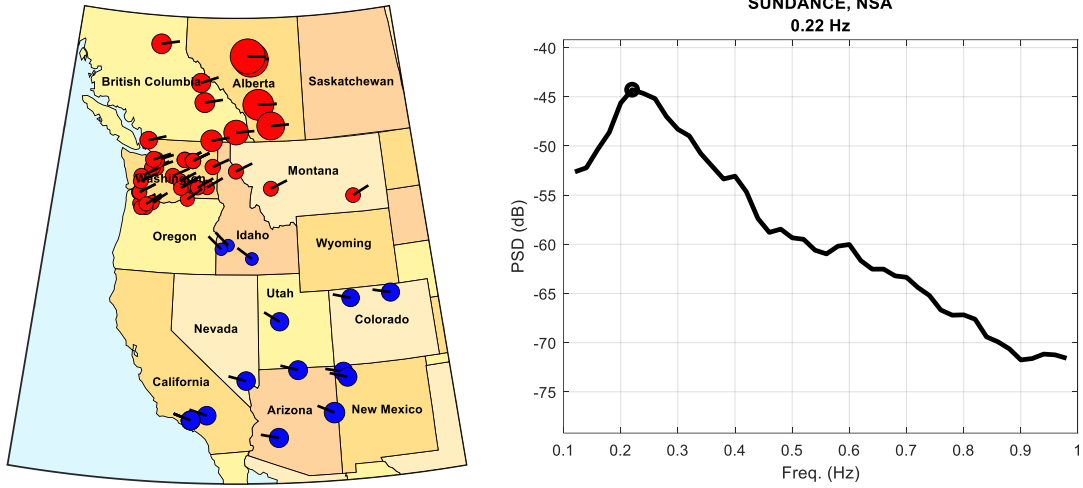


Figure D-24: 2018/05/24 from 17:14:05 to 17:34:00 UTC. PDCI probing condition.

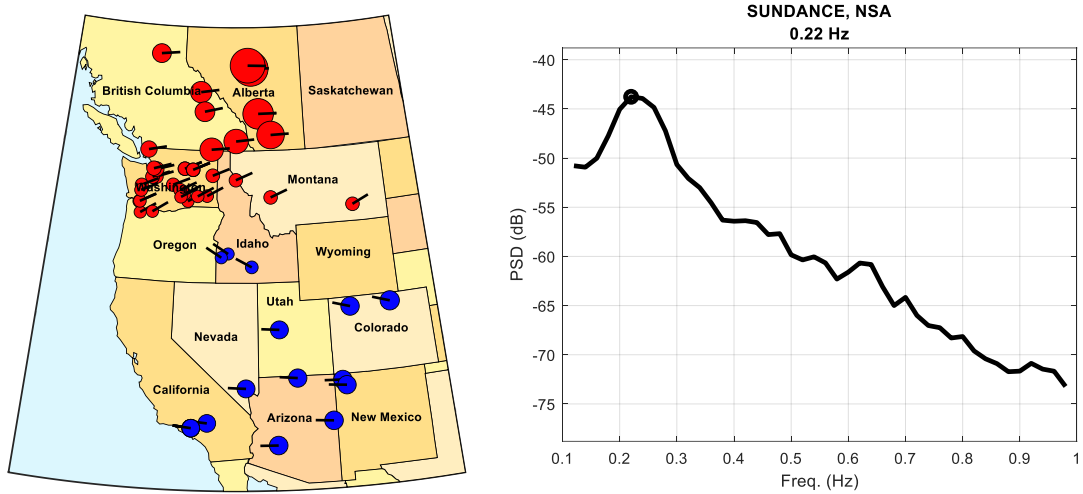


Figure D-25: 2018/05/24 from 17:36:00 to 17:50:00 UTC. Ambient condition.

# Modes of Inter-Area Power Oscillations in the Western Interconnection

2019 Data

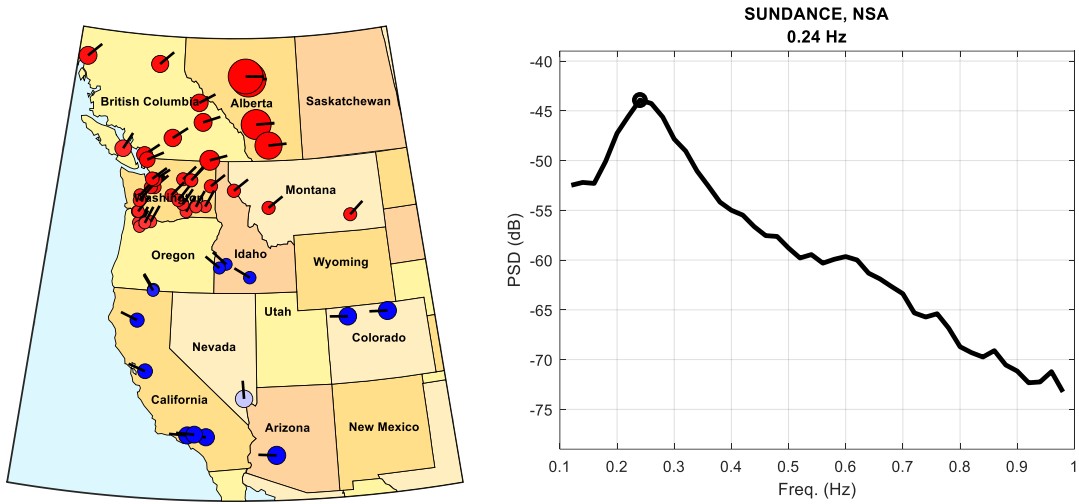


Figure D-26: 2019/05/07 from 14:10:00 to 14:30:00 UTC. Ambient condition.

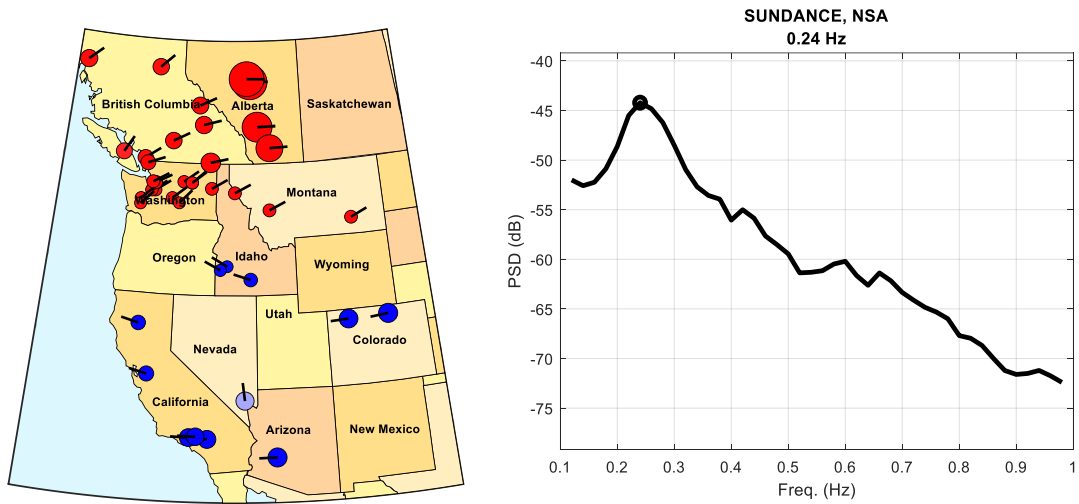


Figure D-27: 2019/05/07 from 17:10:00 to 17:30:00 UTC. Ambient condition.

# Modes of Inter-Area Power Oscillations in the Western Interconnection

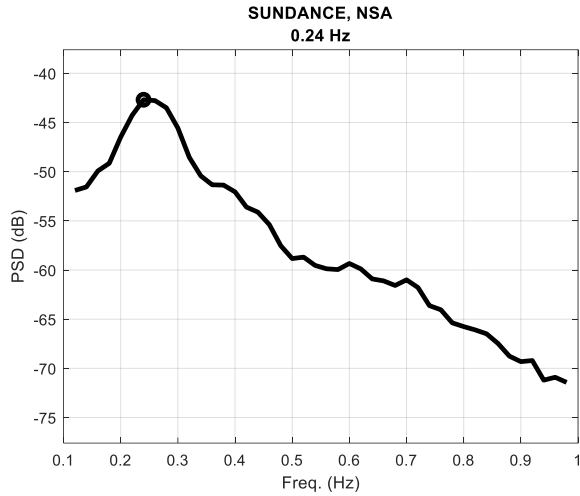
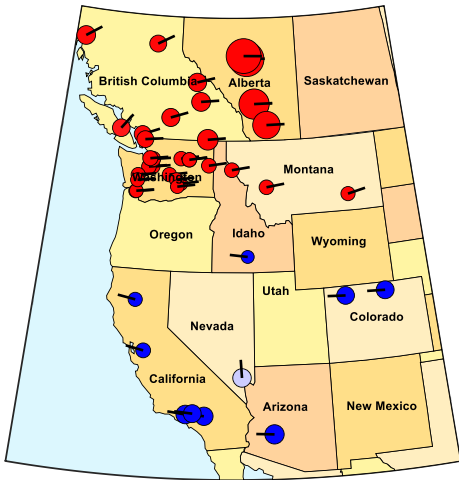


Figure D-28: 2019/05/07 from 17:30:03 to 17:50:03 UTC. PDCI probing condition.

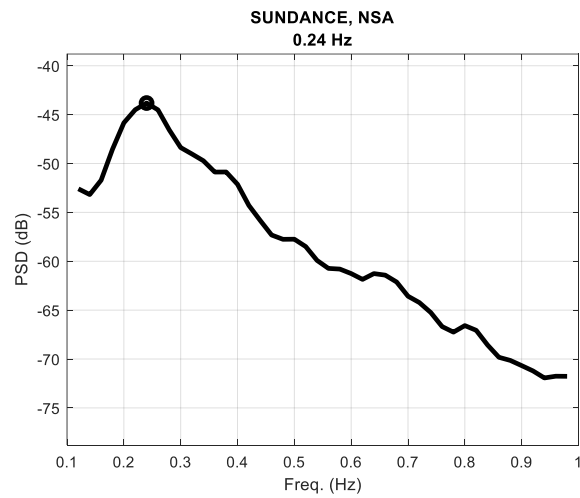
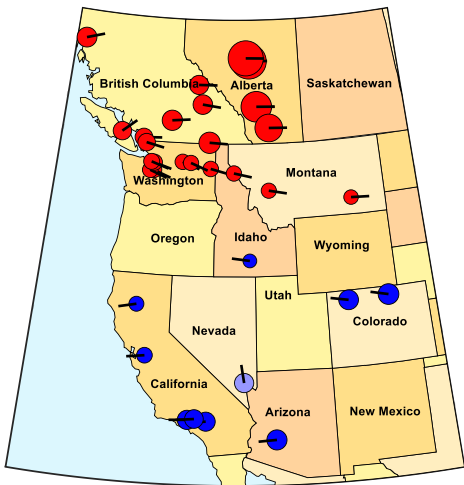


Figure D-29: 2019/05/07 from 21:20:03 to 21:40:03 UTC. PDCI probing condition.

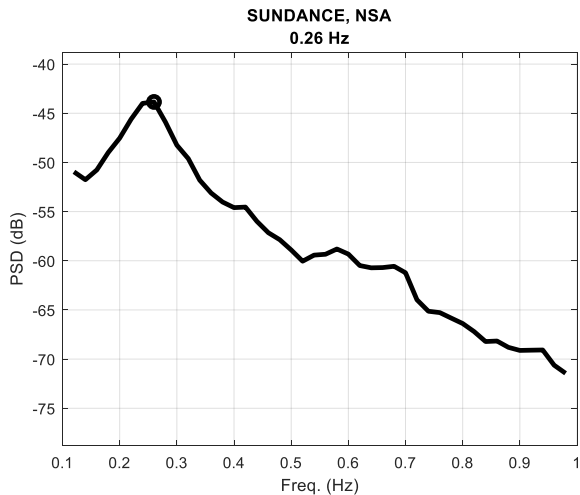
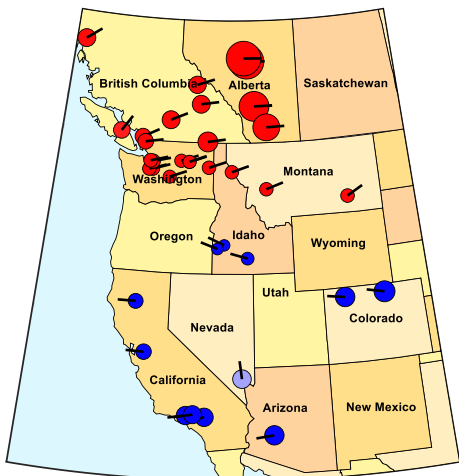


Figure D-30: 2019/05/07 from 22:10:00 to 22:30:00 UTC. Ambient condition.

# Modes of Inter-Area Power Oscillations in the Western Interconnection

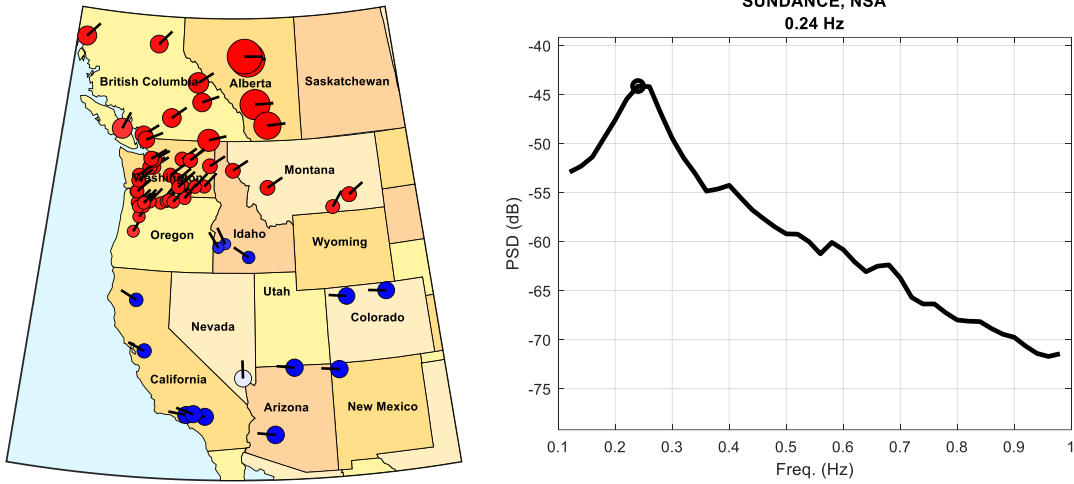


Figure D-31: 2019/05/08 from 02:10:00 to 02:30:00 UTC. Ambient condition.

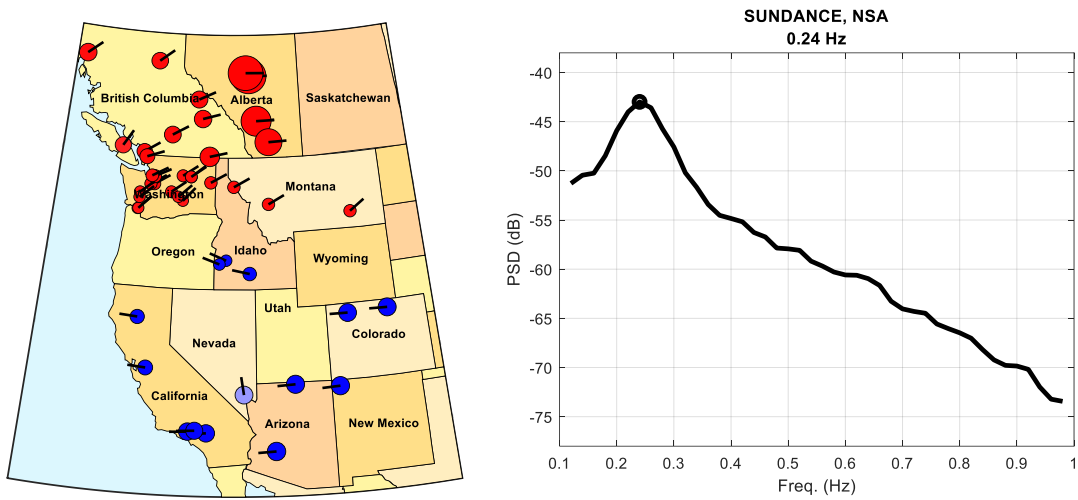


Figure D-32: 2019/05/08 from 06:10:00 to 06:30:00 UTC. Ambient condition.

## Mode Meter Analysis Results

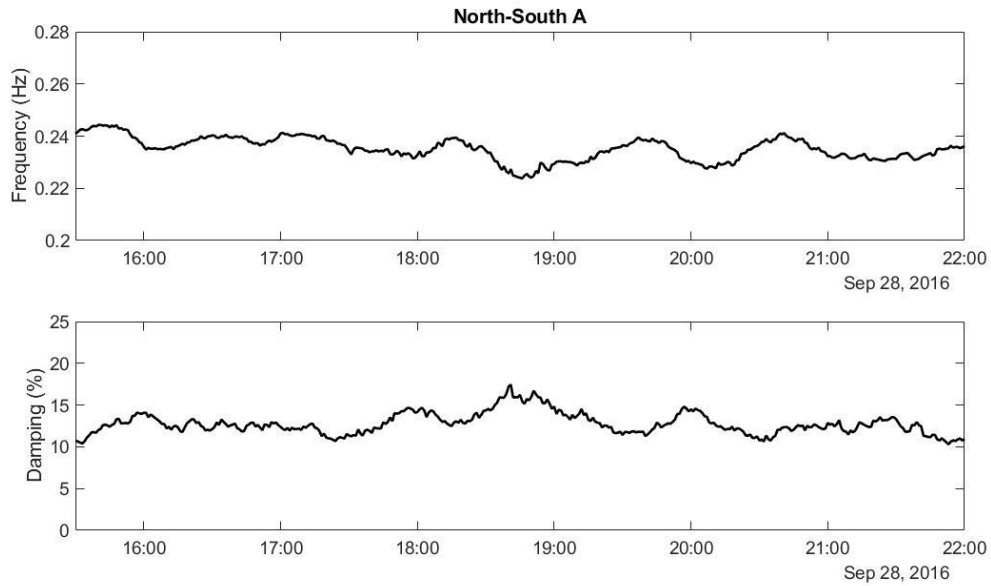


Figure D-33: 2016/09/28 dataset.

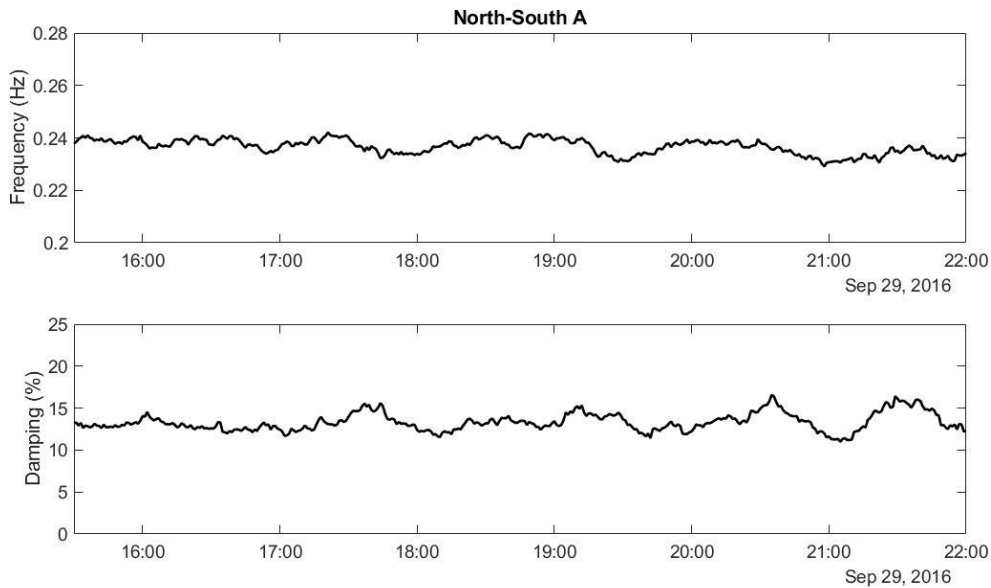


Figure D-34: 2016/09/29 dataset.

## Modes of Inter-Area Power Oscillations in the Western Interconnection

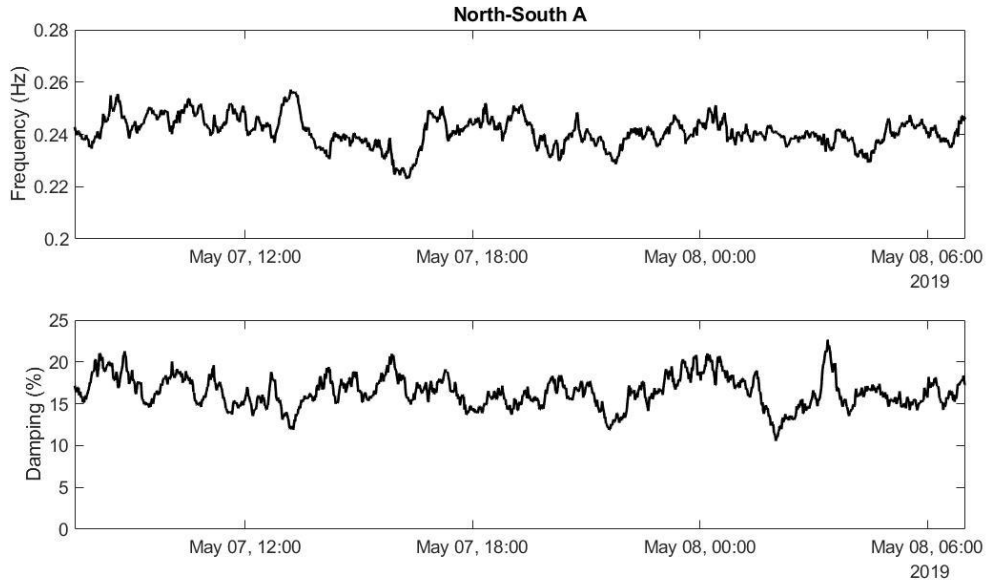


Figure D-35: 2019/05/08 dataset.

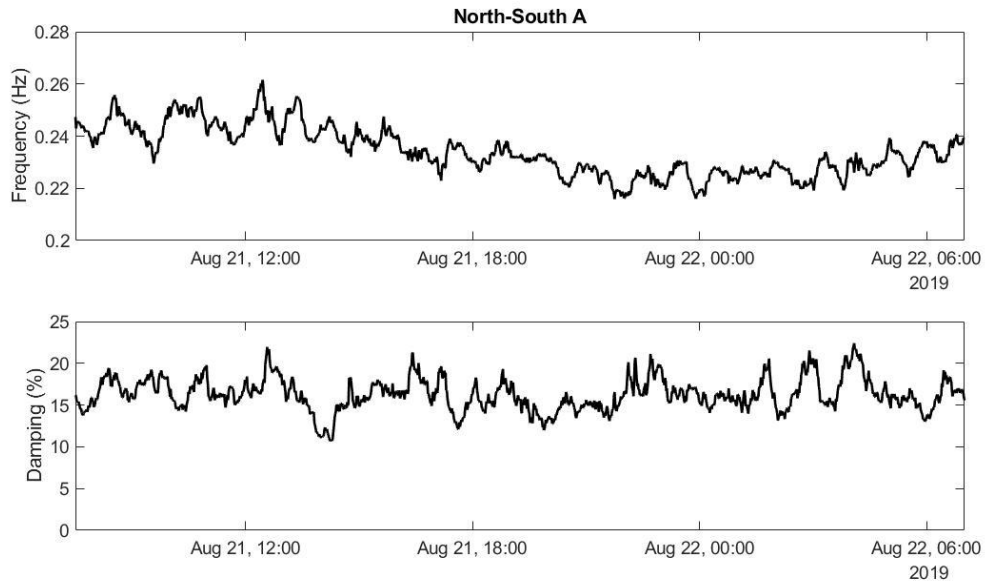


Figure D-36: 2019/08/22 dataset.

Ringdown Analysis Results

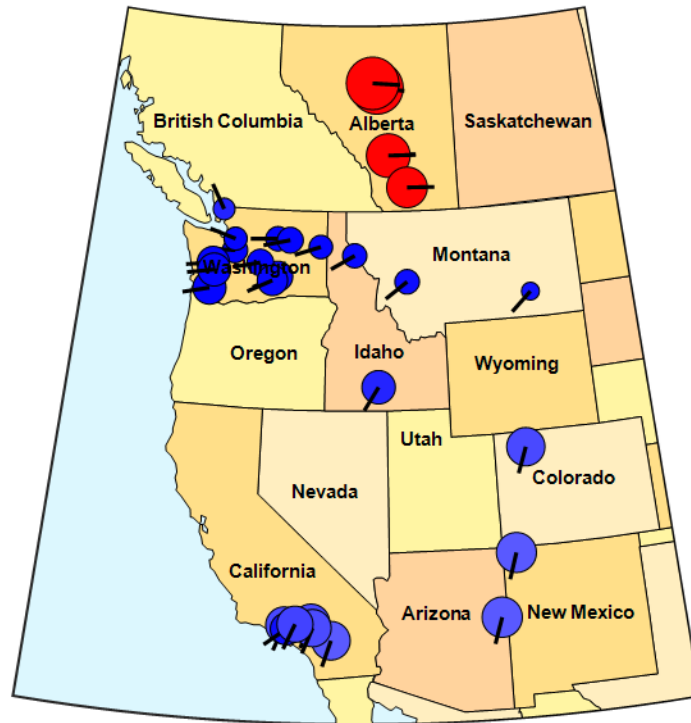


Figure D-37: 2016/09/29 at 17:34 UTC. Estimated at 0.24 Hz, 12.6% damping.

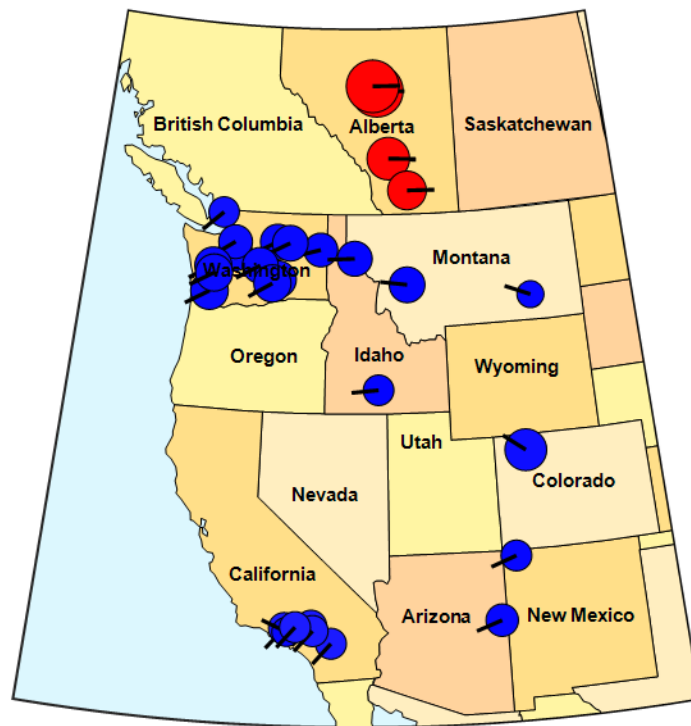


Figure D-38: 2016/09/29 at 20:40 UTC. Estimated at 0.24 Hz, 13.8% damping.

## Modes of Inter-Area Power Oscillations in the Western Interconnection

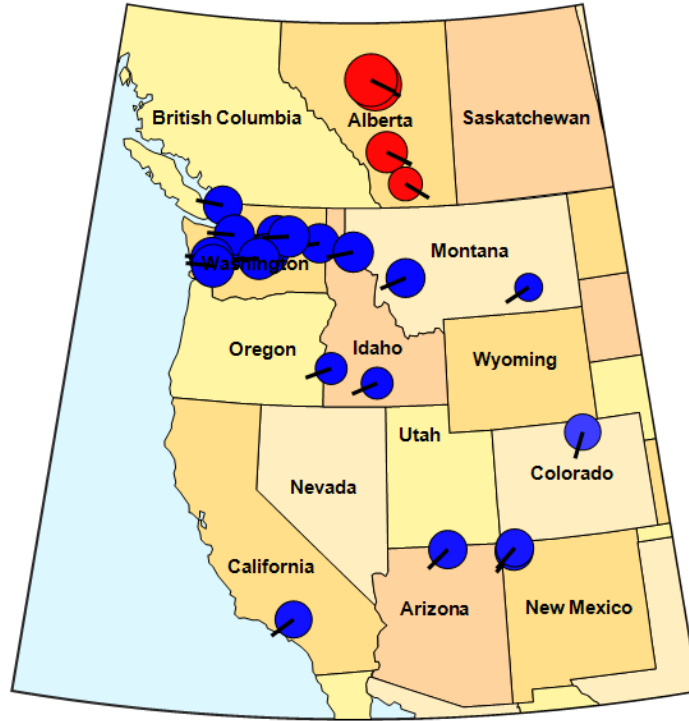


Figure D-39: 2017/05/16 at 17:25 UTC. Estimated at 0.29 Hz, 15.9% damping.

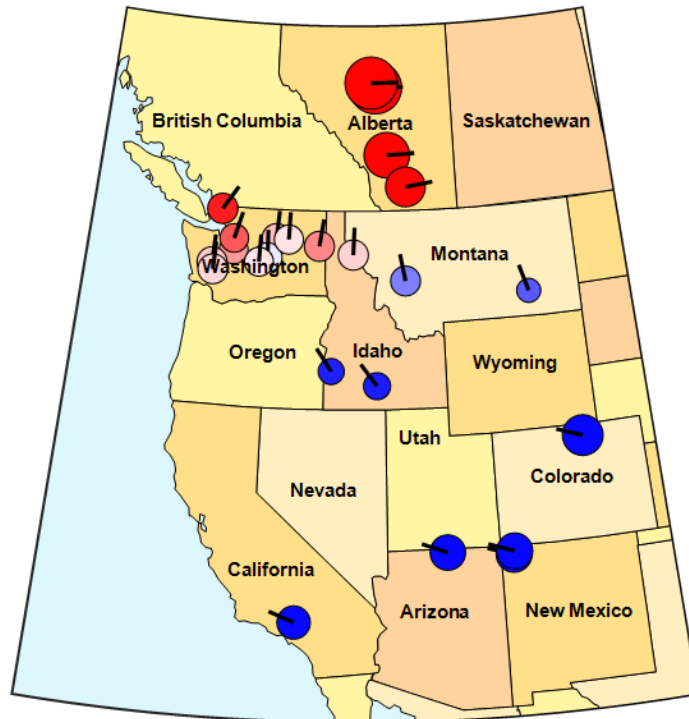


Figure D-40: 2017/05/16 at 17:35 UTC. Estimated at 0.24 Hz, 13.6% damping.

## Modes of Inter-Area Power Oscillations in the Western Interconnection

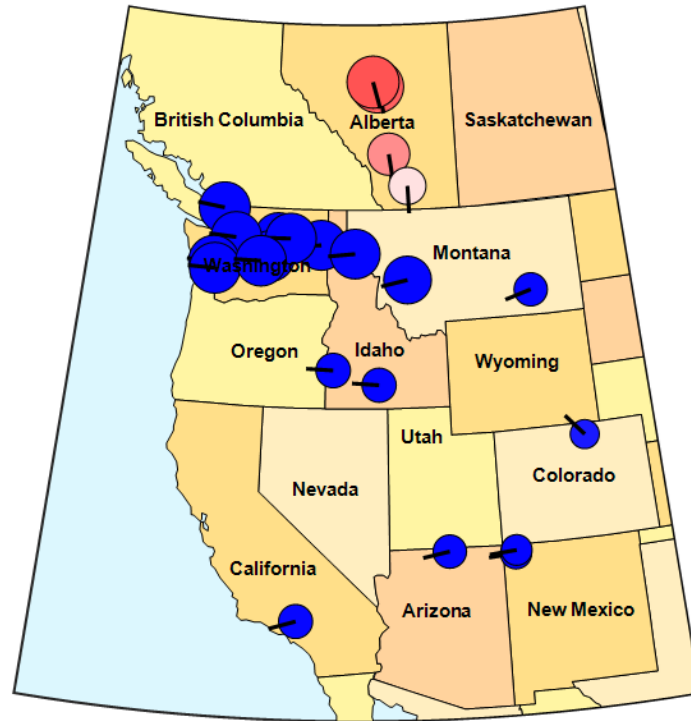


Figure D-41: 2017/05/16 at 18:25 UTC. Estimated at 0.24 Hz, 14.5% damping.

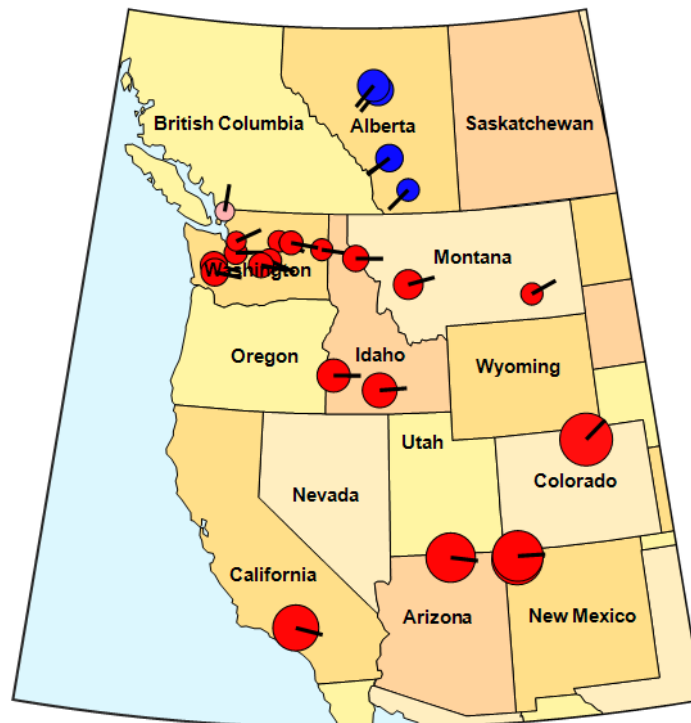


Figure D-42: 2017/05/16 at 18:35 UTC. Estimated at 0.21 Hz, 18.2% damping.

## Appendix E: NSB Mode Analyses

### Correlation Analysis from 2016 through 2019 PMU Data

The following are the mode shape estimates for all the conditions in Table 15 from the section titled, "North-South B Mode." The mode shape is shown on the left and the mode reference signal PSD is shown on the right.

#### 2016 Data

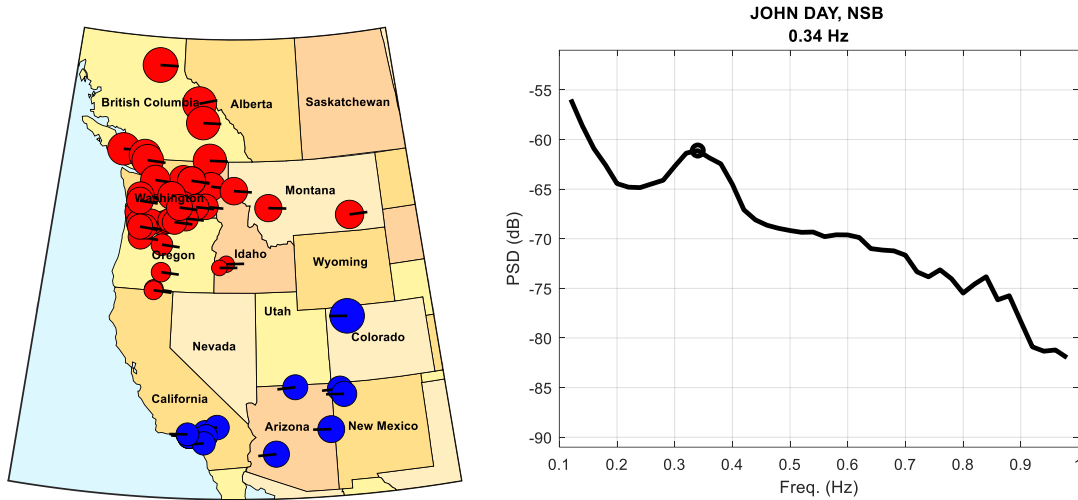


Figure E-1: 2016/09/13 from 17:10:02 to 17:30:00 UTC. Alberta disconnected, PDCI probing condition.

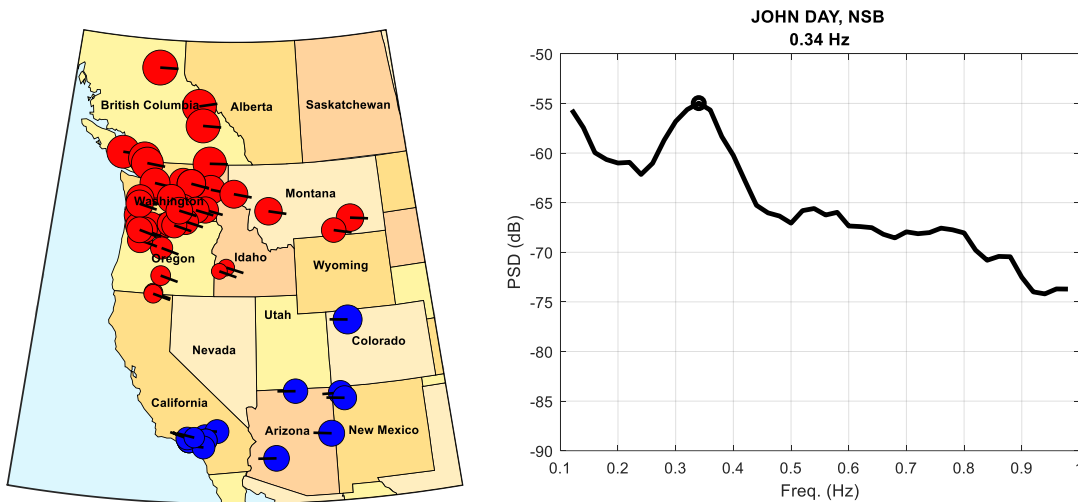


Figure E-2: 2016/09/13 from 18:30:01 to 18:50:01 UTC. Alberta disconnected, ambient condition.

## Modes of Inter-Area Power Oscillations in the Western Interconnection

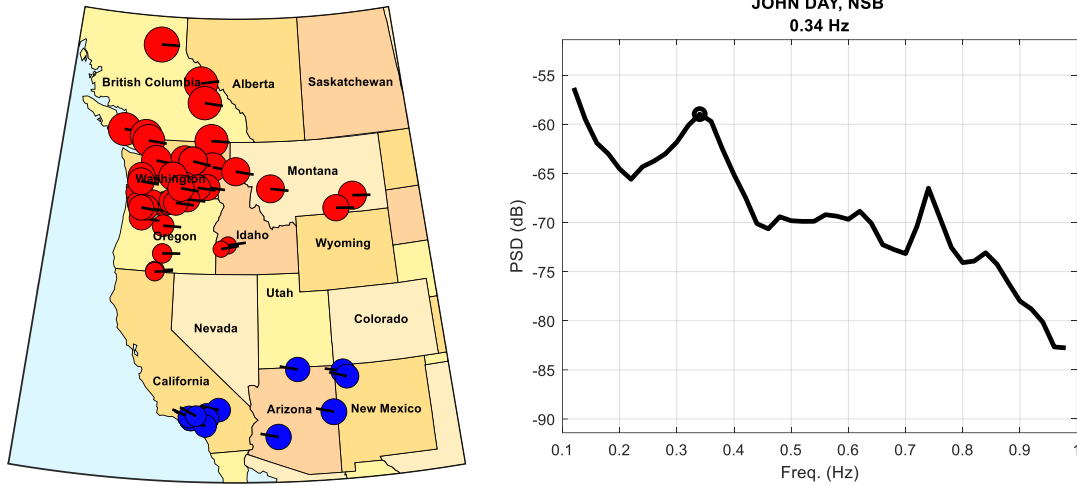


Figure E-3: 2016/09/13 from 22:10:00 to 22:28:00 UTC. Alberta disconnected, ambient condition.

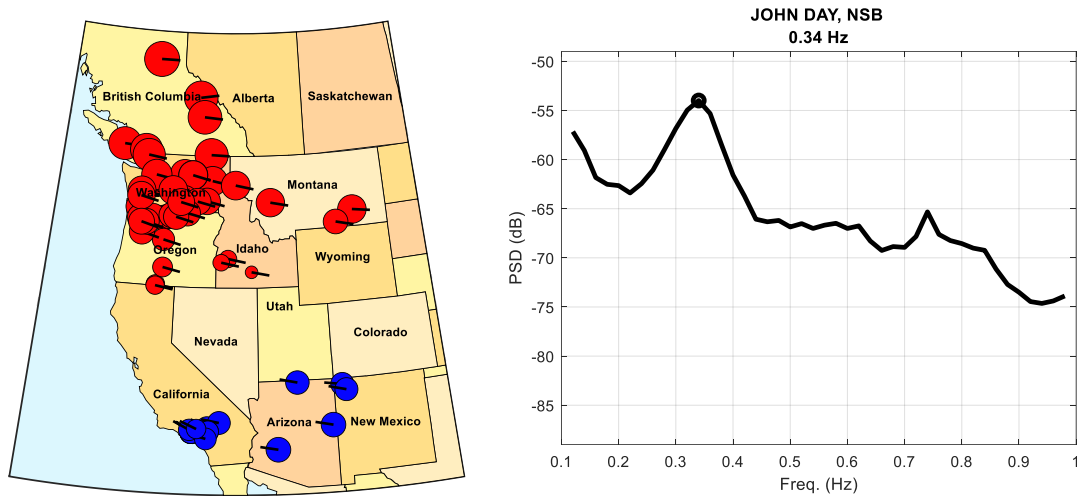


Figure E-4: 2016/09/13 from 22:28:10 to 22:48:10 UTC. Alberta disconnected, PDCI probing condition.

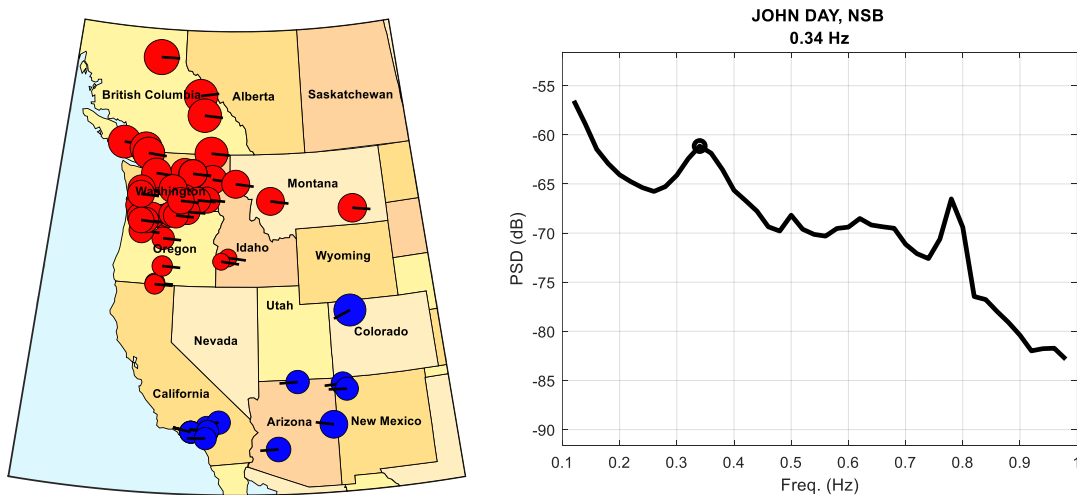


Figure E-5: 2016/09/13 from 23:10:00 to 23:30:00 UTC. Alberta disconnected, ambient condition.

# Modes of Inter-Area Power Oscillations in the Western Interconnection

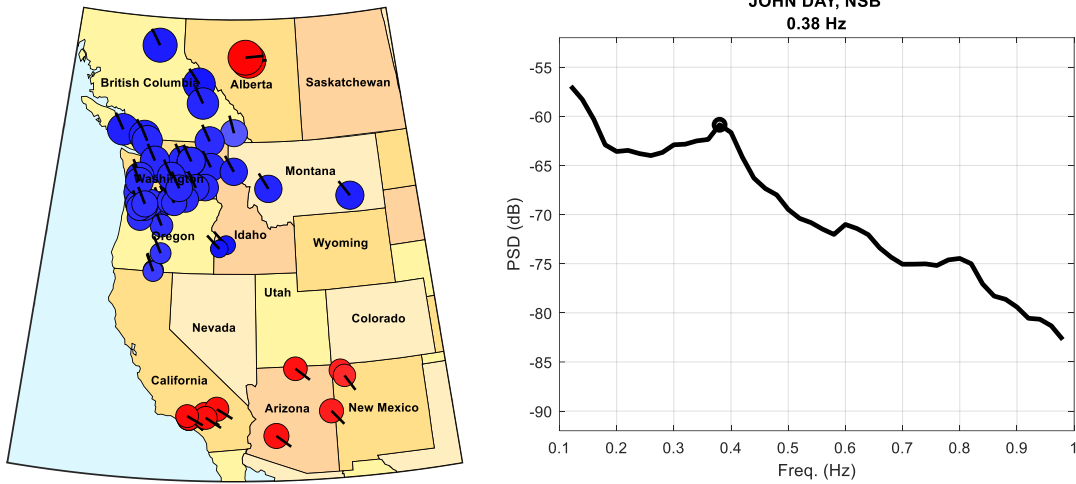


Figure E-6: 2016/09/28 from 15:10:00 to 15:30:00 UTC. Ambient condition.

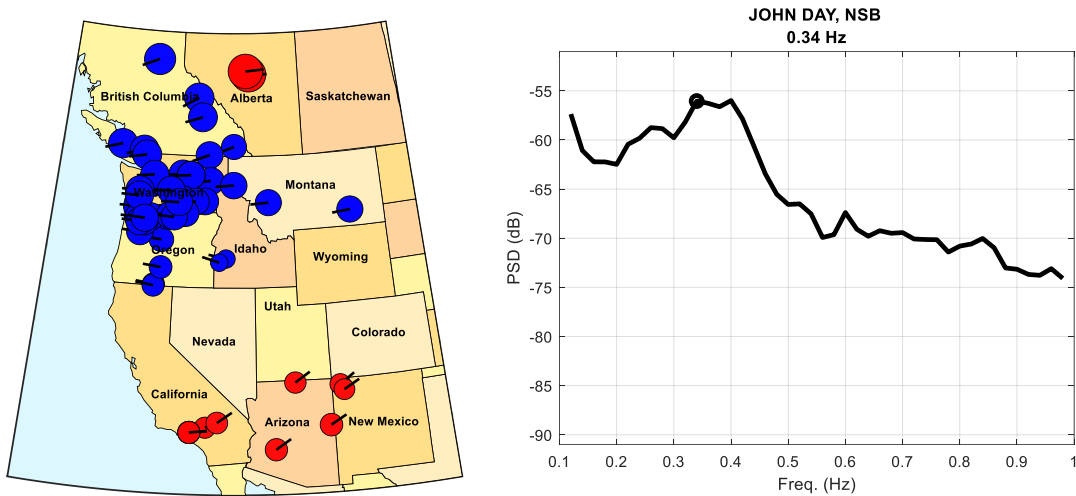


Figure E-7: 2016/09/28 from 16:30:12 to 16:40:12 UTC. PDCI probing condition.

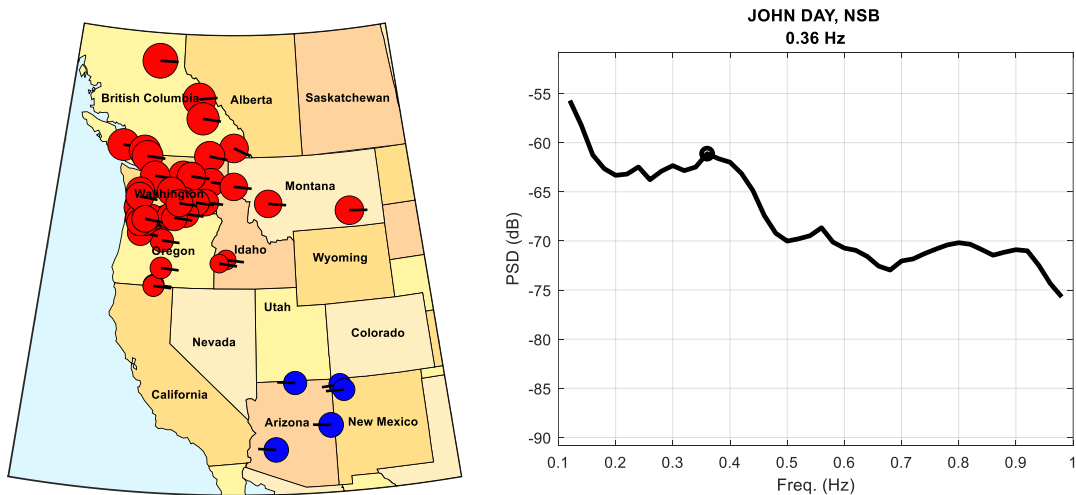


Figure E-8: 2016/09/28 from 17:10:00 to 17:30:00 UTC. Ambient condition.



# Modes of Inter-Area Power Oscillations in the Western Interconnection

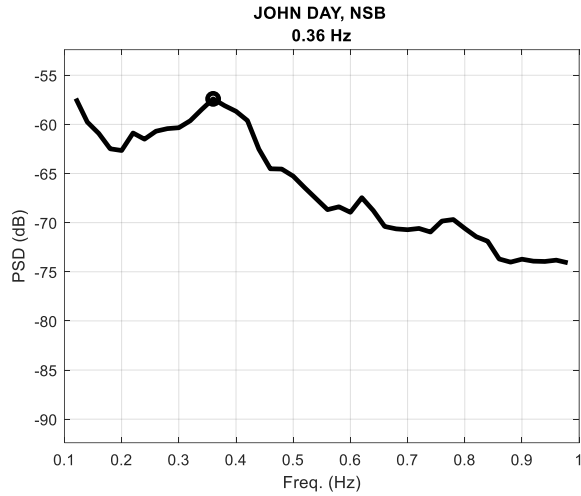
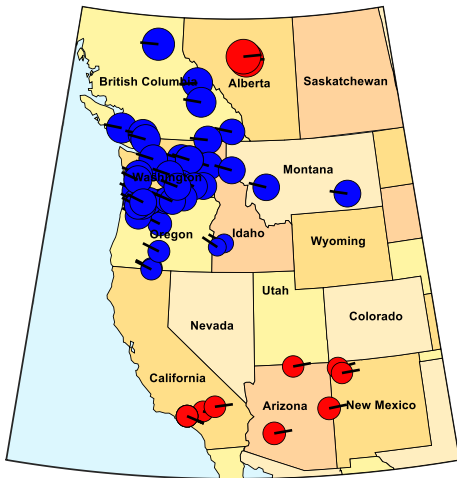


Figure E-9: 2016/09/28 from 18:20:02 to 18:40:02 UTC. PDCI probing condition.

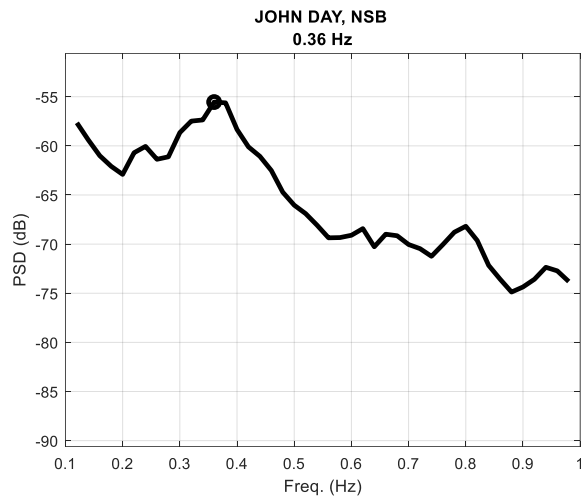
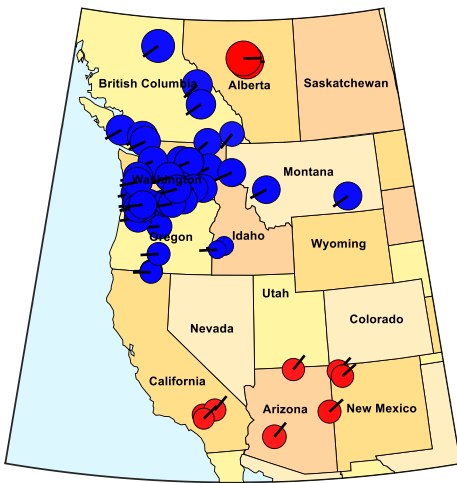


Figure E-10: 2016/09/28 from 20:30:09 to 20:40:09 UTC. PDCI probing condition.

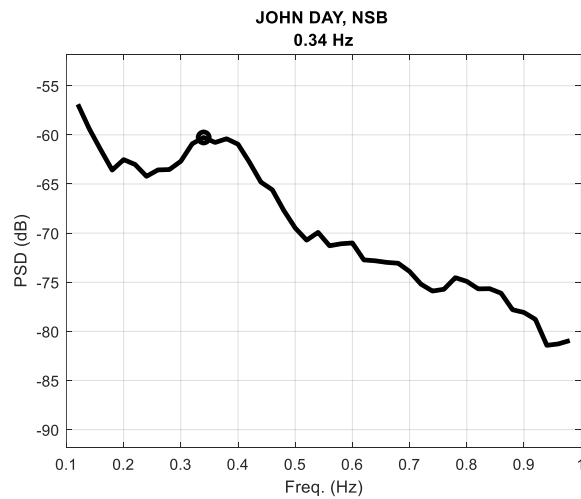
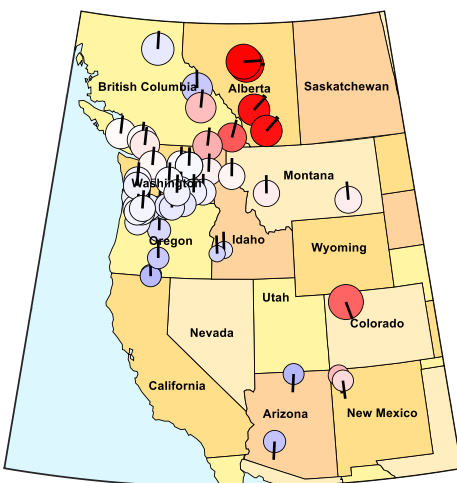


Figure E-11: 2016/09/28 from 21:10:00 to 21:30:00 UTC. Ambient condition.



## Modes of Inter-Area Power Oscillations in the Western Interconnection

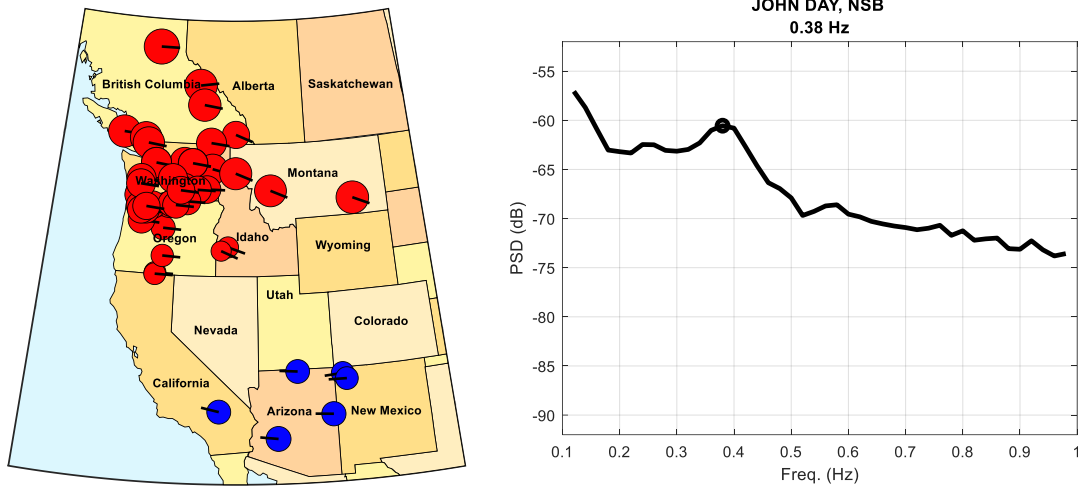


Figure E-12: 2016/09/29 from 15:10:30 to 15:30:00 UTC. Ambient condition.

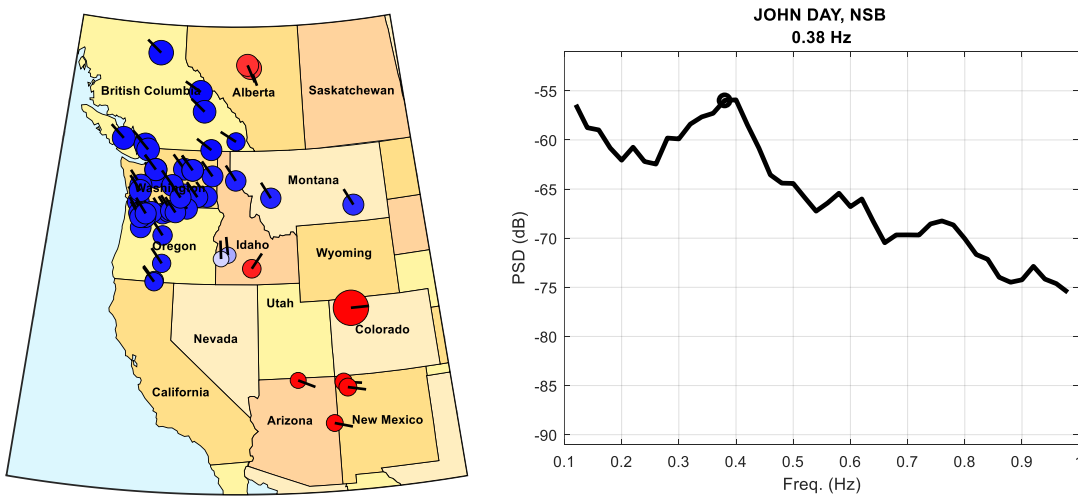


Figure E-13: 2016/09/29 from 16:10:34 to 16:20:34 UTC. PDCI probing condition.

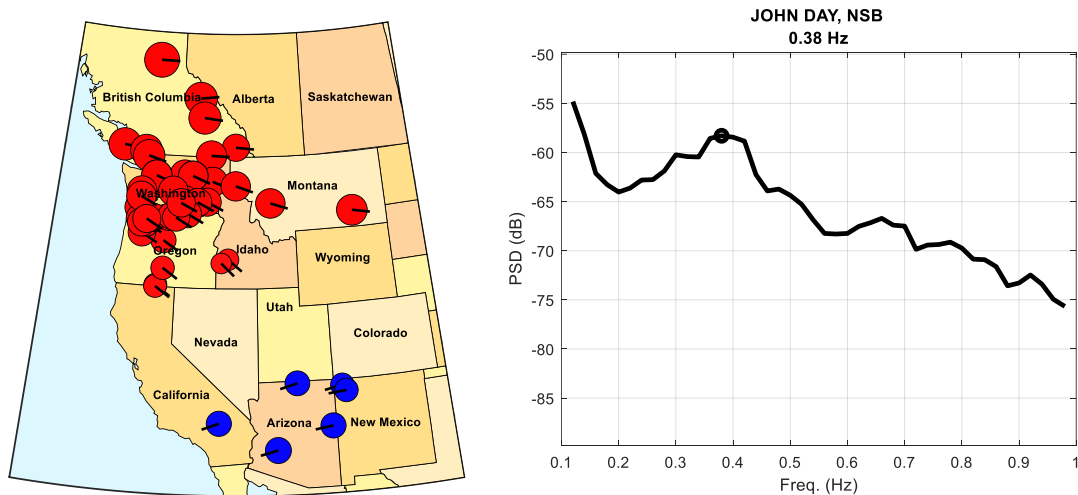


Figure E-14: 2016/09/29 from 17:10:01 to 17:20:01 UTC. PDCI probing condition.

## Modes of Inter-Area Power Oscillations in the Western Interconnection

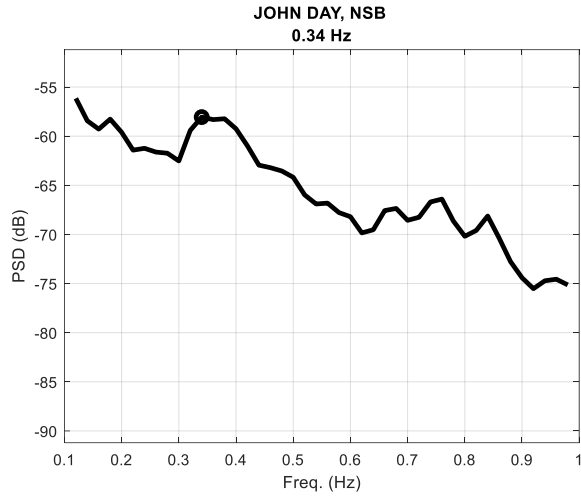
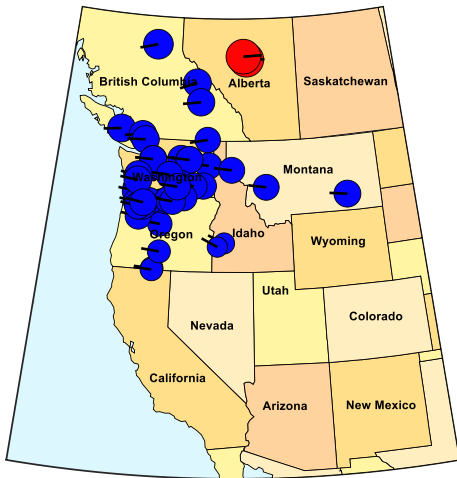


Figure E-15: 2016/09/29 from 18:10:31 to 18:20:31 UTC. PDCI probing condition.

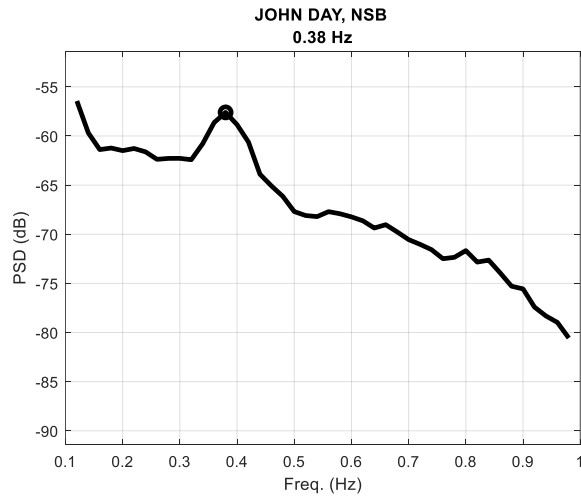
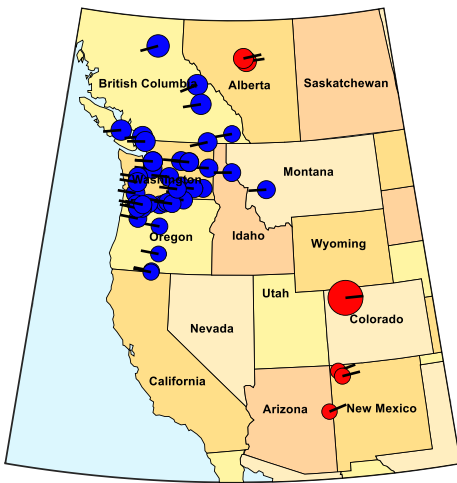


Figure E-16: 2016/09/29 from 19:10:00 to 19:30:00 UTC. Ambient condition.

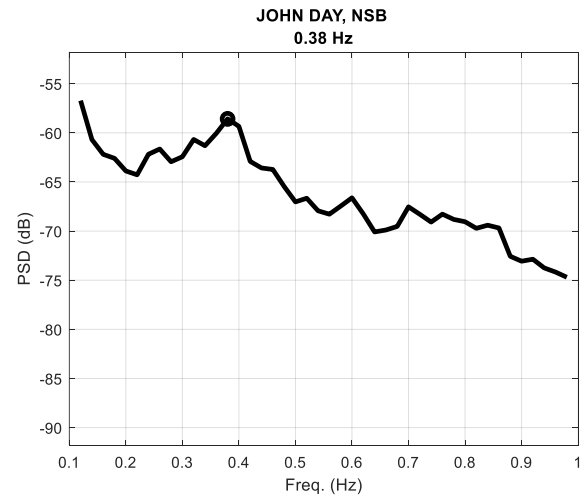
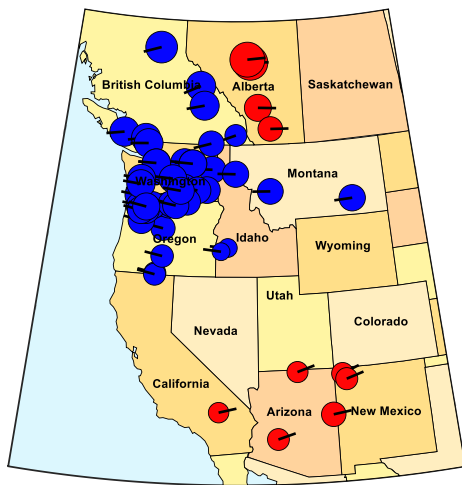


Figure E-17: 2016/09/29 from 20:10:31 to 20:20:31 UTC. PDCI probing condition.

## Modes of Inter-Area Power Oscillations in the Western Interconnection

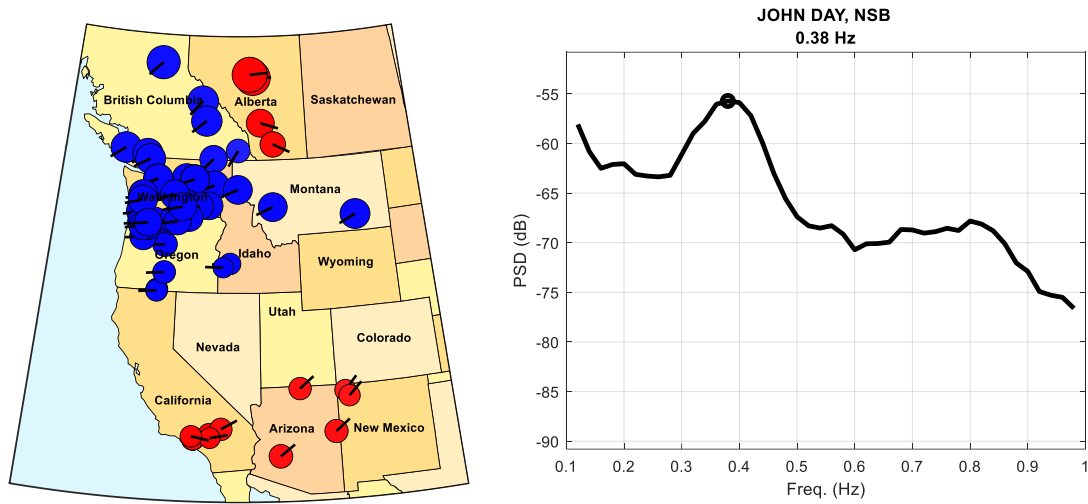


Figure E-18: 2016/09/29 from 21:10:00 to 21:30:00 UTC. Ambient condition.

# Modes of Inter-Area Power Oscillations in the Western Interconnection

2017 Data

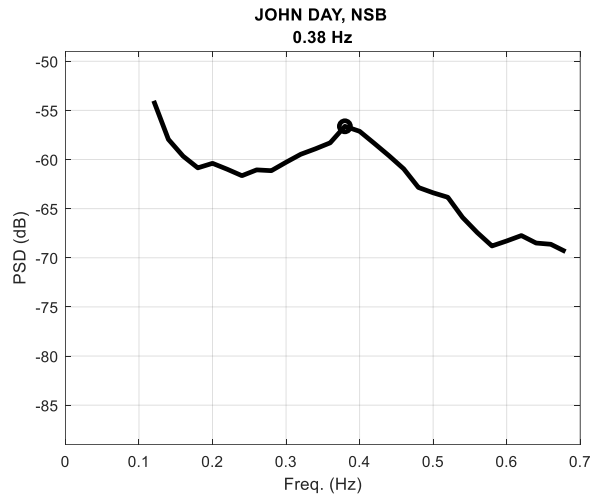
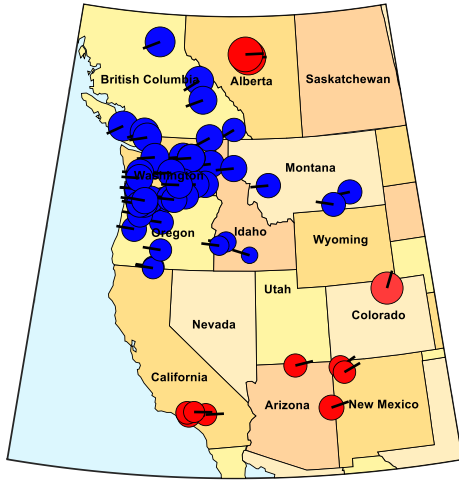


Figure E-19: 2017/05/16 from 16:16:01 to 16:36:01 UTC. PDCI probing condition.

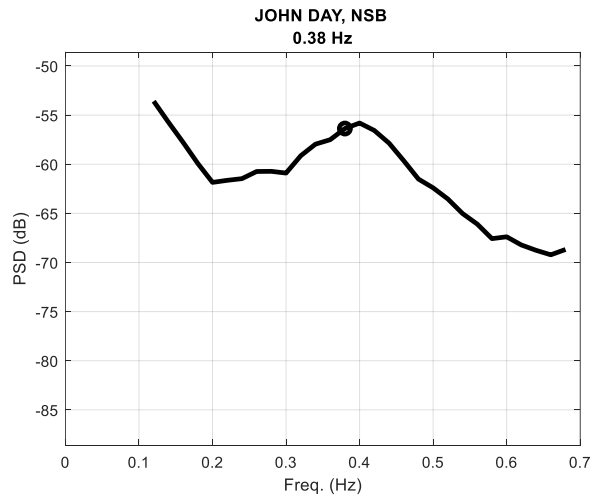
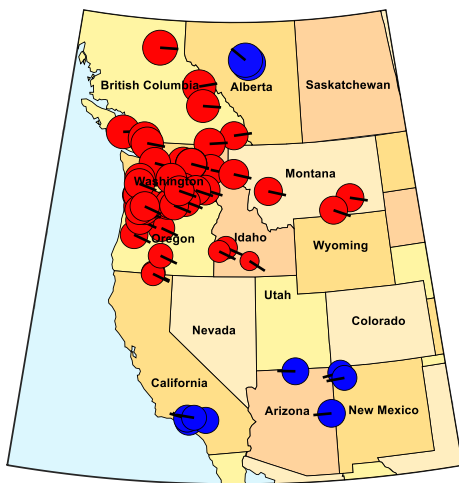


Figure E-20: 2017/05/16 from 20:15:01 to 20:35:01 UTC. PDCI probing condition.

# Modes of Inter-Area Power Oscillations in the Western Interconnection

2018 Data

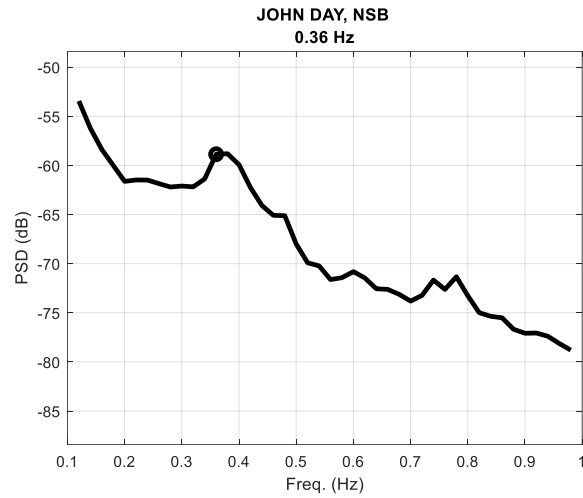
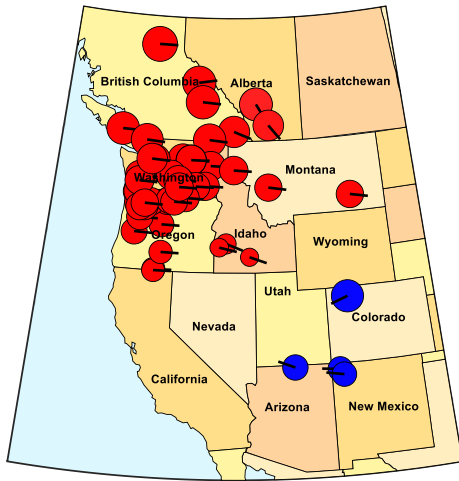


Figure E-21: 2018/05/23 from 16:05:00 to 16:24:30 UTC. Ambient condition.

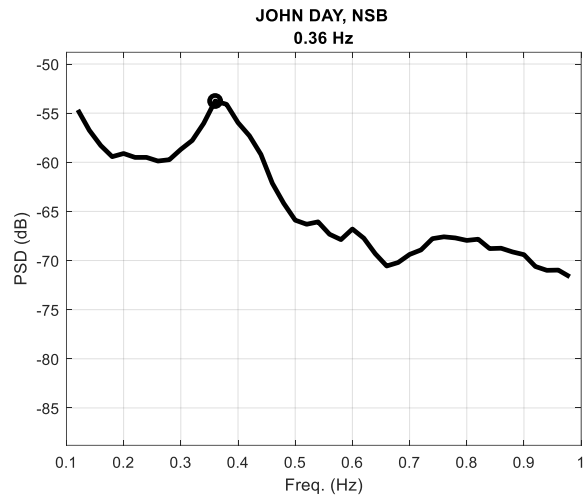
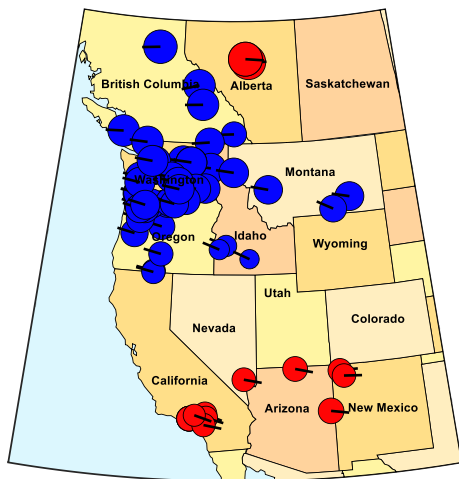
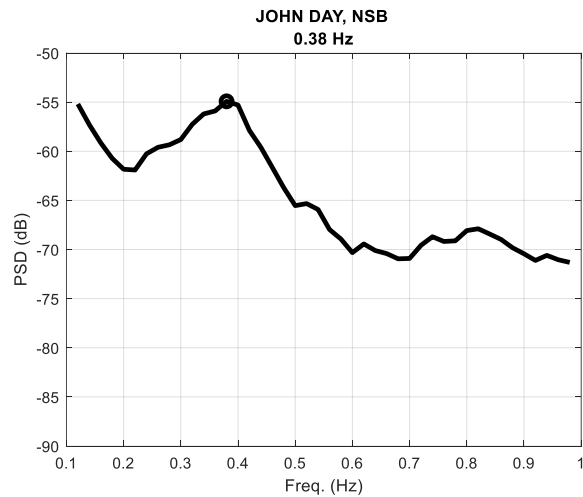
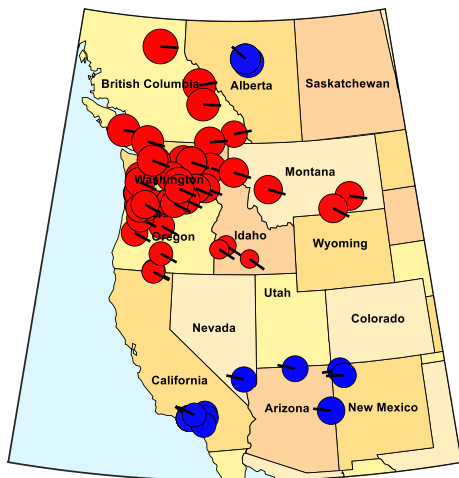


Figure E-22: 2018/05/23 from 16:28:00 to 16:48:00 UTC. PDCI probing condition.



# Modes of Inter-Area Power Oscillations in the Western Interconnection

Figure E-23: 2018/05/23 from 20:15:00 to 20:35:00 UTC. PDCI probing condition.

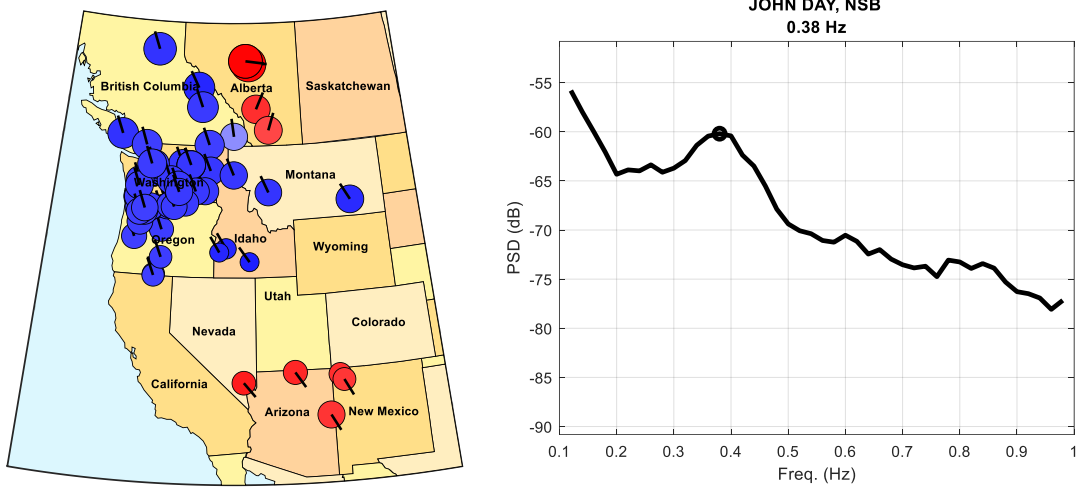


Figure E-24: 2018/05/23 from 20:36:00 to 20:55:00 UTC. Ambient condition.

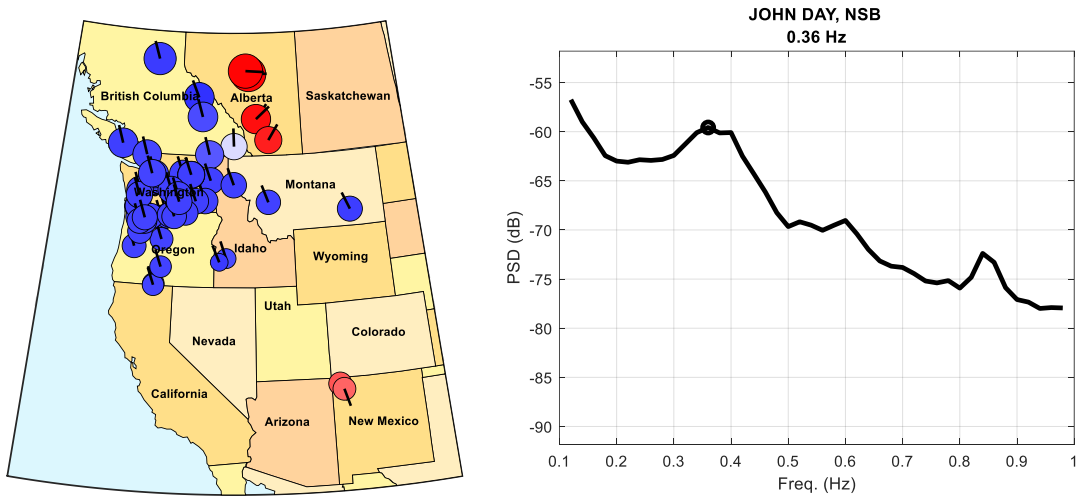
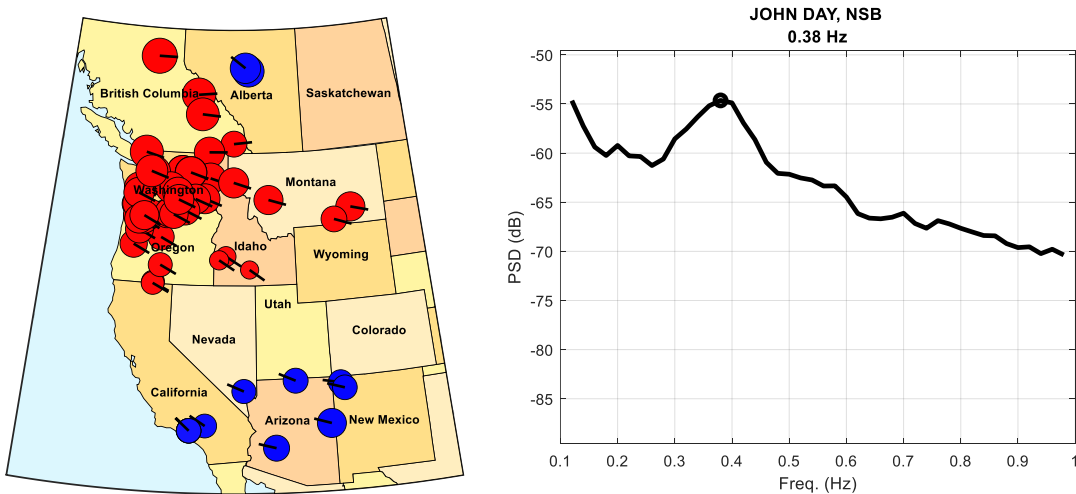


Figure E-25: 2018/05/24 from 00:10:00 to 00:30:00 UTC. Ambient condition.



# Modes of Inter-Area Power Oscillations in the Western Interconnection

Figure E-26: 2018/05/24 from 17:14:05 to 17:34:00 UTC. PDCI probing condition.

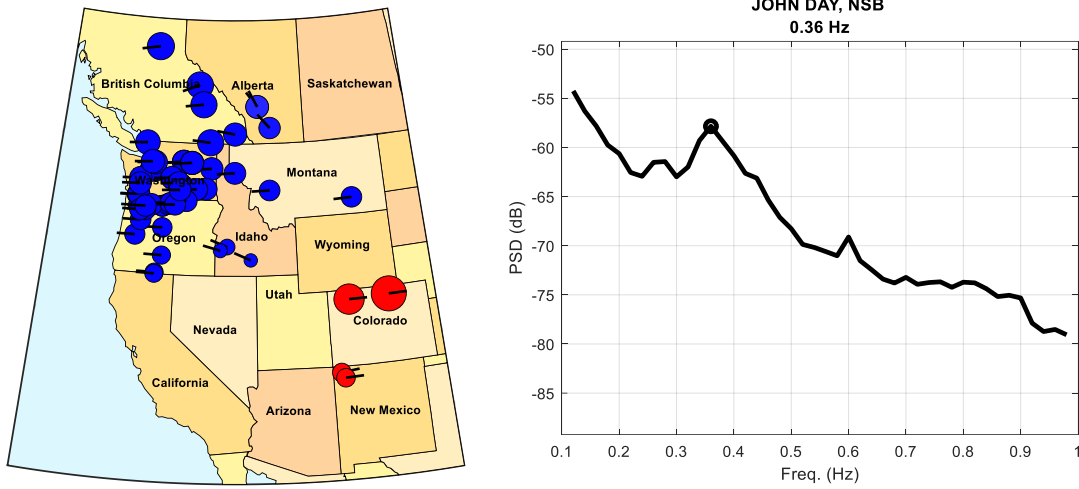


Figure E-27: 2018/05/24 from 17:36:00 to 17:50:00 UTC. Ambient condition.

## 2019 Data

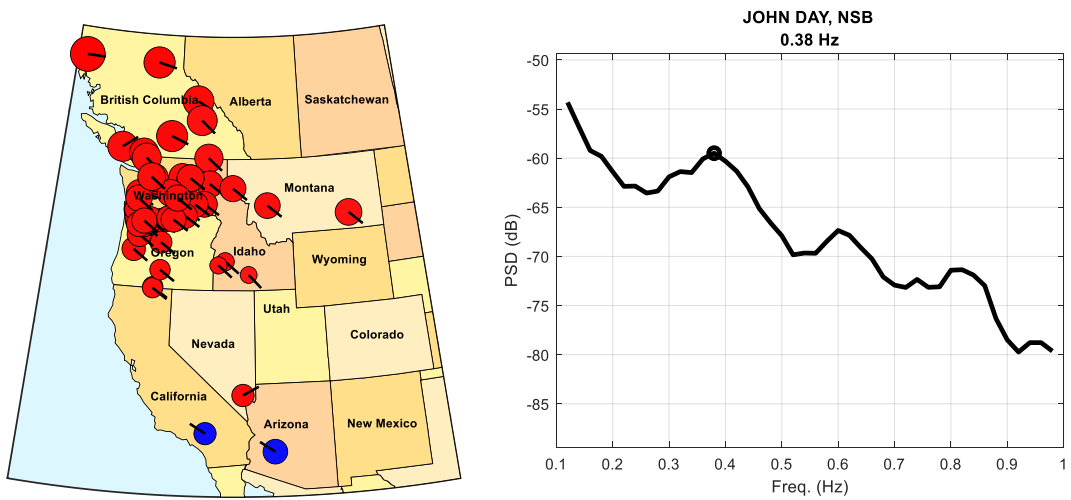


Figure E-28: 2019/05/07 from 14:10:00 to 14:30:00 UTC. Ambient condition.

## Modes of Inter-Area Power Oscillations in the Western Interconnection

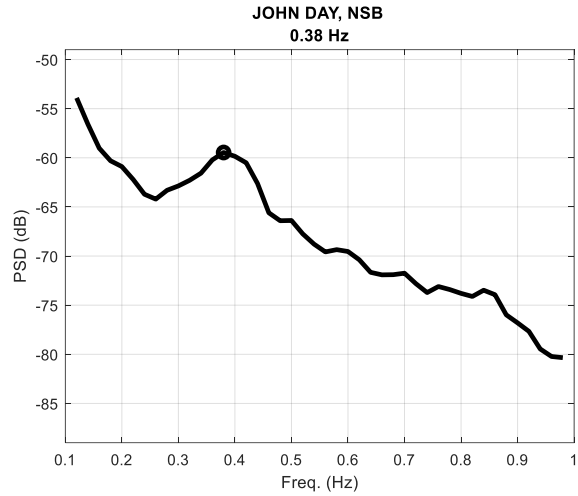
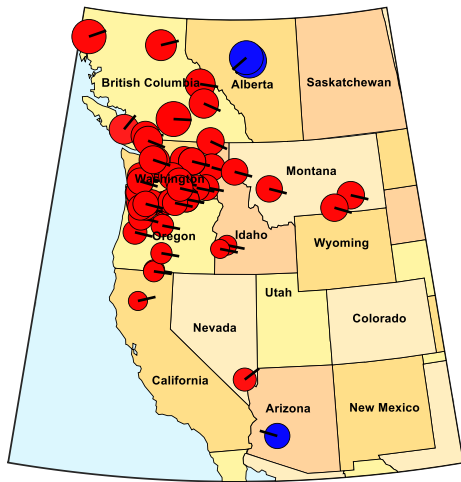


Figure E-29: 2019/05/07 from 17:10:00 to 17:30:00 UTC. Ambient condition.

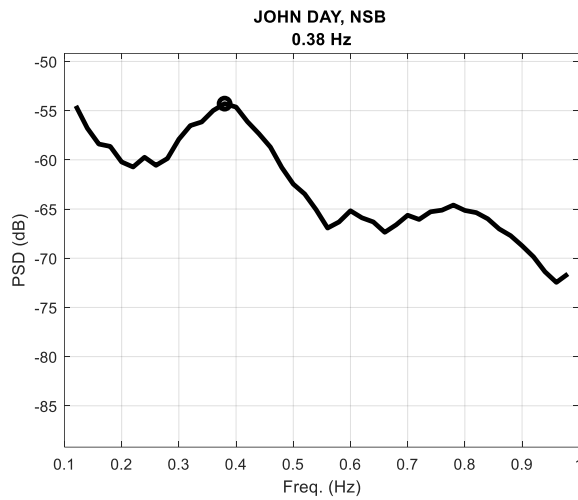


Figure E-30: 2019/05/07 from 17:30:03 to 17:50:03 UTC. PDCI probing condition.

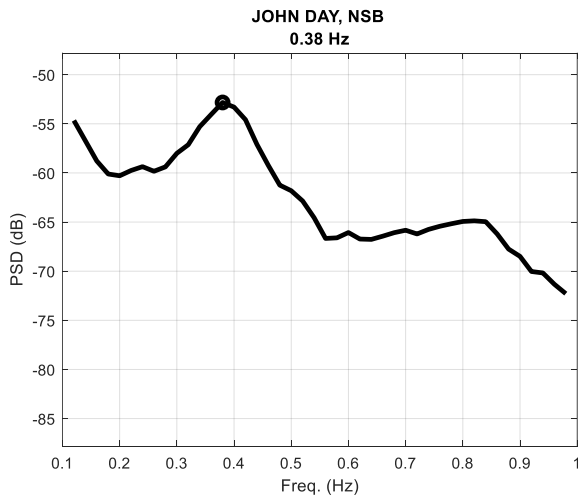


Figure E-31: 2019/05/07 from 21:20:03 to 21:40:03 UTC. PDCI probing condition.

# Modes of Inter-Area Power Oscillations in the Western Interconnection

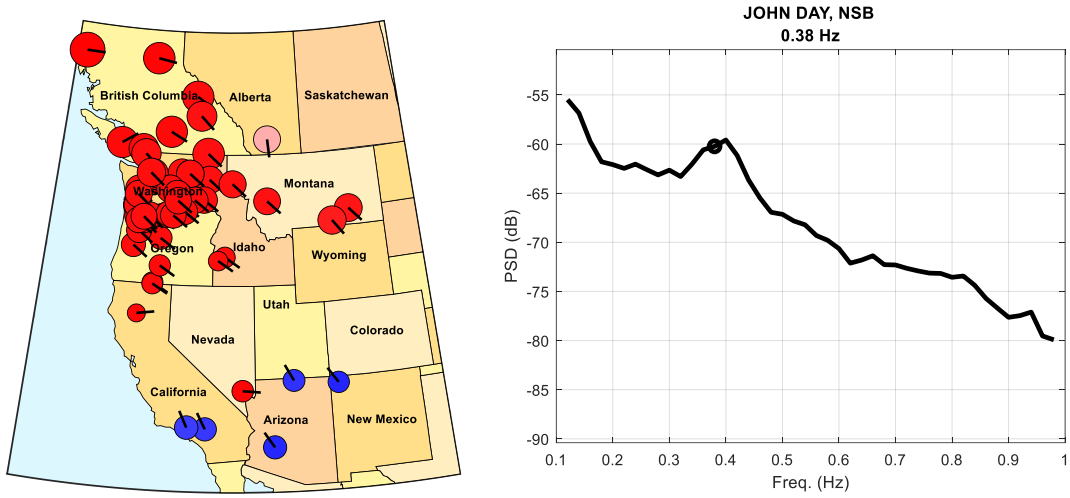


Figure E-32: 2019/05/08 from 02:10:00 to 02:30:00 UTC. Ambient condition.

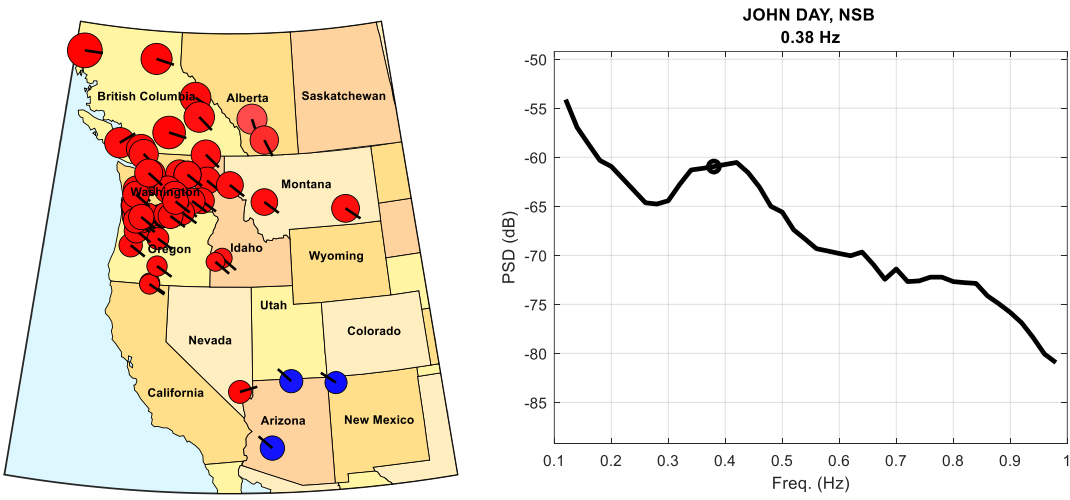


Figure E-33: 2019/05/08 from 06:10:00 to 06:30:00 UTC. Ambient condition.

## Mode Meter Analysis Results

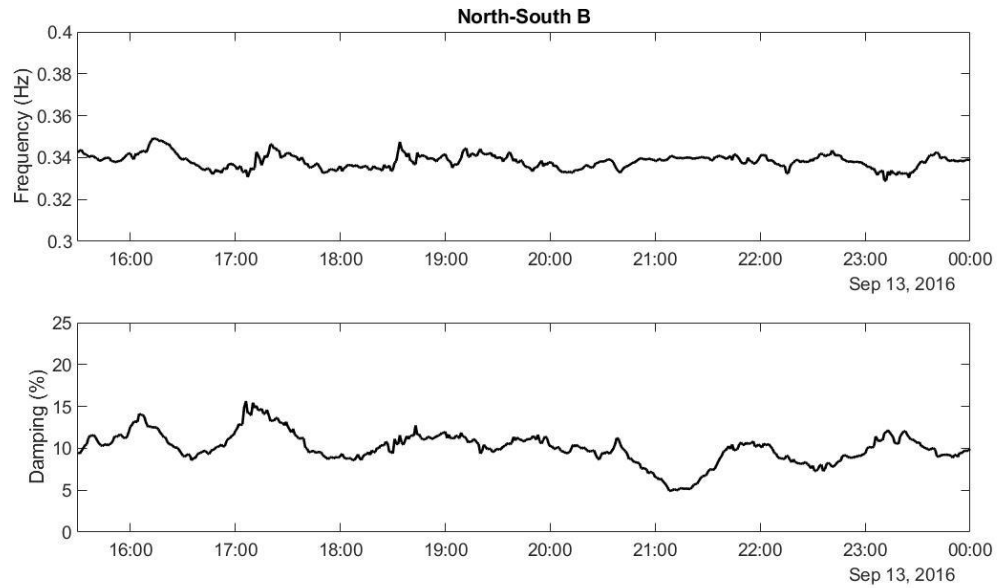


Figure E-34: 2016/09/13 dataset.

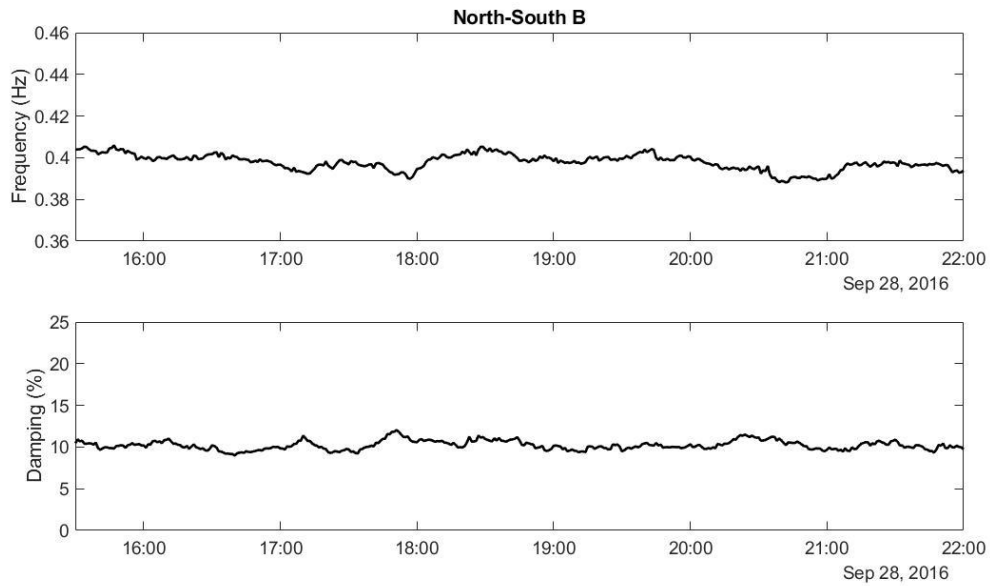


Figure E-35: 2016/09/28 dataset.

## Modes of Inter-Area Power Oscillations in the Western Interconnection

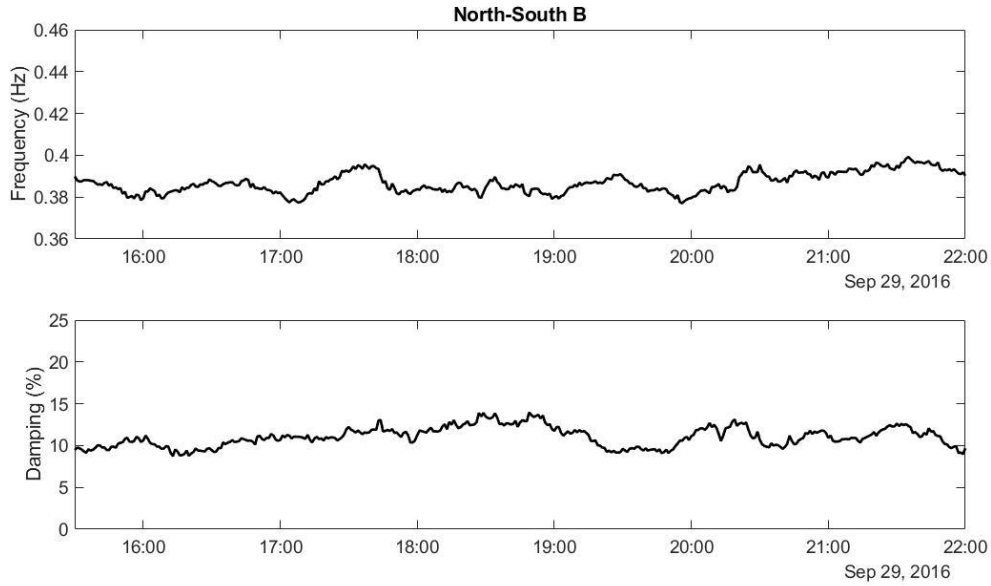


Figure E-36: 2016/09/29 dataset.

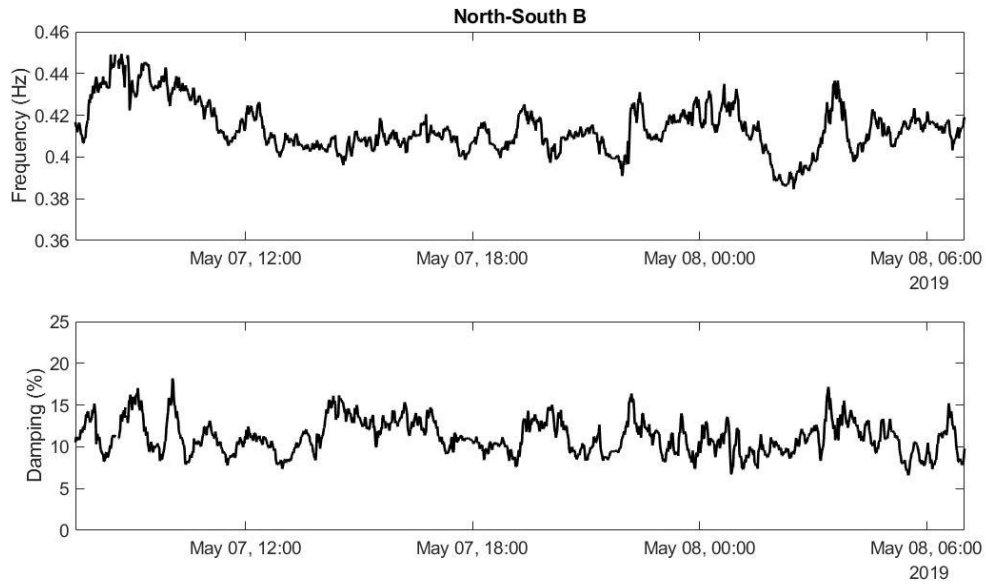


Figure E-37: 2019/05/08 dataset.

## Modes of Inter-Area Power Oscillations in the Western Interconnection

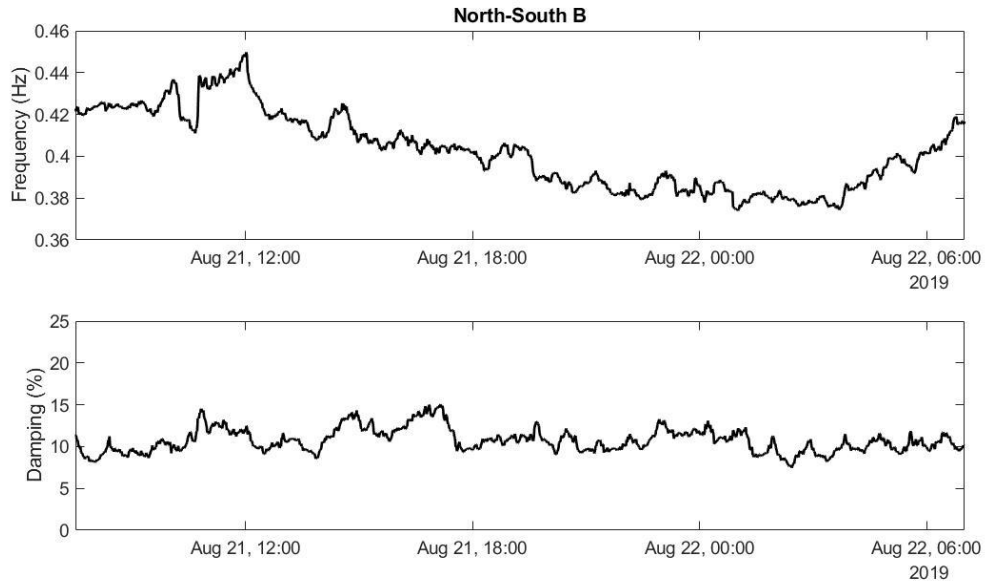


Figure E-38: 2019/08/22 dataset.

### Ringdown Analysis Results



Figure E-39: 2016/09/29 at 17:34 UTC. Estimated at 0.38 Hz, 13.4% damping.

## Modes of Inter-Area Power Oscillations in the Western Interconnection

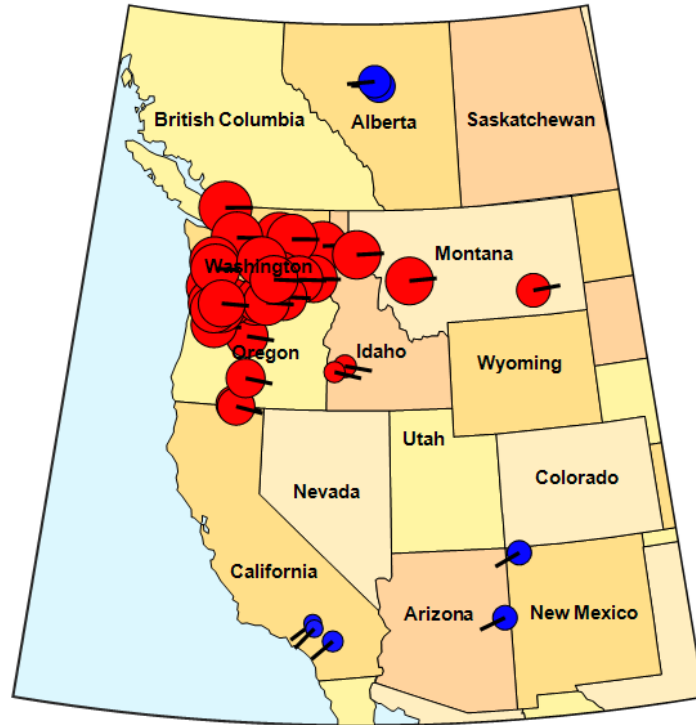


Figure E-40: 2016/09/29 at 17:42 UTC. Estimated at 0.39 Hz, 12.6% damping.

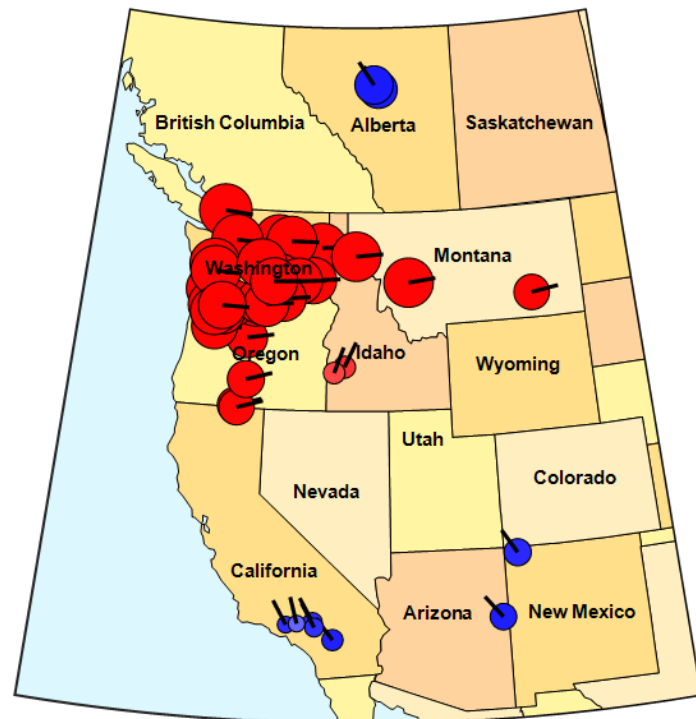


Figure E-41: 2016/09/29 at 20:30 UTC. Estimated at 0.39 Hz, 14.6% damping.

## Modes of Inter-Area Power Oscillations in the Western Interconnection

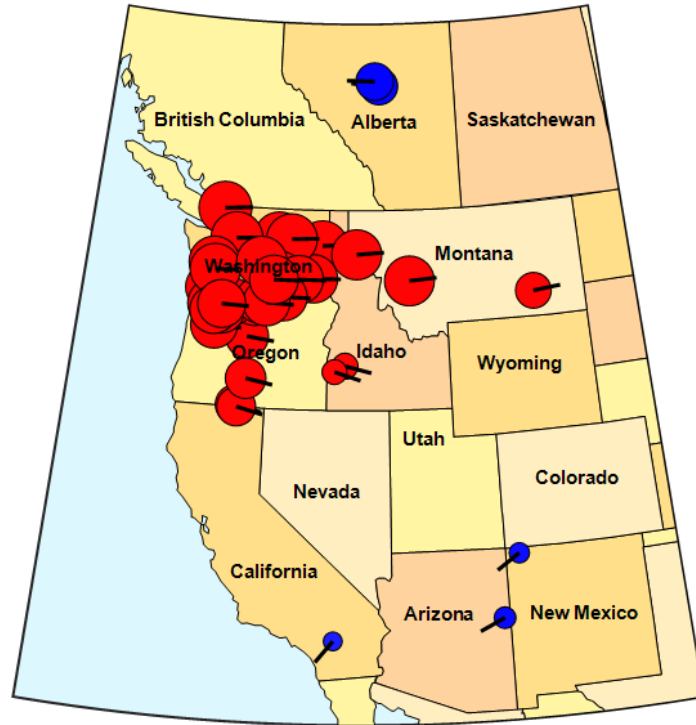


Figure E-42: 2016/09/29 at 20:40 UTC. Estimated at 0.37 Hz, 13.2% damping.

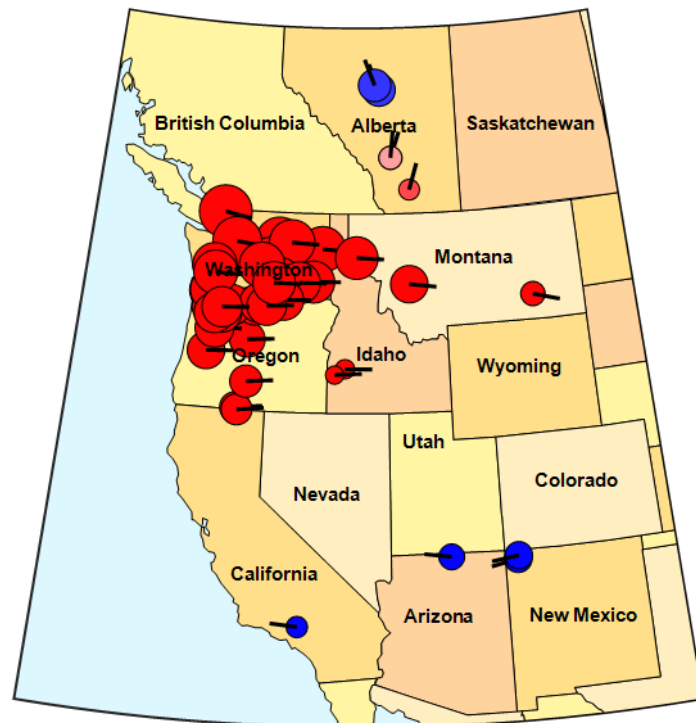


Figure E-43: 2017/05/16 at 17:25 UTC. Estimated at 0.42 Hz, 15.2% damping.

## Modes of Inter-Area Power Oscillations in the Western Interconnection

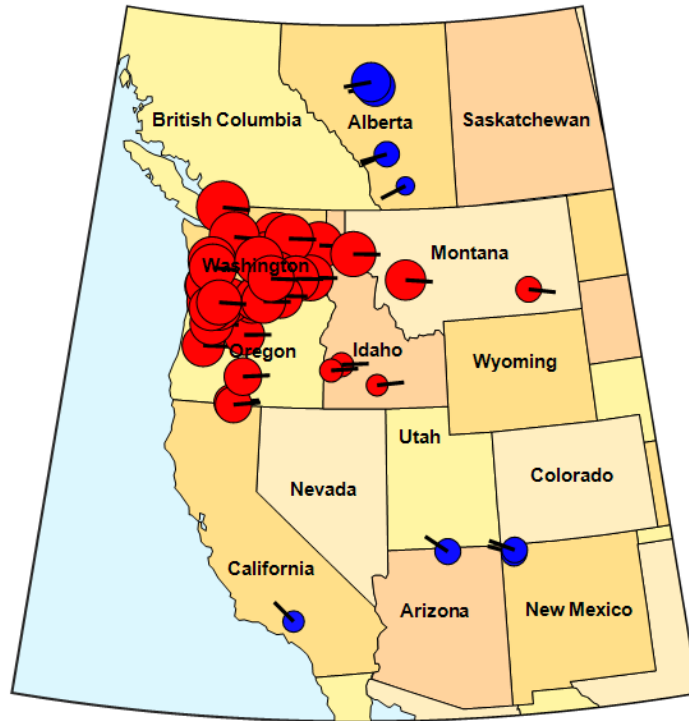


Figure E-44: 2017/05/16 at 17:35 UTC. Estimated at 0.41 Hz, 17.0% damping.

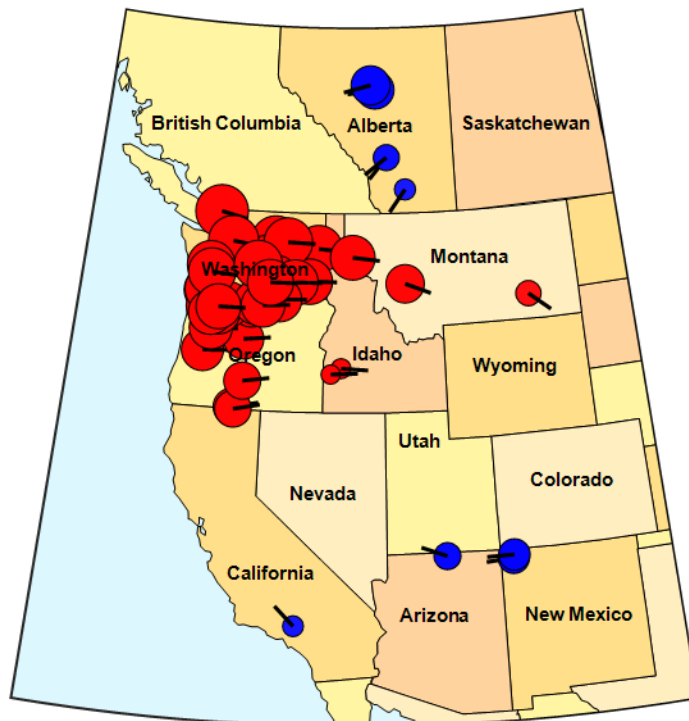


Figure E-45: 2017/05/16 at 18:25 UTC. Estimated at 0.40 Hz, 14.2% damping.

## Modes of Inter-Area Power Oscillations in the Western Interconnection

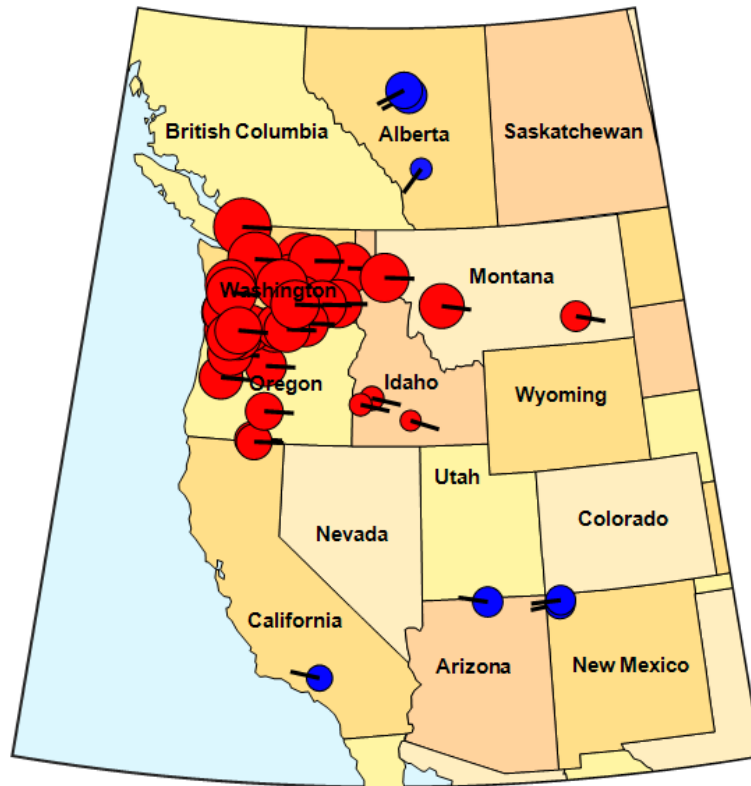


Figure E-46: 2017/05/16 at 18:35 UTC. Estimated at 0.41 Hz, 13.1% damping.

## Appendix F: EWA Mode Analyses

### Correlation Analysis from 2016 through 2019 PMU Data

The following are the mode shape estimates for all the conditions in Table 20 from the section titled, "East-West A Mode." The mode shape is shown on the left and the mode reference signal PSD is shown on the right.

#### 2016 Data

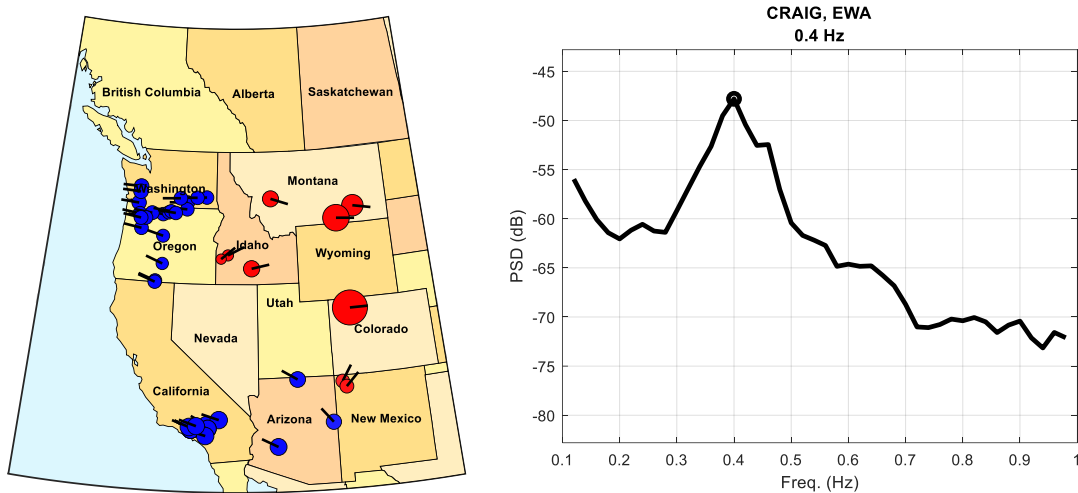


Figure F-1: 2016/09/13 from 17:10:02 to 17:30:00 UTC. Alberta disconnected, PDCI probing condition.

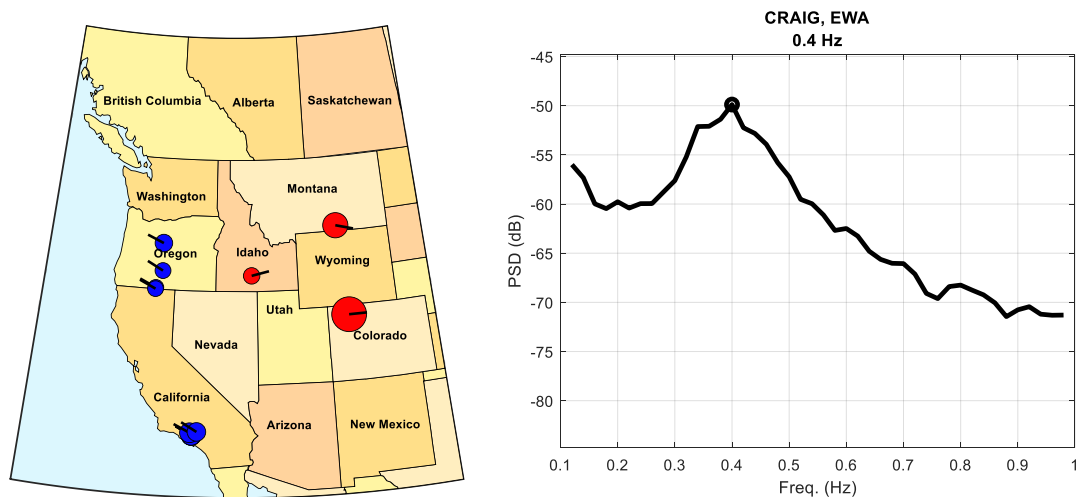


Figure F-2: 2016/09/13 from 18:30:01 to 18:50:01 UTC. Alberta disconnected, ambient condition.

## Modes of Inter-Area Power Oscillations in the Western Interconnection

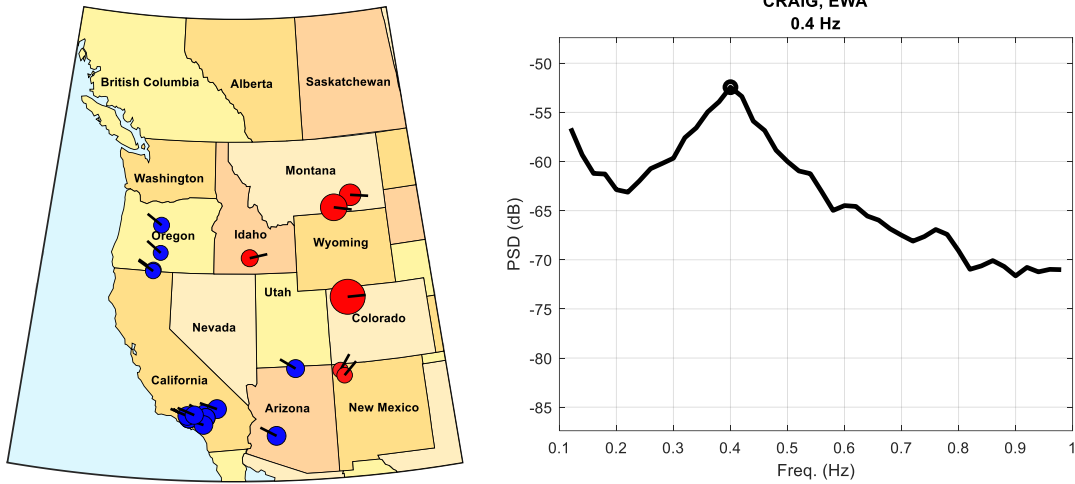


Figure F-3: 2016/09/13 from 22:10:00 to 22:28:00 UTC. Alberta disconnected, ambient condition.

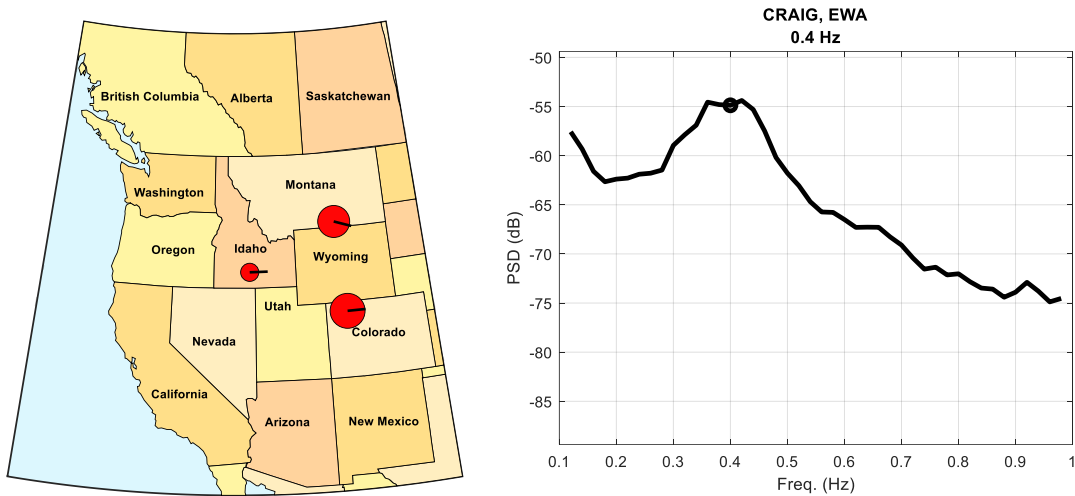


Figure F-4: 2016/09/13 from 22:28:10 to 22:48:10 UTC. Alberta disconnected, PDCI probing condition.

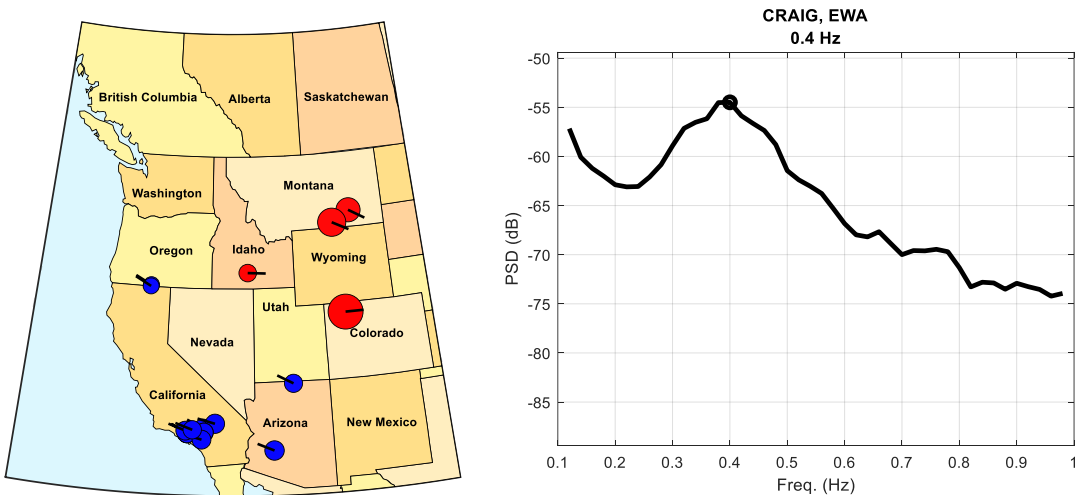


Figure F-5: 2016/09/13 from 23:10:00 to 23:30:00 UTC. Alberta disconnected, ambient condition.

# Modes of Inter-Area Power Oscillations in the Western Interconnection

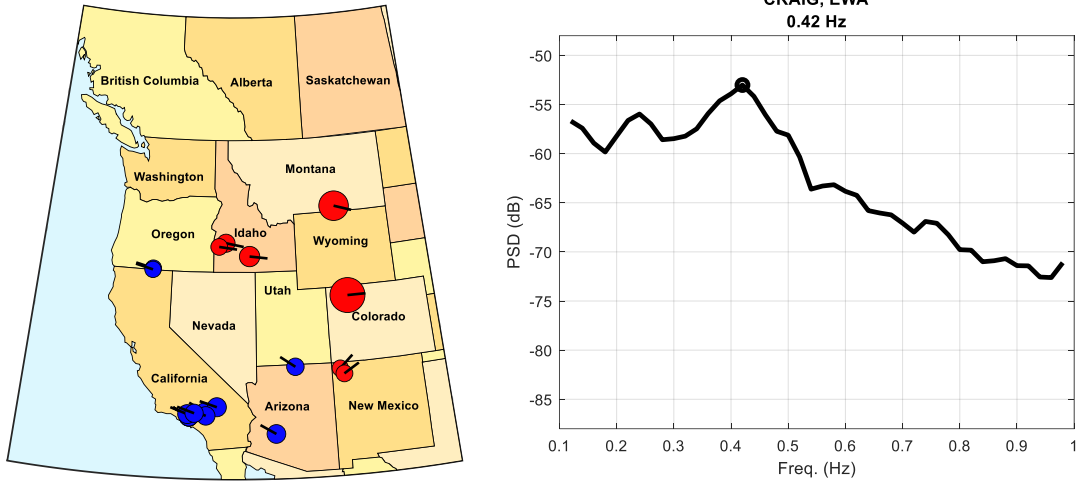


Figure F-6: 2016/09/28 from 15:10:00 to 15:30:00 UTC. Ambient condition.

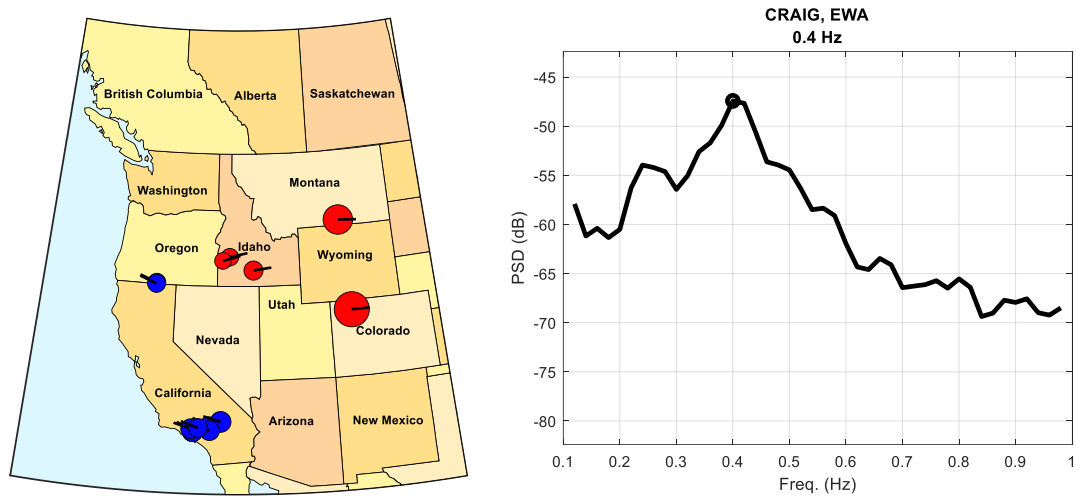


Figure F-7: 2016/09/28 from 16:30:12 to 16:40:12 UTC. PDCI probing condition.

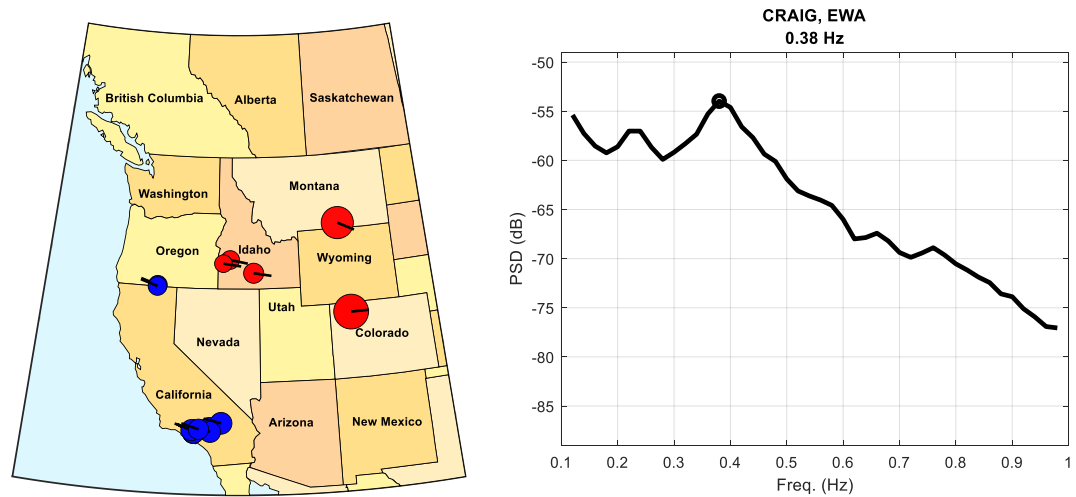


Figure F-8: 2016/09/28 from 17:10:00 to 17:30:00 UTC. Ambient condition.



# Modes of Inter-Area Power Oscillations in the Western Interconnection

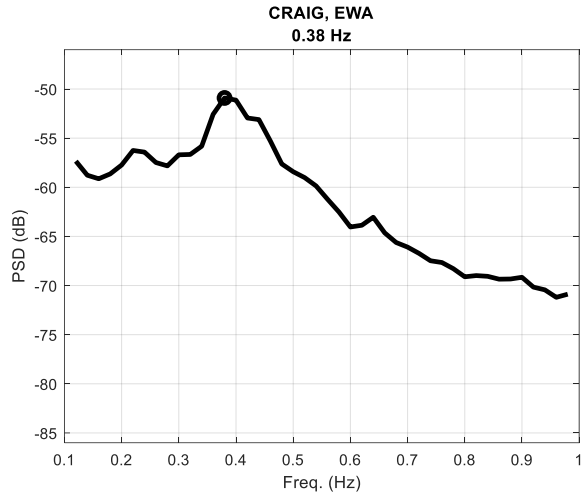


Figure F-9: 2016/09/28 from 18:20:02 to 18:40:02 UTC. PDCI probing condition.

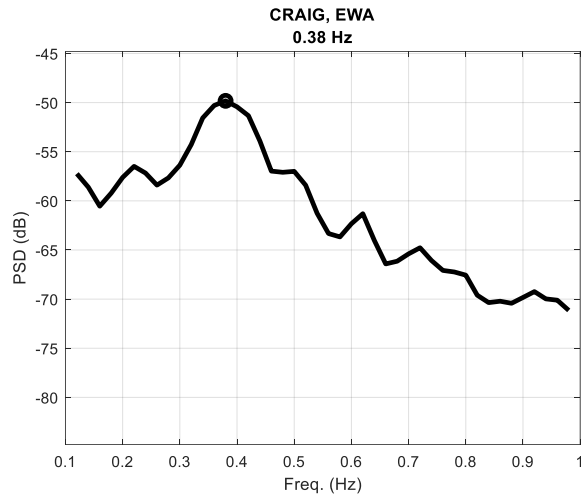
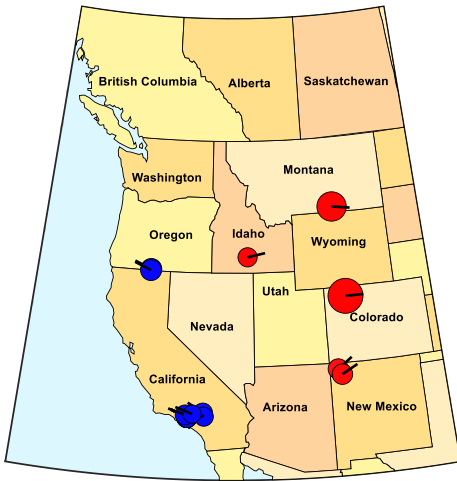


Figure F-10: 2016/09/28 from 20:30:09 to 20:40:09 UTC. PDCI probing condition.

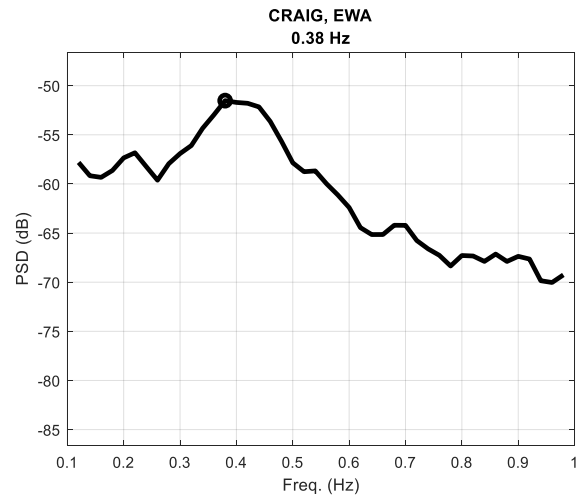
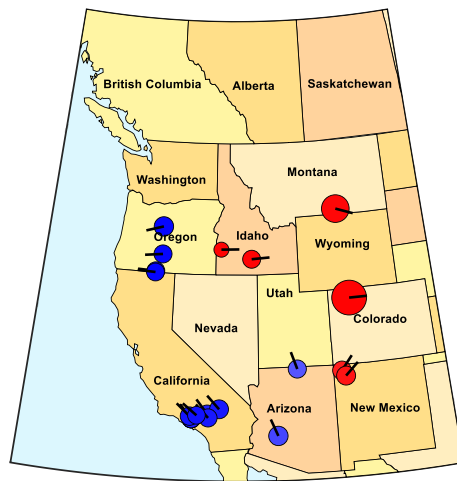


Figure F-11: 2016/09/28 from 21:10:00 to 21:30:00 UTC. Ambient condition.



# Modes of Inter-Area Power Oscillations in the Western Interconnection

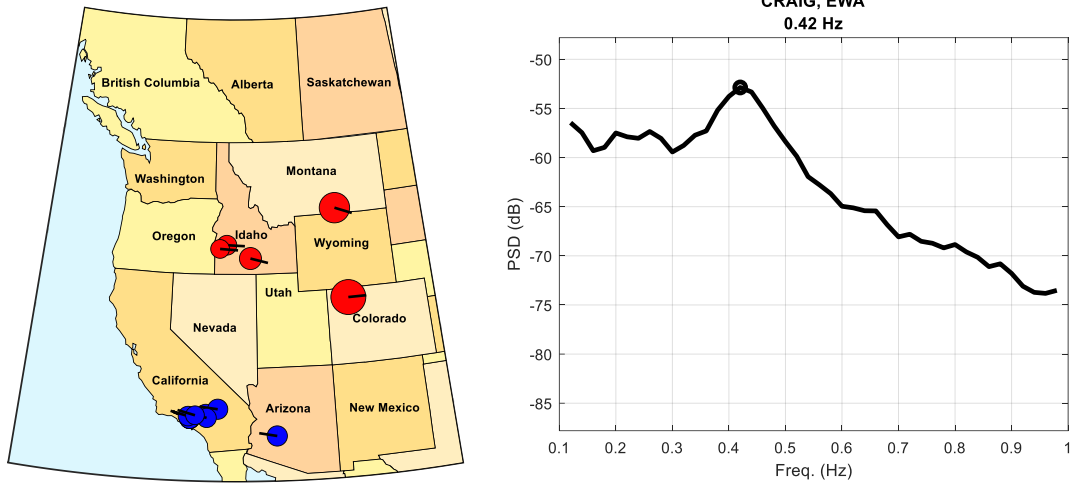


Figure F-12: 2016/09/29 from 15:10:30 to 15:30:00 UTC. Ambient condition.

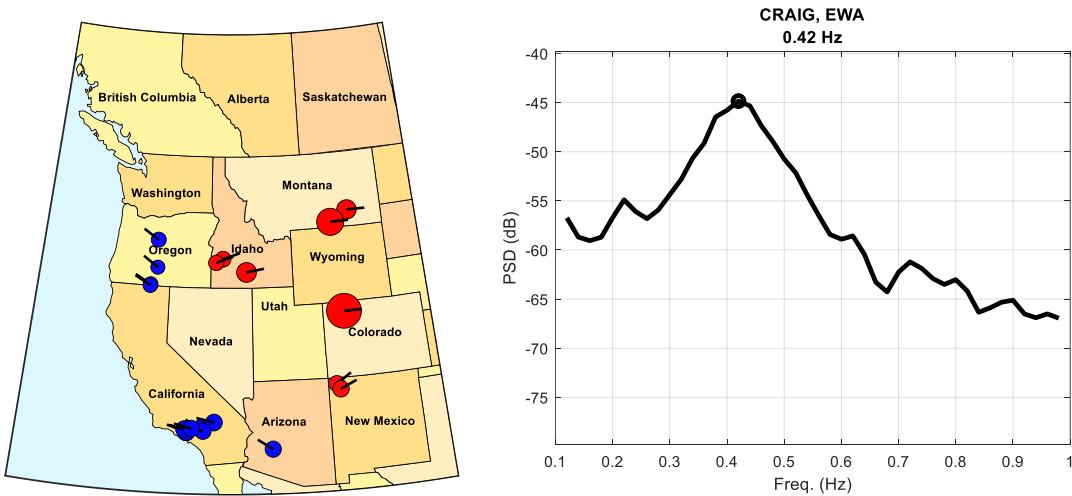


Figure F-13: 2016/09/29 from 16:10:34 to 16:20:34 UTC. PDCI probing condition.

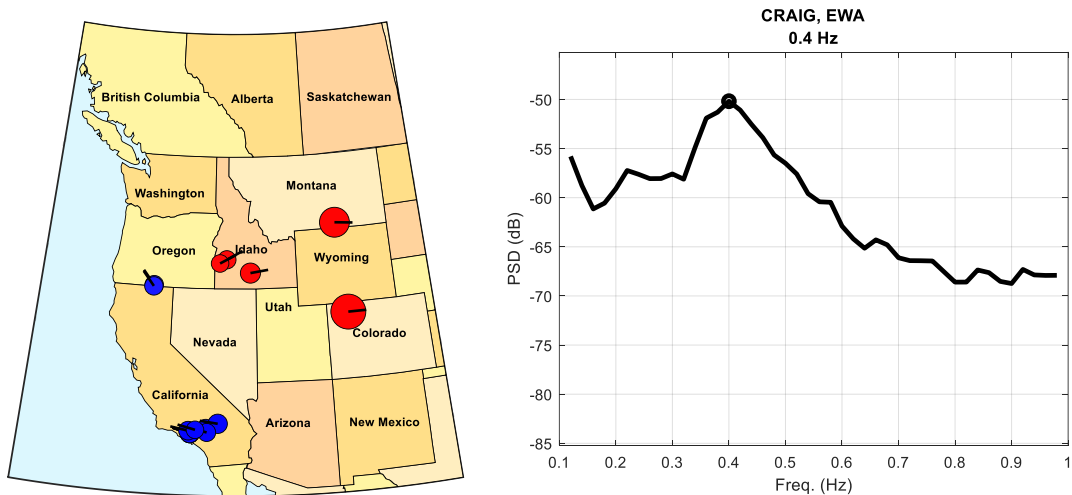


Figure F-14: 2016/09/29 from 17:10:01 to 17:20:01 UTC. PDCI probing condition.



## Modes of Inter-Area Power Oscillations in the Western Interconnection

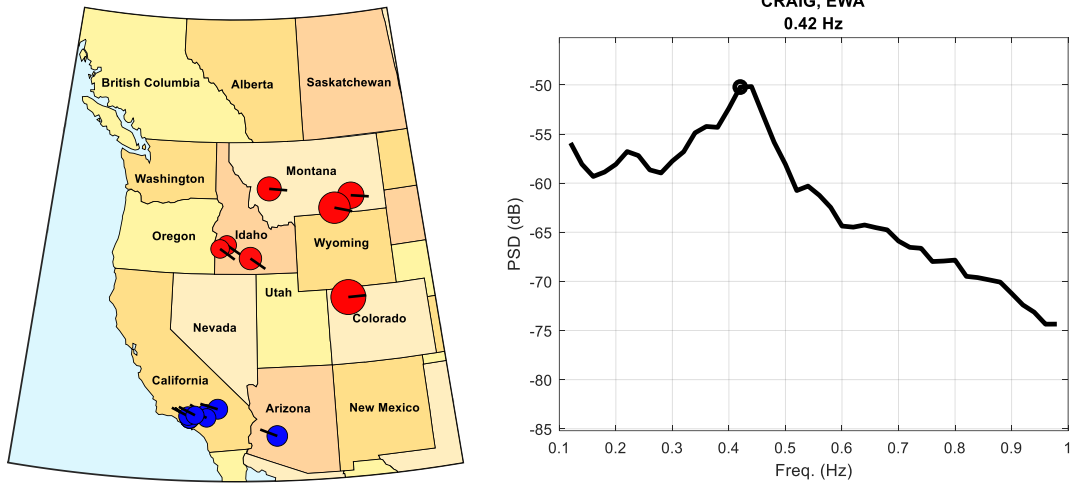


Figure F-15: 2016/09/29 from 18:10:31 to 18:20:31 UTC. PDCI probing condition.

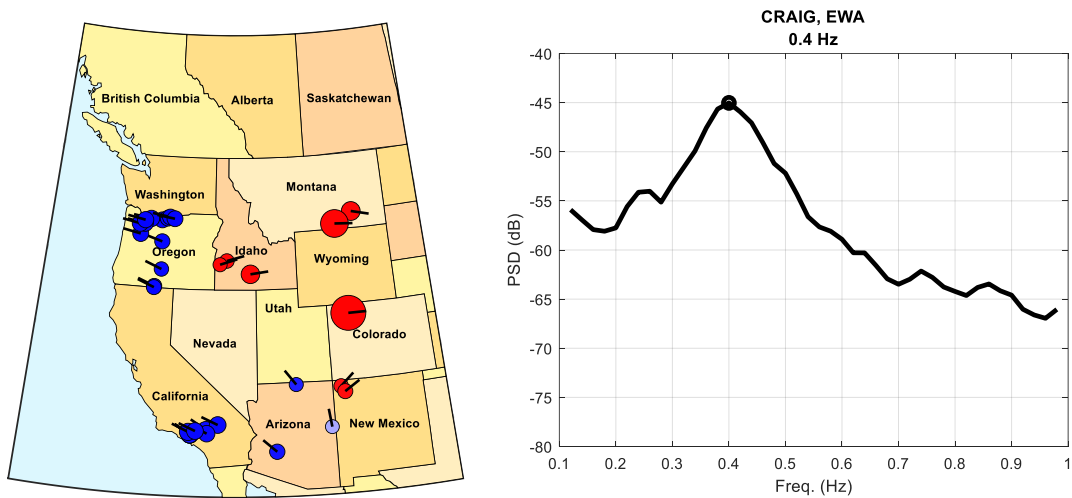


Figure F-16: 2016/09/29 from 19:10:00 to 19:30:00 UTC. Ambient condition.

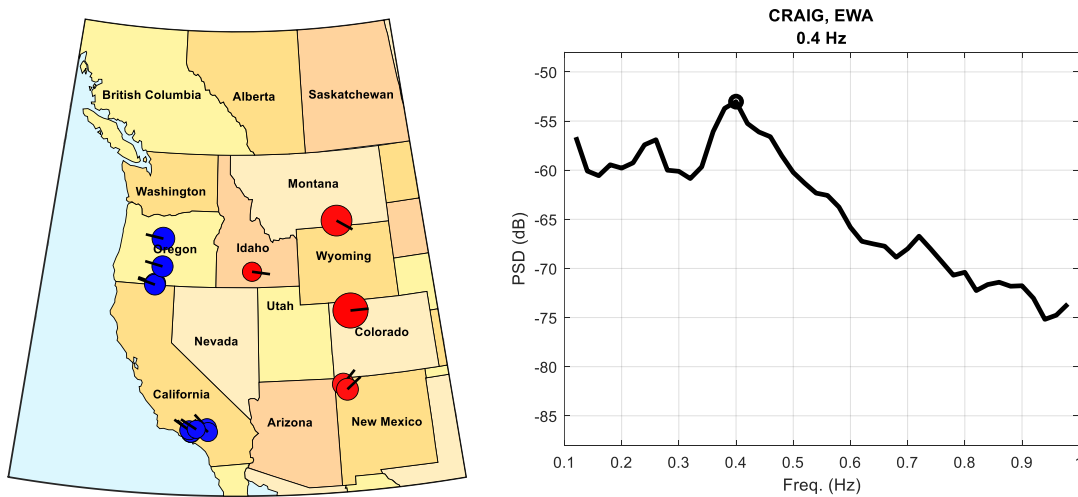


Figure F-17: 2016/09/29 from 20:10:31 to 20:20:31 UTC. PDCI probing condition.

# Modes of Inter-Area Power Oscillations in the Western Interconnection

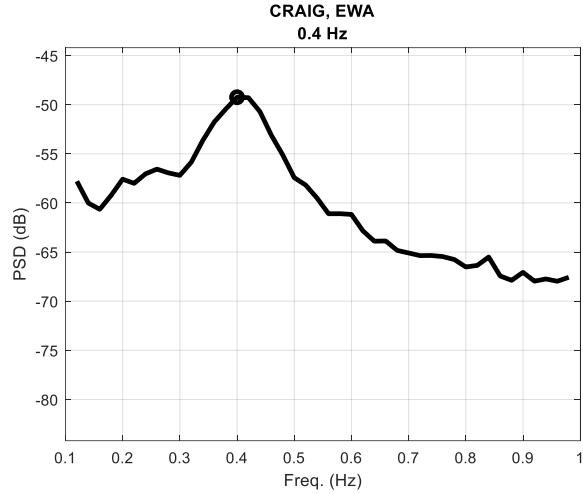


Figure F-18: 2016/09/29 from 21:10:00 to 21:30:00 UTC. Ambient condition.

## 2017 Data

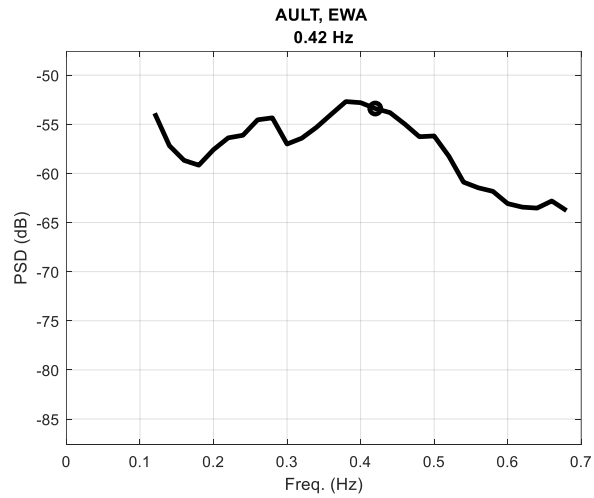
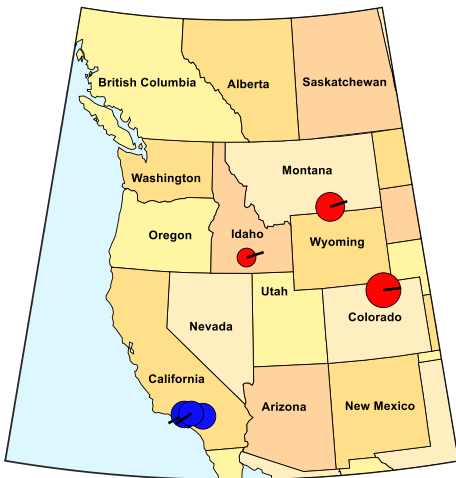
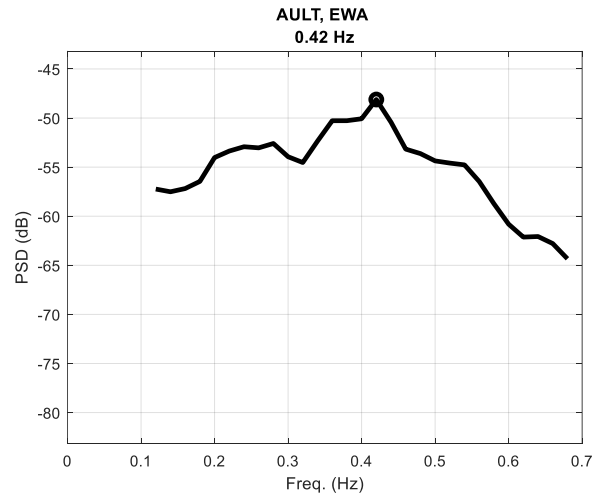


Figure F-19: 2017/05/16 from 16:16:01 to 16:36:01 UTC. PDCI probing condition.



# Modes of Inter-Area Power Oscillations in the Western Interconnection

Figure F-20: 2017/05/16 from 16:36:05 to 16:50:00 UTC. Ambient condition.

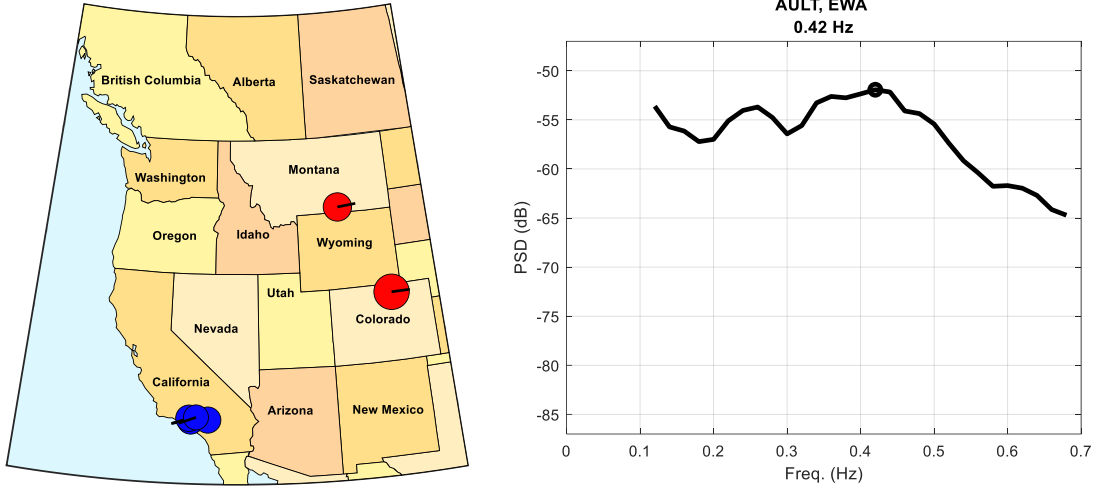


Figure F-21: 2017/05/16 from 20:15:01 to 20:35:01 UTC. PDCI probing condition.

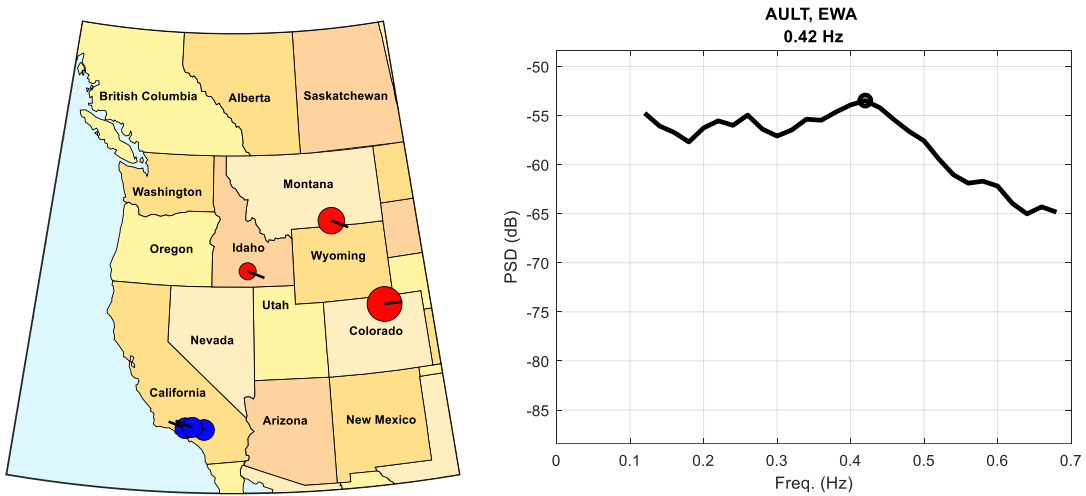


Figure F-22: 2017/05/16 from 20:35:05 to 20:50:00 UTC. Ambient condition.

# Modes of Inter-Area Power Oscillations in the Western Interconnection

2018 Data

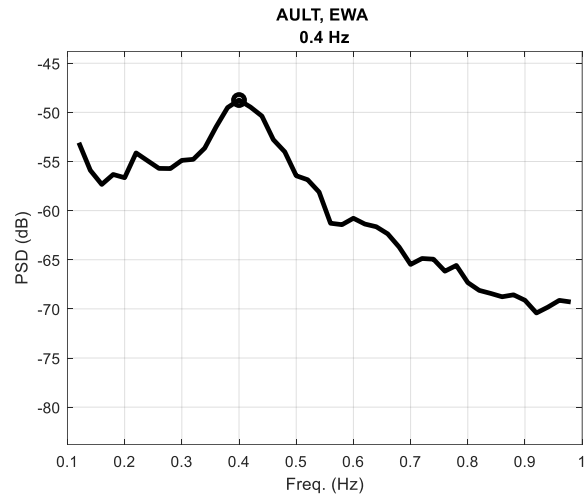


Figure F-23: 2018/05/23 from 16:05:00 to 16:24:30 UTC. Ambient condition.

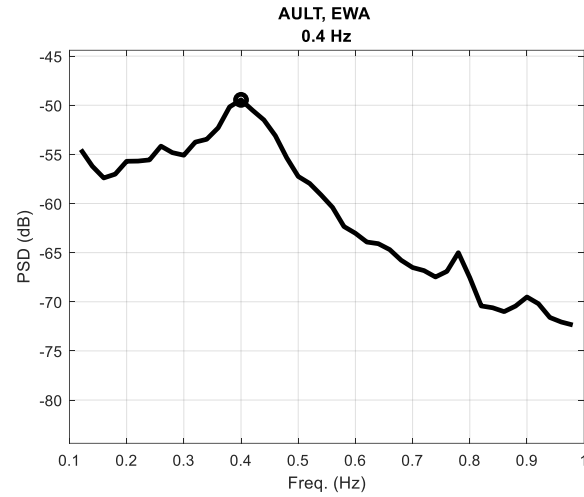
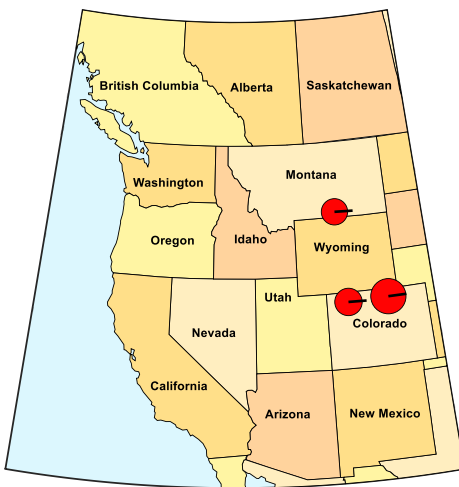


Figure F-24: 2018/05/23 from 16:28:00 to 16:48:00 UTC. PDCI probing condition.

## Modes of Inter-Area Power Oscillations in the Western Interconnection

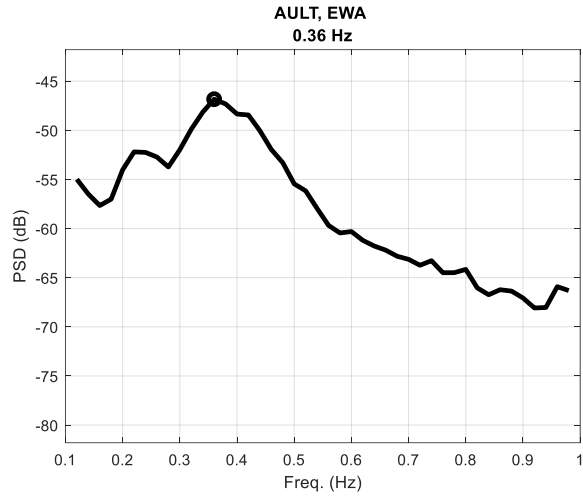


Figure F-25: 2018/05/23 from 20:15:00 to 20:35:00 UTC. PDCI probing condition.

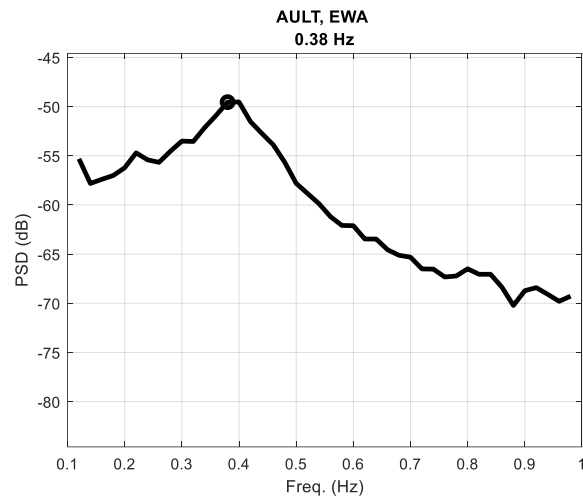


Figure F-26: 2018/05/23 from 20:36:00 to 20:55:00 UTC. Ambient condition.

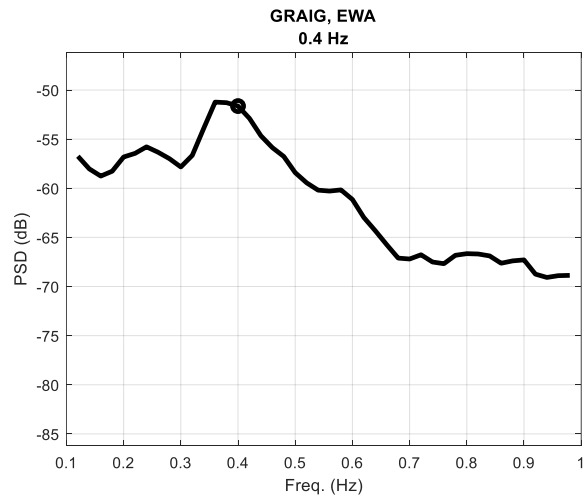
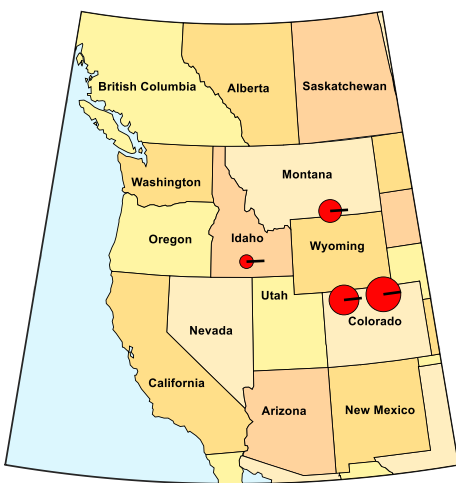


Figure F-27: 2018/05/24 from 00:10:00 to 00:30:00 UTC. Ambient condition.

# Modes of Inter-Area Power Oscillations in the Western Interconnection

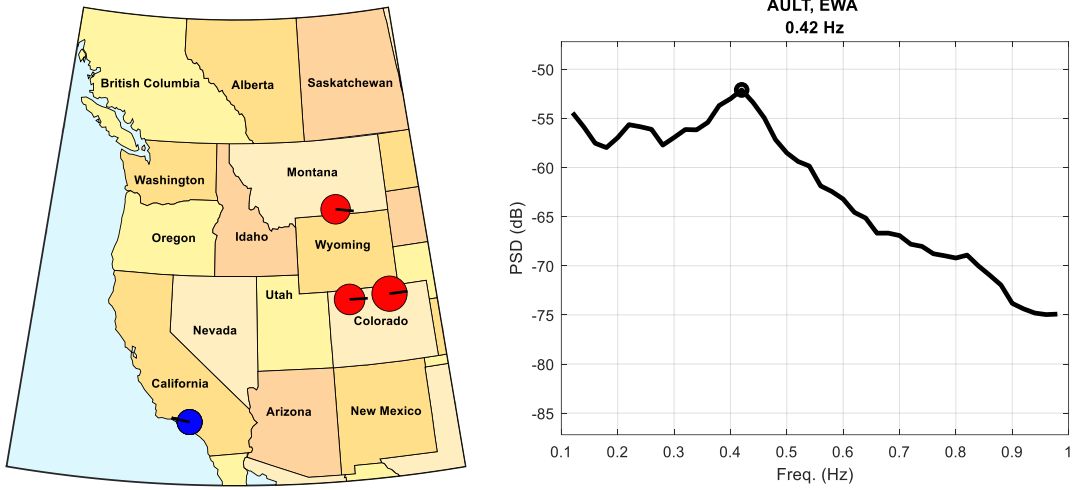


Figure F-28: 2018/05/24 from 17:14:05 to 17:34:00 UTC. PDCI probing condition.

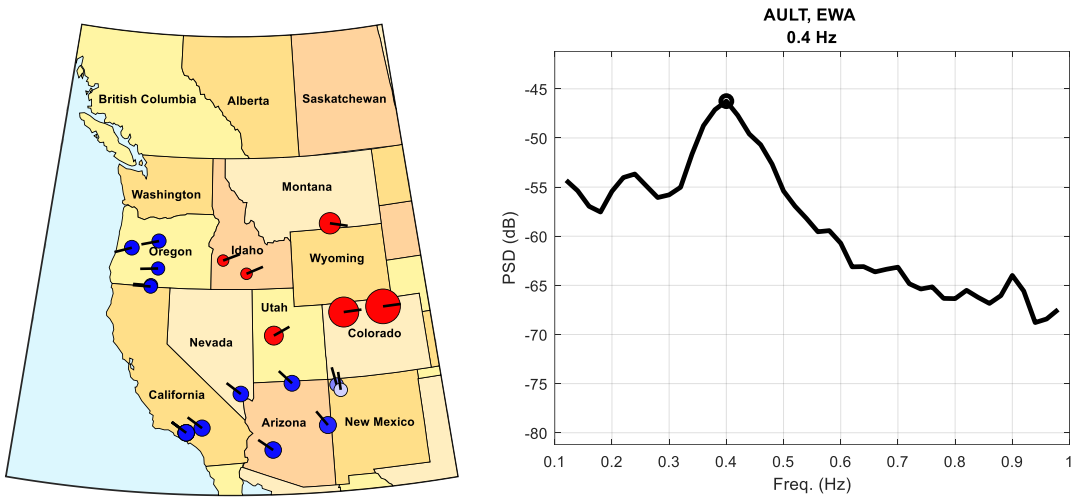


Figure F-29: 2018/05/24 from 17:36:00 to 17:50:00 UTC. Ambient condition.

# Modes of Inter-Area Power Oscillations in the Western Interconnection

2019 Data

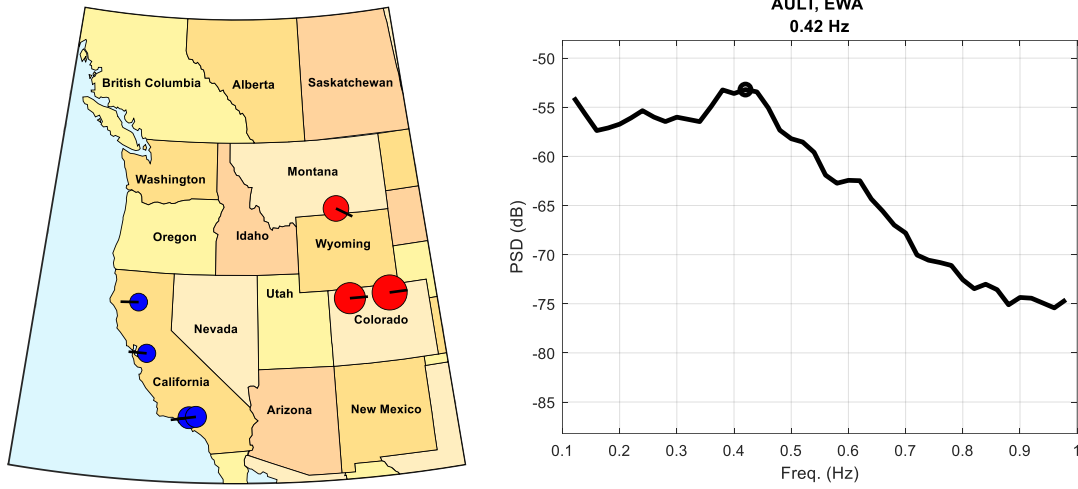


Figure F-30: 2019/05/07 from 14:10:00 to 14:30:00 UTC. Ambient condition.

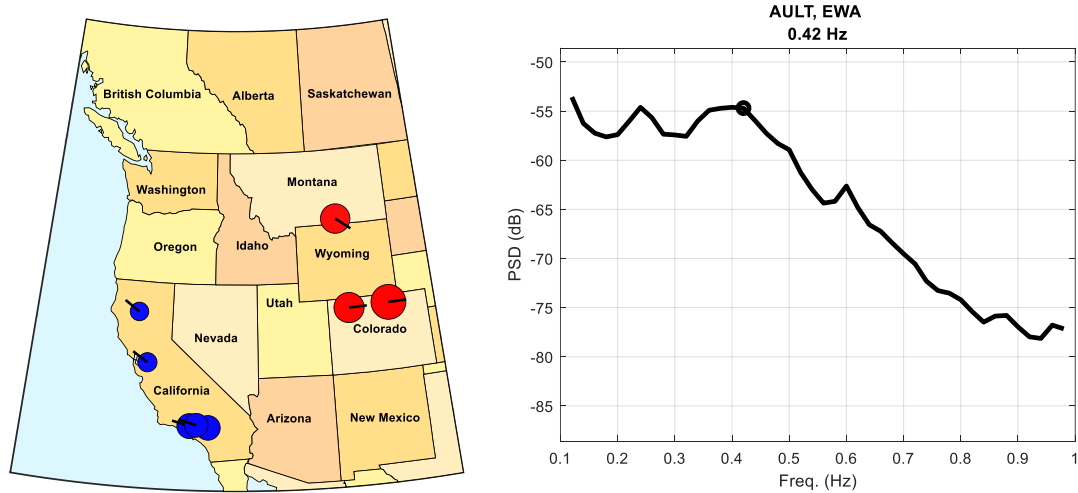


Figure F-31: 2019/05/07 from 17:10:00 to 17:30:00 UTC. Ambient condition.

## Modes of Inter-Area Power Oscillations in the Western Interconnection

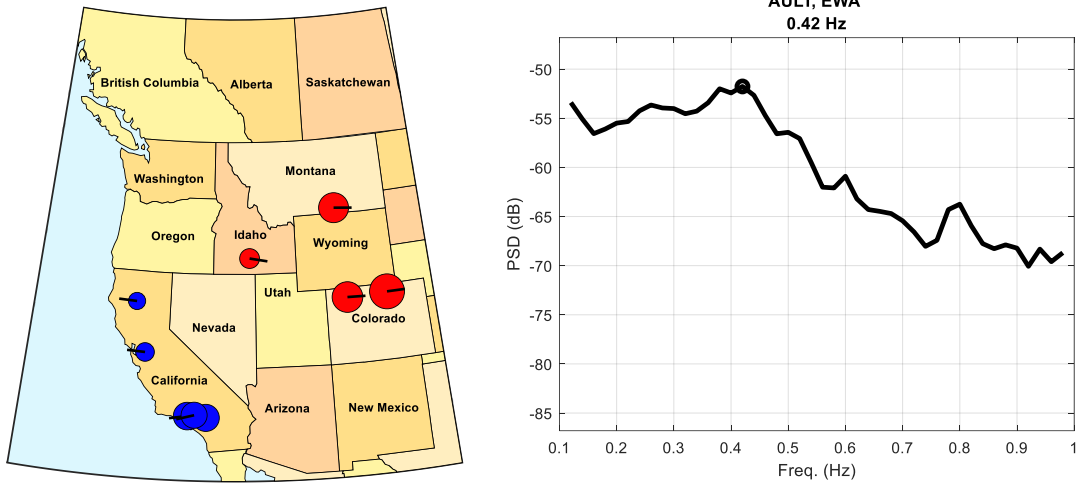


Figure F-32: 2019/05/07 from 17:30:03 to 17:50:03 UTC. PDCI probing condition.

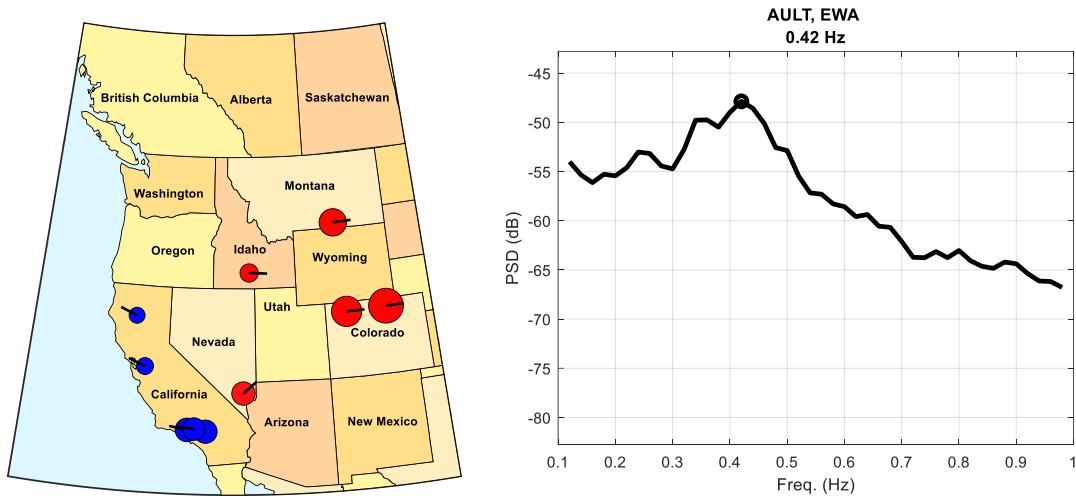


Figure F-33: 2019/05/07 from 21:20:03 to 21:40:03 UTC. PDCI probing condition.

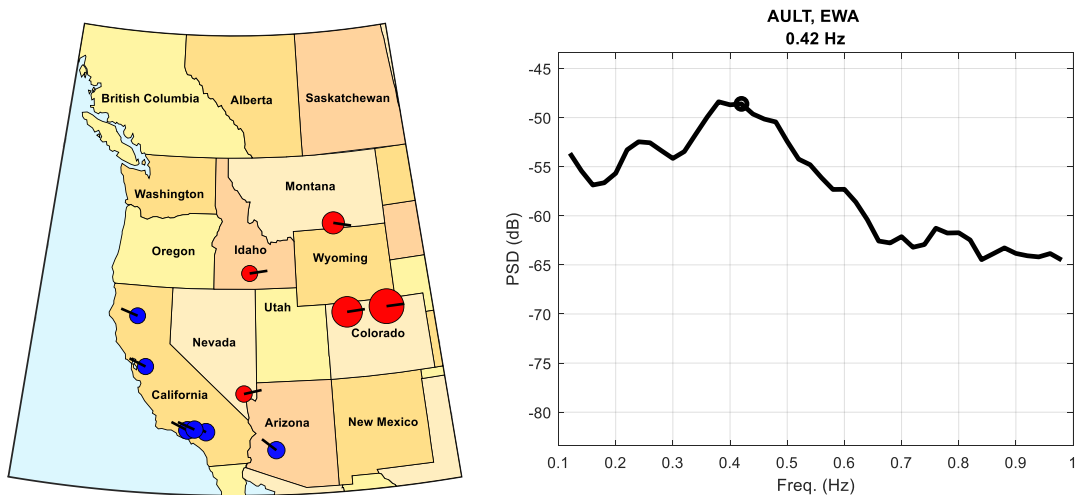


Figure F-34: 2019/05/07 from 22:10:00 to 22:30:00 UTC. Ambient condition.

## Modes of Inter-Area Power Oscillations in the Western Interconnection

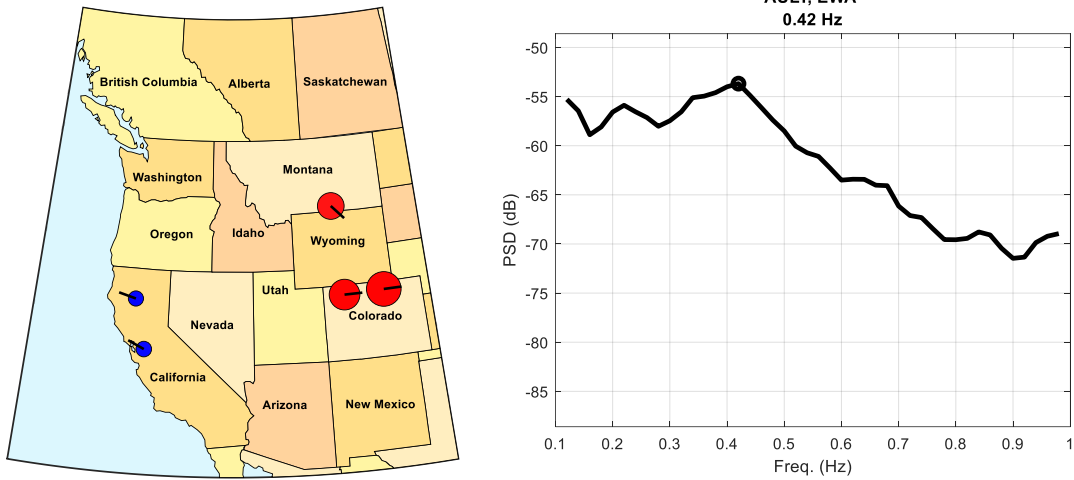


Figure F-35: 2019/05/08 from 02:10:00 to 02:30:00 UTC. Ambient condition.

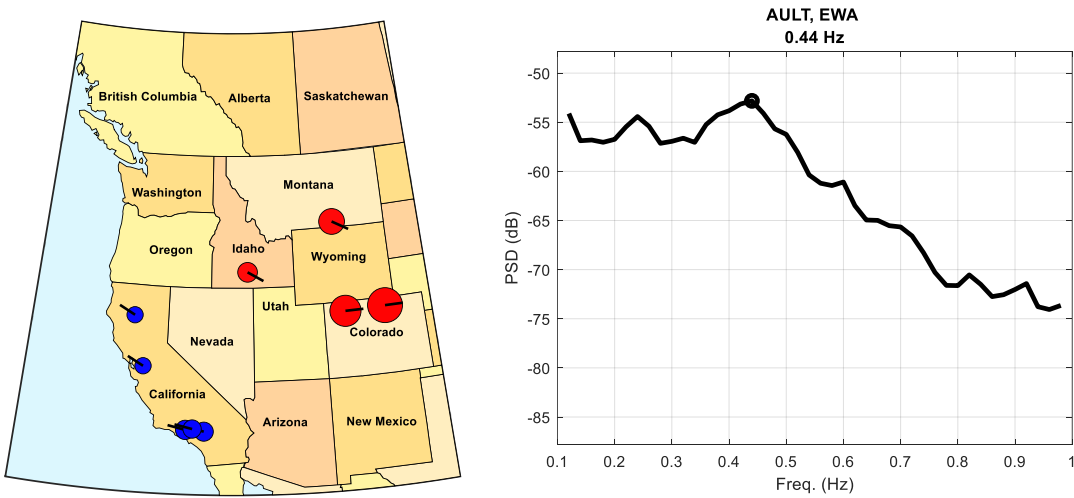


Figure F-36: 2019/05/08 from 06:10:00 to 06:30:00 UTC. Ambient condition.

## Mode Meter Analysis Results

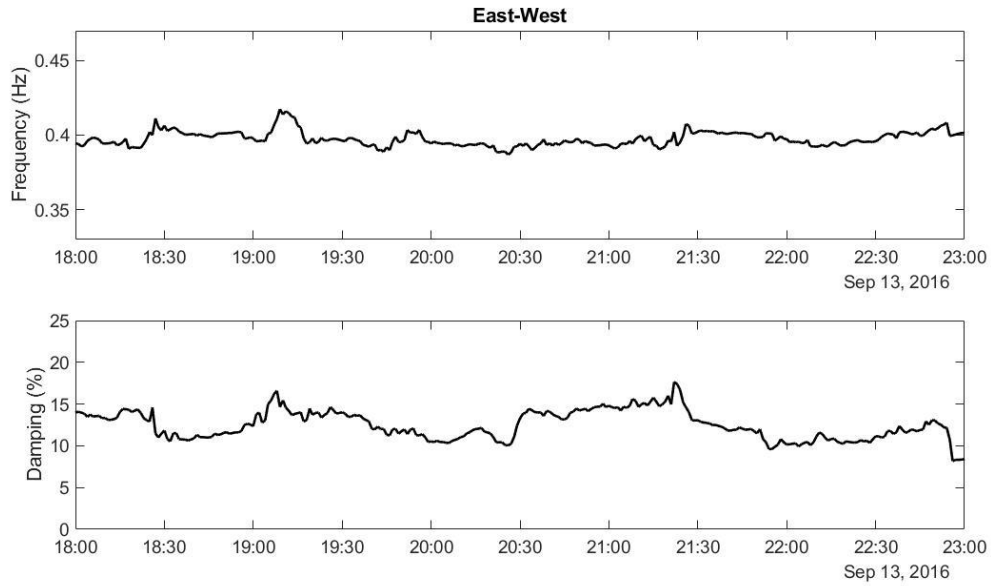


Figure F-37: 2016/09/13 dataset.

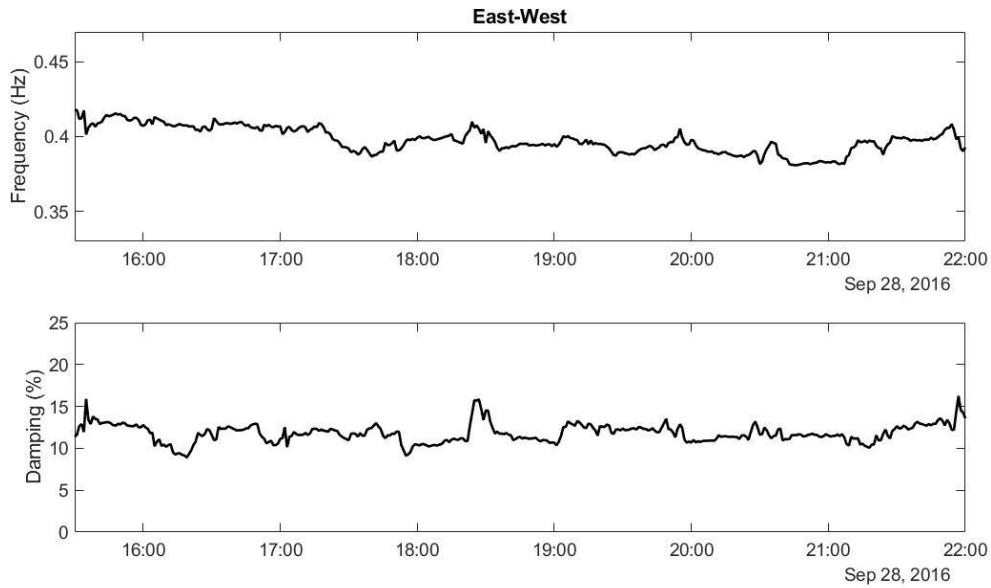
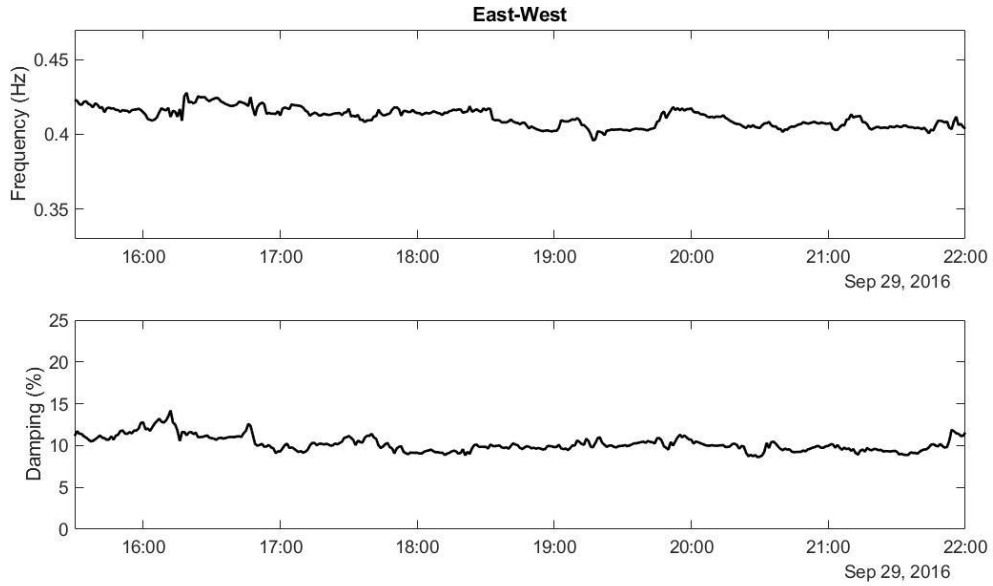
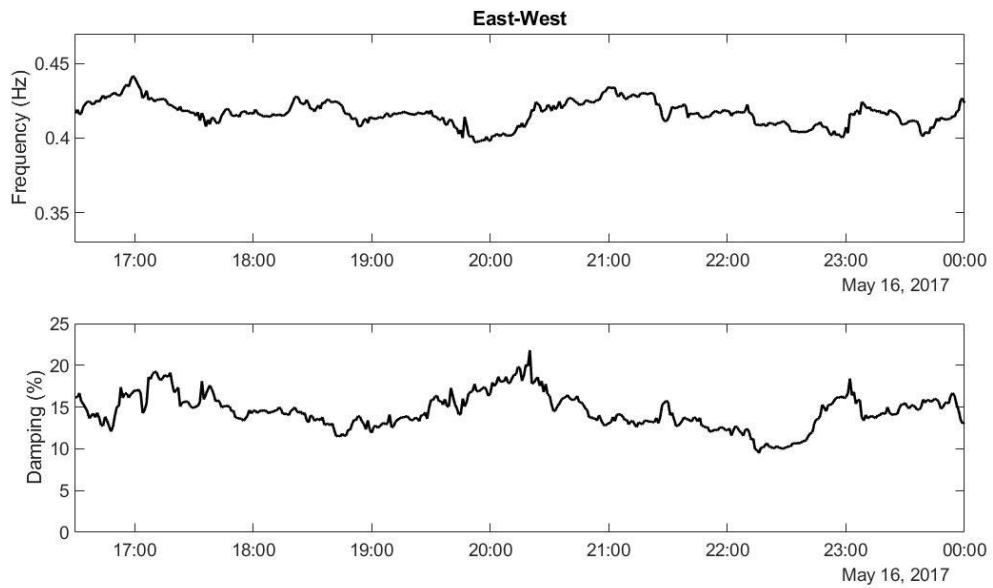


Figure F-38: 2016/09/28 dataset.

## Modes of Inter-Area Power Oscillations in the Western Interconnection



**Figure F-39: 2016/09/29 dataset.**



**Figure F-40: 2017/05/16 dataset.**

## Modes of Inter-Area Power Oscillations in the Western Interconnection

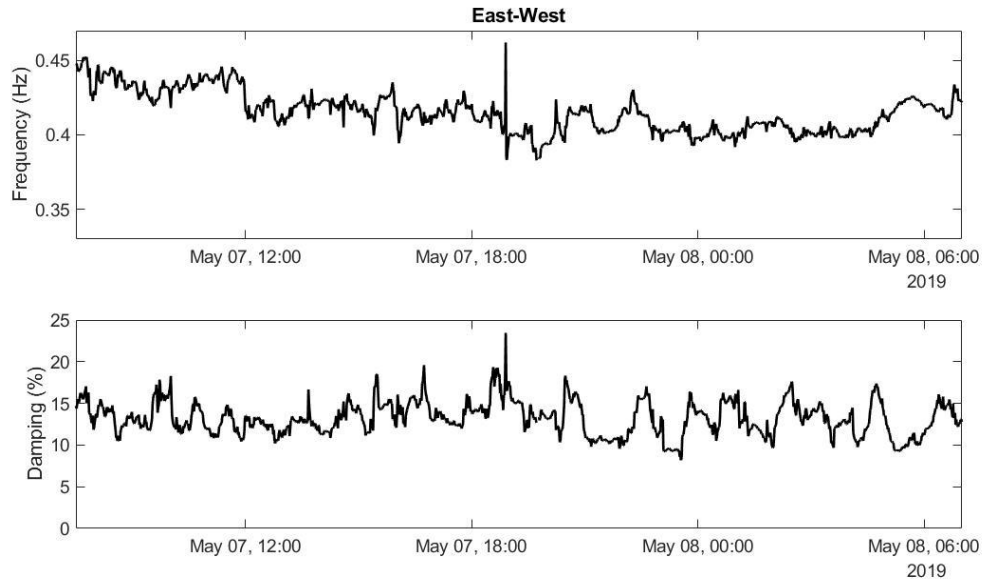


**Figure F-41: 2019/05/08 dataset.**

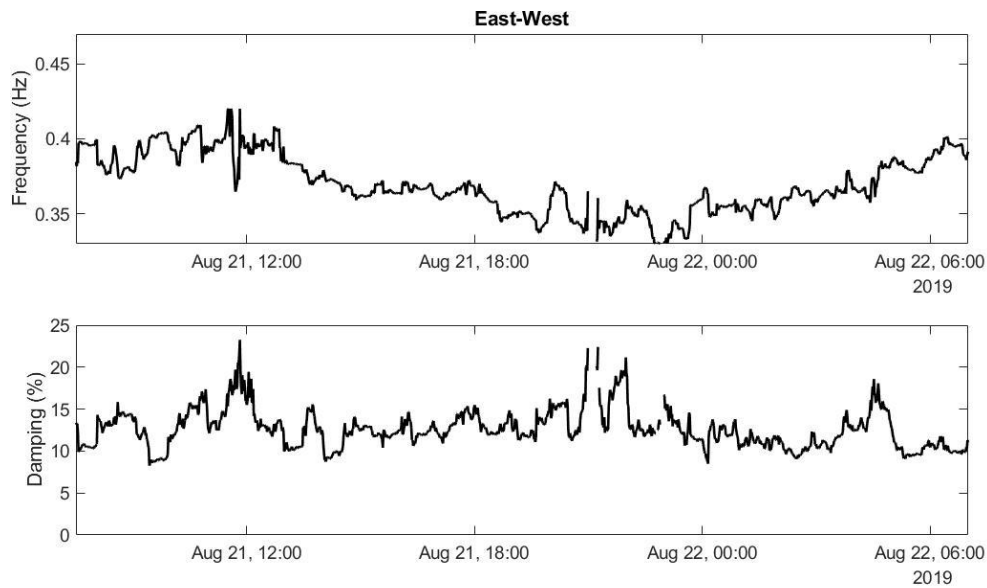


**Figure F-42: 2019/08/22 dataset.**

## Appendix G: MT Mode Analyses

### Correlation Analysis from 2016 through 2019 PMU Data

The following are the mode shape estimates for all the conditions in Table 33 from the section titled, "Montana Mode." The mode shape is shown on the left and the mode reference signal PSD is shown on the right.

#### 2016 Data

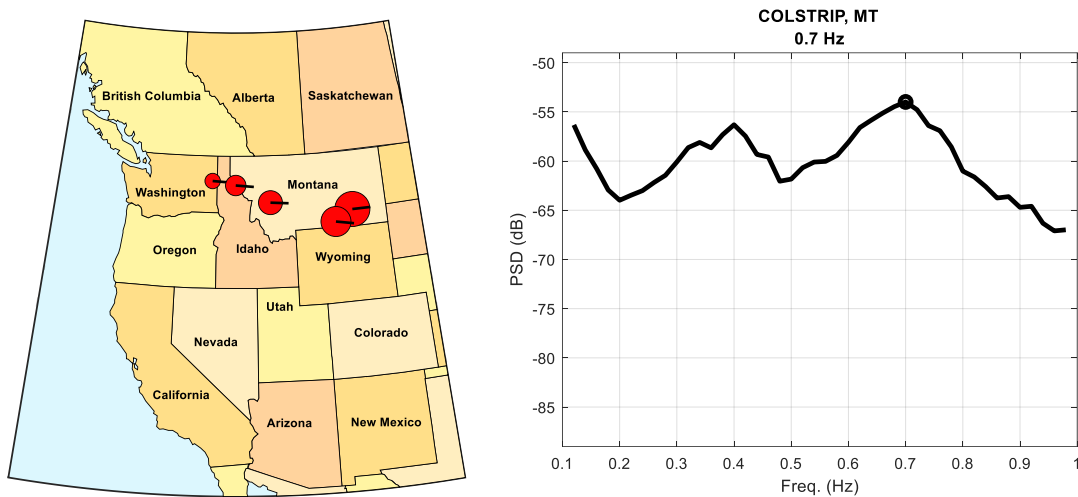


Figure G-1: 2016/09/13 from 17:10:02 to 17:30:00 UTC. Alberta disconnected, PDCI probing condition.

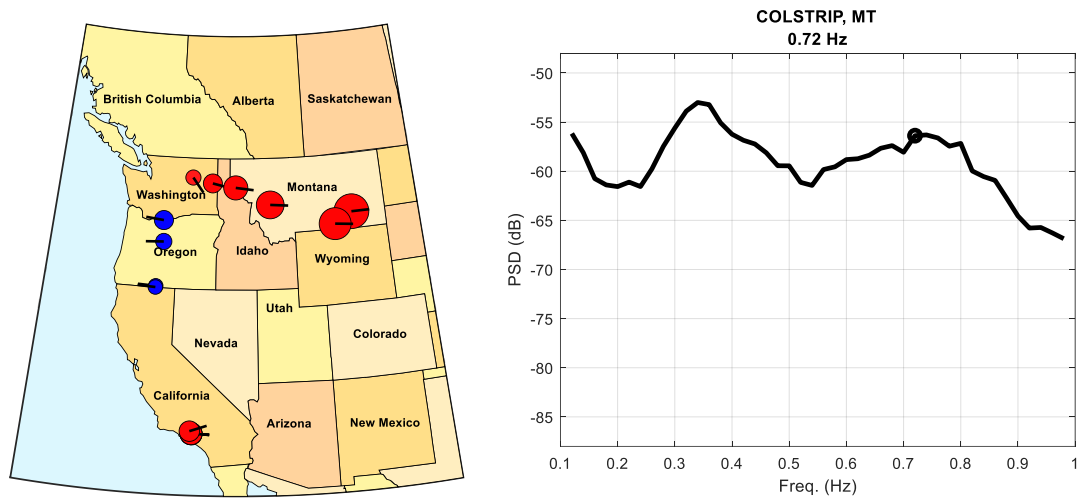


Figure G-2: 2016/09/13 from 18:30:01 to 18:50:01 UTC. Alberta disconnected, ambient condition.

## Modes of Inter-Area Power Oscillations in the Western Interconnection

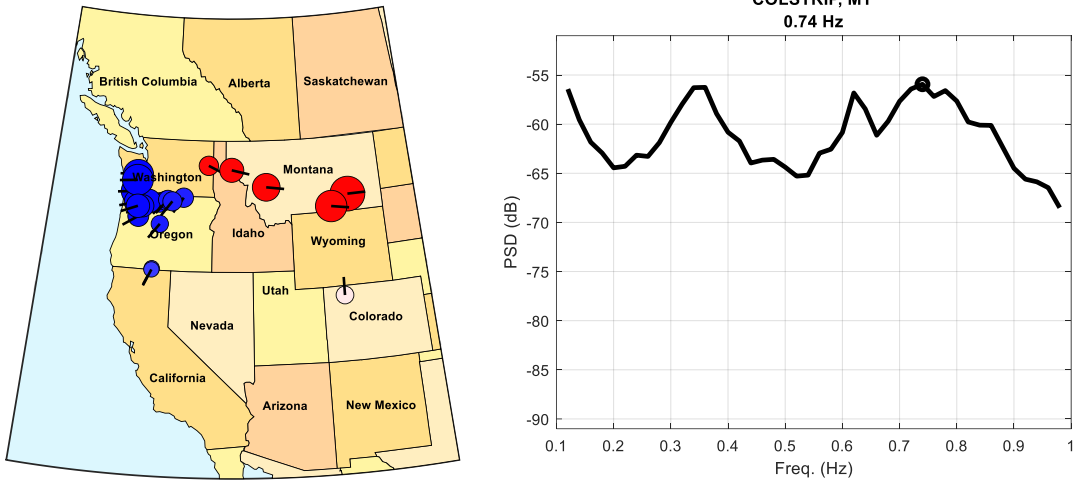


Figure G-3: 2016/09/13 from 22:10:00 to 22:28:00 UTC. Alberta disconnected, ambient condition.

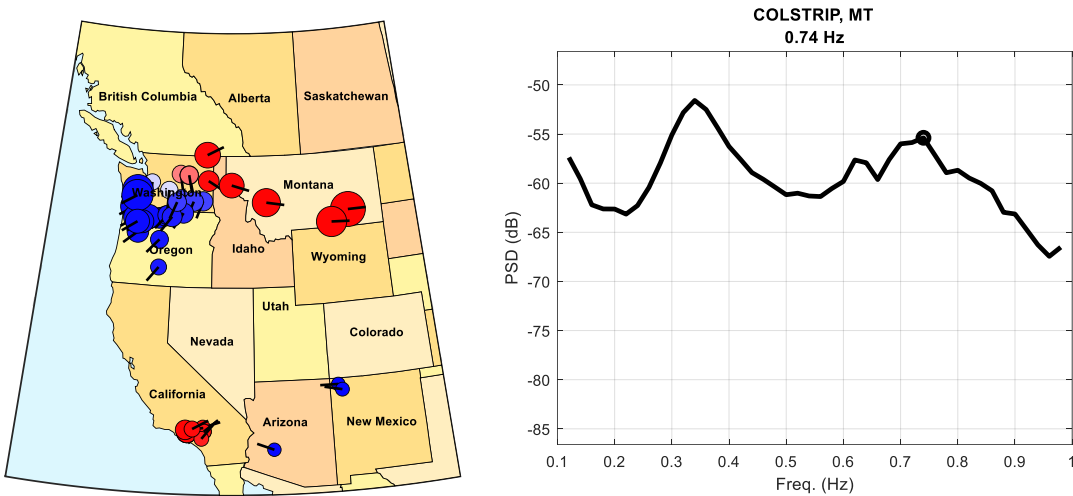


Figure G-4: 2016/09/13 from 22:28:10 to 22:48:10 UTC. Alberta disconnected, PDCI probing condition.

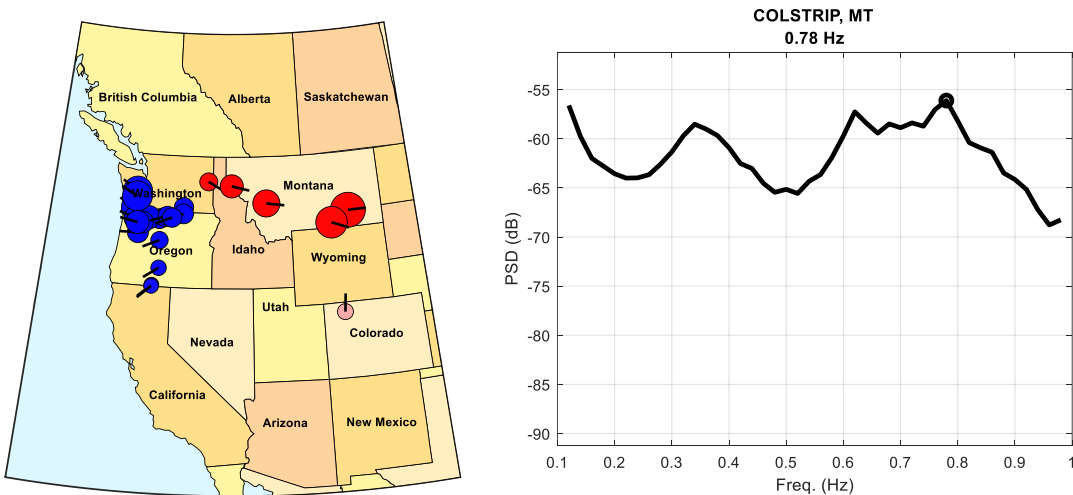


Figure G-5: 2016/09/13 from 23:10:00 to 23:30:00 UTC. Alberta disconnected, ambient condition.

## Modes of Inter-Area Power Oscillations in the Western Interconnection

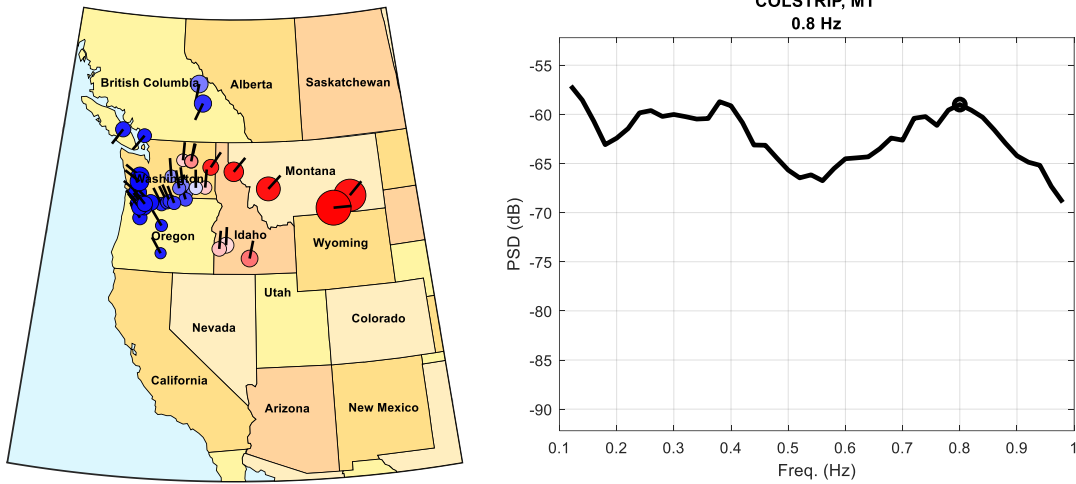


Figure G-6: 2016/09/28 from 15:10:00 to 15:30:00 UTC. Ambient condition.

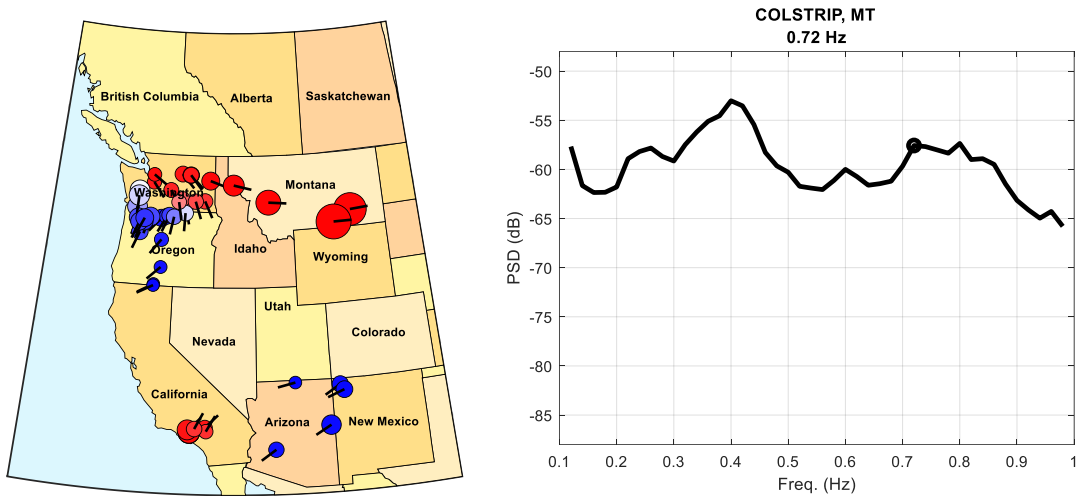


Figure G-7: 2016/09/28 from 16:30:12 to 16:40:12 UTC. PDCI probing condition.

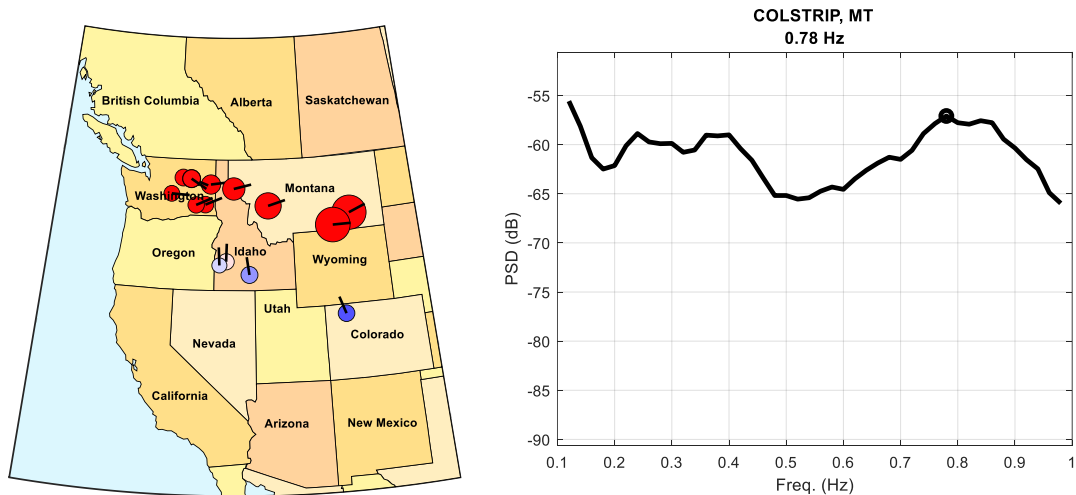


Figure G-8: 2016/09/28 from 17:10:00 to 17:30:00 UTC. Ambient condition.

## Modes of Inter-Area Power Oscillations in the Western Interconnection

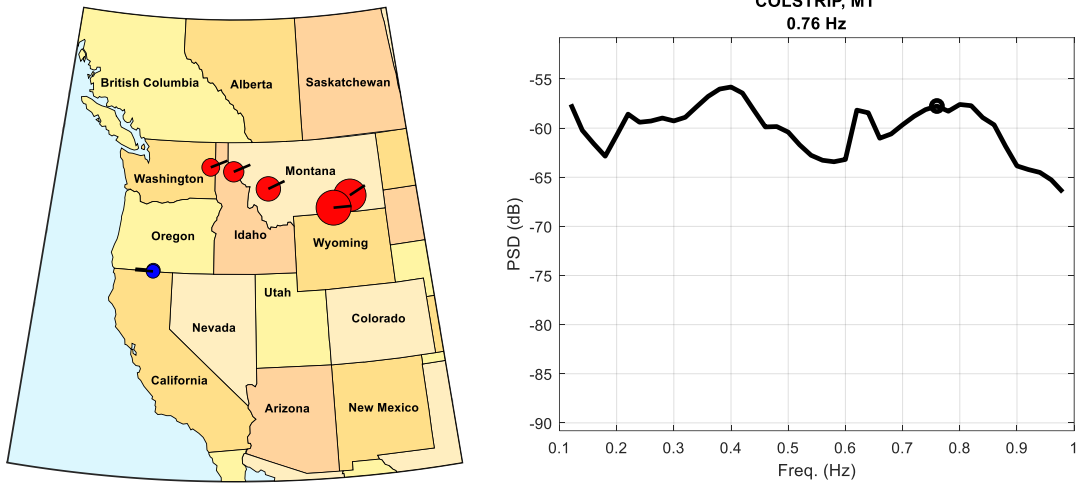


Figure G-9: 2016/09/28 from 18:20:02 to 18:40:02 UTC. PDCI probing condition.

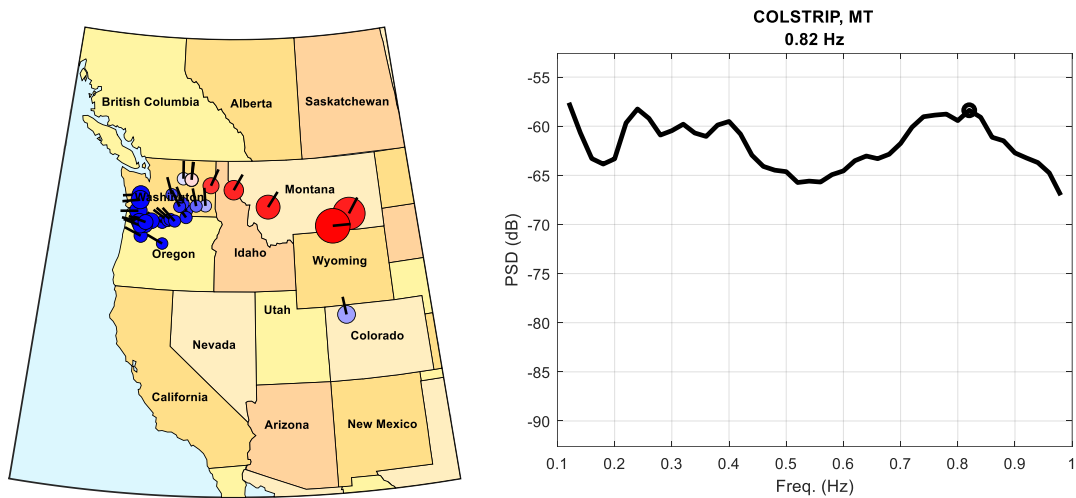


Figure G-10: 2016/09/28 from 18:46:00 to 18:59:00 UTC. Ambient condition.

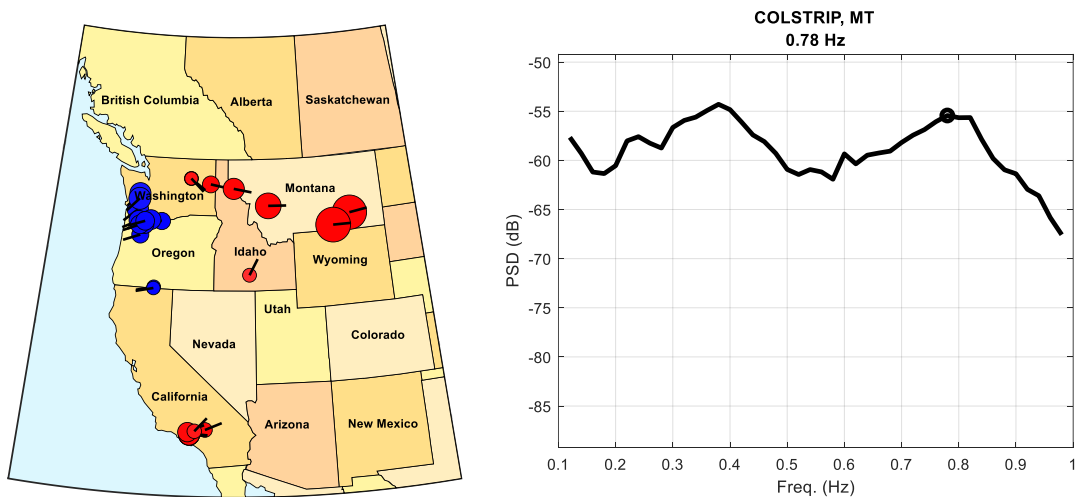


Figure G-11: 2016/09/28 from 20:30:09 to 20:40:09 UTC. PDCI probing condition.

## Modes of Inter-Area Power Oscillations in the Western Interconnection

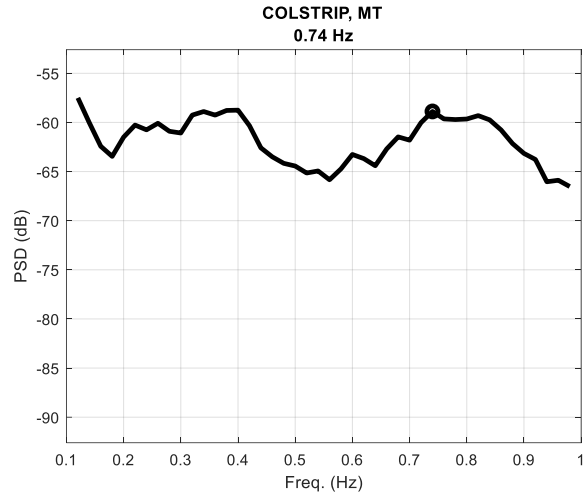


Figure G-12: 2016/09/28 from 21:10:00 to 21:30:00 UTC. Ambient condition.

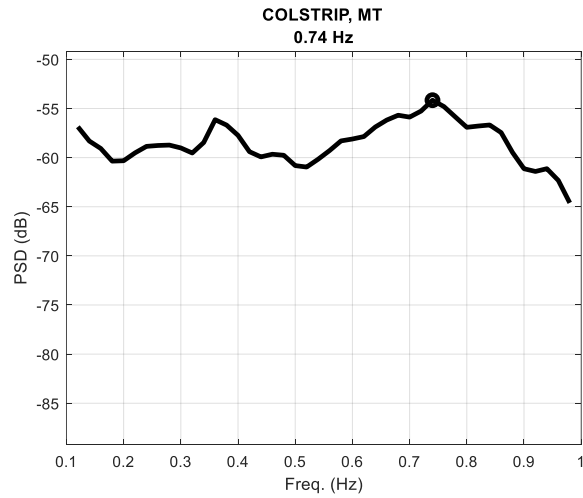
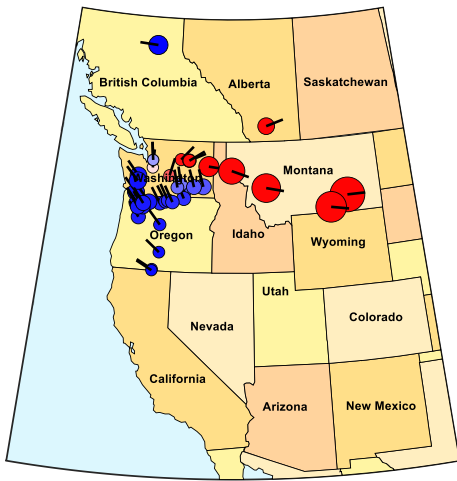


Figure G-13: 2016/09/29 from 15:10:30 to 15:30:00 UTC. Ambient condition.

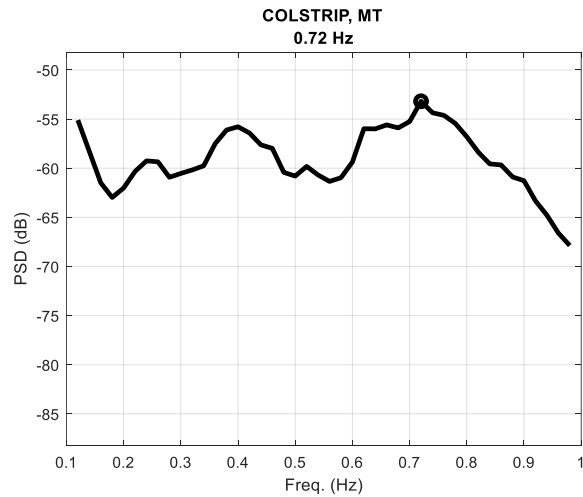


Figure G-14: 2016/09/29 from 17:10:01 to 17:20:01 UTC. PDCI probing condition.

## Modes of Inter-Area Power Oscillations in the Western Interconnection

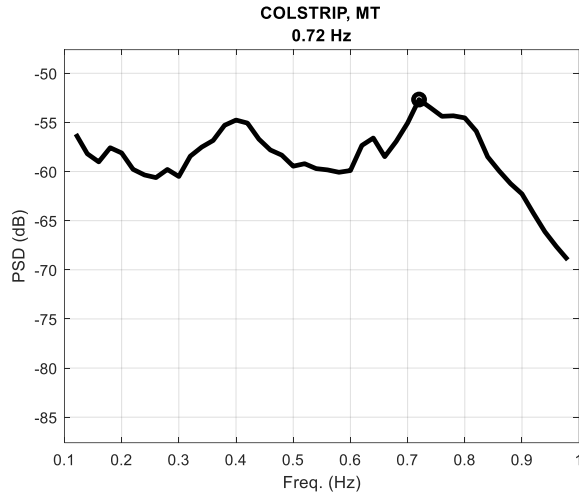


Figure G-15: 2016/09/29 from 18:10:31 to 18:20:31 UTC. PDCI probing condition.

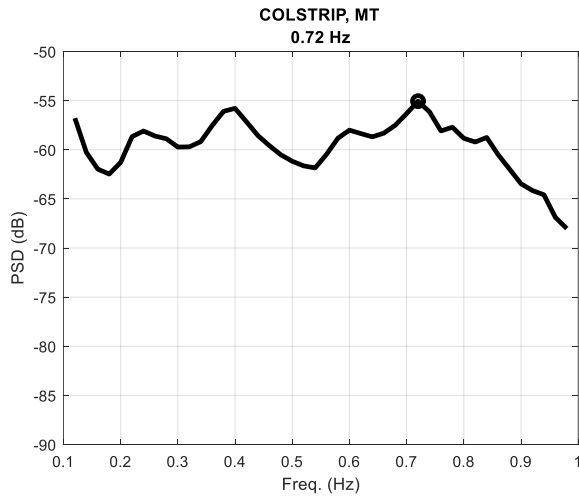


Figure G-16: 2016/09/29 from 19:10:00 to 19:30:00 UTC. Ambient condition.

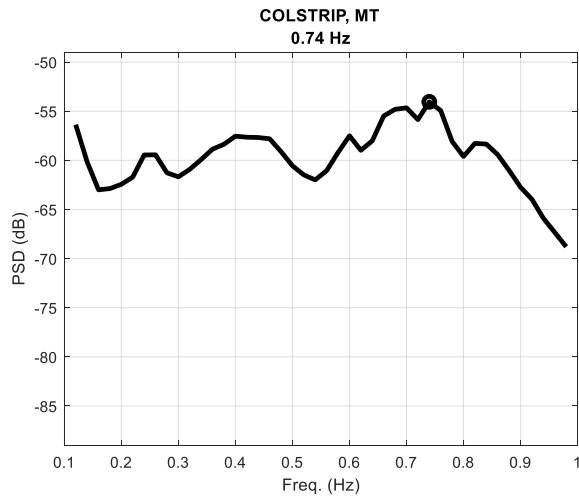


Figure G-17: 2016/09/29 from 20:10:31 to 20:20:31 UTC. PDCI probing condition.

## Modes of Inter-Area Power Oscillations in the Western Interconnection

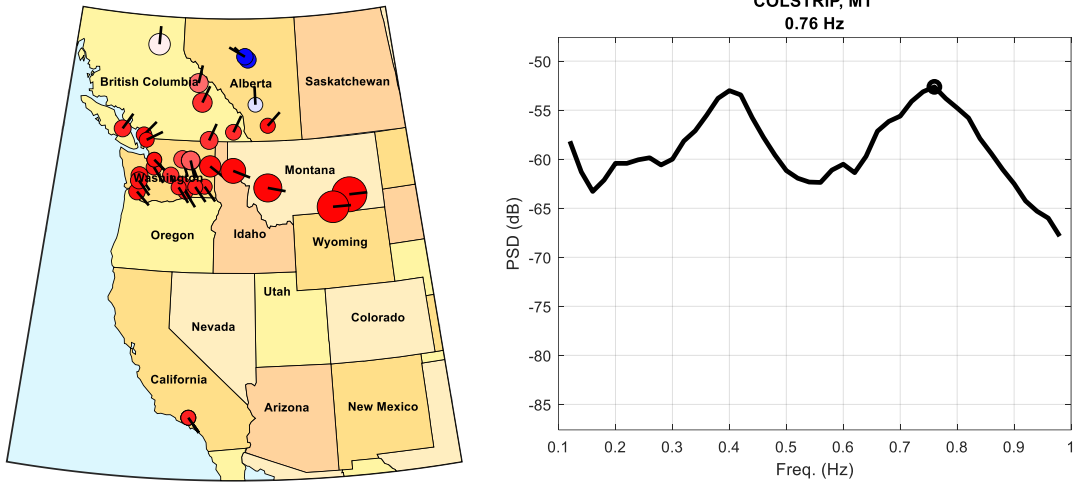


Figure G-18: 2016/09/29 from 21:10:00 to 21:30:00 UTC. Ambient condition.

### 2017 Data

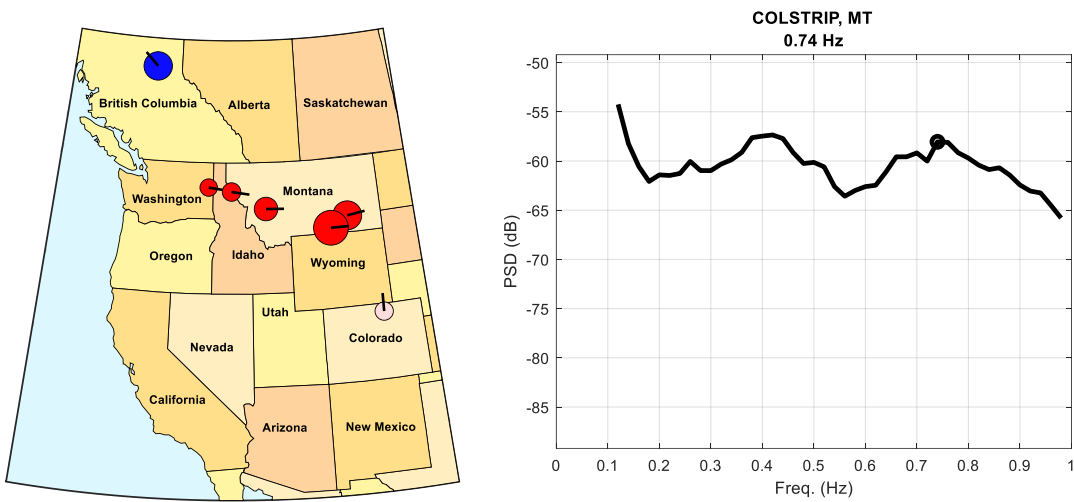


Figure G-19: 2017/05/16 from 16:16:01 to 16:36:01 UTC. PDCI probing condition.

## Modes of Inter-Area Power Oscillations in the Western Interconnection

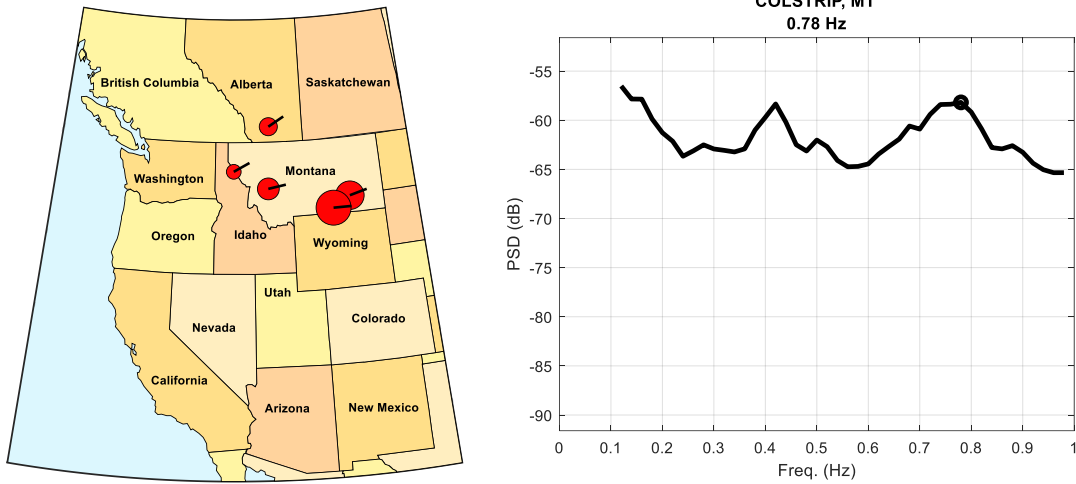


Figure G-20: 2017/05/16 from 16:36:05 to 16:50:00 UTC. Ambient condition.

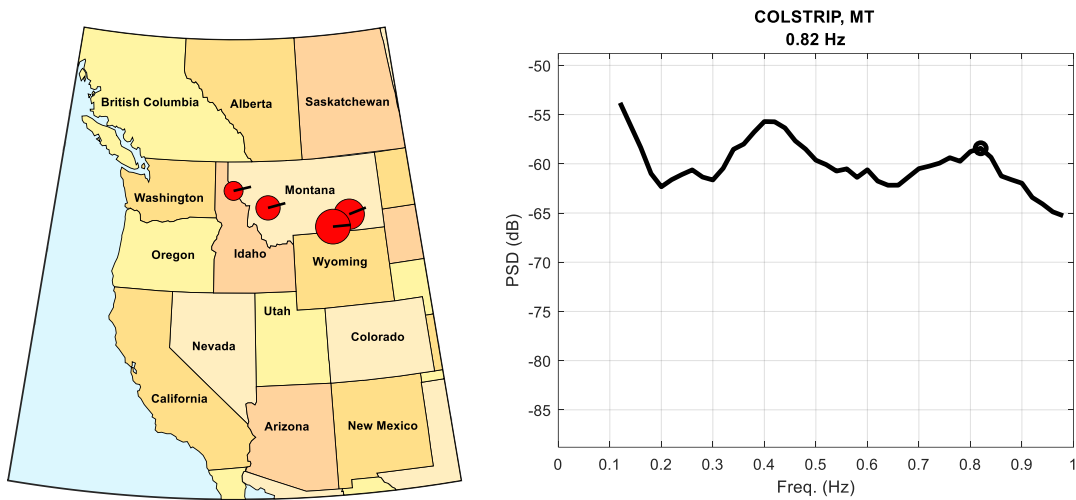


Figure G-21: 2017/05/16 from 20:15:01 to 20:35:01 UTC. PDCI probing condition.

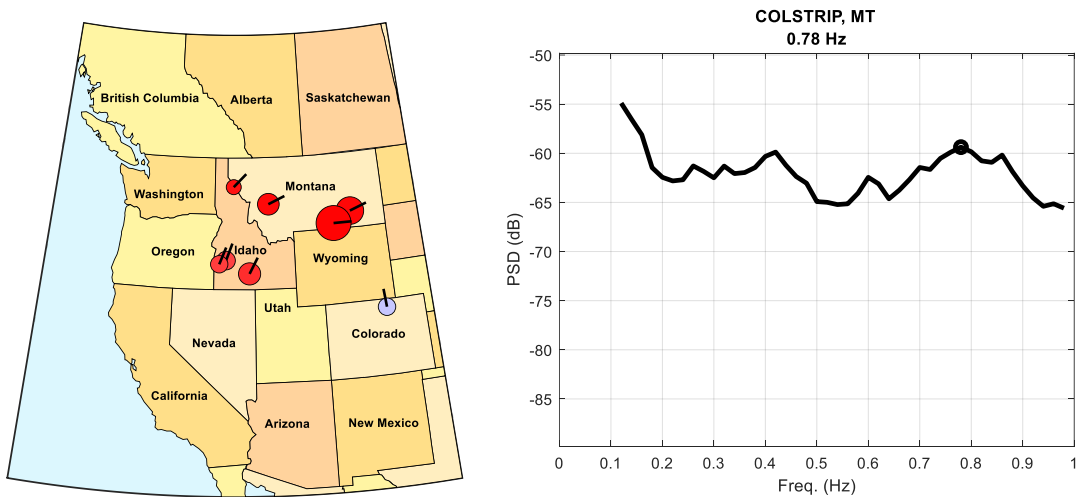


Figure G-22: 2017/05/16 from 20:35:05 to 20:50:00 UTC. Ambient condition.

# Modes of Inter-Area Power Oscillations in the Western Interconnection

2018 Data

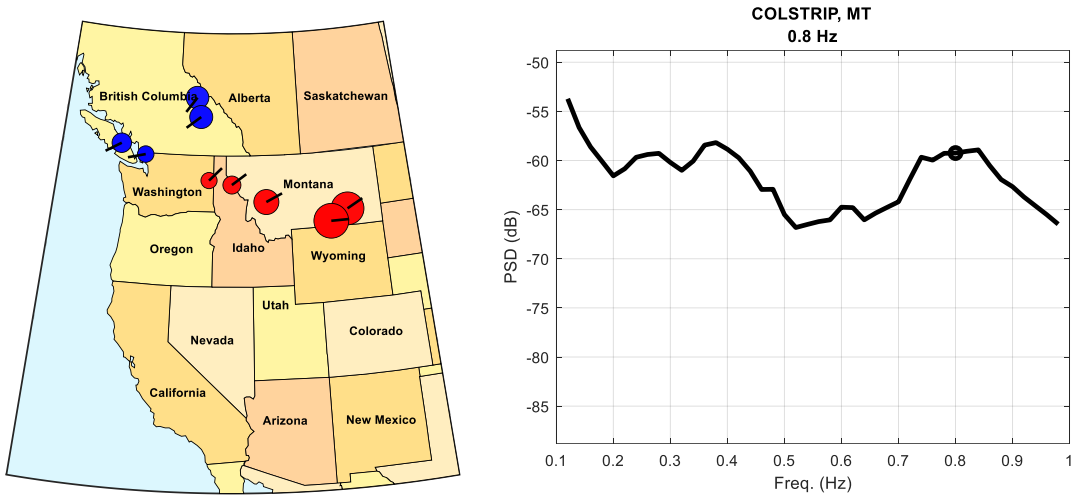


Figure G-23: 2018/05/23 from 16:05:00 to 16:24:30 UTC. Ambient condition.

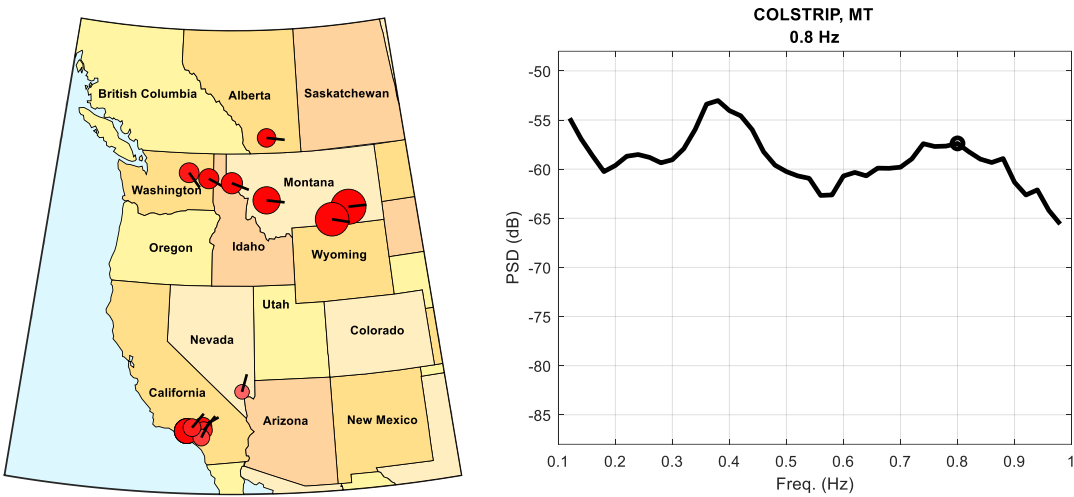


Figure G-24: 2018/05/23 from 16:28:00 to 16:48:00 UTC. PDCI probing condition.

## Modes of Inter-Area Power Oscillations in the Western Interconnection

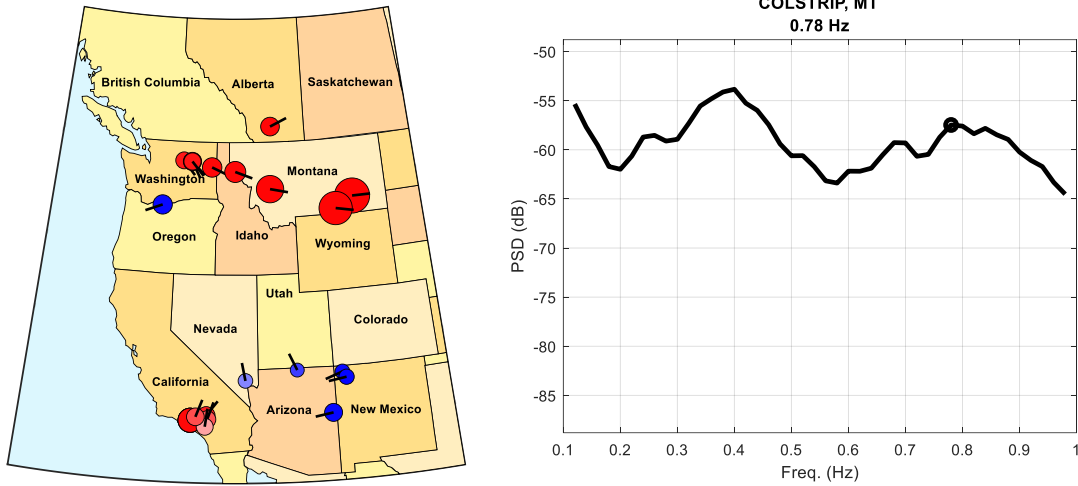


Figure G-25: 2018/05/23 from 20:15:00 to 20:35:00 UTC. PDCI probing condition.

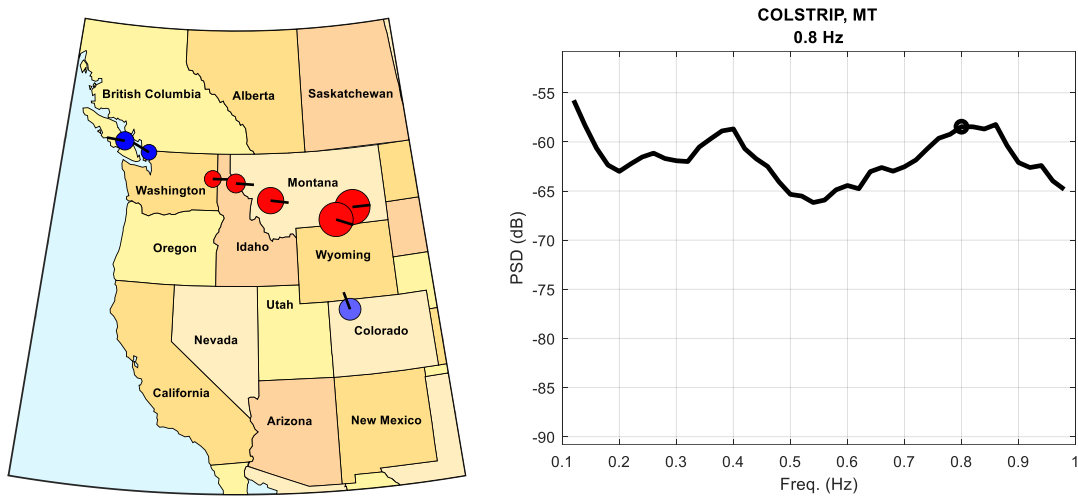


Figure G-26: 2018/05/23 from 20:36:00 to 20:55:00 UTC. Ambient condition.

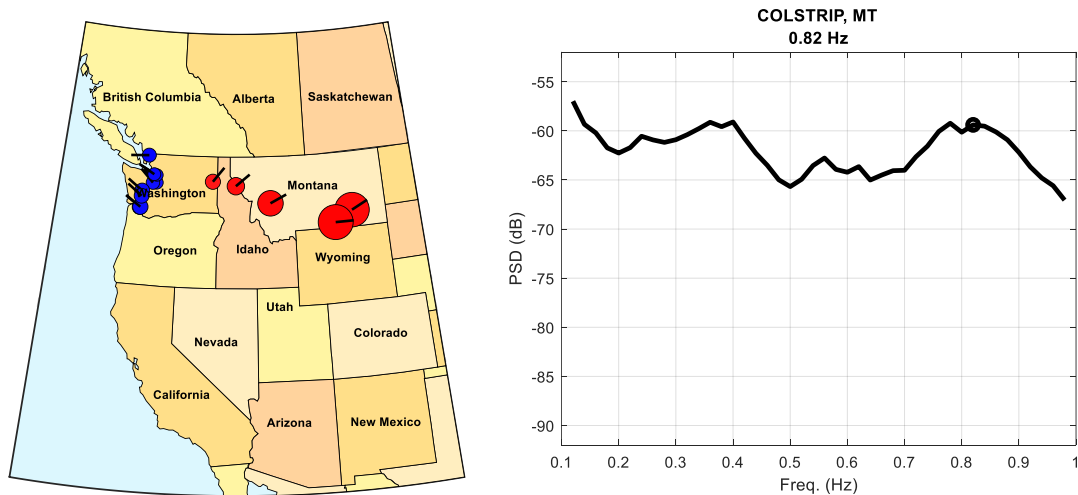


Figure G-27: 2018/05/24 from 00:10:00 to 00:30:00 UTC. Ambient condition.

## Modes of Inter-Area Power Oscillations in the Western Interconnection

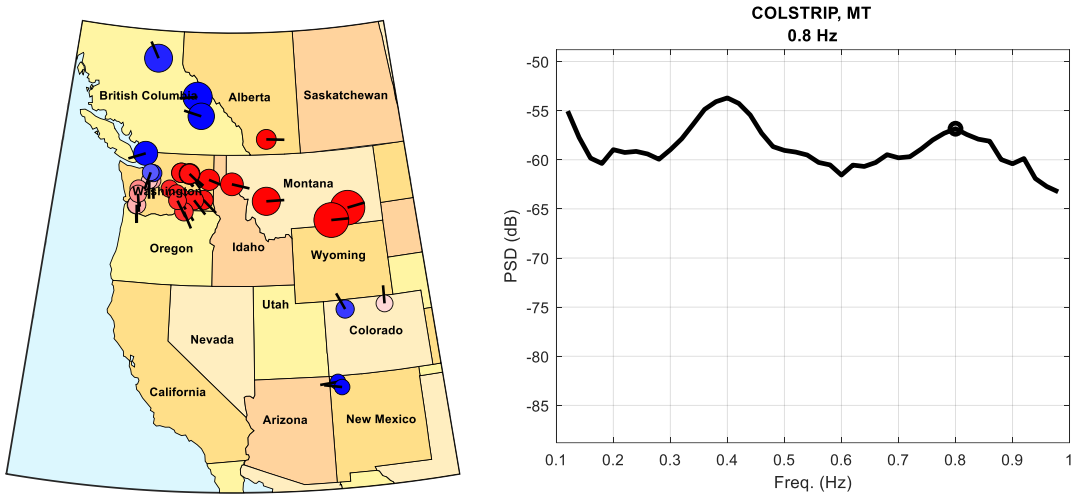


Figure G-28: 2018/05/24 from 17:14:05 to 17:34:00 UTC. PDCI probing condition.

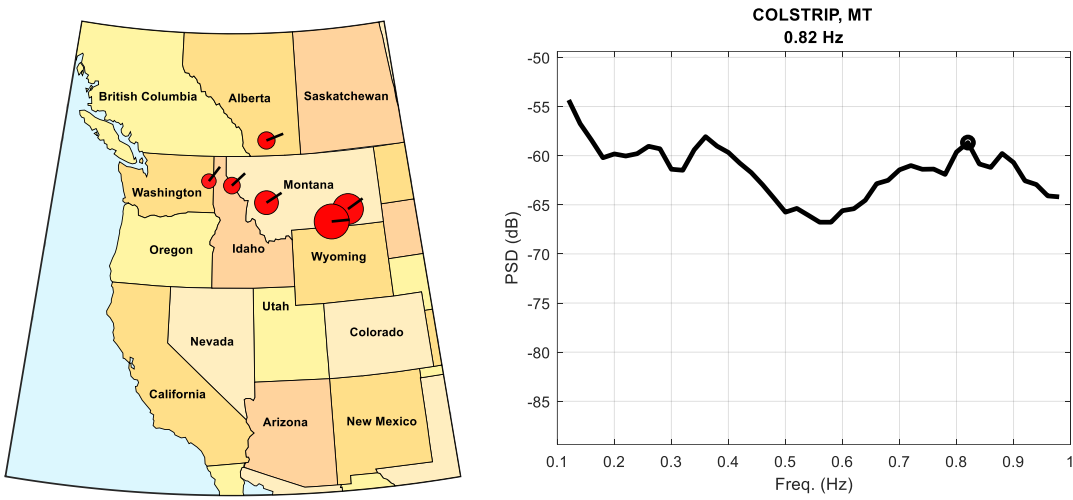


Figure G-29: 2018/05/24 from 17:36:00 to 17:50:00 UTC. Ambient condition.

# Modes of Inter-Area Power Oscillations in the Western Interconnection

2019 Data

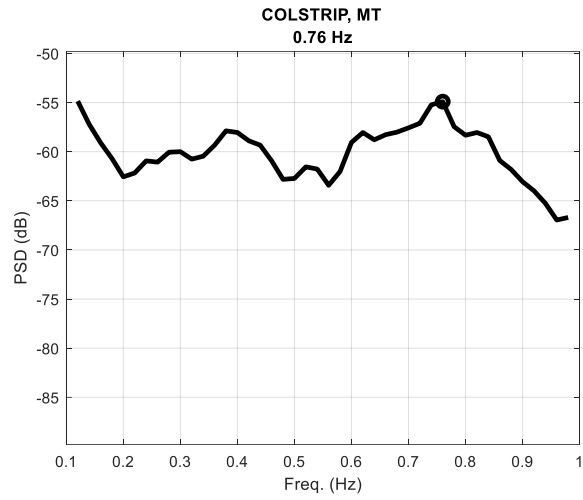


Figure G-30: 2019/05/07 from 14:10:00 to 14:30:00 UTC. Ambient condition.

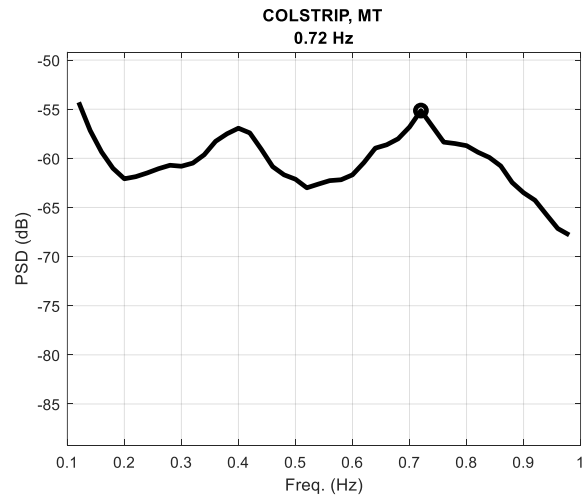


Figure G-31: 2019/05/07 from 17:10:00 to 17:30:00 UTC. Ambient condition.

## Modes of Inter-Area Power Oscillations in the Western Interconnection

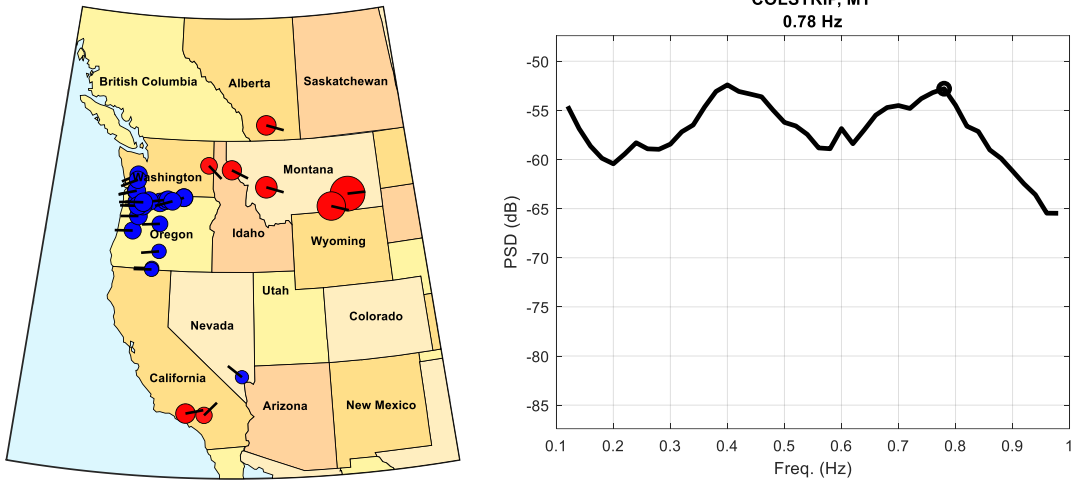


Figure G-32: 2019/05/07 from 17:30:03 to 17:50:03 UTC. PDCI probing condition.

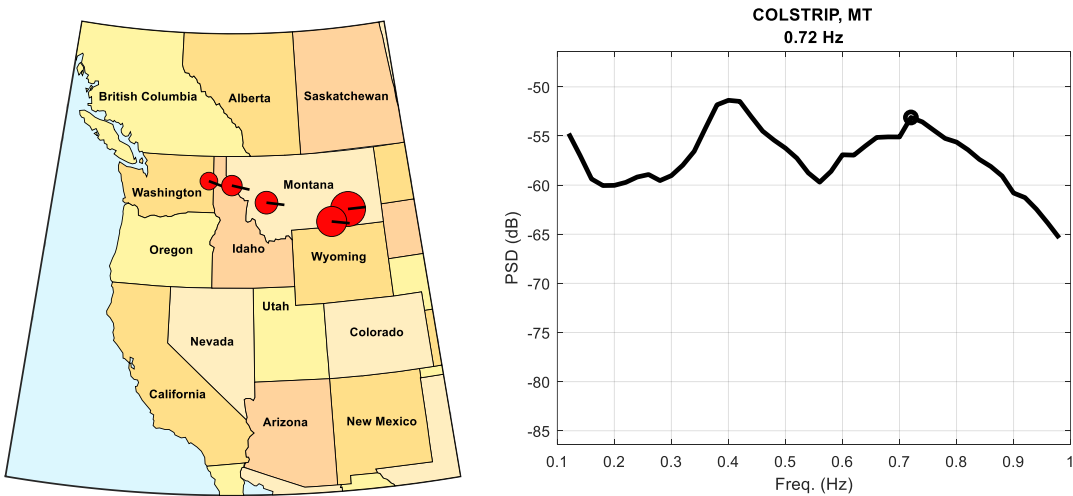


Figure G-33: 2019/05/07 from 21:20:03 to 21:40:03 UTC. PDCI probing condition.

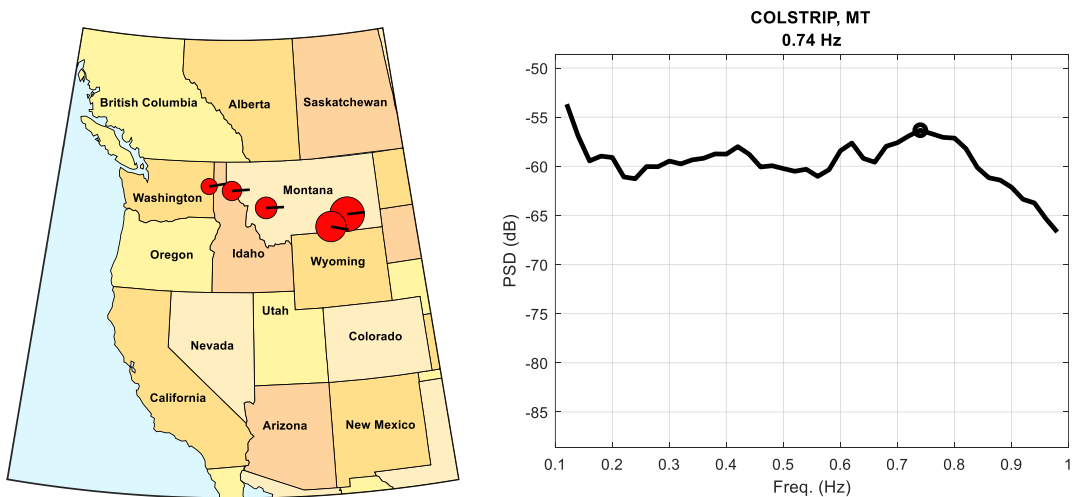


Figure G-34: 2019/05/07 from 22:10:00 to 22:30:00 UTC. Ambient condition.

## Modes of Inter-Area Power Oscillations in the Western Interconnection

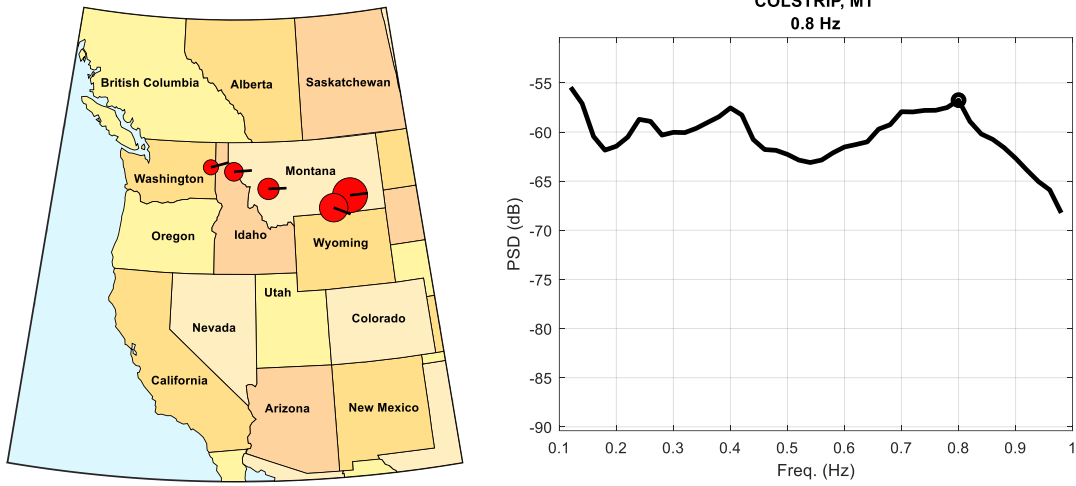


Figure G-35: 2019/05/08 from 02:10:00 to 02:30:00 UTC. Ambient condition.

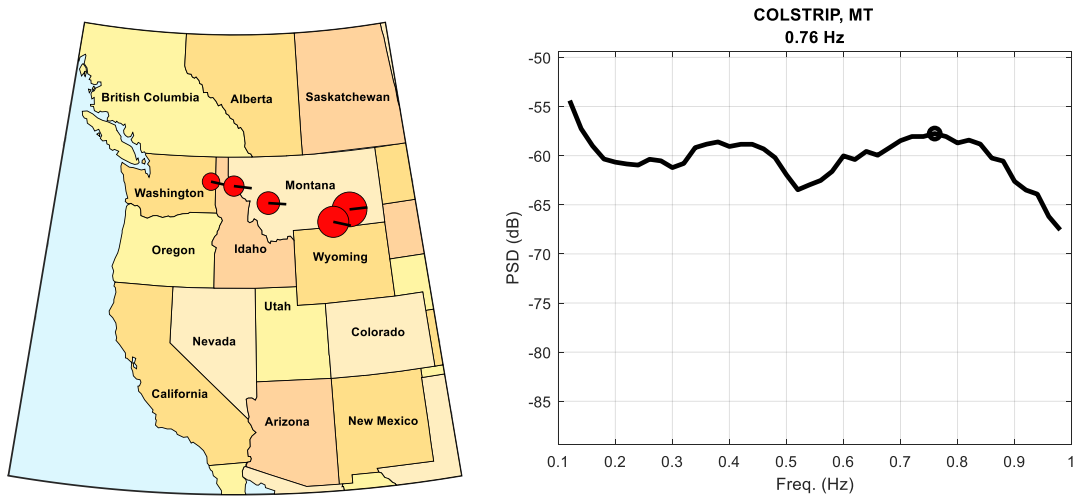


Figure G-36: 2019/05/08 from 06:10:00 to 06:30:00 UTC. Ambient condition.

## Mode Meter Analysis Results

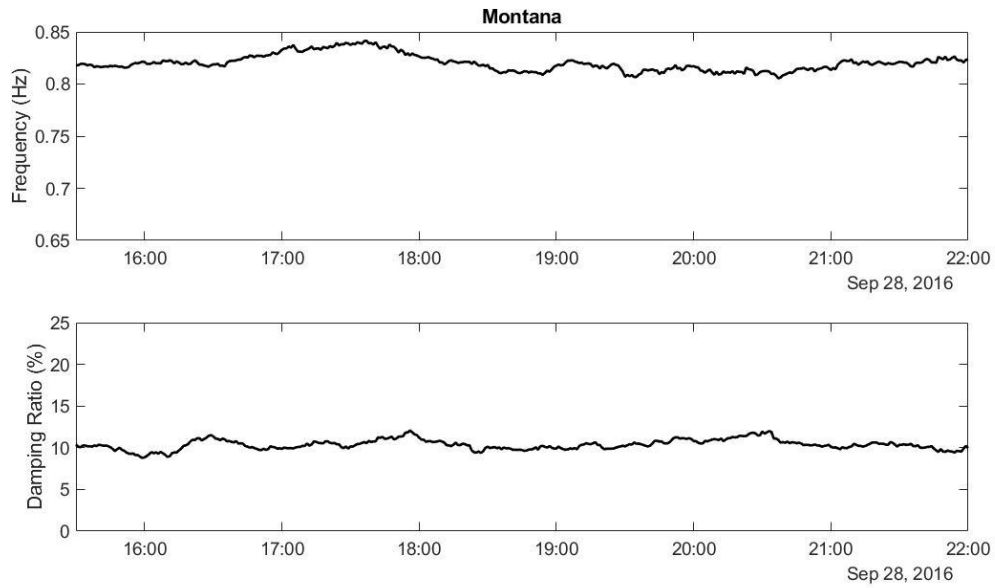


Figure G-37: 2016/09/28 dataset.

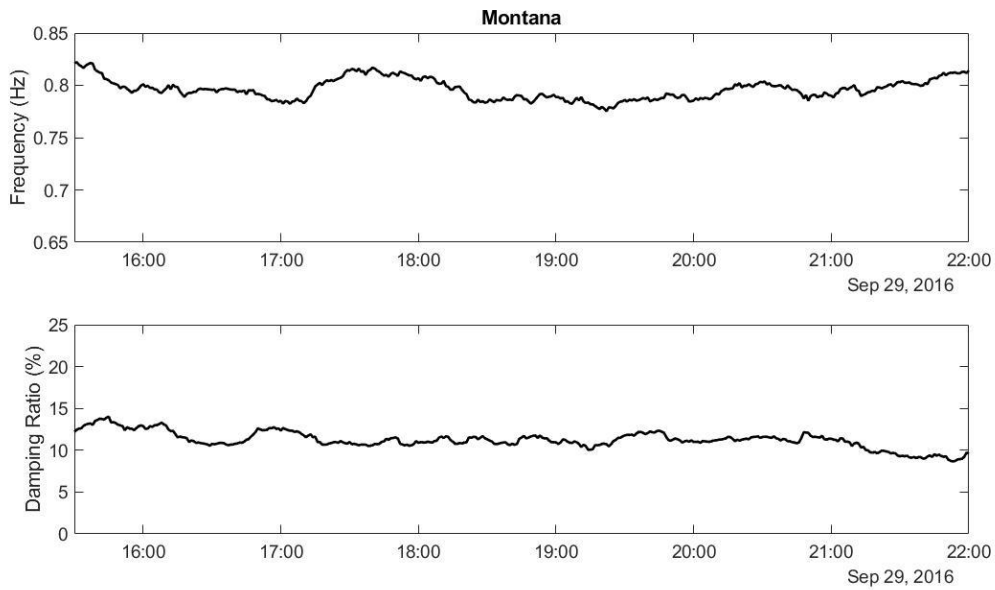


Figure G-38: 2016/09/29 dataset.

## Modes of Inter-Area Power Oscillations in the Western Interconnection

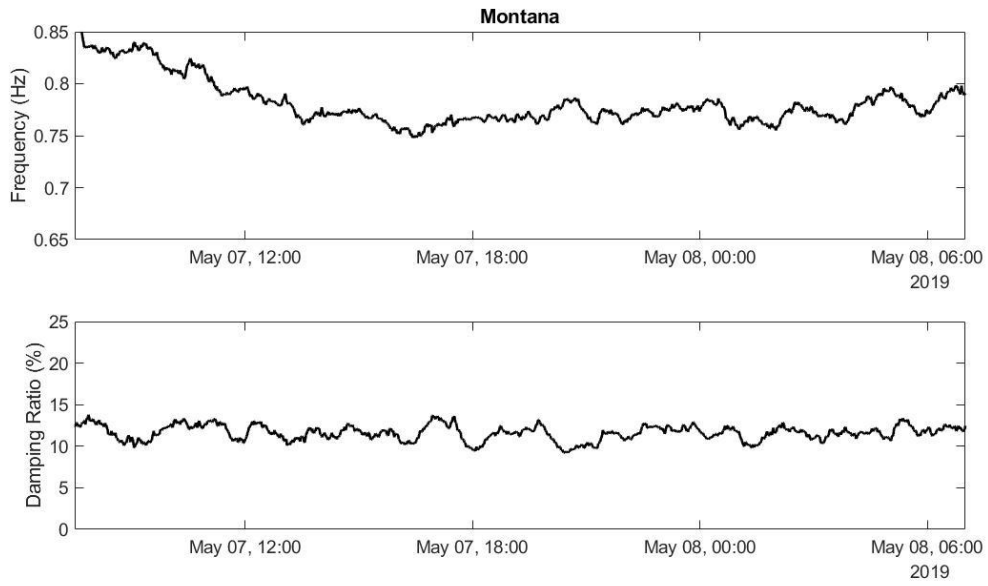


Figure G-39: 2019/05/08 dataset.

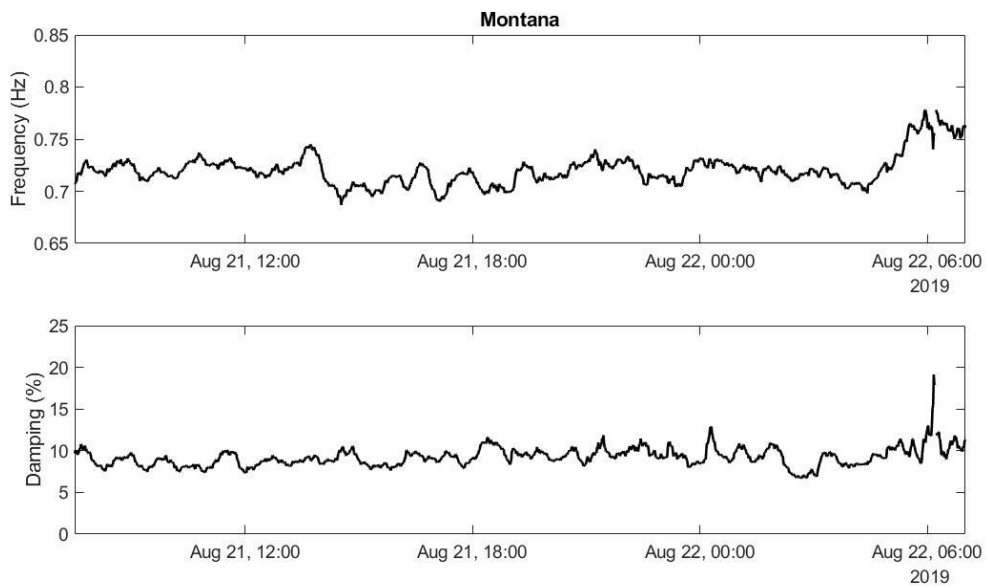


Figure G-40: 2019/08/22 dataset.

## Modes of Inter-Area Power Oscillations in the Western Interconnection

*WECC receives data used in its analyses from a wide variety of sources. WECC strives to source its data from reliable entities and undertakes reasonable efforts to validate the accuracy of the data used. WECC believes the data contained herein and used in its analyses is accurate and reliable. However, WECC disclaims any and all representations, guarantees, warranties, and liability for the information contained herein and any use thereof. Persons who use and rely on the information contained herein do so at their own risk.*

